Diffuse γ-Ray Emission from the Galactic Centre with H.E.S.S.

Diffuse γ-Strahlung aus dem Galaktischen Zentrum mit H.E.S.S.

Der Naturwissenschaftlichen Fakultät
der Friedrich-Alexander-Universität Erlangen-Nürnberg

zur Erlangung des Doktorgrades Dr. rer. nat.

vorgelegt von
Yu Wun Wong

Als Dissertation genehmigt von der Naturwissenschaftlichen Fakultät
der Friedrich-Alexander-Universität Erlangen-Nürnberg

Tag der mündlichen Prüfung: 10th March 2023

Gutachter: Prof. Dr. Christopher van Eldik
Prof. Dr. Stefan Funk

To my mother, father and brother

Abstract

The High Energy Stereoscopic System (H.E.S.S.) experiment uses the Imaging Atmospheric Cherenkov Technique (IACT) to study very-high-energy (VHE) γ-ray astrophysics. Its southern location provides the best opportunity to observe the Galactic Centre region. The Galactic Centre hosts many violent astrophysical objects and molecular gases. The diffuse TeV γ-ray emission in the Central Molecular Zone (CMZ) reveals the existence of powerful cosmic-ray (CR) accelerator(s) in the Galactic Centre. In particular, various studies postulated a PeV accelerator (PeVatron) continuously injecting CR protons to the ambience, resulting in a complex γ-ray morphology and absence of cutoff signature in the diffuse γ-ray spectrum. This study, using 11 years of H.E.S.S. data and an advanced 3D maximum-likelihood analysis method, re-establishes and constrains the diffuse γ-ray emission nature at 0.4 – 100 TeV. CR propagation is modelled and diffuse emission templates for the analysis are built accordingly, by assuming a hadronic origin in the Galactic Centre. This study unveils a CR energy cutoff at couple hundreds of TeV, opposing the postulation of a PeVatron existing in the Galactic Centre. Apart from the scenario of a continuously CR injecting source, an impulsively injecting source cannot be ruled out.

Kurzfassung

Das High Energy Stereoscopic System (H.E.S.S.) basierend auf der Imaging Atmospheric Cherenkov Technique (IACT) untersucht die Astrophysik der sehr hoch energetischen γ-Strahlung. Die Lage in der südlichen Hemisphäre bietet die besten Voraussetzungen um die Region des Galaktischen Zentrums zu beobachten. Das Galaktische Zentrum beherbergt viele emissionsstarke astrophysikalische Objekte und eine starke Anhäufung molekularen Gases. Die diffuse TeV γ-Strahlung in der zentralen molekularen Zone (CMZ) weist auf die Existenz leistungsstarker Beschleuniger für kosmische Strahlung (CR) im Galaktischen Zentrum hin. In unterschiedlichen Studien wurde die Existenz eines PeV-Beschleunigers (PeVatron) postuliert, der kontinuierlich CR-Protonen in seine Umgebung ausstößt, was zu einer komplexen γ-Strahlungsmorphologie und dem Fehlen einer Cutoff-Signatur im diffusen γ-Strahlenspektrum führt. In dieser Studie wird mit H.E.S.S.-Daten, aufgenommen innerhalb von 11 Jahren, und der fortschrittlichen 3D-Maximum-Likelihood-Analysemethode die Natur der diffusen γ-Strahlung im Energiebereich 0,4 – 100 TeV neu bestimmt und eingegrenzt. Die Propagation der CRs wird modelliert und Templates für die zu erwartende diffuse γ-Strahlung werden unter der Annahme eines hadronischen Ursprungs im galaktischen Zentrum erstellt. Diese Studie enthüllt eine CR-Energieschwelle bei einigen Hundert TeV, die der Annahme eines PeVatrons im Galaktischen Zentrum widerspricht. Neben dem Szenario einer kontinuierlich CRs injizierenden Quelle kann auch eine impulsiv injizierende Quelle nicht ausgeschlossen werden.

Table of Contents

"I,
a universe of atoms,
an atom in the universe."

Richard P. Feynman

Chapter 1

Motivation

Day and night, our Earth is exposed to a flux of highly isotropic particles called cosmic-rays (CRs). These particles are highly energetic, yet they are also non-thermal. It is believed that these CRs are energised by a non-thermal mechanism at acceleration sites in the Universe, and are isotropised during the propagation in Galactic magnetic field [80]. To locate these acceleration sites without the influence from the magnetic field, very-high-energy (VHE) gamma-rays (γ-rays) can be used for indirect observation.

One of the popular candidates for the origin of energetic CRs, by no surprise, is the Galactic Centre. The Galactic Centre hosts many astrophysical objects, including the super-massive black hole, supernova remnants and pulsar wind nebulae. In addition, this region is surrounded by a large amount of gas which is called the central molecular zone (CMZ) [1]. If a source in the Galactic Centre is the production site of CRs, these CRs will diffuse and interact with the large-scale gases, producing the VHE γ-rays. Through the study of diffuse γ-ray emission in the CMZ, the diffusion nature of CRs as well as the locations of CR accelerators could be revealed.

Previous studies discussed the possible existence of a Galactic central accelerator that might be responsible for the diffuse γ-ray emission in the CMZ [56, 57, 116, 24]. This accelerator might even be able to accelerate CRs to the PeV energy regime, sources of which are known as PeVatrons. This study, using a state of the art 3D analysis method and increased data from H.E.S.S., aims to study the diffuse γ-ray emission in the CMZ from 0.4 – 100 TeV using a physically motivated template approach. This work will unveil possible CR injection scenarios and discuss possible CR accelerators. Both continuous and impulsive CR injection scenarios will be covered, assuming a hadronic origin in the vicinity of the Galactic Centre. With this advanced analysis technique and modelling, the previous postulation on the existence of a PeVatron in the Galactic Centre is challenged.

This thesis will start with a prologue on γ-ray astronomy in Chapter 2, followed by an introduction of the imaging atmospheric Cherenkov technique with H.E.S.S. in Chapter 3 which is used for γ-ray detection. A detailed methodology of the 3D maximum-likelihood analysis will be explained in Chapter 4. The building of the 3D diffuse γ-ray emission templates will be elaborated in Chapter 5. These are used for the analysis of the diffuse γ-ray emission in the CMZ, which will be shown in Chapter 6. At the end in Chapter 7, a summary of this work will be presented.

"From the ashes a fire shall be woken,
A light from the shadows shall spring."

J.R.R. Tolkien
The Fellowship of the Ring

Chapter 2

Gamma-Ray Astronomy

The discovery of CRs can be traced back to the early 19th century through the phenomenon of electroscope discharge. Their astrophysical origin was later confirmed in balloon experiments of Victor Hess in 1912, which unveiled the existence of ionising radioactive sources outside the atmosphere of Earth [80]. These ionising particles, CRs, are mainly protons ($\approx 85\%$), helium nuclei ($\approx 12\%$), electrons ($\approx 2\%$) with some heavier nuclei ($\approx 1\%$) [80]. The CR particles arrive at Earth with a rather smooth power-law spectrum with energies of up to 10^{20} eV [51]. This legitimately arouses curiosity about the acceleration mechanism of these non-thermal high-energy particles, since their energies are beyond the capabilities of thermal emission mechanisms, and their origin. The latter is a giant challenge due to deflection of their travelling path in the turbulent Galactic magnetic field on the way to Earth, washing the information of their origin away. Yet γ-rays produced from the interactions of CRs with the interstellar medium (ISM) or photon fields have opened the door to γ-ray astronomy in the past few decades, revealing the non-thermal universe. In particular, a number of possible CR origins have been identified.

This chapter provides an introduction to CRs, including their energy spectrum as detected on Earth and well-accepted postulations of their acceleration mechanism, followed by an explanation of γ-rays production from CRs. Finally, possible CR sources from the γ-ray sky will be discussed. With this starter, hopefully the importance of γ-ray observation in relation with CRs can be perceived, which is one of the main purposes and cornerstone of this thesis.

2.1 Cosmic-Rays

CRs are a mixture of charged particles. When they propagate from their production site, the light elements like Lithium, Beryllium and Boron are enriched through interactions with cold interstellar matter, leading to an overabundance of these elements with respect to Solar

System abundances [80]. By studying the measured CR energy spectrum, the nature and acceleration mechanism of these puzzling CRs are unveiled.

2.1.1 Energy Spectrum

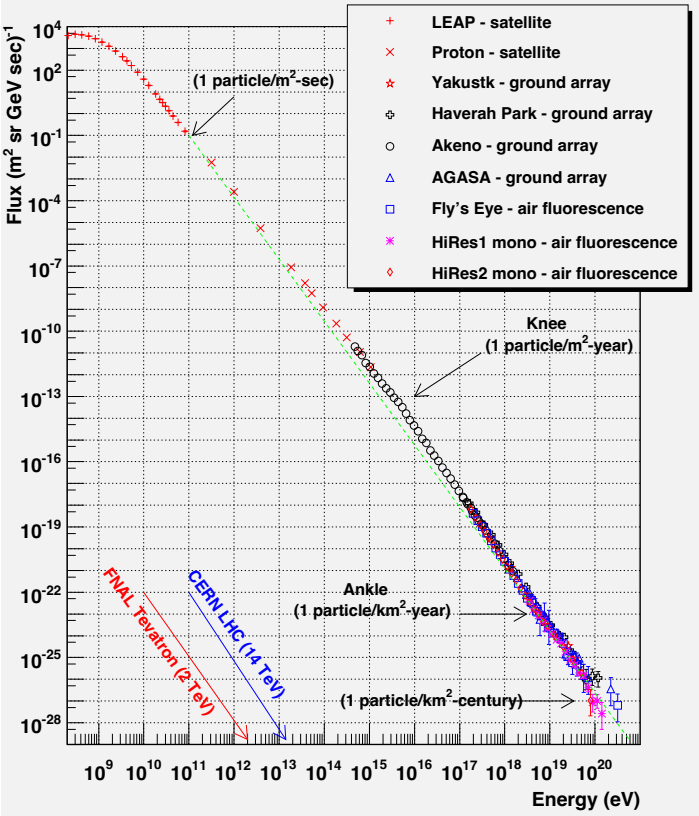

Figure 2.1 All-particle spectrum of CRs over eleven decades of energy from various experiments. The dashed line denotes a E^{-3} spectrum. (Taken from [51])

CR particles diffuse from the interstellar space towards Earth through the outflowing Solar Wind [95]. The fluxes of low-energy particles decrease during periods of high solar activity (and vice versa) due to the disturbance in the interplanetary magnetic field, which impedes the propagation of particles with low energies [80]. This phenomenon is called solar modulation. By taking into account the effects of solar modulation, the observed CR spectrum can be roughly described by power-law distributions with $N(E)dE \propto E^{-\Gamma}dE$ as shown by the various experiments in Figure 2.1, where $\Gamma = 3$ in this case. The flux of CRs, after the correction from the solar modulation, is constant in time. Its energy density is comparable to the energy density of both the thermal gas and magnetic field in the ISM ($w_{\mathrm{CR}} \approx 1$ eV/cm^3) [40].

The observed CRs show a smooth energy distribution despite the existence of numerous different astrophysical sources in the universe. This suggests that only certain astrophysical object populations are able to accelerate CRs, and they probably involve the same acceleration mechanism [119]. Apart from the flattening of the spectrum below 10 GeV, which is due to both the solar modulation and low-energy CRs interacting strongly with ISM via ionisation processes [119], there are four more prominent features in the spectrum that deviate from a smooth distribution.

The first kink is at the CR 'hip', where there is a break at rigidity $R = 300$ GV[1]. This break is more pronounced for protons and heavier elements. The break is caused by a change of the behaviour in the particle transportation, a change of the source(s) contribution to the spectrum, and features in the local properties of the source(s) [119].

The spectrum from $10^{11} - 10^{15}$ eV diverges from the fitted line with $\Gamma \approx 2.7$. The kink which appears at around $3 - 5 \times 10^{15}$ eV is called the 'knee' and confirmed by the KASCADE-Grande experiment [6]. The spectrum steepens to $\Gamma \approx 3.2$ from this point. The existence of the knee is related to a distinct intensity cutoff in the light component of CRs, assuming a rigidity-dependent knee [52]. This postulation is supported by the measurements from KASCADE-Grande and IceTop+IceCube when comparing the knee of the proton spectrum ($E \approx (3-5) \times 10^6$ GeV) and heavy iron spectrum ($E \approx 80 \times 10^6$ GeV) as shown in Figure 2.2.

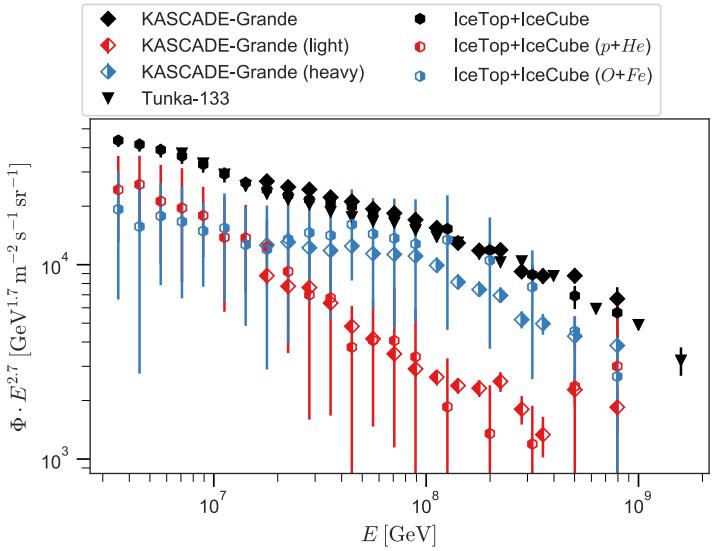

Figure 2.2 The energy spectra of light and heavy particles as measured from knee to ankle region by different observatories. Distinction in the spectra is observed. (Taken from [119])

[1]Rigidity is calculated as $R = pc/Ze$, where p is the momentum, c is the speed of light and Ze is the particle charge.

There is, however, another kink at around 5×10^{18} eV, called the 'ankle'. The spectrum is hardened to $\Gamma \approx 2.65$. It is generally believed that CRs with energies above the ankle have an extragalactic origin, thus the region between knee to ankle represents the transition between the galactic and extragalactic sources [11]. This will be discussed more in Section 2.3. Finally, there is a sudden drop at around 4×10^{19} eV in the spectrum. There are lot of disagreements on the exact position of this drop in various experiments, but this high-energy cutoff is believed to be related to the Greisen–Zatsepin–Kuzmin (GZK) effect, which is a rapid fragmentation from the interaction of the CRs with the cosmic microwave background at energies beyond this regime [119]. This cutoff sets a theoretical upper limit to the maximum energy of the CR flux.

2.1.2 Acceleration Mechanisms

Ionised plasma in the Galaxy has extremely high conductivity. In astrophysical environments with large-scale magnetic fields, the net electric field is zero due to the drifting of the free charges [119]. To create a Lorentz force for particle acceleration, either plasma instabilities or motion of magnetic fields is needed [99].

In the following, second-order and first-order Fermi acceleration related to particle interaction with the magnetised plasma will be discussed. The magnetic reconnection associated with the induction of electric fields from the rearrangement of magnetic field lines will also be explained. In particular, the first-order Fermi acceleration has been the most promising theory of the CR acceleration mechanism. This section refers to the publication from Malcolm Longair [80].

Second-Order Fermi Acceleration

In 1949, Enrico Fermi proposed that particles can be accelerated to high energies by a collision with clouds in the ISM. This can be done by first considering massive and magnetised plasma clouds acting as "magnetic mirrors" due to irregularities in the Galactic magnetic field. These mirrors move randomly with a certain velocity V. When charged particles collide with these mirrors, they gain energy stochastically via reflection with the average energy gain per collision

$$\left\langle \frac{\Delta E}{E} \right\rangle = \frac{8}{3}\left(\frac{V}{c}\right)^2, \tag{2.1}$$

and therefore the average rate of energy increases as

$$\frac{dE}{dt} = \frac{4}{3}\left(\frac{V^2}{cL}\right)E = \alpha E \tag{2.2}$$

if the average time between collisions is $2L/c$. The resulting spectrum can be determined from the diffusion-loss equation

$$\frac{dN}{dt} = D\nabla^2 N + \frac{\partial}{\partial E}[b(E)N(E)] - \frac{N}{\tau_{\text{esc}}} + Q(E), \tag{2.3}$$

where N is the number density of the particle, D is the diffusion coefficient, b is the energy loss rate of the particles, τ_{esc} is the spallation lifetime of the particle and Q is the rate of injection of particles per unit volume. In the case of steady-state and no presence of the sources, Equation 2.3 becomes

$$0 = -\frac{d}{dE}[\alpha E N(E)] - \frac{N(E)}{\tau_{\text{esc}}}. \tag{2.4}$$

By rearranging the equation, one can eventually derive the energy spectrum

$$\frac{dN(E)}{dE} = -\left(1 + \frac{1}{\alpha\tau_{\text{esc}}}\right)\frac{N(E)}{E} \tag{2.5}$$

The second-order Fermi acceleration provides a prediction of power-law feature in the CR energy spectrum, however, several problems remain. The most prominent problem is the very small and slow energy gain by the particles due to the low velocity of the clouds in comparison with the speed of light in the second order $O(V/c)^2$. This also indicates that some collisions will result in energy loss, and large mean free paths of the scattering. This problem was later solved by the postulation of first-order Fermi acceleration, where the diffusive shock is taken into account.

First-Order Fermi Acceleration

In the late 1970s, the proposal, e.g. from Bell (1978), that particles can be efficiently accelerated in strong shock waves has dominated among the rest of CR acceleration postulations. This diffusive shock acceleration pictures particles bounce back and forth in the upstream and downstream regions of the strong shock wave and always approach gases moving towards them. This means particles will always gain energy due to the everlasting head-on collision with gases.

Shock waves can be generated from vigorous events like supernova explosions. These shock waves propagate through the ISM with a velocity greater than the speed of sound and Alfvén speed[2], which are associated with the magnetic field strength and mass density of the ISM. These shock waves can provide a source of acceleration for particles as indicated in

[2] Alfvén speed is calculated as $v_A \equiv B/\sqrt{\mu_0\rho}$, where B is the magnetic field strength, μ_0 is the permeability of the vacuum and ρ is the mass-density.

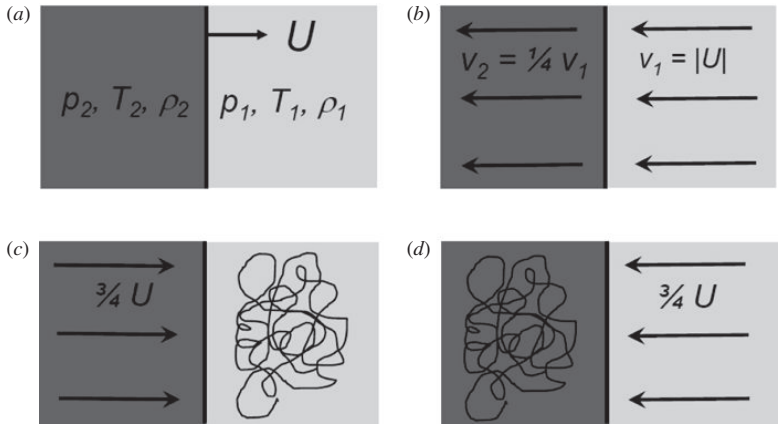

Figure 2.3 The dynamics of high-energy particles in the vicinity of a strong shock wave. (a) Observer frame, (b) reference frame of the shock, (c) reference frame of the upstream gas and (d) reference frame of the downstream gas. (Taken from [80])

Figure 2.3. Consider a shock wave with speed U traversing a flux of high-energy particles (Figure 2.3 (a)). These particles propagate close to the speed of light, and they are present in front of (upstream, light gray) and behind (downstream, dark gray) the shock front with a gyroradius much larger than the thickness of the shock. In the reference frame (Figure 2.3 (b)), the shock front is at rest and the upstream gas flows with the velocity $v_1 = |U|$ towards the shock front and leaving with the velocity v_2 in the downstream. Mass conservation leads to the continuity equation,

$$\frac{\rho_2}{\rho_1} = \frac{v_1}{v_2} = \frac{\gamma+1}{\gamma-1} = 4, \tag{2.6}$$

where γ is the ratio of specific heat capacities of the gas. A monatomic gas has $\gamma = 5/3$, which gives $v_2 = (1/4)v_1$ in the limit of very strong shocks. Therefore particles in the reference frame of the upstream or downstream region (Figure 2.3 (c) and (d)) will always see gas approaching with the same velocity $V = |v_1 - v_2| = (3/4)U$ from the opposite sides. These particles can thus always obtain a small increase of energy whenever they cross the shock front with the head-on collision, and never lose energy through the crossing. They are then scattered elastically in the region behind the shock front so that their velocity distributions become isotropic with respect to that flow. A round trip across the shock and back allows the average energy gain of

$$\left\langle \frac{\Delta E}{E} \right\rangle = \frac{4}{3}\left(\frac{V}{c}\right). \tag{2.7}$$

The derivation of the energy spectrum is different from that of the second-order Fermi acceleration. In this case, one needs to consider there are $N = N_0 P^k$ particles with energy $E = E_0 \beta^k$ after k collisions, where P is the escape probability for particles being swept away in the downstream and β is the fraction of energy gain in a round trip. By eliminating k, these two relations can be written up into

$$N = N_0 \left(\frac{E}{E_0} \right)^{\ln P / \ln \beta}. \tag{2.8}$$

A typical escape probability from the classical kinetic theory gives $P = 1 - (U/c)$ and from Equation 2.7 we know $\beta = 1 + \langle \frac{\Delta E}{E} \rangle = 1 + (U/c)$ when considering one collision only. This eventually leads to an energy spectrum

$$\frac{dN}{dE} \propto E^{-2} \tag{2.9}$$

that is close to the observed CR spectrum, which has index ≈ 2.7 below the knee. There is however a limit to the energy by using this acceleration mechanism alone, which is $E_{max} \approx 10^{14}$ eV [76]. Energies beyond this point up to $10^{18} - 10^{20}$ eV can be obtained by considering non-linear feedback from the back-reactions of the particles on the magnetic field [119], leading to a strongly amplified magnetic field in the shocks of astrophysical sources like supernova remnants and pulsars. The spectral index on the other hand, can even go as steep as $2.2-2.4$ [21]. This will be further elaborated in Section 2.3 when discussing the origin of CRs.

Magnetic Reconnection

In 1950, James Dungey introduced the theory that electric fields generated from spatially rearranged magnetic field lines can provide a source of energy for solar flares [36]. In this, a magnetic field is convected along a plasma with high electrical conductivity with individual field lines. In finite resistivity, two field lines are coming closer until they cut at some point and are being reconnected, changing the topology of the global field line [16]. In the reconnection region where a DC electric field is created, once the velocity of a charged particle exceeds a critical velocity, the particles can accelerate without impediment (i.e. without deceleration from collision with the plasma) [16]. This is called runaway. Though the magnetic reconnection is subject to the limit of flow of charge and the streaming instabilities, this should still be considered in some astrophysical environments with strong magnetic shear, for example the pulsar wind nebulae [26]. The pre-acceleration of particles during the

magnetic reconnection could potentially solve the injection problem in the first-order Fermi acceleration [119].

2.2 Cosmic-Rays to Gamma-Rays

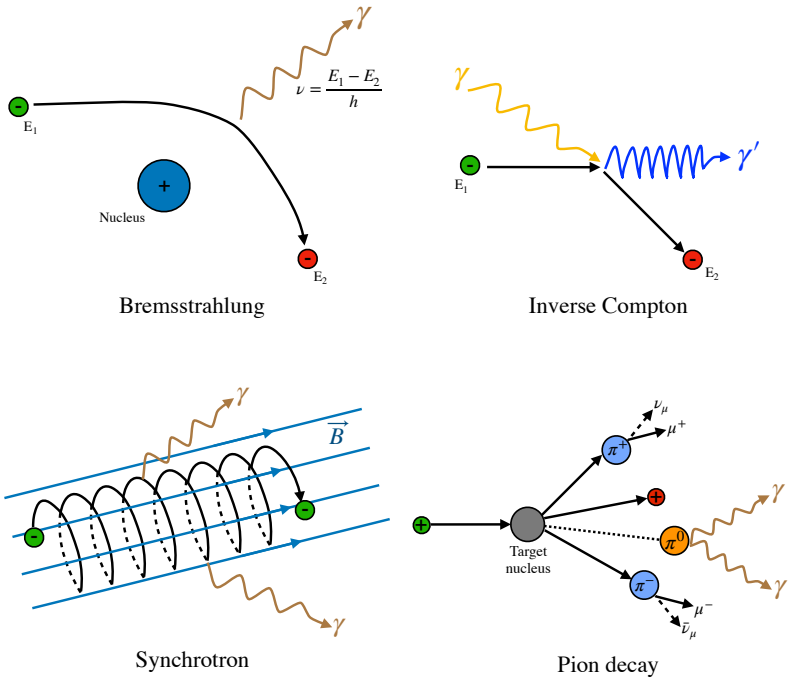

Figure 2.4 The schematics of leptonic (bremsstrahlung, inverse Compton and synchrotron) and hadronic (pion decay) γ-ray production mechanisms. (Taken from [68])

The origin of CRs can be identified through their interactions with gases or photon fields, which cause non-thermal continuum γ-radiation. When CRs diffuse out from a source, they either undergo inelastic collision with the ambient matter or interaction with radiation fields, resulting in the production of pions via

$$\begin{aligned} pp &\rightarrow \sum \pi^{\pm,0} \\ p\gamma &\rightarrow \begin{cases} \Delta^+ \rightarrow p\pi^0/n\pi^+ \\ \sum \pi^{\pm,0} \end{cases} , \end{aligned} \tag{2.10}$$

where $\sum$ is the multi-pion production and Δ is the Delta resonance [119]. These pions then decay into neutral secondaries ($\gamma\nu\bar{\nu}$)

$$\begin{aligned} &\pi^0 \to \gamma\gamma \\ &\pi^+ \to \mu^+ + \nu_\mu \to (e^+ \nu_e \bar{\nu}_\mu) + \nu_\mu \\ &\pi^- \to \mu^- + \bar{\nu}_\mu \to (e^- \bar{\nu}_e \nu_\mu) + \bar{\nu}_\mu \end{aligned} \tag{2.11}$$

that allow tracing back to their origins. The emission of γ-rays can be divided into hadronic γ-ray emission and leptonic γ-ray emission where synchrotron radiation, inverse Compton scattering and bremsstrahlung are involved, as visualised in Figure 2.4. The hadronic emission from the π^0-, also the subdominant η-, decays are the essential building blocks for the construction of the diffuse γ-ray emission template in Chapter 5. The following Sections 2.2.1 and 2.2.2 refer to the publications [70, 119, 18, 105].

2.2.1 Hadronic Gamma-Ray Emission

The π^0 decay shown in Equation 2.11 contributes to the majority of the hadronic γ-ray emission. The kinetic energy threshold for the π^0 production is $E_p = (\gamma_p - 1)m_p c^2 \approx 280$ MeV in the laboratory frame, where γ_p is the Lorentz factor of the non-resting proton [93]. The energy of both the secondary photons is $E_\gamma^{\mathrm{CM}} = m_\pi/2 \approx 67.5$ MeV in the centre of mass frame (CM), whereas the energy in the laboratory frame is

$$E_\gamma = \gamma_\pi (E_\gamma^{\mathrm{CM}} + \beta_\pi p_\gamma^{\mathrm{CM}} \cos\theta_\gamma^{\mathrm{CM}}) = \frac{1}{2} m_\pi \gamma_\pi (1 + \beta_\pi \cos\theta_\gamma^{\mathrm{CM}}), \tag{2.12}$$

where γ_π is the Lorentz factor of π^0, β_π is the ratio of π^0 velocity to the speed of light and $\theta_\gamma^{\mathrm{CM}}$ is the angle of the scattering [105]. In the case where γ-rays are emitted in the direction of motion, consequence energy boundaries are

$$\begin{aligned} \frac{E_\pi(1-\beta_\pi)}{2} \leq E_\gamma \leq \frac{E_\pi(1+\beta_\pi)}{2} \\ \to \frac{m_\pi}{2}\sqrt{\frac{1-v_\pi/c}{1+v_\pi/c}} \leq E_\gamma \leq \frac{m_\pi}{2}\sqrt{\frac{1+v_\pi/c}{1-v_\pi/c}}. \end{aligned} \tag{2.13}$$

In the log-log representation, the γ-ray spectrum is therefore symmetric at the centre of this boundary, which is $m_\pi/2 \approx 67.5$ MeV. This distinct bell-type feature, the pion bump, is expected only from hadronic interactions. Its exact location depends on the spectral index of the parent proton, which typically can be found at an energy between 100 MeV to a few GeV. In particular, this bump disappears completely when the proton index is < 2 [130].

Though the production rate is smaller, η are also produced during the CR interaction with the gas apart from the π^0 [93, 70], result in the γ-ray emission via

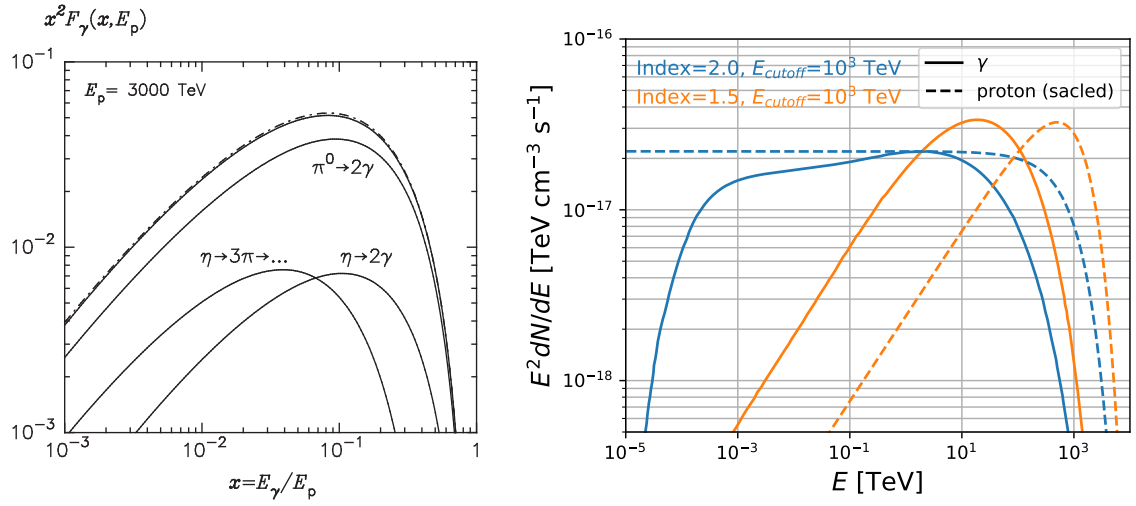

(a) (b)

Figure 2.5 (a) Energy spectra of γ-rays from p-p interactions, including the partial contributions from π^0 and η decays. (Taken from [70]) (b) Energy spectra of γ-rays (solid) and parent protons (dashed) with different proton spectral index.

$$(pp \to pN^*(1535) \to pp\eta) \to \eta \to \begin{cases} 2\gamma & \\ 3\pi^0 & \to 6\gamma \\ \pi^+\pi^-\pi^0 & \to 2\gamma + .. \\ \pi^+\pi^-\gamma & \to \gamma + .. \end{cases} \tag{2.14}$$

To derive the hadronic γ-ray emission spectrum, in particular of interest energy range in above 100 GeV in this thesis, one can make use of Monte Carlo simulations. Open-source codes like *SIBYLL* and *QGSJET* can provide a precise parameterization for high-energy spectra of γ-rays based on proton-proton interactions, as adapted by Kelner et. al. (2016) [70]. Their result is also applied in this thesis for building the diffuse γ-ray emission model (in Chapter 5). Based on their calculation, the energy spectrum of the γ-ray in the energy interval $(E_\gamma, E_\gamma + dE_\gamma)$ can be derived from the proton spectrum dN_p/dE_p using

$$\frac{dN_p}{dE_p} \to \frac{dN_\gamma}{dE_\gamma} = cn_H \int_{E_\gamma}^{\infty} \sigma_{inel}(E_p) \frac{dN_p}{dE_p} F_\gamma(\frac{E_\gamma}{E_p}, E_p) \frac{dE_p}{E_p}, \tag{2.15}$$

where c is the speed of light, n_H is the hydrogen gas density, $\sigma_{inel}(E_p)$ is the cross-section of inelastic proton-proton interactions and $F_\gamma(\frac{E_\gamma}{E_p}, E_p)$ is the number of photons in the interval $(\frac{E_\gamma}{E_p}, \frac{E_\gamma}{E_p} + d\frac{E_\gamma}{E_p})$ per collision. F_γ and σ_{inel} are parameterized from the above-mentioned simulation.

The resulting γ-ray spectra from the hadronic emission can be seen in Figure 2.5. In Figure 2.5 (a), the γ-ray spectrum induced by a mono-energetic proton is shown with the inclusion of the partial contributions from the more significant π^0 decay and the less prominent η decay. In Figure 2.5 (b), the γ-ray spectra resulting from parent proton spectra with different spectral indices are shown. Three messages are delivered from these plots: firstly the contribution from η decay is not negligible, secondly a cutoff at E_{cutoff} in the proton spectrum will already affect the γ-ray spectrum at $\sim 10^{-2}E_{\text{cutoff}}$, thirdly the γ spectrum does not necessarily follow the shape of the proton spectrum even at high energy, especially if the protons are undergoing energy-dependent diffusion. This will be discussed in more detail in Chapter 5.

The proton cooling time is estimated as $\tau \approx 6 \times 10^7 (\frac{n_H}{1\text{cm}^{-3}})^{-1}$ yr in the case of inelastic collision [4]. This corresponds to $\tau \sim 10^7$ yr for a typical density of $n_H \approx 1$ cm^{-3}, thus only giving minor influence on the γ-ray spectrum. This is different to the energy-dependent cooling due to leptonic emission presented in the following section.

2.2.2 Leptonic Gamma-Ray Emission

The highly relativistic leptonic secondaries ($e^- e^+$) from the above-mentioned $\pi^\pm$ decay in Equation 2.11 or other existing relativistic leptonic particles will interact with the surrounding gas in a radiation field and a magnetic field. Here three cases need to be considered:

Inverse Compton Scattering

The low-energy photon from the radiation field (e.g. cosmic microwave background, infrared, X-ray or optical photons [19]) can gain energy to the γ-ray regime in collision with a highly relativistic electron. There are in general two cases needed to be considered depending on the photon energy in the electron rest frame before the scattering: the Thomson limit in which the photon energy is much less than $m_e c^2$ and thus only a small fraction of the energy lost for electron per collision with the quicker loss rate $-dE_e/dt \propto E_e^2 T^4$; and the extreme Klein-Nishina limit in which the photon energy is much larger than $m_e c^2$ and a sizeable fraction of the energy lost for electron in a single collision due to the more prominent electron recoil with a slower loss rate $-dE_e/dt \propto \ln(E_e) T^2$. The electron cooling time is $\propto E_e^{-1}$ in the former case whereas $\propto E_e$ in the latter case.

In the case of power-law populated electrons, the resulting photon energy spectra are

$$\frac{dN_e}{dE_e} \propto E_e^{-\alpha} \rightarrow \frac{dN_\gamma}{dE_\gamma} \propto \begin{cases} E_\gamma^{-(\alpha+1)/2} & \text{Thomson limit} \\ E_\gamma^{-(\alpha+1)} & \text{extreme Klein-Nishina limit} \end{cases} \tag{2.16}$$

A spectral severe softening is therefore expected depending on the energy range of the target photon spectrum due to the transition from the Thomson limit to the extreme Klein-Nishina limit, where a large fraction of electron energy is lost. The maximum energy gain for the photon is $E_{\gamma,\max} \approx 4\gamma^2 E_\gamma$, the seed photons can get into the GeV−TeV regime at high Lorentz factors of $10^2 - 10^3$.

Synchrotron Radiation

Synchrotron photons are emitted when the acceleration of the relativistic charged particles is perpendicular to the velocity due to deflection during traversing a magnetic field with a strength of B. The energy loss rate for such emissions depends on the magnetic field as $-dE_e/dt \propto \frac{e^4}{m_e^4} E_e^2 B^2$, where e is the electron charge and m_e is the electron mass. Although both electrons and protons can emit synchrotron radiation, emission from protons is strongly suppressed due to a factor of $(m_e/m_p)^4 \approx 10^{-13}$ weaker radiation.

The electron cooling time is $\tau \propto E_e^{-1}$. For the power-law distributed electrons, the corresponding high-energy photon spectrum without and with simple cooling [79] is

$$\frac{dN_e}{dE_e} \propto E_e^{-\alpha} \rightarrow \frac{dN_\gamma}{dE_\gamma} \propto \begin{cases} E_\gamma^{-(\alpha+1)/2} & \text{without cooling} \\ E_\gamma^{-(\alpha+2)/2} & \text{with cooling} \end{cases} \tag{2.17}$$

This process is particularly important for sources with high magnetic fields. Although the emitted photons are typically in the keV energy regime, they can further upscatter through the above-mentioned inverse Compton scattering. The combined process is called synchrotron self-Compton scattering [72].

Bremsstrahlung

In bremsstrahlung emission, a photon is emitted when an electron is decelerated by an atom or pure Coulomb field. There are three cases of bremsstrahlung, namely the strong shielding, weak shielding and the unshielded case. Yet all result in the energy loss rate of $-dE_e/dt \propto E_e$, in which the strong shielding has the greatest loss rate [18]. A huge fraction of energy is lost in each bremsstrahlung event, similar to that of the extreme Klein-Nishina limit for inverse

Compton scattering. The electron cooling time, on the other hand, is energy independent as $\tau = E_e/\dot{E}_e \approx 4 \times 10^7 (\mathrm{cm}^{-3}/\mathrm{n})$ yr.

The photon energy spectra cannot be derived analytically for both the weak shielding and unshielded cases. However, one can obtain the energy spectrum for the case of strong shielding as

$$\frac{dN_e}{dE_e} \propto E_e^{-\alpha} \rightarrow \frac{dN_\gamma}{dE_\gamma} \propto E_\gamma^{-\alpha} \tag{2.18}$$

if the lower limit of the initial incident electron energy E_e is equal to the photon energy E_γ. Bremsstrahlung is an effective mechanism of γ-ray emission at GeV energies but not beyond, yet this is important for air shower development which will be discussed in Section 3.1.1.

Distinguishing Hadronic and Leptonic Emission

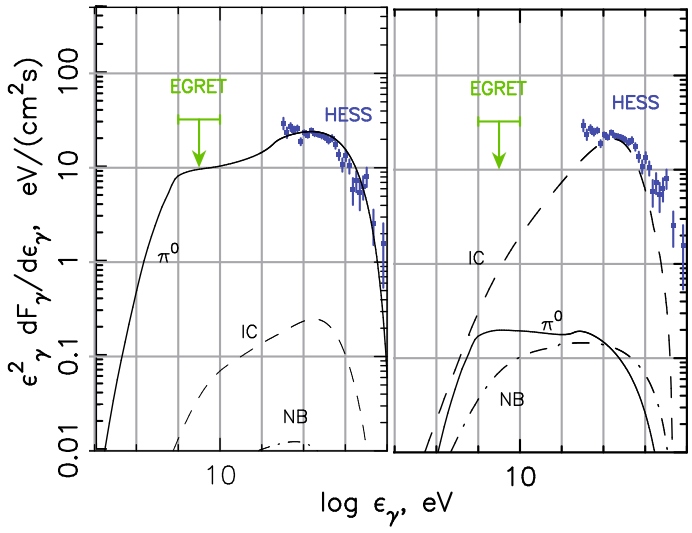

Figure 2.6 γ-ray spectral energy distribution of a supernova remnant (RX J1713.7-3946). The left computed with the hadronic model and right computed with the leptonic model. The solid curve corresponds to γ-ray emission from π^0-decay, whereas the dashed and dash-dotted curves indicate the Inverse Compton (IC) and Nonthermal Bremsstrahlung (NB) emissions. (Taken and adapted from [13])

Since both hadronic and leptonic γ-rays can reach the TeV energy regime, and the fact that there is currently no instrument that has the optimal settings for detecting the pion bump for all Galactic objects, it is difficult to distinguish them for these Galactic sources. One way to distinguish the emission scenario is by performing a broad-band fit to the spectral energy distribution (SED), considering the magnetic field strength at the shock and the

ambient proton/electron density [119]. In particular, the X-ray synchrotron spectrum is fitted and fixed with functions of magnetic field strength B and non-thermal electron density n_e. The increase of B implies the necessity to decrease n_e, which then reduces the contribution from inverse Compton emission and favors the contribution from hadronic emission at TeV energy. Another way is by measuring the spectral index of the γ-ray spectrum from GeV to TeV energy range. A hard spectrum is expected for the leptonic emission while a soft spectrum is expected for the hadronic emission [111, 40]. At the TeV regime, a sharper fall-off towards 100 TeV is expected from the leptonic emission as illustrated in Figure 2.6. Some above-mentioned spectral features can be seen, i.e. the pion bump and the contribution from the effective inverse Compton scattering, the less prominent bremsstrahlung and the missing of the ineffective synchrotron radiation at high energy.

2.3 Origin of Cosmic-Rays in the Gamma-Ray Sky

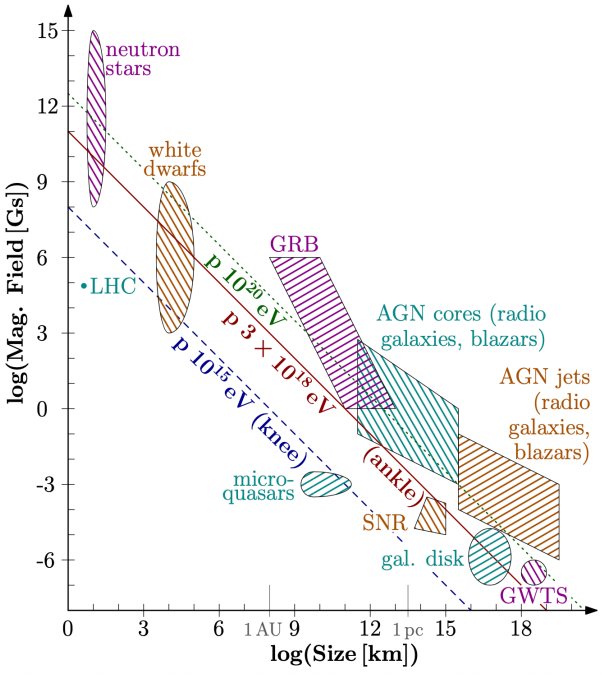

Figure 2.7 The classical Hillas diagram indicating the size and magnetic field strength of each CR acceleration candidate. The knee (10^{15} eV), ankle (3×10^{18} eV) and maximum energy (10^{20} eV) lines are shown. (Taken from [119])

The last part of this chapter is about the possible acceleration sites of high-energy CR particles. The fact that the CR flux is non-correlated with the intensity of the activity of

the Sun is a good indication of the extra-solar origin. Nowadays it is believed that CRs with energies up to 10^{18} eV are being accelerated inside the Galaxy, while those beyond this energy range have an extra-Galactic origin [23]. This transition between the low- and high-energy CRs is related to the particle gyroradii becoming comparable to the thickness of the Galactic disk ($\approx$ 360 pc) when considering a typical ISM magnetic field of $\approx 3\mu G$ [69]. Several models [14, 47] have been developed for explaining such transition.

Similarly, possible acceleration sites can be approximated by calculating the maximum energy that a particle can attain from each type of astrophysical object based on a constraint that a particle will escape from the source when the gyroradius is exceeding the size of the source R. This is called Hillas criterion and can be related to the charge of the particle Ze and the magnetic field of the accelerator B through [119]

$$E_{\max}^{\text{Hillas}} = ZecB\Gamma_{sh}\beta_{sh}R \tag{2.19}$$

in the presence of relativistic shocks, where Γ_{sh} is the boost factor of the shock front and $\beta_{sh} = v_{sh}/c$ is the shock velocity in units of the speed of light. Possible sources at different Hillas criteria without consideration of boosting effects can be seen in Figure 2.7. Examples of TeV γ-ray accelerators are:

Supernova remnants The remaining structure from a supernova explosion via thermonuclear explosion of an accreting white dwarf or from the collapse of a massive star. Particles can accelerate effectively in the shock associated with the expansion of supernova ejecta [121].

Pulsar wind nebulae The relativistic wind powered by the rapidly rotating and intensely magnetised neutron star, the pulsar, that was created from the collapse of massive stars. This leads to an effective particle acceleration in the surrounding ejecta [42].

Active Galactic nuclei Supermassive black holes located in the centre of galaxies accrete matter and emit jets. AGNs with relativistic jets at orientation close to the line of sight are called blazars. The flux of the continuum radiation from the source are enhanced by the effect of Doppler boosting [91, 1].

Compact binary systems This system consists of two astronomical bodies, typically a neutron star or a black hole. Termination of the pulsar wind or the internal shocks in the jet formed in the vicinity of the black hole can accelerate particles effectively [1].

Stellar clusters The mass of stars lost through the stellar wind, which then interacts with the ambient ISM and forms shocks. A collection of shocks will trigger the formation of super-bubbles (expanding cavities) that foster effective acceleration [124].

Star-burst galaxies Galaxies with high supernova explosion rates, e.g. due to galaxy mergers, that foster particle acceleration [1].

Clusters of galaxies The largest gravitationally bound structures in the Universe, including galaxies, gas and especially dark matter. γ-rays are produced via CRs interacting with the inter-cluster medium and photons from cosmic microwave background [17].

Gamma ray bursts The short-lasting solitary events of extragalactic origin, occurring a few per day throughout the universe with a duration of seconds, prompted γ-rays via the relativistic fireball shock model [85].

Yet in any physical scenario, apart from the size of the source, the maximum energy is limited by the acceleration ability of the accelerator, presumably linked to the age of the system, and the energy loss via the radiation or interaction in the local medium

2.3.1 PeVatron Candidates

Note that it is quite unlikely that there are multiple contributions from different sources to the observed CR spectrum in Figure 2.1, due to the absence of pronounced features below the cosmic knee. Thus it is in general believed that only a single source or class is contributing to the CR spectrum, with the source power calculated based on the energy required to maintain the observed flux of CRs against their escape from the Galaxy [40]:

$$W_{\rm CR} = [w_{\rm CR}(\pi R^2)h]/t_d \approx 10^{41}\text{erg s}^{-1}, \tag{2.20}$$

where local energy density $w_{\rm CR} \approx 1$ eV/cm^3, radius $R \approx 15$ kpc, thickness $h \approx 100$ pc and confinement time[3] $t_d \approx 3 \times 10^6$ yr (based on the overabundance of Li, Be, and B in the arriving CRs with respect to those in our solar system due to spallation of heavier CR nuclei by interstellar gas [80]) in the Galactic disk.

The sources that are capable of accelerating particles to at least the PeV energy regime without any breaks are called PeVatrons. CRs in this energy regime are confined by the interstellar magnetic field and thus are presumably of galactic origin [40]. The discovery of

[3]The amount of CRs grammage needed to produce these element abundance is $\mu \approx 5$ g/cm^2. The confinement time is therefore calculated as $t_d = \mu/\rho c$, where $\rho \approx 1$ particle/cm^3 is the mean gas density in the Galactic disk and c is the speed of light

PeVatrons would thus prove our current understanding of the CR acceleration mechanism and reveal the nature of the cosmic knee. In this section, PeVatron candidates within the current detection limit will be presented, namely supernova remnants, pulsar wind nebulae and lastly, past studies on the diffuse emission around the Galactic Centre.

Supernova Remnants

Supernova remnants (SNRs) are the structures that remain from supernova explosions, and they remain the most popular candidates for the origin of galactic CRs. There are mainly two types of varieties, the most common shell-type remnants with emission originating from an expanding shell, or the Crab-type remnants possessing a central pulsar source with maximum brightness in the centre [80]. Example of such SNRs can be found in Figure 2.8.

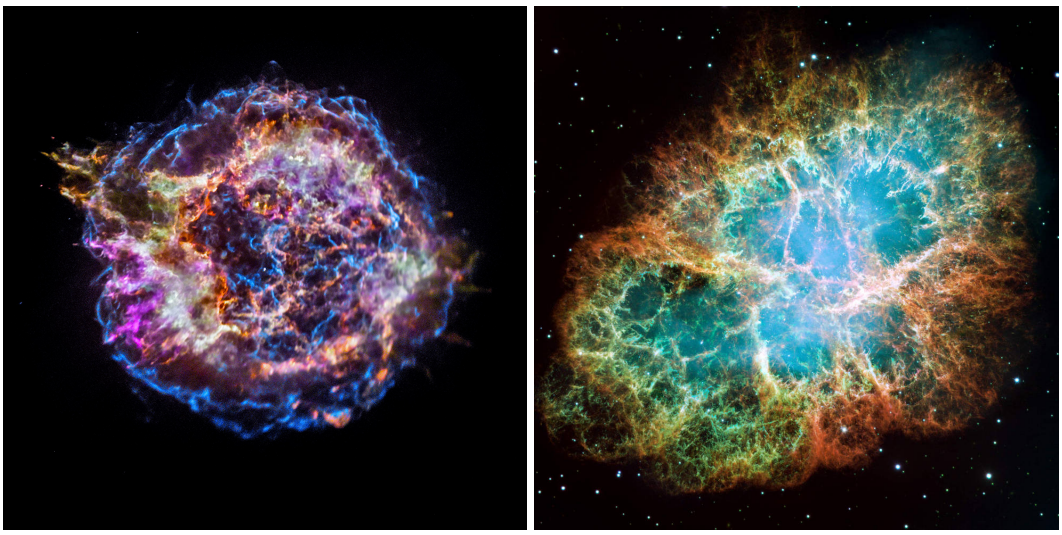

(a) Cassiopeia A (b) Messier 1 (The Crab Nebula)

Figure 2.8 Examples of a shell-type (a) and Crab-type (b) SNRs. The Crab Nebula consists of a SNR and pulsar wind nebula. (Taken from [87, 88])

In the supernova explosion, as illustrated in Figure 2.9, the liberated energy causes supersonic expansion of a sphere of very hot gas. Through ejecting the gas, a shock front is formed ahead of the expanding sphere, and the interstellar gas is swept up. The shocked gas is heated and intense X-rays are emitted. When the swept-up mass is greater than the ejected mass, the expanding sphere starts to decelerate and gas inside the sphere catches to the shell of the sphere. When the flow of the gas becomes supersonic, a shock wave is formed at the inner edge of the shell. When the internal shock wave propagates back towards the origin, the ejected gas is heated and soft X-rays[4] are emitted. A further expansion of the sphere

[4]X-rays with photon energies below 5 keV.

will lead to a decrease in temperature behind the shock front, leading to energy dissipation through recombination of atoms. The SNR then eventually merges into the ISM [80].

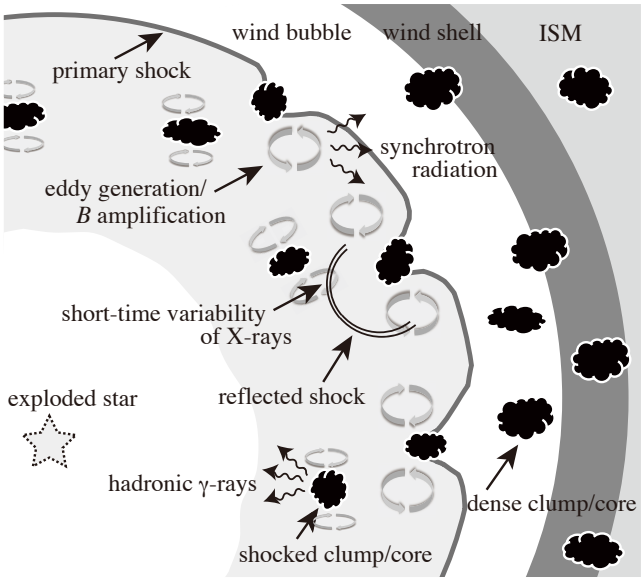

Figure 2.9 Schematic of the shock–cloud interaction of a supernova remnant. (Taken from [101])

If 10% of the explosion energy is used for accelerating particles, the power transferred form supernova to CRs is related by [40]

$$W_{\mathrm{SN}\to\mathrm{CR}} = 10\% E_{\mathrm{SN}} \nu_{\mathrm{SN}} \approx 10^{41}\ \mathrm{erg/s}, \tag{2.21}$$

where the typical supernova explosion energy is $E_{\mathrm{SN}} \approx 10^{51}$ erg and the supernova rate in the Galaxy is $\nu_{\mathrm{SN}} \approx 3$/century. This power coincides with the required PeVatron power in Equation 2.20.

The acceleration mechanism operating at the supernova remnant shocks, specifically the young shell type, is directly related to first-order Fermi acceleration with non-linear feedback from the strongly amplified magnetic field as mentioned in Section 2.1.2. The non-linear feedback comes from the plasma instability driven by the streaming CRs in the upstream precursor, which can amplify the magnetic field ahead of the shock [12, 121]. The CRs can then accelerate rapidly and reach the energy at the knee. Further acceleration beyond this point is possible for heavy stars that explode into their own wind, which is called wind-SNRs [119].

The measured index through the γ-ray, also the X-ray, observation coincides with the prediction in Equation 2.9, which is ≈ 2 [40]. The X-ray emission is due to the synchrotron radiation from relativistic electrons, whereas the γ-ray emission from the supernova can be

interpreted as either hadronic emission (from π^0 decay) or leptonic emission (from inverse Compton scattering of electrons in the cosmic microwave background radiation field) [40]. The first case is related to the high acceleration efficiency coupled with hard energy spectra of protons, while the second case is related to the fact that almost all young SNRs have a synchrotron origin [1, 40].

Possible SNRs PeVatron are for example SNR G.28.6-0.1 and SNR G40.5-0.5 [28].

Pulsars and Pulsar Wind Nebulae

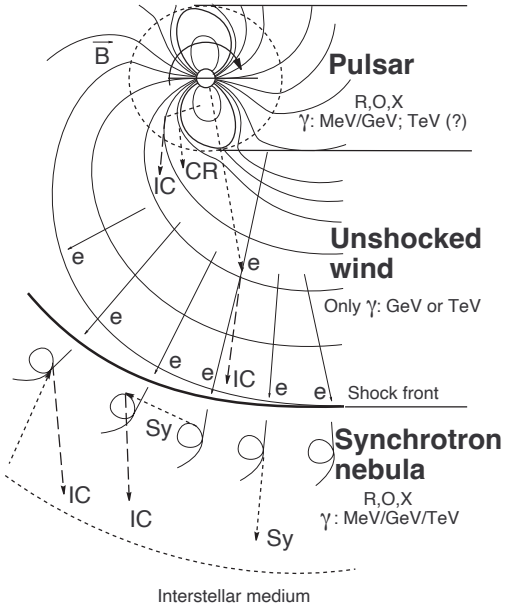

Figure 2.10 The radiation mechanisms of nonthermal emission associated with rotation powered pulsars. (Taken from [5])

Pulsars are densely packed, highly magnetised and rapidly rotating neutron stars that form at supernova explosions and emit electromagnetic radiation from their magnetic poles. The γ-rays are emitted in three distinct regions as illustrated in Figure 2.10 [1]. These are the pulsar magnetosphere that hosts several GeV to 30 GeV photons, the cold unshocked ultrarelativisitic wind that generates 10 GeV to 1 TeV radiations through inverse Compton scattering and the pulsar wind nebula. This pulsar wind nebula is the result of a termination of the magnetohydrodynamic (MHD) wind by the reverse shock. It can produce TeV γ-rays and also leads to the acceleration of electrons to energies above 100 TeV, which then contribute to leptonic γ-ray production in different diffuse radiation fields [1].

While some studies suggest that the energy budget of the pulsar is not enough to produce the CR flux at the knee [119], other studies, which consider the impact of pair production

in aligned pulsar magnetosphere, suggest CRs could accelerate to 1 PeV with luminosities of 5×10^{35} erg/s for a typical millisecond pulsars, and even up to 10 EeV with luminosities of 5×10^{43} erg/s for young millisecond pulsars [50]. The most prominent example of such accelerator is the Crab nebula (Figure 2.8b). Some studies also suggest the possibility of the formation of the knee from clusters with both PWNs and SNRs, i.e. the Vela cluster [38] and MGRO J1908+06 [104].

Past Studies on Diffuse Emission Around the Galactic Centre

The arrival directions of CRs are extremely isotropic in the sky and depend very weakly on the energy of the particle. This isotropic feature is due to the fact that the trajectories of CRs are isotropized during diffusion in the turbulent Galactic magnetic field. It is therefore important to locate the CR acceleration sites through indirect methods, namely through observing the γ-emission from CR interactions with the ambient gas. High-energy protons cannot be confined in the central region, so the diffuse component of γ radiation can be easily extended to much larger regions. Previous CR measurements have indicated an energy-dependent CR grammage (g/m^2) and thus energy-dependent confinement time $t_{\rm esc}(E) \propto E^{-\delta}$ of CRs in the Galaxy. The term δ is typically related to the scatter of CRs on the random MHD waves and discontinuities, which arise in the magnetized plasmas due to field perturbations [108]. According to the standard quasi-linear theory of plasma turbulence, the magnetic field is assumed to follow a power-law spectrum

$$\Delta B^2_{\rm res}(k_{\rm res}) = A^2 B^2 (k_{\rm res} L)^{-1+\delta}, \tag{2.22}$$

where $\Delta B_{\rm res}$ is the amplitude of the random field B at the resonant wave number $k_{\rm res} = 1/r_g$ and r_g is the gyroradius, $L \approx 100$ pc is the basic scale of the interstellar turbulence and A is a constant, charaterizing the relative value of the random field on the charateristic scale L [100]. In the case of $r_g \leq L$, the corresponding particle diffusion coefficients in parallel ($D_{\parallel}$) and perpendicular ($D_{\perp}$) direction can then be expressed as

$$D_{\parallel} = lv/3, \quad D_{\perp} = gA^4 lv/3 \tag{2.23}$$

with $l = A^{-2} L (r_B/L)^{\delta}$, where v is the particle velocity and $g \approx 0.1 - 0.5$ is a constant not well defined in the modern theory [100]. The value δ varies in different turbulent theories, $\delta = 1/3$ in particular for the Kolmogorov spectrum and $\delta = 1/2$ for the Kraichnan hydromagnetic spectrum [100, 23]. The lack of information on the magnetic field irregularities is an obstacle to determine the diffusion coefficient. One way to overcome this challenge is through the interpretation of the CR data, in which a spatial diffusion coefficient can be defined as

$$D \approx \frac{h^2}{t_{\rm esc}} \approx D_0 (\frac{E}{10\ {\rm GeV}})^{\delta}, \tag{2.24}$$

where h is the average travelling distance for particles at all energies before leaving the Galaxy and D_0 is typically lying between $10^{28} - 10^{29}$ cm^2/s. The derivation of the slope of the diffusion coefficient can be done by looking at the ratio between the fluxes of cosmic boron and carbon [23], in which boron is the secondary nucleus produced by the fragmentation of the element (e.g. the carbon that is primarily produced in sources like SNRs). This typically gives $\delta \in (0.3...0.6)$, depending on the CR diffusion model [23]. For a CR injection spectrum of $Q_{\rm CR}(E) \propto E^{-\alpha}$, the equilibrium spectrum of CRs in the Galaxy is [40]

$$N_{\rm CR} \propto Q_{\rm CR}(E) \times t_{\rm esc} \propto E^{-\alpha-\delta}. \tag{2.25}$$

With the observed CR spectral index of 2.7 around the knee, this gives $\alpha \approx 2.1 - 2.4$. Since a high value for δ would indicate that high-energy CRs escape too quickly from being isotropized by the Galactic magnetic field, i.e. creating anisotropy at high energies, the typical expected values are $\alpha \approx 2.4$ and $\delta \approx 0.3$. This is a compromise of both the chemical abundance and isotropy of CRs [40]. It should also be noticed that even if a small value for δ is chosen, the sources around the CR source might affect the level of isotropy.

The detection of TeV γ-rays from the Galactic Centre has been possible since 2004, e.g. by H.E.S.S. [56, 59, 57], MAGIC [116], VERITAS [24] and Whipple [74], giving evidence of the existence of high-energy particle accelerator(s) in the central 3 pc region of our Galaxy [1]. A point source named HESS J1745-290 is found located closely at the Galactic Centre with an unknown identity. Several potential counterparts of HESS 1745-290 have been suggested. For example, the compact radio source Sgr A* at the dynamical centre of our Galaxy (which is a supermassive black hole (SMBH)), the diffuse region at the entire central 1pc filled by dense molecular clouds and CRs, the young supernova remnant (SNR) Sgr A East, the Pulsar Wind Nebula (PWN) G359.95-0.04 and the dark matter halo [1]. Various features of these sources can be related to the TeV γ-ray emission. For example, the termination shock of a hypothetical wind from SMBH Sgr A* or PWN G359.95-0.04 can cause acceleration of electrons which then produce γ-rays. The hadronic interactions in SNR Sgr A East, through injection of protons and nuclei into the surrounding dense gas regions, can also produce the same effect [1]. Some also suggest the presence of a few thousand millisecond pulsars from the past merger of globular clusters, causing γ-rays production through acceleration of inverse-Compton scattered electrons [10, 122].

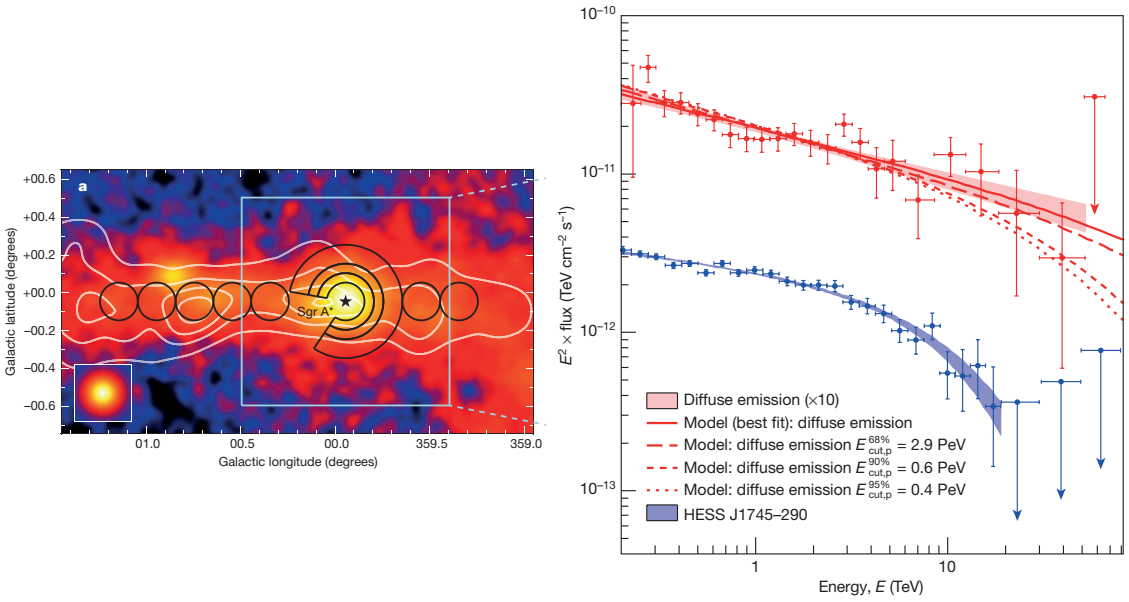

(a) (b)

Figure 2.11 (a) VHE γ-ray image of the Galactic Centre region. The colour scale indicates the γ counts. White contour indicate the density distribution of molecular gas. (b) VHE γ-ray spectra of the diffuse emission and HESS J1745-290. (Taken from [3])

It is in general believed that the diffuse γ-ray emission around the Galactic Centre has a hadronic origin, due to the spatial distribution of the γ–ray emission correlating well with the gas density in the region from the CS radio-observation [122]. The γ-ray spectrum of up to $\sim$100 TeV, as illustrated in Figure 2.11, could be fitted with a power-law with index ≈ 2.3 and the proton index is derived to be ≈ 2.4 [3], which is harder than the CR galactic background with index ≈ 2.7. The intensity is also enhanced by a factor of $3-10$ with respect to the CR background. These two observations hint at the possibility of the linkage of HESS J1745-290 (potentially Sgr A*) to a PeVatron at the Galactic Centre.

Notice that there is however a cutoff at around 10 TeV for HESS J1745-290, presumably due to γ-rays interacting with the ambient infrared radiation field. The infrared photons with wavelengths of $50-500$ μm are emitted by dust (heated by stellar light), leading to the absorption and attenuation of photons from pair production ($\gamma\gamma \to e^+e^-$). For γ-rays with even higher energy (≤ 300 TeV), the absorption is mainly due to the cosmic microwave background radiation field. The absorption probability will even increase if sources are on line-of-sight that pass close to the Galactic Centre [123]. Thus the cutoff is not considered as a conflict with possibility of HESS J1745-290 being a PeVatron.

2.4 Summary

In this chapter, the key aspects to remember are:

- CRs arrive at Earth with energies up to 10^{20} eV and with spectral index of ≈ 2.7. The study of CRs can reveal their nature and origin, yet the deflection of their travelling path has washed out this information.
- γ-rays are emitted when CRs interact with gas or photon fields at their origin and they can travel straight to Earth. The study of γ-rays can diagnose CRs.
- Several astrophysical objects can potentially be the production site(s) of CRs, based on γ-ray observations. Some PeVatron candidates were postulated.
- This thesis aim at study the diffuse γ-ray emission in the CMZ via CR interaction with the ambient gases, which is a good way to locate the source and nature of CRs.
  - Note that previous related studies suggested the Galactic Centre has a potential PeVatron. This study with updated data and analysis methods, however, puts the statement in question.

In the next chapter, the detection method of γ-rays on Earth will be discussed. With the modern and progressing instrumentation and analysis chain, the diffuse γ-ray emission from the Galactic Centre can be well studied and the nature of CRs in this complex region can be unveiled.

"If you look on the ground in search
of a sixpence, you don't look up,
and so miss the moon."

W. Somerset Maugham

Chapter 3

Imaging Atmospheric Cherenkov Technique with H.E.S.S.

Very high-energy γ-ray emission can serve as a diagnostic probe to study non-thermal phenomena in the universe, in particular to search for the sources of CRs. Yet due to atmospheric absorption, TeV γ-rays produced along with CRs cannot be observed directly on Earth, but rather indirectly via Cherenkov radiation coming from the interaction of γ-rays with the atmosphere. Large telescope arrays have been built in the last few decades to measure this signal, which gives information of the parent CRs.

This chapter particularly focuses on the detection technique of very high-energy γ-rays, with the explanation on the generation mechanism of Cherenkov radiation. The analysis chain of the γ-ray measurement using H.E.S.S. will then be introduced, including the instrumentation, reconstruction and connection of the γ-ray properties. These are the essential elements for the high level analysis in the next chapters.

3.1 Very High-Energy Gamma-Ray Detection on Earth

As mentioned in Section 2.2.1, CRs can initiate γ-ray emission via interactions with gas or photon fields. The generated secondary photons, the γ-rays, can traverse the Galactic magnetic field from the production site to Earth without deflection. Both the energy and entrance direction of these γ-rays in the atmosphere can reveal information on the parent CRs. As can be seen in Figure 3.1, different experimental setups can be used to detect the γ-rays at different energies.

For photon energies between 0.1 GeV $\leq E_\gamma \leq$ 100 GeV, this is called the **high-energy (HE)** γ-ray regime [112]. One relies on space-based telescopes for the detection from low

Earth orbit because the atmosphere is blocking the γ-rays. For instance Fermi-LAT measures the tracks and energy of the electron-positron pair produced by a γ-ray when hitting thin metal sheets [39]. Yet the detection area is insufficient for higher energy photons in space-based observation due to a drop of CR counts towards higher energies.

For photon energies between 0.1 TeV $\leq E_\gamma \leq$ 100 TeV, this is called the **very high-energy (VHE)** γ-ray regime [89] and is the focus regime of this thesis. The detection of γ-rays in this regime relies on ground-based telescopes, which have much larger detection area in comparison to space-based telescopes. A detection method called imaging atmospheric Cherenkov technique (IACT, Section 3.1.2) can be used. The IACT instrument detects the optical Cherenkov light created from electromagnetic showers (Section 3.1.1), which are secondary products coming from the interaction of incoming γ-rays and the atmosphere. The reconstruction of incoming γ-rays is possible afterwards. Examples of observatories/experiments are H.E.S.S. (Section 3.2), MAGIC, VERITAS and the future CTAO and ASTRI. The downside of this technique is the requirement of a dark environment in order to detect the faint Cherenkov light.

For photon energies $E_\gamma >$ 100 TeV, this is called the **ultra high-energy (UHE)** γ-ray regime [89]. The detection also relies on ground-based telescopes, yet requires the above-mentioned shower particles to reach the ground level and pass the detection units, which are water tanks on the ground. The Cherenkov light is produced in those water tanks and being measured. With this method, observations can be performed day and night. Examples of such observatories are HAWC, LHAASO and the future SWGO.

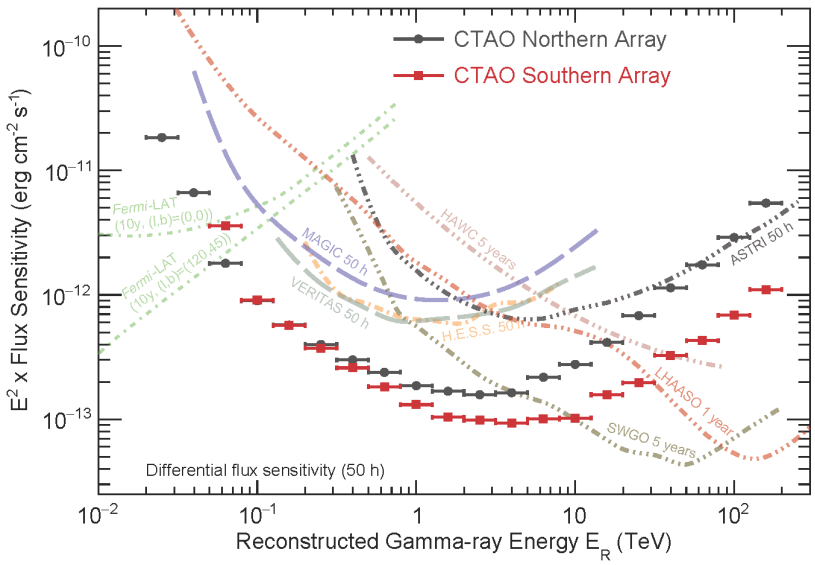

Figure 3.1 A rough comparison of the differential sensitivity of different instruments. (Taken from [30] in prod5 version v0.1)

Again the focus of this thesis is on the VHE regime with the use of H.E.S.S. The details of extensive air showers, Cherenkov radiation and IACTs will be explained in the following Sections.

3.1.1 Extended Air Showers and Cherenkov Radiation

Extended Air Showers

When a high-energy photon ($> 2m_e c^2$) enters the Earth's atmosphere, an electron-positron pair can be produced when the photon is close to an atmospheric nucleus (mainly nitrogen, oxygen, and argon). The nucleus is needed to fulfill the condition of simultaneous conservation of momentum and energy. When the electron or positron gets decelerated in the Coulomb field of an nucleus, a high-energy photon is produced due to bremsstrahlung. These pair production and bremsstrahlung process alternate, in this way an electromagnetic cascade is produced. The cascade develops until the ionisation losses of the electrons/positrons are greater than the losses from bremsstrahlung. The critical energy for the cascade particles at this point is $\sim$ 86 MeV in air [37]. The maximum number of the cascade particles and the depth of the cascade are proportional to the initial energy of the incoming photon. Beyond this critical point, the number of particles in the cascade drops drastically and the cascade will stop. This electromagnetic cascade is also known as an electromagnetic air shower. A schematic diagram of such showers can be seen in Figure 3.2 (Left).

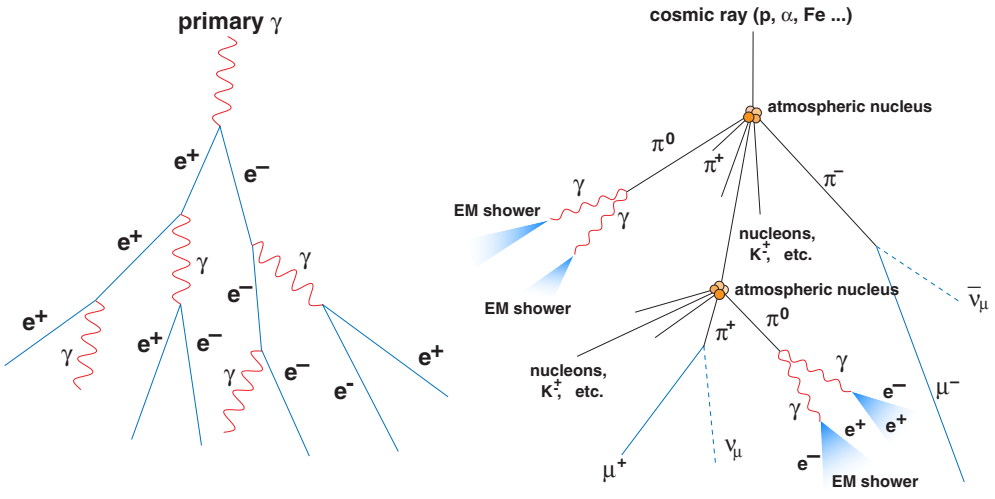

Figure 3.2 Left: Schematic illustration of an electromagnetic air shower as originating from an incoming photon. Right: Schematic illustration of a hadronic air shower as originating from an incoming hadron. (Taken from [126])

Similarly a background of high-energy charged particles arrive at Earth (mainly protons). They also producing air showers with a rate up to 10^4 larger than that initiated by high-energy photons [39]. Unlike electromagnetic air showers, numerous strong interactions with the atmospheric nuclei occur and produce various hadronic secondaries, mostly charged and neutral pions. While some secondaries are short-lived, the long-lived particles (i.e. baryons, charged pions and kaons) create the hadronic shower core [37]. These secondaries further decay into photons and leptons, thus several hadronic and electromagnetic sub-showers are developed. A schematic diagram of the hadronic shower can be seen in Figure 3.2 (Right). Note that the muonic shower components and their subsequent electromagnetic secondaries can even reach the ground due to a small energy loss [37], forming a distinctive "muon ring" on the telescope camera that allows later optical calibration in Section 3.2.2 [45].

Hadronic showers are regarded as background for the γ-ray measurement. Only the γ-ray induced air showers are able to reveal the location of the parent CRs, whereas the CRs get deflected during travel. A distinguishment on the hadronic background can be done based on the shape of the air shower. The hadronic shower exhibits a wider lateral distribution than the electromagnetic shower due to large transverse momentum being transferred in the strong interactions. More details on such cuts will be discussed in Section 3.2.

Cherenkov Radiation

The particles inside the cascade carry a huge amount of kinetic energy. This allows them to travel with a velocity v that is greater than the speed of light in the same dielectric atmospheric medium, i.e. $v > c/n$, in which the refractive index of the atmosphere is larger than vacuum ($n > 1$). In this case, the particles radiate even if moving with a constant velocity according to the Liénard–Wiechert potentials [80]. During the process, the particle polarises the dielectric atmospheric medium, the atmospheric molecules are excited and return back to the ground state by emitting photons. Spherical wavefronts are formed with phase velocity equals to c/n. Since the particles are fast-moving, the polarisation field around the particles is still asymmetric along the direction of propagation after the particles pass by. The wavefronts of the radiation are therefore able to add up coherently at a specific angle $\cos\theta = c/nv$ with respect to the velocity vector of the particle. This is called the Huygens' construction [80] as shown in Figure 3.3. At the end a pool of Cherenkov radiation can be seen, yet the observable duration on ground is extremely small ($\sim$ns).

The density of the atmosphere plays a big role in the height of the first cascade branch. For a 1 TeV particle, this corresponds to an altitude of $\sim$25 km above the sea-level with the maximum shower extension happening at $\sim$10 km above the sea-level. The angle of the Cherenkov emission is $\sim 1^\circ$, resulting in a ring light pool with diameter of $\sim$200 m

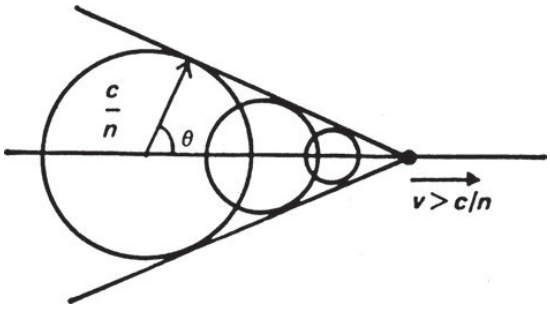

Figure 3.3 Illustration of Huygens' construction for the wavefront of coherent radiation of a charged particle moving at constant velocity $v > c/n$ through a dielectric medium with refractive index $n > 1$. (Taken from [80])

on the ground. Since the emission angle depends also on the atmospheric density, it will increase when the altitude decreases. Thus the Cherenkov light arrives on the ground in rings from each part of the particle track. The Cherenkov radiation has a continuous frequency spectrum, the relative intensity is approximately proportional to the frequency. In this case, the higher frequencies (the shorter wavelengths) regime are more intense in Cherenkov radiation that is seen as blue. The difference between the Cherenkov light on the ground from the electromagnetic and hadronic air showers are illustrated in Figure 3.4 (based on simulation). As discussed, the γ-ray induced shower produces a concentrated patch of light pool, while the hadronic induced shower has greater lateral spread due to greater dispersion of the various cascade particles.

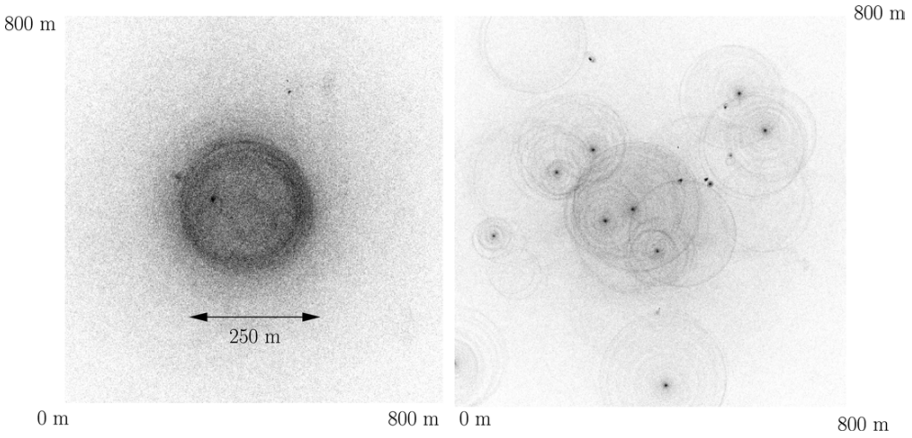

Figure 3.4 Distribution of Cherenkov light on the ground from a 300 GeV γ-ray shower (left) and a 1 TeV proton shower (right) taken from Monte Carlo simulations. (Taken from [1])

3.1.2 Imaging Atmospheric Cherenkov Technique

The CRs cause the production of γ-rays, which travel straight to the Earth. These very high-energy γ-rays initiate electromagnetic air showers that produce Cherenkov light. As discussed in the previous section, the Cherenkov light is spread over a large light pool with extremely faint signal and short duration, which can be detected with IACTs. For instance H.E.S.S. uses a large spherical reflector to collect the faint signal. The fast-grained cameras in the focal plane of the large reflector allow the capture of the image of the short flash, allowing one to reconstruct the parameters of the initial γ-ray. These include their arrival direction and the energy.

Due to the projection effect during the typical camera exposure time of $\sim$10 ns, the image of the shower has an elliptical shape as illustrated in Figure 3.5. Each pixel on the camera consists of a photomultiplier tube which converts the photons to an electric signal via the photoelectric effect in order to amplify and record the signal. The shape of the shower signal does not only allow the reconstruction of the properties of the incoming γ-ray, but also allows a separation of the electromagnetic and hadronic background shower, which will be discussed in more detail in Section 3.2.2.

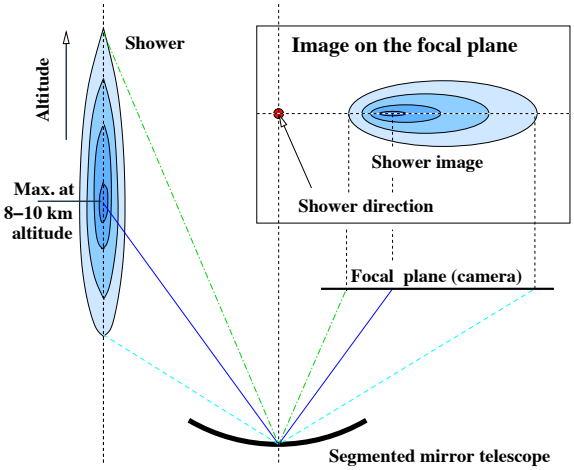

Figure 3.5 Shower imaging by a telescope. The shower image in the camera has the shape of an ellipse. (Taken from [125])

For a targeted observation, the IACT instrument points in the direction of an astronomical source at night in order to record the Cherenkov light. The observations are usually divided into chunks of $\sim$30 min, called runs. The duration is a trade-off between collecting enough events and avoiding systematics from changes in observational conditions [32]. For observations involving faint sources, many runs that spread over years might be needed for analysis. These runs are typically taken with different pointing directions around the source of interest.

In the classical analysis approach as will be mentioned in Section 3.2.4, the source is offset around the centre of the field of view. These are called wobble observations, which can average out systematics from the telescope camera [32].

Two or more IACT instruments can form a stereoscopic system. For H.E.S.S., they are arranged typically with a distance of $\sim$ 100 m apart from each other and point to the same showers from different angles. A three level trigger system is typically defined in H.E.S.S. [3]. First, a single pixel trigger threshold is required, which is 4 photo-electrons within 1.5 ns. Second, a camera trigger threshold is required, for which a coincidence of 3 pixels is required within a sector, where a sector is a square group of 64 pixels and a camera has 38 overlapping sectors. Third, a telescope trigger threshold is required, which is a coincidence of at least 2 telescopes triggering within 80 ns. At the end the digitized signals are sent to the central data acquisition (DAQ) system. With this stereoscopic system, the hadronic background showers can be partially eliminated due to their inhomogeneous light pool as observed by the multi-telescopes, and particularly the narrower light pool from the muon induced showers cannot trigger enough telescopes [53]. This way the stereoscopic system improves the telescope sensitivity and angular and energy resolution.

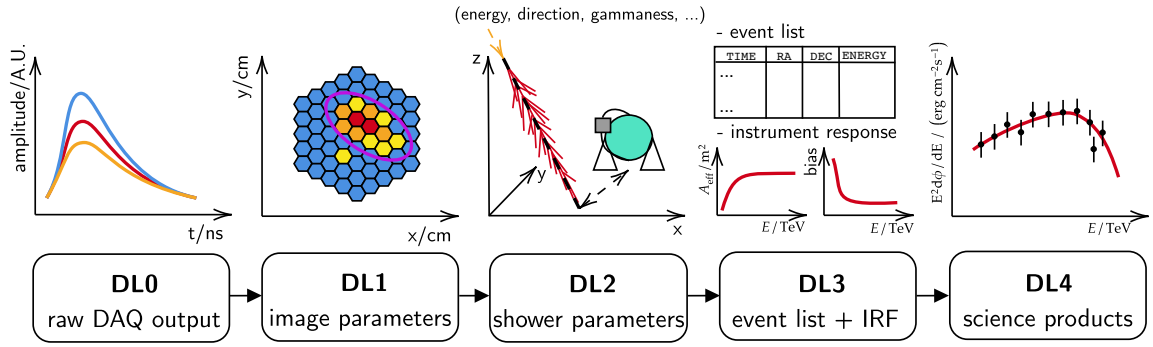

Figure 3.6 Schematisation of the progressive data reduction and data levels of an IACT. (Taken from [92])

The different data products are segmented into 5 levels as shown in Figure 3.6. The goal is to get from raw DAQ output (DL0) to the sceince products (DL4). The image parameters (DL1) are determined from the raw DAQ output (DL0). The shower parameters (DL2) can then be reconstructed to store and build the event list and the instrument response function (DL3). At the end the science products (DL4) are out, these include the spectral result and the morphology of the target sources. The chain from DL1 to DL3 will be discussed in the following section, and the process from DL3 to DL4 will be discussed in Chapter 4.

3.2 The H.E.S.S. Experiment

The High Energy Stereoscopic System (H.E.S.S.) consists of an array of 5 IACTs located in the Khomas Highland of Namibia at 1800 m above sea level, the excellent observation location towards the southern hemisphere and conditions have made it a perfect spot to observe the Galactic Centre. Four of the five telescopes are smaller in size and form a square. They are labelled as CT1-4 (Cherenkov Telescope). The fifth one is larger in size and was put in the centre of this array. It is called CT5. The CT1-4 have been in service since 2004 (H.E.S.S. I era) and CT5 has been operated with CT1-4 since 2012 (H.E.S.S. II era), the CT1-4 have been upgraded with new cameras in 2016 (H.E.S.S. IU era) [63].

Figure 3.7 The H.E.S.S. experiment in phase II era. CT1-5 are shown and CT5 is in the centre of the plot. (Taken from [63])

3.2.1 Instrument

The following refer to the telescope overview in [63].

CT1-4

CT1-4 are four Cherenkov telescopes built with steel structure. As can be seen in Figure 3.7, they have the altitude-azimuth mounted hexagonal reflective dish that consists of 382 round mirror segments mounted in Davies-Cotton fashion. The dish has a diameter of 13 m. The mirror area is 105 m^2, which is needed in order to collect Cherenkov light from the γ-rays with an energy of 100 GeV and above. These telescopes provide a field of view of 5° and have a focal length of 15 m, resulting in $f/d \approx 1.2$. The camera has a pixel size

of 0.16°. For a stereoscopic observation, which results in improved angular and energy reconstruction and background suppression as mentioned in Section 3.1.2, at least two telescope are needed. The four telescopes are arranged in a square with side length of 120 m, which was optimised for the maximum sensitivity at the given energy threshold based on Monte Carlo simulations [3, 115].

CT5

The CT5 is at the centre of the telescope arrays. Due to its larger dish size, a parabolic mirror shape is used instead of the Davies-Cotton geometry to minimise time dispersion [98]. The parabolic shape is approximated by a grid of 5×5 planar mirror support segments, aligned to approach a parabola. The facets are in hexagonal shape rather than round shape to optimise coverage. There are 875 hexagonal facets with a dish diameter of 28 m. This gives a total mirror area of 614 m^2 with focal length of 36 m, providing a field of view of 3.2°. CT5 can extend the detectable energy range from the array down to energies of ~ 30 GeV.

Pointing Direction

The observations from the telescopes are characterised by their pointing direction, namely the zenith (ϑ) and the azimuth (ϕ) angle. The zenith angle ϑ is defined as 0° pointing upwards and increases when pointing towards the lower altitude (ground). When the zenith angle increases, the line-of-sight distance to the shower maximum increases roughly as $l_{\max} \propto z_{\max}/\cos\vartheta$. This decreases the projected dimension of the shower by a factor of $\sim \cos\vartheta$ and increases the Cherenkov lightpool by $\sim 1/\cos\vartheta$, resulting in the intensity of the Cherenkov images to decrease by $\cos^2\vartheta$. The energy threshold and the effective area are therefore increased by $\sec^2\vartheta$ [1].

Moreover, the geomagnetic field can cause distortion and rotation of the shower image due to the deflection of charged particles [25, 31]. This induces a larger azimuthal spread of the shower due to the north-south magnetic field lines. This results in a decrease in light density and increase in energy threshold. Monte Carlo simulation are needed to account for the effect as a function of the azimuthal direction [31].

3.2.2 Reconstruction

Calibration and Image Cleaning

Before proceeding to any analysis, it is important to at first perform calibration. This means to correct the signal charge of each camera pixel for instrumental effects, such as the

electronic/thermal noise and the starlight/moonlight from the night sky background (NSB). The muon rings mentioned in Section 3.1.1 also take part in calibrating the optical reflectivity of the mirrors [45]. After an image is read out, image cleaning takes place. This task focuses on removing the NSB from the image for further analysis. This task is particularly important since only pixels in the shower image participate in the further analysis. A dual-threshold algorithm is usually used to mask the pixels containing noise, i.e. pixels with intensity above 4 p.e. are kept if at least one of the neighbour pixels has intensity above 7 p.e. for a typical analysis [60].

Event Reconstruction

Numerous physical parameters have to be extracted from the Cherenkov image, including the type of the primary particle and its energy and direction, the first interaction depth, the impact point, which is the imaginary point if the primary particle hits on the Earth's surface, and the altitude of the maximum shower extension. In the classical Hillas reconstruction [64], these can be inferred from shower image by elliptical geometry, for example the nominal distance between the camera centre and the image centre of gravity (d), the ellipse length (L) and width (W), the orientation and finally the image size, which is the total charge deposited in the ellipse. These parameters are called the Hillas parameters as shown in Figure 3.8. The direction of the shower is typically estimated from the ellipse length and the image size, whereas the energy of the particle is generally estimated from the image size and the impact point, however not in a straightforward way. Lookup tables are required and built using Monte Carlo simulation to reconstruct the energy as a function of every reconstructed distance, offset (distance between reconstructed shower direction and camera centre), size and zenith angle of an event [3]. Since the optical efficiency of the telescopes changes with time, the lookup tables have to be updated regularly.

As mentioned, the stereoscopic system in H.E.S.S. allows reconstructing the event direction by intersecting the major axes of the shower images in the camera plane and on the ground. A weighted average (based on image amplitude and the angle between the axes) is then taken from all intersection points to provide an estimate of the arrival direction of the primary γ-ray. The shower impact point on the ground can also be derived in similar procedure, where the intersections of the directions between the image centroid and the optical axis are determined. The energy can then be estimated from a weighted average over the individual single-telescope energy estimates.

A reconstruction technique which outperforms the classical Hillas reconstruction in terms of angular resolution is the Image Pixel-wise fit for Atmospheric Cherenkov Telescopes (ImPACT). This technique is based on the likelihood fitting of camera pixel amplitudes to

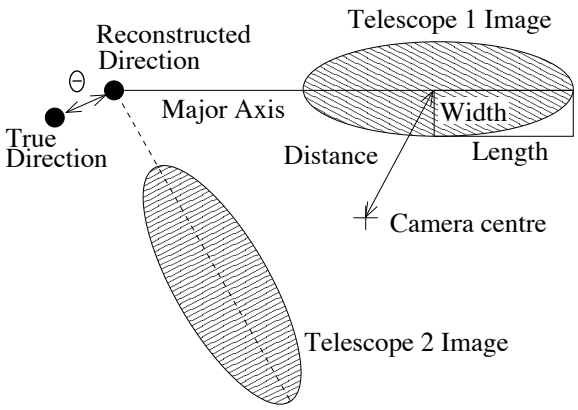

Figure 3.8 Illustration of simple Hillas parameters calculated for a shower image. (Taken from [3])

an expected image template, directly generated from Monte Carlo simulations. An image template library is first created for a large number of fixed primary particle properties in the air shower, including energy, zenith angle, impact distance and depth of shower maximum. The expected shower properties are generated by performing a multi-dimensional interpolation of the template library and then compared to the individual camera images using a likelihood fit. The primary particle properties can then be reconstructed by performing a multi-dimensional fit (source position in sky, impact position on the ground, energy and depth of shower maximum) [96]. With the use of ImPACT reconstruction, the angular resolution performance is improved by $\sim 50\%$ at 500 GeV and $\sim 15\%$ at 100 TeV. The energy resolution, on the other hand, is significantly improved at all energies, in particular at low energies (improvement of $\sim 50\%$). A sensitivity improvement of around a factor of 2 in observation time over traditional Hillas-based reconstruction for point source observations is achieved [97].

Gamma-Hadron Separation

After determining the event character, γ-hadron separation is the next step. This is mainly done by comparing their image shape as shown in Figure 3.9, in which the γ shower has smaller spread with elliptical shape and proton shower has larger spread with irregular shape. Among the events recorded by IACTs, only $\sim 0.01\%$ represent true γ-ray events. The separation of γ events from the background events is extremely difficult due to the fact that the probability density functions of both event types always overlap, in particular the electromagnetic shower initiated by π^0 and electrons [32].

For the standard approach, using the typical mean-scaled-width method, one computes the width and the corresponding dispersion σ_W as a function of image size, impact point,

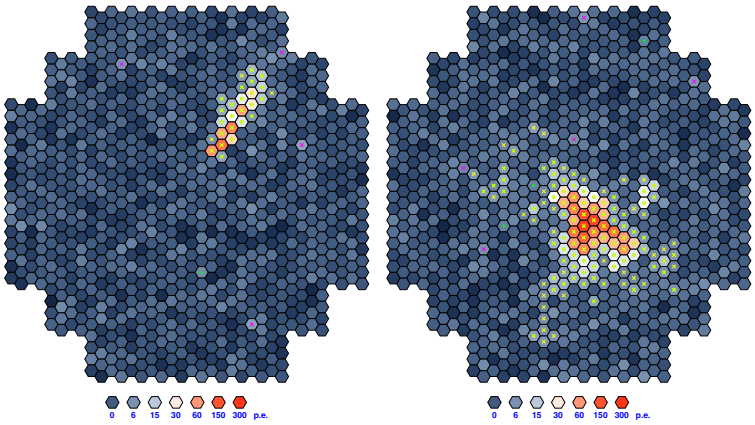

1.0 TeV gamma shower 2.6 TeV proton shower

Figure 3.9 The γ-induced (left) and hadron-induced (right) shower images as recorded by the camera. (Taken from [125])

offset and zenith angle, through the Monte Carlo simulation. The mean reduced scaled width (MRSW), which is the best parameters to distinguish image shapes, can then be expressed as

$$\mathrm{MRSW} = \frac{1}{N_{\mathrm{tel}}} \sum_{i}^{N_{\mathrm{tel}}} \frac{W_i - < W >_i}{\sigma_{W,i}} \tag{3.1}$$

A similar calculation is made for mean reduced scaled length (MRSL) and both values are stored in lookup tables. The γ-hadron separation is performed by making simple box cuts on MRSW and MRSL, also later on the image size and θ (the angular offset in shower direction reconstruction). In this way, huge amounts of the hadronic background are removed. Yet some hadronic events are inevitably classified as γ events due to their image properties being too 'γ-like'. The γ-hadron separation therefore falls into the dilemma of either using loose cuts to attain very high γ-ray efficiency but large background contamination, or using hard cuts to achieve significantly reduced background contamination but at the cost of loosing γ-ray efficiency. The two selections also have an influence on the energy threshold, in which the low-energy shower has relatively more statistical fluctuations and the hard selection usually impose a higher energy threshold [32]. Thus the cuts are defined into standard, hard or loose and have to be chosen wisely depending on the observation target.

In the last decade, the Toolkit for Multivariate Data Analysis (TMVA) has been introduced to improve the separation power through boosted decision trees (BDTs). BDTs are a machine learning algorithm that extends the simple cut-based analysis to multivariate algorithms. It considers the nonlinear correlations between input parameters and effectively ignores parameters without separation power [94]. Compared to the decision tree (DT), BDT considers the misclassified events with a boost weight in the training of the next tree and

thus results in a forest of trees that increases the stability of the method. For the γ-hadron separation with BDTs, the training parameters are based on Hillas parameters, including the mean reduced scaled width (MRSW), mean reduced scaled length (MRSL), mean reduced scaled width off[1]. (MRSWO), mean reduced scaled length off (MRSLO), depth of the shower maximum (X_{max}) and averaged spread in energy reconstruction between the triggered telescopes ($\Delta E/E$) [94]. Since the energy- and zenith-dependency of some input parameters leads to a zenith- and energy dependent BDT classification, the γ-ray selection cuts are optimised in zenith and energy bands. In this way the TMVA background rejection method yields a 20% improvement in sensitivity compared to the classical approach.

3.2.3 Instrument Response Functions

The Instrument response functions (IRFs) provide a linkage between the true and the reconstructed event parameters through Monte Carlo simulation. They are used to transform the physical properties of the γ-ray, i.e. the sky direction, energy and time, to the reconstructed characteristics of an event [73]. The IRFs consist of the effective area, energy dispersion, point spread function and the FoV background model. The IRFs strongly depend on the observation conditions such as the pointing direction and the instrument optical efficiency. By computing multidimensional lookup tables, the expected properties can be interpolated from the measurement. The lookup tables have a temporal nature, in which they need to be reproduced regarding any changes on the system, e.g. the degrading optical efficiency or updating the system components.

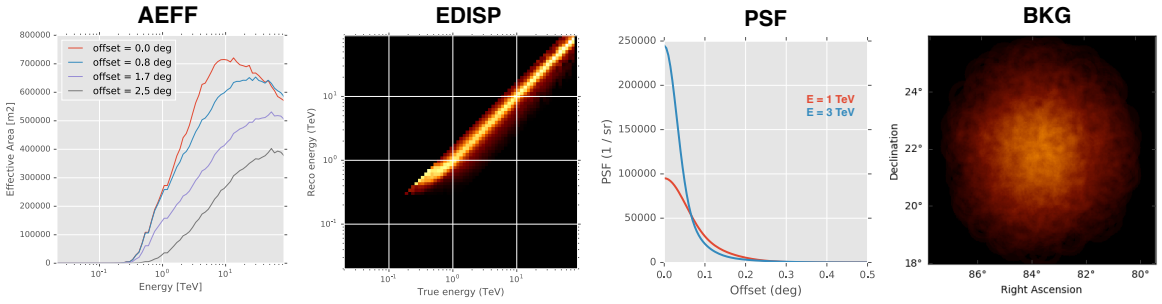

Figure 3.10 Illustration of major components of IACT DL3 data (using a H.E.S.S. I Crab nebula observation), including effective area (A_{eff}), energy dispersion (E_{disp}), point spread function (PSF) and background model (BKG). (Taken from [33])

The adaptation of the IRFs to the high level analysis will be discussed in Section 4.2, while the individual components, as illustrated in Figure 3.10, will be discussed in the

[1]The *off* denotes the prediction for an hadronic event [94]

following. Here the notation *true* and *reco* represent the true and reconstructed nature, while p and E are the FoV position and energy of the primary photon respectively. Note also that there are the *full-enclosure*, which are lookups for extended sources, and *point-like* IRF, which are lookups for point sources. The former stores the IRFs as a function of the offset with respect to the source position, while the latter calculates the IRFs components after applying a cut in direction offset [113]. In this analysis, the *full-enclosure* IRFs are used. The following details of IRFs refer to [114, 113, 58].

Effective Area

The effective detection area of the array, $A_{\text{eff}}(p_{\text{true}}, E_{\text{true}})$ [m^2], is defined as the product of the detector collection area and the array detection efficiency for a particular γ-hadron separation cuts (Section 3.2.2). The detection efficiency is depending on the observation conditions such as pointing zenith and azimuth angle and optical efficiency, which can be determined by Monte Carlo simulations. An example of the A_{eff} can be seen in Figure 3.10. There is a sharp rise at the low energies due to the system threshold. This can especially be seen for those events with smaller angular offset. The drop at high energies is due to a decrease in the γ-hadron cut efficiency at this point. This is related to the shower images getting too large in the camera, resulting in it being harder to pass the γ-hadron cut.

Note that the exposure can be obtained by multiplying the effective area with the observation livetime (the time the telescope is actually able to take data [110]).

Energy Dispersion

The energy dispersion, $E_{\text{disp}}(E_{\text{reco}}|p_{\text{true}}, E_{\text{true}})$ [TeV^{-1}], is defined as the probability to reconstruct the photon energy E_{reco}. The migration axis $\mu = \frac{E_{\text{reco}}}{E_{\text{true}}}$ can be used, such that the energy dispersion can re-written into $E_{\text{disp}}(\mu|p_{\text{true}}, E_{\text{true}})$. The reconstructed energy is sensitive to several systematic effects, e.g. atmospheric effects, optical response of the instrument and camera response. An energy bias is the average of ΔE over many events, where ΔE is defined via the true γ-ray energy E_{true} and its reconstructed energy E_{reco}:

$$\Delta E = \frac{E_{\text{reco}} - E_{\text{true}}}{E_{\text{true}}} \tag{3.2}$$

Note that this energy bias is strong at both low and high energies. A positive bias, meaning an overestimation of E_{reco}, appears at low energies due to only events with upward fluctuation in image size are selected at around the instrument threshold. On the contrary a negative bias, meaning an underestimation of E_{reco}, appears at high energies due to the opposite effect where an upper energy limit typically at 100 TeV is set in simulations. Therefore a safe

energy threshold is defined in the analysis to avoid energies with large bias, typically with the energy bias less than 10%. As mentioned at the end of Section 3.2.1, this energy threshold increases with the increasing zenith angle due to a decrease in the image size.

Point Spread Function

The point spread function, $PSF(p_{\mathrm{reco}}|p_{\mathrm{true}}, E_{\mathrm{true}})$ [sr^{-1}], is the probability to reconstruct the position p_{reco}, and is usually derived from Monte Carlo simulation of point-like sources. The PSF is typically expressed in terms of the angular separation $\theta = p_{\mathrm{true}} - p_{\mathrm{reco}}$, such that $PSF(\theta|p_{\mathrm{true}}, E_{\mathrm{true}})$. At positions further away from the peak of the point spread function, the binning can be more coarse because the PSF changes very slowly with increasing distance to the peak [58].

The angular resolution is inferred from the distributions of the squared angular distance (θ^2). It is typically defined as the 68% containment radius of the distribution. It depends on the zenith angle and the FoV offsets. The typical 68% containment radius for H.E.S.S. is $\sim 0.077^\circ$ [57, 59].

3.2.4 Background

The background can be interpreted as the acceptance of the telescope system to γ-like hadronic events that survive all cuts. The background rate depends on several parameters, namely the number of telescopes and their positions, the event reconstruction and γ-hadron separation method, the zenith-dependent observational conditions and also the energy. The acceptance is a function of E_{reco}, p_{reco}, zenith angle (ϑ) and azimuth angle (ϕ). There are in general two approaches to estimate the background. The standard approach in point-like analysis estimates that solely from the data, i.e. via the Reflected method or the Ring method [15]. Another way is to construct a background model from the archival data and treat it as an IRF, i.e. the 3D FoV method [84] used in this thesis.

Reflected and Ring Background

In the classical approach, the ON and OFF regions need to be defined. The ON region is the region where γ-ray sources are expected, whereas the OFF region contains no known γ-ray source. In the Reflected method, a number of OFF regions are defined as source-free regions of equal size to the ON region, and reflected around the observation position with the same offset as that to the ON region to account for the local inhomogeneities [15]. Under the assumption of radial symmetry of the camera acceptance, the correction factor of the acceptance is calculated simply as the ratio of area of ON region and OFF regions. This

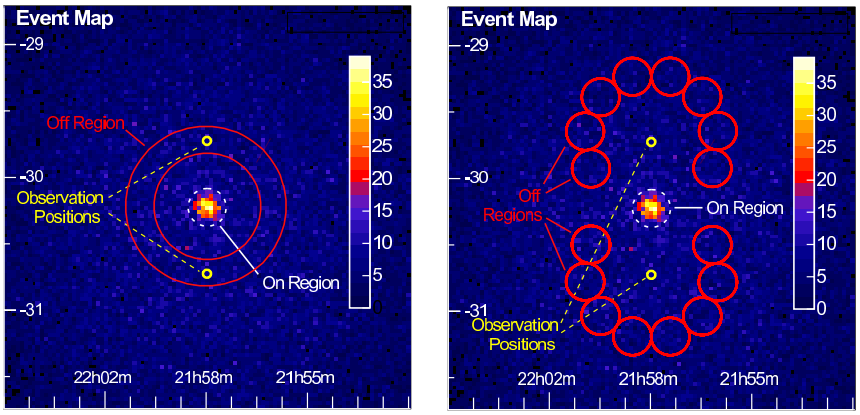

Figure 3.11 The schematics of Ring (Left) and Reflected (Right) background models. (Taken from [15])

method is suitable for the 1D spectral analysis. In the Ring method, the OFF region is defined as source-free region of equal ring distance from the ON region, yet a correction factor must be applied in the calculation of the acceptance due to different sizes of the ON/OFF region and the varying acceptance at each point of the ring [15]. This method is suitable for the 2D spatial analysis. The schematics of the Reflected and Ring background can be found in Figure 3.11. Despite the good background estimation performance on point-like sources and small extended sources using the two methods, they are both not ideal for the analysis of largely extended sources, e.g. the diffuse emission at the Galactic Centre. This is due to the insufficient background control region within the field of view covered by the extended signals.

FoV Background Model

An advanced way to estimate the background is by building a 3D model. By constructing a model of acceptance, the expected background can be predicted over the field-of-view (FoV) and as a function of the energy. Here the brief steps of building such a FoV background are introduced [84]:

1. A number of H.E.S.S. observations, away from the Galactic plane, are selected to construct the model. In this case, only the residual cosmic-ray background will be modelled. Due to the dependency of the background rate with various observational parameters, a tailored background model needs to be constructed for each observation in the following steps.

2. Building initial models in an equatorial coordinate system based on the zenith ϑ and azimuth ϕ angle, with 8 bins of $\vartheta \in [0°, 60°]$ and 2 bins of $\phi \in [-90°, 270°]$. Events close to known γ-ray sources are discarded.

3. Performing a normalisation fit of the model for each observation at each energy bin and masking known γ-ray source regions. Re-performing the fit for all observations. The normalisation is now independent of the zenith angle. The same procedure is performed for other parameters, i.e. the transparency coefficient and the optical phase.

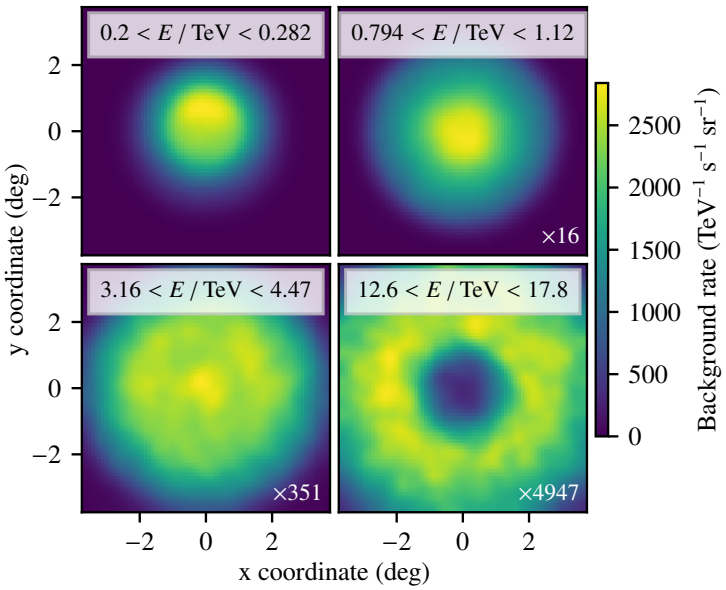

Figure 3.12 The visualisation of the FoV background model constructed from archival observations. The background estimation in four energy bins at zenith angle $20° \leq \vartheta \leq 30°$ and azimuth angle $90° \leq \phi \leq 270°$. (Taken from [84])

An example of such a background model can be seen in Figure 3.12. An asymmetry on the first map along the y-axis is observed, this is related to the altitude- or zenith- dependence of the background rate. Fainter structures are observed at larger zenith, imposing a higher detection threshold. The background shape is symmetric and peaks at the centre at around 1 TeV, while a ring feature is developed at the highest energy. The ring feature is related to the increase of background rate at larger offset angles due to the underperformance in the γ-hadron separation when the shower image gets too large in the camera. Note that an analysis energy threshold is needed to avoid large variation of the background rate close to the instrument energy threshold, and the strong influence from the observation condition. Unlike the classical approach presented above, FoV background estimation is suitable for the

3D spectral and spatial analysis. This is especially ideal for the analysis on largely extended regions, such as the diffuse emission at the Galactic Centre.

To account for the different observational effects in the observations, e.g. the muon efficiency, the atmospheric transparency and the variation of the NSB, a run-wise FoV background model is built by applying a spectral correction for each run. The methodology of applying the 3D run-wise background model to the high level analysis will be discussed in Chapter 4.

3.3 Summary

In this chapter, the key aspects to remember are:

- The highly energetic γ-rays produced from parent CR sources can travel and be detected on Earth indirectly via Cherenkov light, in our case using the H.E.S.S. telescopes
- The recorded showers provide information on incident γ-rays and allow background rejection
- IRFs provide a linkage between reconstructed and true γ-ray properties
- An advanced background model is applied to take into account the irreducible background present in observations of extended sources in analyses

In this way, the diffuse γ-ray emission in the CMZ from few hundreds GeV to 100 TeV can be detected and studied on Earth, revealing the nature of CRs in the complex Galactic Centre region. In the next chapter, the methodology of a 3D likelihood analysis will be presented, which will eventually help determine the best model description of the diffuse γ-ray emission from the Galactic Centre.

"I'm delirious. Spots are crawling
before my eyes."
"Those are spiders."

Diana Wynne Jones
Howl's Moving Castle

Chapter 4

Methodology of the 3D Maximum-Likelihood Analysis

For any experimental measurements in astrophysics, a major concern is the correctness of the theory describing the measured data. This can be done via hypothesis testing, through which the consistency of model and data is studied and the best model is selected, based on the concept of probability. In this chapter, the maximum-likelihood method for getting the best-fit model description will be introduced, followed by an explanation on its application in 3D (with two spatial dimensions and one energy dimension) using the open-source Python package for γ-ray astronomy, *Gammapy* (γ_π, version 0.19) [114].

This 3D analysis is an advanced and particularly useful way to study crowded regions with overlapping and large extended sources, which is the case for the diffuse γ-ray emission at the Galactic Centre. The methodology has been applied to a deep analysis of this region in Chapter 6.

4.1 Introduction to the Maximum-Likelihood Method

4.1.1 Binned Maximum-Likelihood

The maximum-likelihood method is a way of calculating the probability of a model reproducing the data. The term 'binned' means that the data follow a certain type of distribution in each defined bin. In the analysis of γ-ray counting measurements, the Poisson distribution is most appropriate due to the expected numbers of events being low as compared to other distributions, e.g. Gaussian. The Poisson distribution takes the form

$$P_i(n_i;\mu_i) = \frac{\mu_i^{n_i} e^{-\mu_i}}{n_i!}, \tag{4.1}$$

where n_i and μ_i represent the number of measured photons and predicted photons in the i-th bin respectively. The joint probability of the model to predict the measured result can be described by the likelihood $L = \prod_i P_i$. To estimate the best parameters of the model, one can maximise the likelihood or equivalently minimise the negative log-likelihood

$$\mathscr{L} = -\ln L = -\sum_i \left[n_i \ln(\mu_i) - \mu_i - \ln(n_i!) \right] \tag{4.2}$$

Yet in order to quantify the goodness of the model that predicts the number of photons, the so-called hypothesis testing is needed. One can make use of the likelihood ratio test from Wilks [127], which allows the estimation of the relative significance of the test model through

$$\mathrm{TS} = -2\ln\left(\frac{L_0(M_0)}{L_1(M_1)}\right) \approx \chi^2_m, \tag{4.3}$$

where L_0 and L_1 represent the maximum likelihood of model M_0 and M_1 respectively. The model M_0 is under the null hypothesis while M_1 is under the alternative hypothesis with fewer constraints. In γ-ray data analysis, M_0 can be assumed as that the data are composed of background, while M_1 in addition proposes the existence of some γ-ray sources apart from background. M_0 is nested in M_1, which means the number of parameters of M_0 is a subset of M_1. The test statistics (in the asymptotic limit of high statistics and assuming none of the model parameters is close to its physical boundaries), is then following a chi-squared distribution with m degree of freedom, where m is the difference of the number of parameters in M_1 and M_0 [77].

To compute the probability of obtaining a defined or greater TS value under the assumption that the null hypothesis is true, one further determine the right-tail p-value

$$p(\mathrm{TS}) = \int_{\mathrm{TS}}^{\infty} \chi^2_m(x)dx, \tag{4.4}$$

where the probability density function of the chi-squared distribution for $x > 0$ is

$$\chi^2_m(x) = \frac{x^{m/2-1} e^{-x/2}}{2^{m/2}\Gamma(m/2)}. \tag{4.5}$$

A small p-value indicates that the null hypothesis is very unlikely to be correct. In this case, the model M_1 is preferred in comparison to the model M_0. In practice, it is convenient to

convert the TS in unit of Gaussian standard deviation. Consider the simplest case where $m = 1$, the Equation 4.4 can be written as [81]

$$p(\mathrm{TS}) = \int_{\mathrm{TS}}^{\infty} \frac{1}{\sqrt{2\pi x}} e^{-x/2} dx. \tag{4.6}$$

By substituting $y = \sqrt{x}$, this can be expressed as

$$p(\mathrm{TS}) = \Big(\int_{-\infty}^{-\sqrt{\mathrm{TS}}} + \int_{\sqrt{\mathrm{TS}}}^{\infty} \Big) \frac{1}{\sqrt{2\pi}} e^{-y^2/2} dy. \tag{4.7}$$

The resulting p-value equals integration over the standard normal distribution. The corresponding unit of Gaussian standard deviation is

$$S = \sqrt{\mathrm{TS}}. \tag{4.8}$$

Note that the degree of freedom m increases when more spatial and spectral model components are added to M_1, thus the corresponding p-value with different χ^2_m have to be evaluated in the individual cases. The situation will be even more complex if some of the model components are degenerated to the null hypothesis due to absence of counts, leading to an over-estimation of the significance of M_1 [77]. With the use of Monte Carlo simulations, a better and accurate conversion for TS values to statistical significance has been achieved [77].

4.1.2 Counts Statistics

The statistics used in γ-ray analysis is divided into the W [7] and Cash [22] statistics, depending on whether the knowledge of the background is assumed. In this section, and as reference to the nomenclature in *Gammapy*, the observed and estimated counts are denoted as N_{observed} and $N_{\mathrm{estimated}}$ respectively. These counts follow a Poisson distribution with the expected value denoted as $\mu_{\mathrm{predicted}}$, this expected value is also called the predicted counts.

To begin with, for a classical observation approach where the background is unknown, a detector points into the direction close to the suspected γ-ray source for a time interval t_{ON} and measures $N_{\mathrm{observed,ON}}$ photons. Based on the type of background estimation method (e.g. as mentioned in Section 3.2.4), $N_{\mathrm{observed,OFF}}$ photons are measured in the OFF control regions. In this kind of classical analysis, the estimated number of γ-ray signals, i.e. the excess counts, can be calculated as [15]

$$N_{\mathrm{estimated,sig}} = N_{\mathrm{observed,ON}} - \alpha N_{\mathrm{observed,OFF}} \approx N_{\mathrm{observed,ON}} - \mu_{\mathrm{predicted,bkg}}, \tag{4.9}$$

where

$$\alpha = \frac{\int_{\mathrm{ON}} A_{\mathrm{ON}}(\theta_x, \theta_y, \phi_z, t) d\theta_x d\theta_y d\phi_z dt}{\int_{\mathrm{OFF}} A_{\mathrm{OFF}}(\theta_x, \theta_y, \phi_z, t) d\theta_x d\theta_y d\phi_z dt}, \tag{4.10}$$

in which $A_{\mathrm{ON,OFF}}$ is the system acceptance of the γ-ray like events that depends on the position (θ_x, θ_y) in the FoV, the zenith angle ϕ_z of the observation, the exposure time t for the ON and OFF observation. Note that $\alpha << 1$, e.g. due to much larger OFF than ON regions, will result in higher statistical significance due to smaller background fluctuations, on the other hand this may increase the systematic errors [15]. The OFF measurement is therefore generally taken not too far from the ON observation in terms of space and time in order to limit this systematic.

Alternatively one can assume that the background counts follow a Poisson distribution with the expected value $\mu_{\mathrm{predicted,bkg}}$ directly from a FoV background model, which is free of the statistical fluctuations as compared to the estimation using $\alpha N_{\mathrm{observed,OFF}}$. These two approaches are denoted into W statistics ($\alpha N_{\mathrm{observed,OFF}}$) and Cash statistics ($\mu_{\mathrm{predicted,bkg}}$). The details of W statistics can be found in Appendix A. The Cash statistics has been applied in the analysis of this thesis, where a 3D FoV background is used as already briefly discussed in Section 3.2.3. In this case, the likelihood is written as

$$\begin{aligned} L(N_{\mathrm{ON}}, \alpha; \mu_{\mathrm{sig}}) &= P(N_{\mathrm{ON}}; \mu_{\mathrm{sig}} + \mu_{\mathrm{bkg}}) \\ &= \frac{(\mu_{\mathrm{sig}} + \mu_{\mathrm{bkg}})^{N_{\mathrm{ON}}}}{N_{\mathrm{ON}}!} e^{-(\mu_{\mathrm{sig}} + \mu_{\mathrm{bkg}})}. \end{aligned} \tag{4.11}$$

The Cash statistics is expressed as [114]

$$C = -2\ln L = 2(\mu_{\mathrm{sig}} + \mu_{\mathrm{bkg}} - N_{\mathrm{ON}} \ln(\mu_{\mathrm{sig}} + \mu_{\mathrm{bkg}})). \tag{4.12}$$

The significance is computed as $S = \sqrt{TS} = \sqrt{C_0 - C_1}$, where

$$C_0(\text{null hypothesis}) \rightarrow \mu_{\mathrm{sig}} = 0; \tag{4.13}$$

$$C_1(\text{alternative hypothesis}) \rightarrow \mu_{\mathrm{sig}} = N_{\mathrm{ON}} - \mu_{\mathrm{bkg}}. \tag{4.14}$$

Eventually this leads to the Li & Ma significance for the perfectly known background model [77] as

$$S = \sqrt{2}\left[\mu_{\mathrm{bkg}} + N_{\mathrm{ON}}\left(\ln\frac{N_{\mathrm{ON}}}{\mu_{\mathrm{bkg}}} - 1\right)\right]^{1/2}. \tag{4.15}$$

4.2 3D Analysis Tool: *Gammapy*

Gammapy (γ_π) is an open source Python library for γ-ray astronomy. The adaptation of the 3D likelihood fit, i.e. two spatial dimensions and one energy dimension, gives a remarkable advantage and new insight towards the analysis in crowded and complex regions. The model fitting, the fluxpoint estimation and the adaptation of systematics uncertainties will be discussed in the following sections.

4.2.1 Model Fitting

As discussed in the previous section, the number of predicted events is related to the likelihood, which is a probability density function. For a specific observation i, the likelihood can be derived by integrating the probability density P_i with a particular model M over the time t, energy E and FoV position p via [73]

$$\mu_i(M) = \int_{\text{GTI}} \int_{\text{Ebounds}} \int_{\text{ROI}} P_i(p', E', t'|M) dp' dE' dt' \tag{4.16}$$

where the prime (unprime) denotes the reconstructed (true) quantities, GTI denotes the good time interval (the observation times of the given events [58]), Ebounds denotes the energy bounds and ROI denotes the region of interest. The model M in particular consists of multiple components j such that $P_i(p', E', t'|M) = \sum_j P_i(p', E', t'|M_j)$, from which

$$P_i(p', E', t'|M_j) = \int_{p,E,t} R_i(p', E', t'|p, E, t) \times M_j^S(p, E, t) dp dE dt. \tag{4.17}$$

The function M_j^S is defined as the celestial source model with true quantities, each component is given by

$$M^S(p, E, t) = M_S(p|E, t) \times M_E(E|t) \times M_T(t), \tag{4.18}$$

assuming factorisation into a spatial, spectral and temporal model component. The function $R(p', E', t'|p, E, t)$, on the other hand, is the instrument response function that is related to the effective area, PSF and energy dispersion as discussed in Section 3.2.3. It can be expressed as

$$R(p', E', t'|p, E, t) = A_{\text{eff}}(p, E, t) \times PSF(p'|p, E, t) \times E_{\text{disp}}(E'|p, E, t). \tag{4.19}$$

In particular, $\int PSF(p'|p,E,t)dp' = \int E_{\rm disp}(E'|p,E,t)dE' = 1$. It is discussed in Section 4.1.2 that the FoV background model $\mu_{\rm bkg}(E')$ can be taken into account in the Cash statistics, where it can be adjusted with a normalisation term *norm* and tilting term *tilt* via

$$\mu_{\rm bkg}(E') \rightarrow \mu_{\rm bkg}(E') \times {\rm norm} \times (\frac{E'}{1\ {\rm TeV}})^{-{\rm tilt}} \tag{4.20}$$

to account for unavoidable variations of the level of night sky background and atmosphere transparency per observation run. The model fitting is performed using MINUIT [67], which outputs the covariance matrix and errors of the individual model parameters. The essential model components used in this thesis are [114]:

Point Source Spatial Model

$$\phi({\rm lon},{\rm lat}) = \delta({\rm lon}-{\rm lon}_0, {\rm lat}-{\rm lat}_0) \tag{4.21}$$

Gaussian Source Spatial Model

$$\phi({\rm lon},{\rm lat}) = \left\{4\pi(1-\cos\sigma)[1-\exp(-1/(1-\cos\sigma))]\right\}^{-1} \exp\left(-\frac{1}{2}\frac{1-\cos\theta}{1-\cos\sigma}\right) \tag{4.22}$$

Remark: It is symmetric and therefore normalised to 1 on the sphere, where θ is the sky separation to the model centre and σ is the extension of the source.

Power Law Spectral Model

$$\phi(E) = \phi_0 \cdot \left(\frac{E}{E_0}\right)^{-\Gamma} \tag{4.23}$$

Exponential Cutoff Power Law Spectral Model

$$\phi(E) = \phi_0 \cdot \left(\frac{E}{E_0}\right)^{-\Gamma} \exp(-(\lambda E)^{\alpha}) \tag{4.24}$$

Remark: The parameter α is typically set to 1.

Special Treatment for Diffuse Emission Model

A special treatment is needed to account for the diffuse γ-ray template used in this thesis. A 3D (again 2D for spatial and 1D for energy) diffuse emission model is built and adapted into a customised spatial template model. A norm spectral model is defined to include a normalisation parameter to the template model. The construction of such diffuse emission template will be discussed in Chapter 5.

4.2.2 Significance and Fluxpoint Estimation

The best fit models are obtained from the above-mentioned likelihood fitting. To proceed, two methods can be used to estimate the significance and fluxpoints respectively based on the analysis needs.

For a spatial analysis where one wants to look at the residual over the combined energy bins, the significance can be estimated through the backward folding [114]. In this case, the PSF is neglected and there is no re-optimization of the model parameters. The best-fit flux and significance at each pixel are given by the excess over the null hypothesis using the Li & Ma formalism. This can be done via the *Gammapy* class **ExcessMapEstimator**.

For a spectral analysis where one is interested in the spectral energy distribution, forward folding is used [114]. From the global best fit source component, the flux from the source of interest is re-fitted by wrapping a scaling model on top of it. This re-fitting process is done for each defined energy bin independently, leading to changes in the normalisation factor in different energy bins. The resulting new flux is the estimated fluxpoint. For an accurate estimation, the other source components need to be re-optimised. This can be done via the *Gammapy* class **FluxPointsEstimator**. For spectral points with TS<4, upper limits are computed using a 95% confidence interval.

4.2.3 Error Estimation

To assess the fit quality, one can perform the likelihood scan for each parameter by altering its value at around the best-fit result. A parabolic shape is expected in the scan profile, which ensures a good error estimation. The 1σ and 2σ deviations from the mean indicate the 68% and 95% confidence intervals respectively. As mentioned in Section 4.2.1, the errors of individual parameters can be extracted from the covariance matrix after the fit is performed. The error bands can therefore be plotted for each model through error propagation. Furthermore, the confidence intervals of the parameters can also be assessed through a 2D confidence contour. The surface likelihood profile is computed by scanning two parameters of interest, which later convert to a surface of statistical significance σ. Often both 1σ and 2σ contours are plotted, giving the ellipsoidal shapes around the best-fit value.

4.2.4 Nuisance Parameter Fit

Systematic uncertainties arise due to e.g. mismodelling of the hadronic background. There are different ways of calculating such energy-dependent systematics, for instance by looking at the data and model deviation in source-free regions of the dataset [103], or more accurately

by interpolating the systematics bias from all runs in the source-free regions [86]. These systematics can be included into the 3D likelihood fit by adapting nuisance parameters in fitting classes, as implemented by Katrin Streil (2022, priv. com. [107]). These nuisance parameters are correlated such that systematic uncertainties, but not uncorrelated statistical uncertainties, are eliminated. This method has already been applied to various scientific observations such as diffuse emission or dark matter annihilation in the complex Galactic Disk [29, 106].

To account for systematic uncertainties, Gaussian background perturbations ΔB are introduced to the likelihood function [29]. These perturbation terms are also called nuisance parameters. These revise the Poisson distribution as defined in Equation 4.1 into

$$P_i(n_i;\mu_i) = \frac{\mu_i^{n_i} e^{-\mu_i}}{n_i!} \cdot e^{\left[-\frac{1}{2}\Delta B_i \Sigma_{j=0}^{N} (K^{-1})_{ij} \Delta B_j\right]}, \tag{4.25}$$

where the covariance matrix $K_{ij} \equiv \langle \Delta B_i \Delta B_j \rangle$ is introduced. The total correlation matrix is defined as $K = K_E \otimes K_S$, in which K_E and K_S are the spectral and spatial correlation matrix respectively. The spectral and spatial parts can be expressed as

$$(K_E)_{aa\prime} = \sigma_E^2 \cdot e^{\left[-\frac{1}{2}\left(\frac{\log_{10}(E_a/E_{a\prime})}{l_E}\right)^2\right]}; (K_S)_{bb\prime} = \sigma_S^2 \cdot e^{\left[-\frac{1}{2}\left(\frac{\|\vec{r_b}-\vec{r_{b\prime}}\|}{l_S}\right)^2\right]}. \tag{4.26}$$

where $\sigma_{E/S}$ and $l_{E/S}$ are the correlation amplitude and length in each energy/spatial bin. The spatial correlation length can typically be estimated from a Fourier transformation of the residual map. Note that here it is assumed there is no correlation between the energy bins and therefore l_E is set to be infinitesimally small. This is because the correlation is assumed to be in the order of the energy resolution, which is much smaller than the chosen energy bins. In this case the exponential term in the spectral correlation matrix is set to 1. The spatial systematic amplitude can also be assumed to be 1 if each spatial bin shares the same background systematic within an energy bin. The computational time is, however, costly by running such a nuisance fit for each spatial and energy bin. Thus the nuisance parameter cube is often downsampled so that one bin of downsampled nuisance cube can act on multiple original neighboring bins, with a weighted systematic uncertainty.

4.3 Summary

In this chapter, the key aspects to remember are:

- The analysis can be done using the 3D (2D for space and 1D for energy) maximum-likelihood method implemented in *Gammapy* (γ_π), which will help determining the best model description for the diffuse γ-ray emission from the Galactic Centre.

With modern instrumentation and an advanced analysis tool, the diffuse γ-ray emission in the CMZ can be well studied. In the next chapter, the construction of a 3D (2D for space and 1D for energy) diffuse γ-ray emission template will be introduced, which will be used in the analysis of this thesis.

"You can't cross the sea merely by standing and staring at the water."

Rabindranath Tagore

Chapter 5

Building 3D Diffuse Gamma-Ray Emission Template

The study of diffuse γ-ray emission is an indirect method of locating CR accelerators in the Galaxy, as discussed at the end of Chapter 2. The target region of this thesis is around the complex Galactic Centre where abundance of gases exist. In this work, a CR proton injecting source located at Sgr A* is assumed. To construct a diffuse γ-ray emission model that can later be used in the γ-ray analysis in Chapter 6 for comparing expected γ-ray flux with measurements by H.E.S.S., one needs to consider several building elements. These include the energy-dependent CR propagation, the molecular distribution of the gas in the central molecular zone (CMZ), the production of γ-ray from proton-proton interactions and the adaptation of the resulting model into *Gammapy* for further analysis. All of these will be discussed in this Chapter, followed by a general description of the diffuse γ-rays properties.

5.1 Building Elements of Diffuse Emission Template

5.1.1 Cosmic-Ray Diffusion

The motion of charged particles is strongly influenced by the Lorentz force, which is created by magnetic fields present in every astrophysical environment. Irregularities in the magnetic field, which might be due to the fluctuations in the field and the instabilities caused by streaming motions of the particles, lead to the random scattering of the particles. Due to the presence of magnetic fields throughout the Galaxy, high-energy charged particles can be considered to diffuse from their sources through the interstellar medium [80]. In the simple case where there is no convection and no energy losses, the net flux of particles $q(\vec{r},E,t)$ can be described by a diffusion coefficient $D(\vec{r},E,t)$ and the gradient of particle density

$\nabla n(\vec{r},E,t)$ using the Fick law:

$$\vec{q}(\vec{r},E,t) = -D(\vec{r},E,t)\nabla n(\vec{r},E,t). \tag{5.1}$$

As the total number of particles is conserved, it holds that $\frac{\partial n(\vec{r},E,t)}{\partial t} = -\nabla\vec{q}(\vec{r},E,t)$. By assuming a scalar diffusion coefficient $D(\vec{r},E,t) = D(E)$, one can derive the classical diffusion equation

$$\frac{\partial n(\vec{r},E,t)}{\partial t} = D(E)\nabla^2 n(\vec{r},E,t), \tag{5.2}$$

where ∇^2 is the Laplace operator. In the case of spherically symmetric diffusion,

$$\frac{\partial n(\vec{r},E,t)}{\partial t} = D(E)\frac{1}{r^2}\frac{\partial}{\partial r}\left[r^2\frac{\partial n}{\partial r}\right]. \tag{5.3}$$

The impulsive point source solution of this diffusion equation in an infinite volume is given by a three-dimensional Gaussian distribution [8]:

$$n(\vec{r},E,t) = \frac{N_p}{[4\pi D(E)t]^{3/2}}\exp(-\frac{r^2}{4D(E)t}), \tag{5.4}$$

where N_p is the total number of particles being injected at the origin at time $t = 0$. For a continuous point source where the particles are liberated continuously at a constant rate $\dot{N}_p$, one can essentially sum up the Equation 5.4 in small enough time intervals. The general solution can therefore be obtained by integrating Equation 5.4 [27]:

$$\begin{aligned} n(\vec{r},E,t) &= \frac{1}{[4\pi D(E)]^{3/2}}\int_0^t \dot{N}_p(t')\exp(-\frac{r^2}{4D(E)[t-t']})\frac{dt'}{[t-t']^{3/2}} \\ &= \frac{\dot{N}_p}{4\pi D(E)r}\mathrm{erfc}(\frac{r}{\sqrt{4D(E)t}}). \end{aligned} \tag{5.5}$$

In a steady state scenario, in which the particle distribution no longer changes with time, the Equation 5.3 turns into $\frac{\partial}{\partial r}\left[r^2\frac{\partial n}{\partial r}\right] = 0$. Therefore one expects a general solution [27] of

$$n(\vec{r},E,t) = B + \frac{A}{r}, \tag{5.6}$$

where A and B are constants determined from the boundary conditions at each E. Suppose the number density is n_1 and n_2 at distance a and b respectively, this leads to $A = \frac{a(n_1-(n_2b-n_1a))}{b-a}$ and $B = \frac{n_2b-n_1a}{b-a}$. This $1/r$ behaviour is indeed present in the simulation of the continuous injection in steady-state using different approaches, as shown in Figure 5.1. Note that the result using a summation of Equation 5.4 at each defined time step does not

produce exactly the same result as using Equation 5.5 and Equation 5.6 due to the computational limitation on the size of the time interval. A consistent result is expected if the time interval is infinitely small.

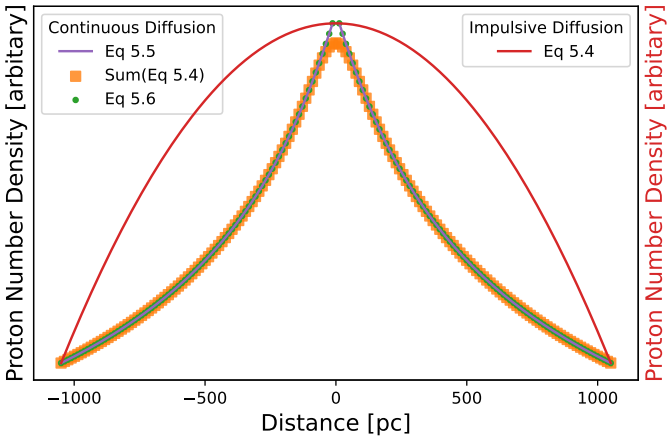

Figure 5.1 The simulated proton distribution from the continuously (steady-state) and impulsively injecting point source using different equations in Section 5.1.1. The distribution is illustrated at a proton energy of 0.1 TeV.

In order to save time for the later optimization process of the diffusion parameters, only a quarter of the diffused particles are simulated in a cube. The distribution is then reflected to the rest of the regions. This is feasible due to the diffusion being spherically symmetric. The resulting CR distribution is in 4D, where 3D are for space and 1D is for proton energy.

Note that the CR diffusion can also be computed using the numerical finite difference method, known as the Forward Time Centered Space (FTCS) method. The nurmerical method gives an advantage in making it needless to solve the diffusion equation (which can be complicated when convection, re-acceleration or proton losses are involved). A convolutional kernel can also be used to facilitate the computing process, though still slower than the mathematical approach when considering the simple diffusion case. Details of this computational method can be found in Appendix A.

5.1.2 Gas Distribution in the CMZ

The diffused protons collide with the ambient hydrogen gas of the molecular clouds (MC(s)) in the CMZ, and consequently produce γ-rays (see Section 5.1.3). The construction of a 3D distribution of the MCs is therefore essential to complete the simulation. The MC structures in the CMZ have been studied by different observers [120, 102, 129], mainly using the $C^{32}S$ $J = 1 - 0$ and ^{12}CO $J = 1 - 0$ (and ^{13}CO $J = 1 - 0$), as well as the OH main lines.

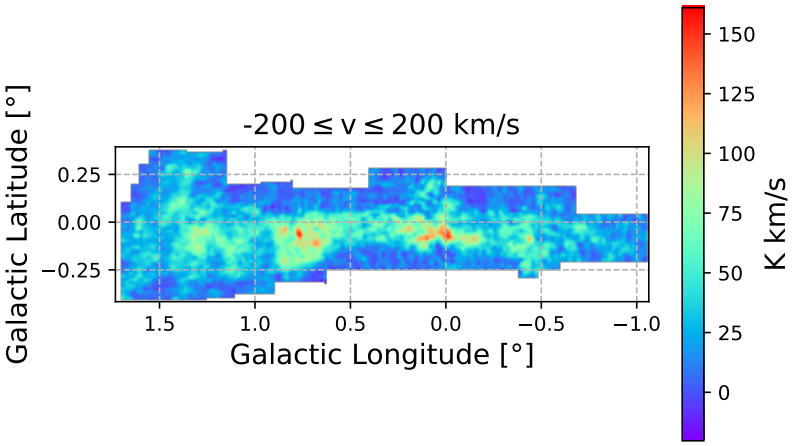

Figure 5.2 The molecular distribution in the CMZ from the CS observation by Tsuboi et al. (1999) [120]. The map is integrated from -200 $\leq v \leq$ 200 km/s.

As discussed by Tsuboi et al. (1999) [120], CO lines have been commonly used to identify the structure of the MCs due to sufficient sensitivity in the high-velocity range of $|v| \geq 30$ km s^{-1}. However in the low velocity range of $|v| \leq 30$ km s^{-1}, they strongly suffer from both background and foreground contaminations. On the other hand, CS emission is expected to be nearly free from strong contamination because it has a higher critical density, $n(H_2) \cong 10^4$ cm^{-3}. Since the MCs in the Galactic Centre region may have densities high enough to excite the CS lines (because the strong tidal force destroys molecular cloud envelopes with low density), it is promising that the entire structure of the MCs can be evaluated in the CS lines. The CS map used in this analysis integrated with different local standard of rest (LSR) velocities can be seen in Figure 5.2.

One disadvantage of solely using this CS map is the absence of line-of-sight information. To overcome this deficiency, one can project the CS map onto a model that is able to adequately distribute the molecular material along the line-of-sight. Several previous studies also used this kind of method [90, 116]. As illustrated in Figure 5.3, two molecular cloudlets with equal excitation temperatures and optical depths but different distances, display the same CO emission lines, but distinctive OH absorption lines [129]. In this way one can estimate the relative position of MCs along the line-of-sight to the Galactic Centre by combining information from CO emission and OH absorption. Examples of such models in terms of face-on LSR velocity distribution can be found in Figure 5.4. Since both the CS data and CO/OH model are distributed with LSR velocity, this allows the projection of the CS map at different velocity bands onto the line-of-sight. The CO/OH model can be obtained from Sawada [102] or Yan [129]. The general steps of constructing the molecular cloud map are the following:

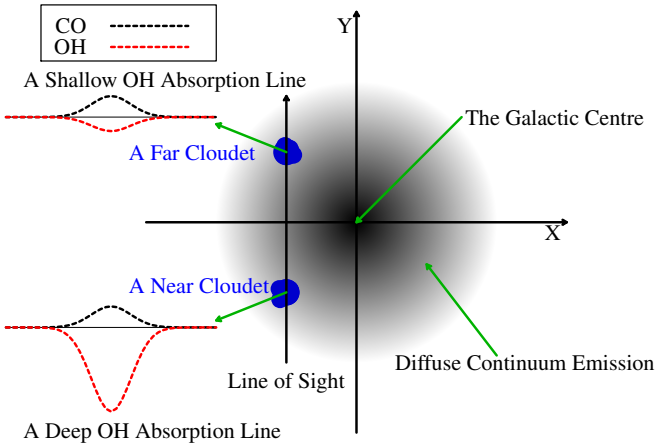

Figure 5.3 Principles of deriving the relative positions of molecular clouds. The black dashed lines and red lines represent CO emission and OH absorption lines, respectively. (Taken from [129])

1. Integrate the CS maps in different velocity bands $v_i \in$ [-200, -160, ... , 160, 200] km/s. The maps are integrated in 40 km/s rather than 10 km/s bins[1] due to the following procedure at (2).

2. The CS data is projected onto the CO/OH model by matching the velocity and longitude coordinate (i.e. when using Sawada's model [102]) or both longitude and latitude coordinates (i.e. when using Yan's model [129]), depends on the structure of the CO/OH model. If no match can be found, the CS data is projected onto the origin of the z-coordinate (line-of-sight) at $z = 0$. In order to avoid data clumping at the origin, the CS data is being integrated into a larger velocity band before the process, as mentioned at procedure (1). Note that rebinning is performed on the CO/OH model in order to retain the line-of-sight resolution at a certain level, i.e. Sawada's model is refined by a factor of 9 and Yan's model is refined by a factor of 5. This rebinning also needs to be taken into account when projecting the CS data at $z = 0$.

3. The CS data is in the unit of brightness temperature [K km s^{-1}]. A weighted density value is assigned to the individual bins such that the total mass of the molecular cloud is within $(3-8) \times 10^7 M_\odot$ [120] and the mass in the inner 150 pc is within $(3^{+2}_{-1}) \times 10^7 M_\odot$ [56], as estimated in the previous publications. The finalized maps have the unit of density [m^{-3}].

[1]The 10 km/s is the minimum band width given by the CS observation. The 40 km/s is chosen as a reference from the study in [90].

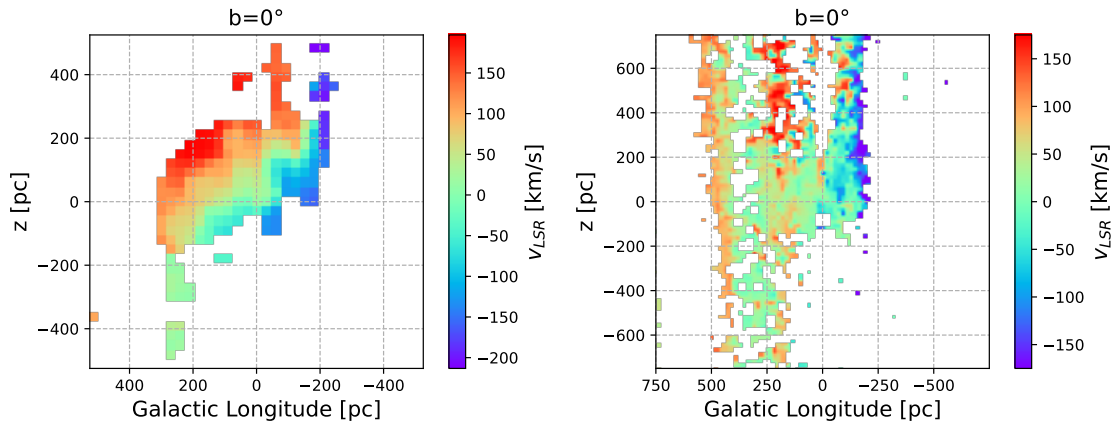

(a) Sawada et al. (2004) [102].

(b) Yan et al. (2017) [129].

Figure 5.4 The face-on velocity distribution map at galactic latitude $b = 0°$. For (a), the map is only available for $b = 0°$. For (b), it is available in the range of $-2.12° \leq b \leq 1.87°$, yet $b = 0°$ is shown for comparison. Distinctions on the velocity distribution and the line-of-sight coverage can be seen.

Three MCs maps are being used in the analysis (Chapter 6) to cross-check the diffusion parameters. First one is the Sawada-Tsuboi (ST) map, which is computed by projecting Tsuboi's CS data onto the Sawada's CO model. The bin size of the CO model was originally in 30 pc and it is rebinned to 3.3 pc, which is compatible to the pixel size of the H.E.S.S. data. The extension of the Tsuboi map is $1.73° \leq l \leq -1.06°$ and $-0.42° \leq b \leq 0.39°$, whereas the extension of the Sawada model is $3.54° \leq l \leq -3.54°$, -525 pc $\leq z \leq 525$ pc and only available at $b = 0°$. Second one is the Yan-Tsuboi (YT) map, which is obtained by projecting Tsuboi's CS data onto the Yan's CO/OH model. The bin size of the CO/OH model was originally $\approx$18 pc and is being rebinned to ≈ 3.6 pc. Yan's CO/OH model gives a greater coverage along the galactic plane as well as extends along the galactic latitude, which is $7.87° \leq l \leq -7.62°$, $-2.12° \leq b \leq 1.87°$ and -2.9 kpc $\leq z \leq 2.9$ kpc. The last one is the Yan (Y) map, which is built by converting velocity into the brightness velocity such that the resulting MCs map gives a greater coverage than the CS observation. No data projection is needed in this case. All the maps built for this thesis can be found in Figure 5.5. Due to the low spatial resolution of the data from Yan, the structure of molecular clouds near the Galactic Centre where the continuum emission varies rapidly cannot be resolved [129]. Therefore the MC distribution along the line-of-sight is different when comparing Yan's map to Tsuboi's map.

Note that Sawada assumed the sun-to-earth distance to be 8.5 kpc whereas Yan used 8.34 kpc in the calculation. In addition, the origin of the data from Yan is set to the position of Sgr A*. These differences have to be taken into account in the projection procedure.

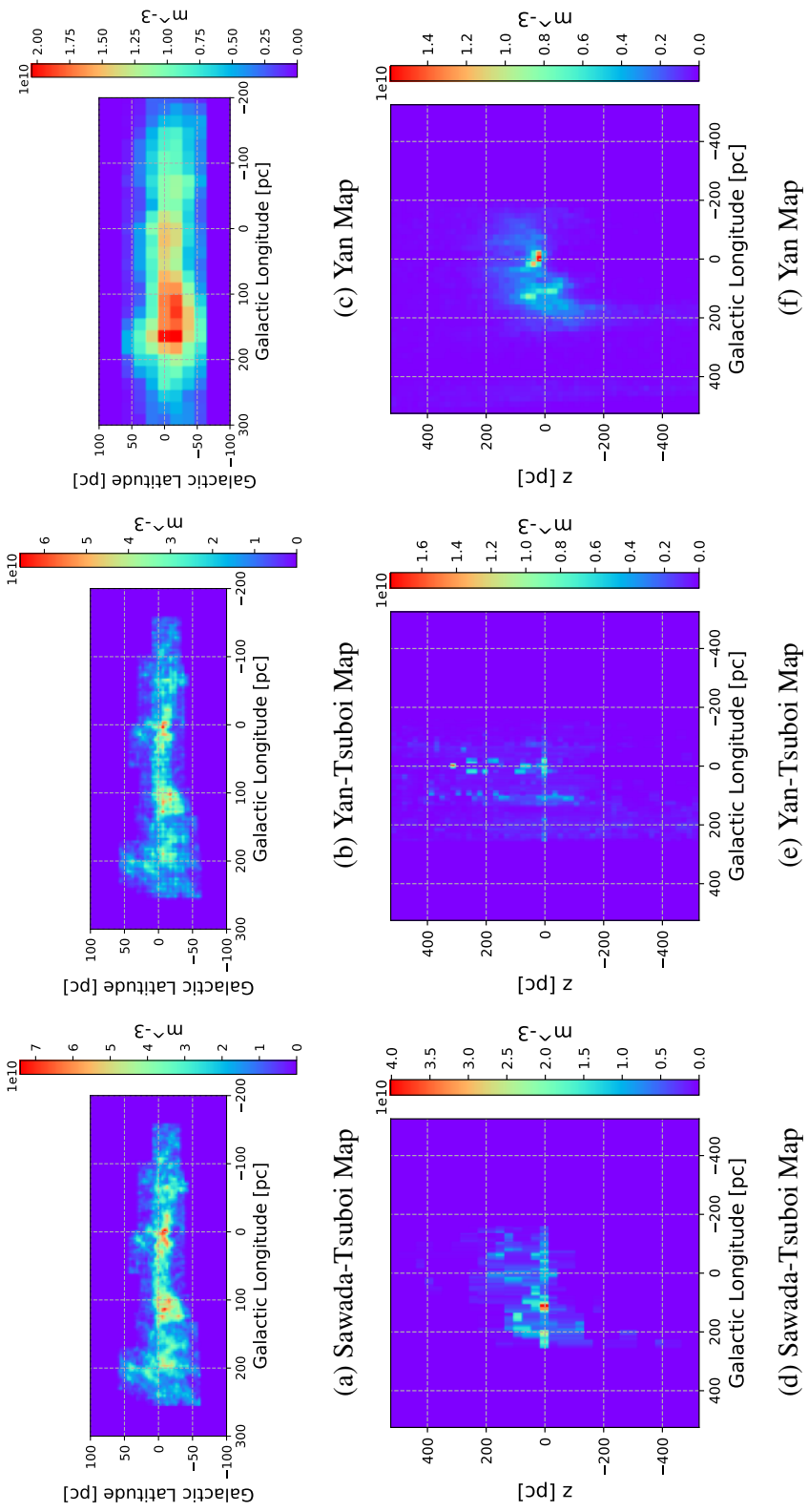

Figure 5.5 The maps of MC distribution from the Sawada-Tsuboi projection (Left), Yan-Tsuboi projection (Middle) and Yan (Right). Top panel: MC distribution along the line-of-sight. Bottom panel: MC face-on-distribution.

5.1.3 Proton-Gamma Conversion

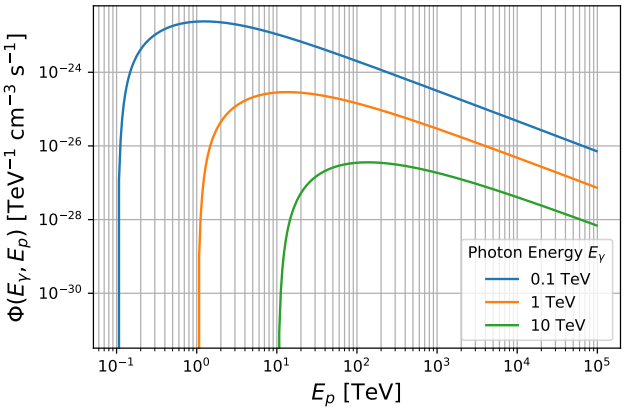

Figure 5.6 The γ-ray flux at different photon energies E_γ as a function of the incident proton energy E_p by assuming the proton energy distribution of E_p^{-2}.

The parameterization of the energy spectrum of γ-rays produced in inelastic proton-proton collisions is based on the simulation performed by Kelner et al. (2006) [70]. The calculation of the γ-ray spectra includes both π^0 and η-meson decay channels (namely $\pi^0 \to 2\gamma$, $\eta \to 2\gamma$, $\eta \to 3\pi^0 \to 6\gamma$ and $\eta \to \pi^+\pi^-\pi^0 \to 2\gamma$), with high accuracy in the primary proton energy range of 0.1 TeV $\leq E_p \leq 10^5$ TeV. The production rate of γ-rays in the energy interval $(E_\gamma, E_\gamma + dE_\gamma)$ can be described by the function [70]

$$\Phi_\gamma(E_\gamma) \equiv \frac{dN_\gamma}{dE_\gamma} = cn_H \int_{E_\gamma}^{\infty} \sigma_{inel}(E_p) J_p(E_p) F_\gamma(\frac{E_\gamma}{E_p}, E_p) \frac{dE_p}{E_p}, \tag{5.7}$$

as already discussed in Section 2.2.1, where c is the speed of light, n_H is the hydrogen gas density, $\sigma_{\rm inel}(E_p)$ is the cross-section of inelastic proton-proton interactions, $J_p(E_p)$ is the proton energy spectrum and $F_\gamma(\frac{E_\gamma}{E_p}, E_p)$ is the number of photons in the interval $(\frac{E_\gamma}{E_p}, \frac{E_\gamma}{E_p} + d\frac{E_\gamma}{E_p})$ per collision.

To facilitate the conversion process, a two-dimensional look-up table finely binned in both E_γ and E_p is created. The rate of γ-ray emission of any given spatial bins can be obtained by multiplication of gas density and the number density of protons together with the E_p entries of this look-up table. The resulting γ-ray emission rate as a function of the incident proton energy E_p, assuming a proton energy spectrum of E_p^{-2}, is shown in Figure 5.6. The result is verified by the γ-ray energy spectrum derived by (Kelner et al. 2006) [70], in which a power law energy spectrum with cutoff is being used to describe the proton distribution. The corresponding γ-ray energy spectrum derived from the look-up table in this work is shown in Figure 5.7. A clear agreement between the two works for $E_\gamma \geq 0.1$ TeV can be

seen. Specifically, the hardening of the spectrum at around $E_\gamma \approx 0.1$ TeV when using the energy-dependent cross-section in the calculation and the impact of proton energy cutoff E_{cutoff} is noticeable at energies $E_\gamma \geq 10^{-2} E_{\text{cutoff}}$. The discrepancy at $E_\gamma < 0.1$ TeV is due to the energy range being beyond the interest of the H.E.S.S. measurement, and thus the δ-functional approximation as suggested by the author is not being used in this calculation.

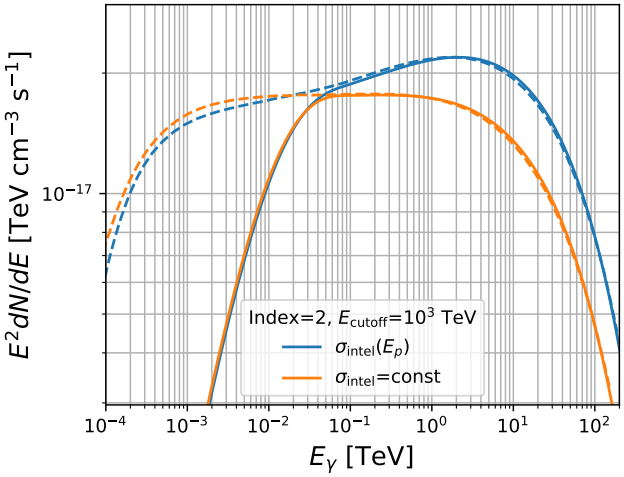

Figure 5.7 The γ-ray energy spectrum calculated with energy-dependent and energy-independent cross-section σ_{intel} by assuming the proton energy distribution follows the power law with exponential cutoff. The solid and dased lines denote the spectra derived by this work and by Kelner et al. (2016) respectively. The discrepancy at $E_\gamma < 0.1$ TeV with the graph produced by Kelner et al. (2006) is due to a different selection of the energy range and thus different treatment is needed below this point.

5.2 3D Diffuse Emission Template

By deriving the proton distribution after the propagation (3D in space + 1D in energy) and the hydrogen molecular gas distribution in the CMZ (3D in space), the energy-dependent proton-γ conversion can be performed by considering the inelastic proton-proton collision. This results in a distribution of γ-ray emission rate per unit energy (3D in space + 1D in energy). To derive the γ-ray flux, one assumes that the radiation from each grid is emitted isotropically over the solid angle and that the Galactic Center is 8.5 kpc away from Earth. This flux map is then integrated along the line-of-sight (2D in space + 1D in energy) to proceed for further analysis (in Chapter 6) using the *Gammapy* package (presented in Chapter 4).

In Section 5.1.1, the propagated proton distribution was discussed by considering both the continuous (in Equation 5.5: $n(\vec{r},E,t) = \frac{\dot{N}_p}{4\pi D(E) r}\text{erfc}(\frac{r}{\sqrt{4D(E)t}})$) and impulsive (in Equa-

tion 5.4: $n(\vec{r},E,t) = \frac{N_p}{[4\pi D(E)t]^{3/2}}\exp(-\frac{r^2}{4D(E)t}))$ injection from a source. Two inputs are necessary in both of these injection scenarios, namely the proton injection spectrum and the diffusion coefficient. The injection spectrum is assumed to be power-law like due to the general nature of the cosmic-ray spectrum, yet the choice of power-law with exponential cutoff cannot be ruled out. Therefore the proton injection spectra used in this thesis are

$$\propto \begin{cases} E_p^{-\alpha} & \text{, without cutoff} \\ E_p^{-\alpha} e^{-E_p/E_{\text{cutoff}}} & \text{, with cutoff.} \end{cases} \tag{5.8}$$

The diffusion coefficient is defined by Equation 2.24 ($D \approx D_0(\frac{E}{10\,\text{GeV}})^{\delta}$), in which D_0 and δ are the free parameters. Note again that the simple diffusion is considered in this analysis, assuming no proton and energy losses. In this case, there are in total five free parameters involved in building the diffuse γ-ray emission template, namely the proton spectral index α, the proton energy cutoff E_{cutoff}, the diffusion constant D_0, the diffusion slope δ and the total number of injected proton N_p from 0.1 TeV $\leq E_p \leq 10^5$ TeV.

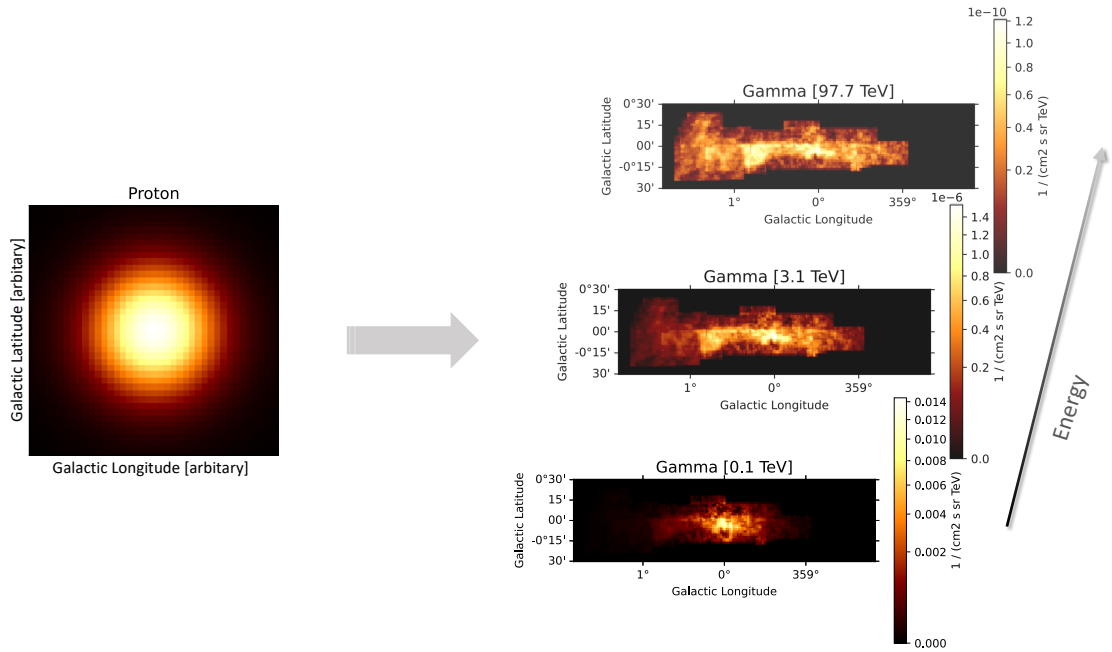

Figure 5.8 Example of a distribution of the diffused proton along the line-of-sight (Left), and the resulting γ-ray flux map at different γ-ray energy (Right). For an energy-dependent diffusion, protons with higher energies diffuse to a greater range.

In the analysis, protons with energies from 100 GeV to 100 PeV are considered. By following the above-mentioned template construction method, an example of the proton

diffusion map and γ-ray flux map is illustrated in Figure 5.8. The protons are diffused spherically, and the resulting γ-ray fluxes at different energies can be seen. Since in principle all protons contribute to the low-energy γ-ray flux, the flux intensity is, therefore, largest at low energies. On the other hand, since the low-energy protons have a smaller diffusion range as compared to the high-energy protons, they are more confined at the central region and thus give a more concentrated flux distribution at the central region for low-energy γ-ray. Note that the template parameters are chosen with exaggerated values such that the clear differences of the γ-ray flux at different energies are shown.

5.3 Template Properties

Before proceeding to the analysis result in Chapter 6, some of the basic diffusion properties will be discussed in the following sections. All illustrations have assumed a diffusion time of 10^6 years (note that the diffusion time is inversely proportional to the diffusion coefficient D). Both properties from the continuous and impulsive injection scenarios will be covered.

Effect of D_0 and δ on the Diffusion Coefficient

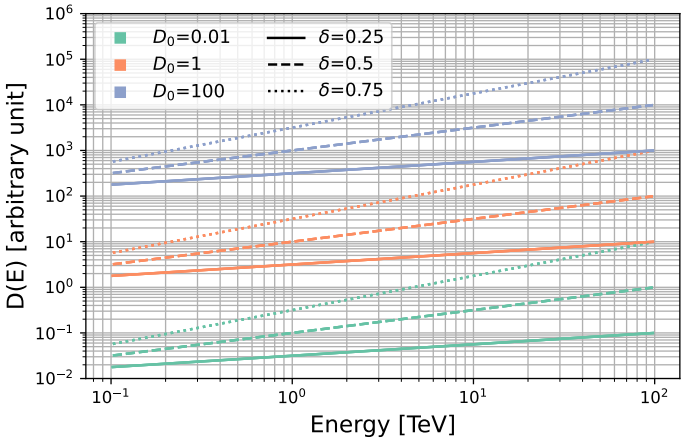

Figure 5.9 The diffusion coefficient $D(E)$ in terms of different combinations of D_0 and δ. The D_0 is in the unit of pc^2/s. The colors indicate the value of D_0 and the different lines indicate the value of δ.

As discussed in Section 2.3.1, the diffusion coefficient $D(E)$ is proportional to the travelling distance squared of the protons in the Galaxy as given by Equation 2.24. It can be re-written in terms of the parameters D_0 and δ. Since D_0 acts as a normalisation factor, increasing D_0 will increase the $D(E)$ as indicated in Figure 5.9. The parameter δ

acts on the energy term, which affects the shape of the diffusion coefficient. In this case, a slope developed as shown in the Figure 5.9, where high-energy protons propagate to a relatively larger travelling distance in comparison with the low-energy protons when $\delta > 0$. By increasing δ, this effect gets exaggerated.

Effect of Diffusion Coefficient on the Proton Distribution

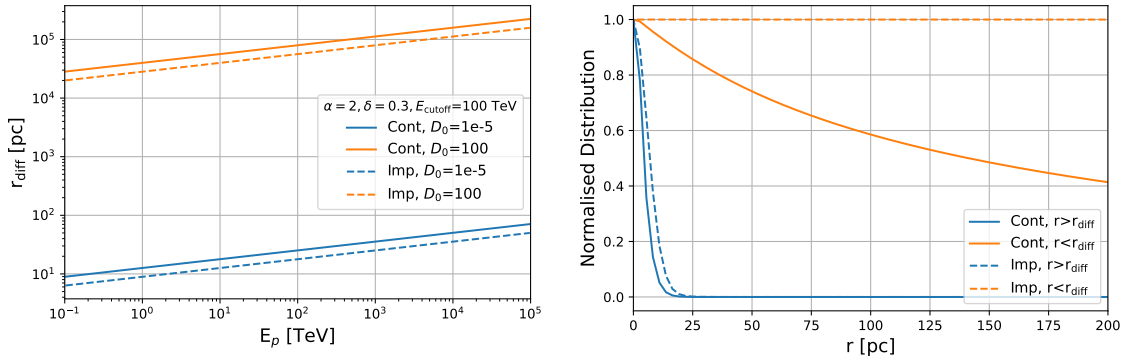

(a) (b)

Figure 5.10 The effect of D_0 on r_{diff} (a) and the effect of r_{diff} on the CR distribution (b) in both the continuous and impulsive injection scenarios. The plot (b) is the consequence of plot (a). The values of the diffusion parameters are written in the text, D_0 has the unit of pc^2/yr. The CR distributions are normalised to 1 in (b).

The D_0 and δ have an impact on the magnitude of the diffusion coefficient $D(E)$, which at the end affect the proton distribution. The diffusion radius r_{diff} is defined as $\sqrt{4DT}$ and $\sqrt{2DT}$ for the continuous and the impulsive diffusion respectively based on the Equation 5.4 and 5.5. By fixing the values of α, δ and E_{cutoff}, the effect of D_0 on r_{diff} can be seen in Figure 5.10 (a). Given the size of the CMZ is $\approx$ 250 pc, there are some position r larger the particle diffusion range if D_0 (and so as $D(E)$) is too small (as indicated in the blue colors). This eventually affect the proton distributions as shown in Figure 5.10 (b). When $r > r_{\text{diff}}$, protons are not able to cover the entire CMZ region. When $r < r_{\text{diff}}$, protons fill out the whole CMZ region, and the steady state can be reached. This means protons follow a $1/r$ distribution in the continuous diffusion case and follows a *constant* distribution in the impulsive diffusion case.

Shapes of Proton and Gamma Spectra

The proton spectra change when the CR propagation is taken into account, as mentioned in Section 2.3.1. For the steady state diffusion where $r < r_{\text{diff}}$, the proton spectral index after

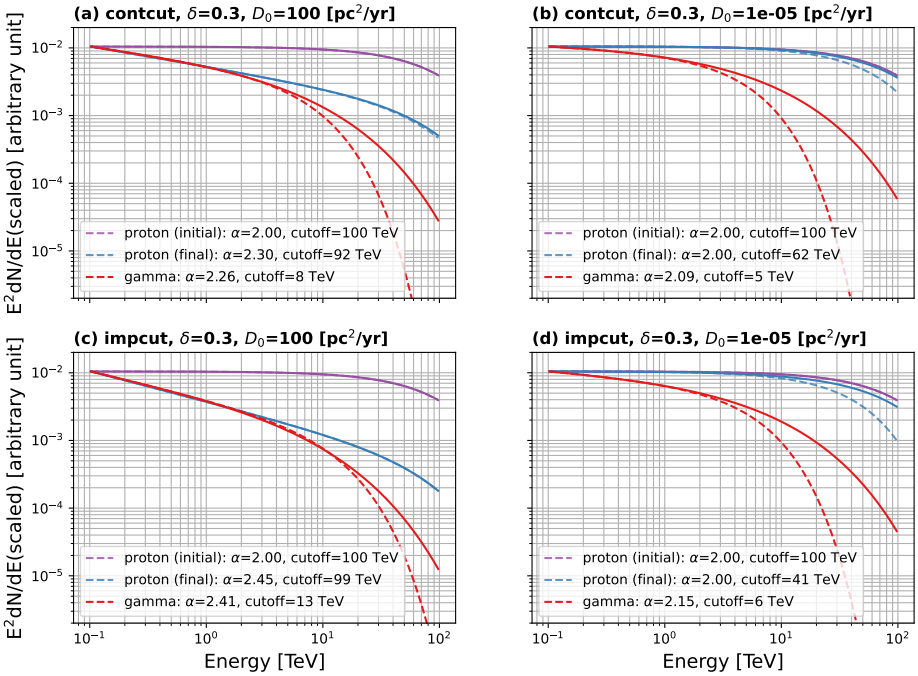

Figure 5.11 The injection proton, diffused proton and γ-ray spectra with proton injection spectral index of 2, the energy cutoff at 100 TeV and different combination of δ and D_0. The solid lines are the result and the dashed lines are the fit.

the particle diffusion α_f can be expressed as

$$\begin{aligned} \alpha_f &\approx \alpha_i + \delta, \text{ continuous} \\ \alpha_f &\approx \alpha_i + 3\delta/2, \text{ impulsive.} \end{aligned} \tag{5.9}$$

These relations can indeed be seen in Figure 5.11 (a) and (c), where the proton spectra are softened after the propagation in general. Though the resulting γ-ray spectra cannot be perfectly fitted by the power-law with an exponential cutoff function as the proton spectra, their spectral shapes are similar. The spectral indexes of the diffused proton and γ-ray spectra are close, i.e. $|\alpha_p - \alpha_\gamma| < 0.1$ The spectral energy cutoff of the γ-ray spectra are approximately one-tenth of that from the proton spectra. It can also be seen that a cutoff at E_0 in the proton spectrum will already affect the γ-ray spectrum at $\sim 10^{-2}E_0$, as mentioned in Section 2.2.1.

In the non-steady state where $r > r_{\text{diff}}$, the proton spectra have only slight changes as shown in Figure 5.11 (b) and (d). This is because only a small portion of protons have propagated out from the Galactic Centre. The spectral indexes of the diffused proton and γ-ray spectra are larger, i.e. $\alpha_\gamma - \alpha_p > 0.1$. Both spectra cannot be described by the power-

law with an exponential cutoff function due to the energy-dependent proton-γ conversion (Section 5.1.3).

Degeneracy of Gamma Spectra

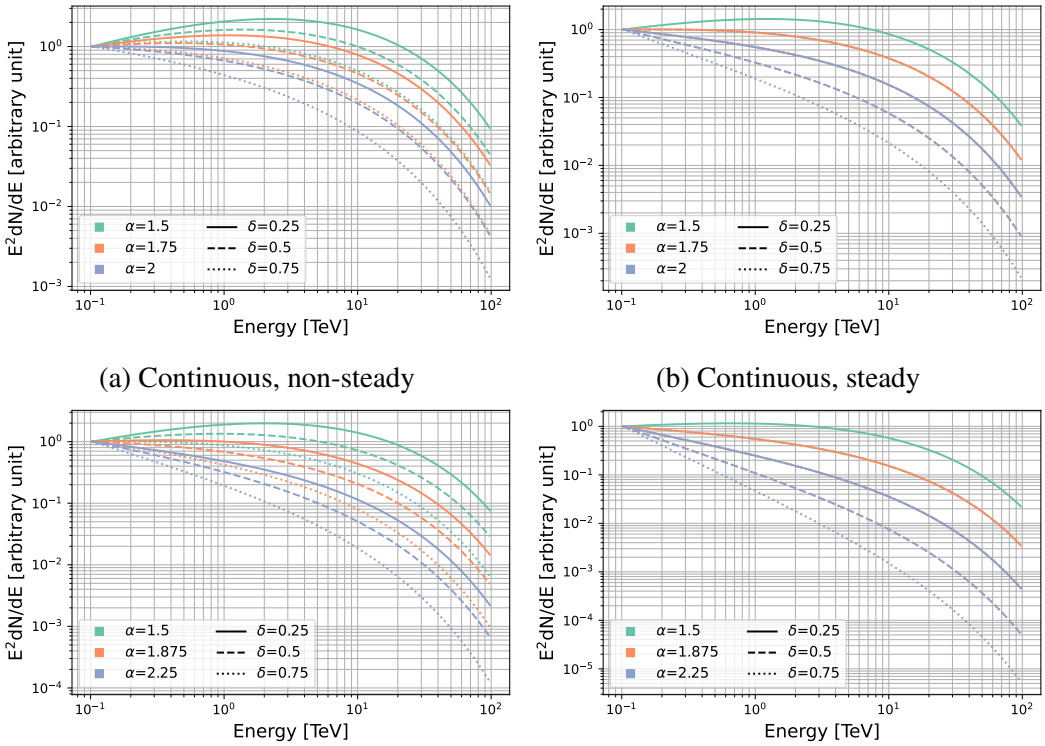

(a) Continuous, non-steady

(b) Continuous, steady

(c) Impulsive, non-steady

(d) Impulsive, steady

Figure 5.12 The γ-ray spectra with different combination of α and δ for the continuous and impulsive injection scenarios. E_{cutoff} is fixed to 100 TeV. The D_0 for the non-steady state is 10^{-5} pc^2/yr and for the steady state is 100 pc^2/yr. The colors indicate the value of α and the different lines indicate the value of δ.

The diffusion parameters determine the shape of the propagated proton spectrum. Since the γ-ray spectrum shares a similar shape as the proton spectrum, the Equation 5.9 implies the degeneration of the γ-ray spectra. For the non-steady state in both the continuous and impulsive cases, the degeneracy is not recognisable as shown in Figure 5.12 (a) and (c). By changing the values of α and δ, the deviations of the spectral shape can be seen. Yet in the steady state, the degeneracy is clearly observed. By selecting different values of α and δ, the spectra degenerated according to Equation 5.9. The 9 combinations of the listed parameters in 5.12 (b) and (d) are degenerated into 5 spectra, where α_f is $\in (1.75,\ 2,\ 2.25,\ 2.5,\ 2.75)$ and $\in (1.875,\ 2.25,\ 2.625,\ 3,\ 3.375)$ for the continuous and impulsive cases respectively.

The spectral degeneracy in the steady state imposes the difficulty to determine the exact values of the proton injection index and the CR diffusion coefficient. The latter is particularly related to the puzzling Galactic magnetic field irregularities. The determination of the diffusion parameters in the steady state thus requires the consideration of other physical properties, for instance the linkage with the possible CR injection sources by comparing the spectra, power and lifetime. The general values of D_0 and δ from other measurements or theories can also be used as a reference.

5.4 Summary

In this chapter, the key aspects to remember are:

- The diffuse γ-rays emission can be modelled via considering CR propagation from the Galactic Centre and the hadronic interaction with gases in the CMZ.
- Several properties of the diffusion emission template have revealed, including the spectral degeneracy in the steady-state diffusion.

With energy-dependent proton-γ conversion as well as the line-of-sight projected gas data, the resulting 3D templates are believed able to provide a high accuracy on describing the diffuse γ-ray emission in the CMZ. In the next chapter, the analysis results by using both continuous and impulsive CR injection templates will be presented respectively.

"I think prime numbers are like life.
They are very logical but you could
never work out the rules."

Mark Haddon
The Curious Incident of
the Dog in the Night-Time

Chapter 6

Analysis of Diffuse Gamma-Ray Emission in the CMZ

To study the diffuse γ-ray emission from the Galactic Centre in the CMZ, two kinds of CR injection scenarios are modelled. These include the continuous and the impulsive CR injection from the source, assumed to be a single source close to the Galactic Centre. By adapting the physically motivated model templates of these two injection scenarios to the analysis, a new insight into the diffuse γ-ray emission in the CMZ is presented in this thesis. The existence of a PeVatron in the Galactic Centre is inspected and the possible additional central component is investigated.

In this chapter, the high level H.S.S.S. analysis will be reported. In this context, the available H.E.S.S. data and their selection criteria for the complex Galactic Centre region analysis are presented. The construction of the dataset using *Gammapy* will be explained. The use of the FoV background onto the dataset as well as the quantification of the background uncertainty will be presented. Both the continuous and impulsive diffuse γ-ray emission models will be studied using the 3D maximum-likelihood analysis technique. This includes the determination of the parameters of the FoV sources and components, and the diffuse emission originating from the hadronic interaction with the molecular gas. Detailed morphological and spectral results will be discussed, as well as a cross-check using different gas tracers. In the end the impact of the systematic uncertainties on the background model for the physics results will be investigated.

6.1 Introduction to the Galactic Centre Region

The analysis region of this thesis is defined as a $\sim 4^\circ \times 4^\circ$ region centered at $(l, b) = (0^\circ, 0^\circ)$. As visualised in Figure 6.1 (a), the γ-ray sources in the inner Galactic region ($l < 1^\circ$) include HESS J1745-290, HESS J1747-281, HESS J1746-285 and HESS J1741-302. All of these are considered to be point sources with power-law spectra as indicated in the HGPS (H.E.S.S. Galactic Plane Survey in VHE γ-rays, 2018) [59], except for HESS J1745-290 which features an exponential cutoff at around 10 TeV. In the outer Galactic region ($l > 1^\circ$), there is a point source HESS J1741-302 and several Gaussian sources, including HESS J1745-303, HESS J1746-308 and HESS J1747-248 with power-law spectra.

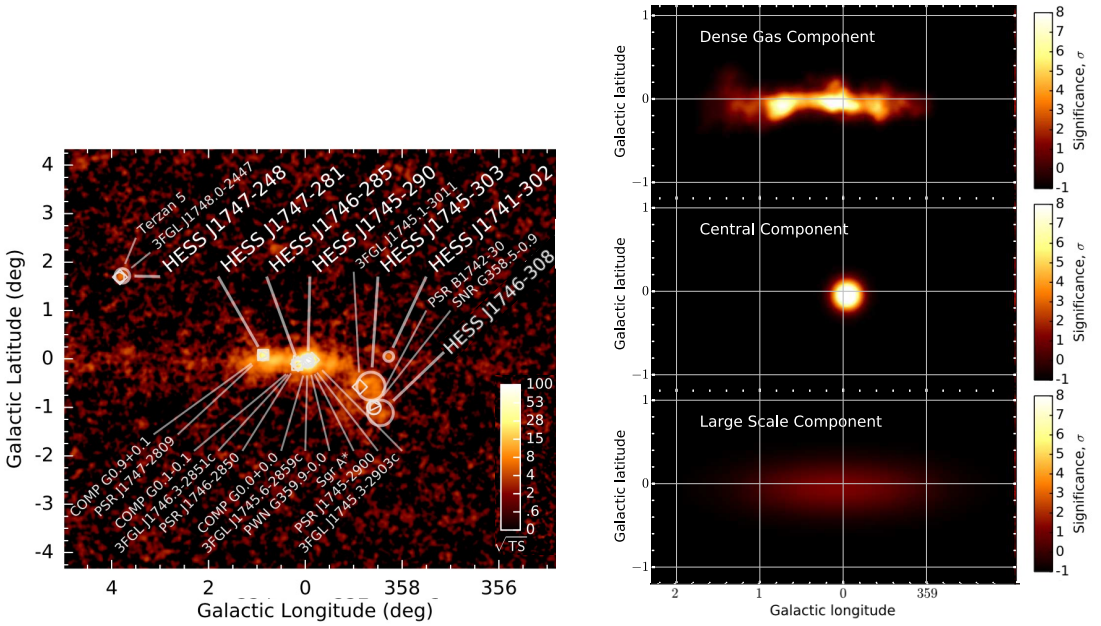

(a) (b)

Figure 6.1 The sources and components in the Galactic Centre region. (a) HGPS (2018) sources and associations. The background image shows $\sqrt{\Delta TS}$ (= σ) of the VHE γ-ray excess assuming a point source morphology. (b) The H.E.S.S. (2018) study of the (dense gas) diffuse emission, (large scale) foreground emission and the additional Gaussian central component. (Taken and adapted from [59, 57])

Among these sources, HESS J1745-290 is particularly prominent due to its relatively high γ-ray luminosity and lack of indication of flux variability [122]. It has number of potential associations as briefly explained in Section 2.3.1, such as Sgr A East, PWN G359.95-0.04 and Sgr A*. Sgr A East could, for instance, accelerate protons in the extended shell of the SNR through shock, creating the enhanced γ-ray luminosity without the mentioned flux variability. Sgr A East is however disfavoured due to the offset from the precise centroid

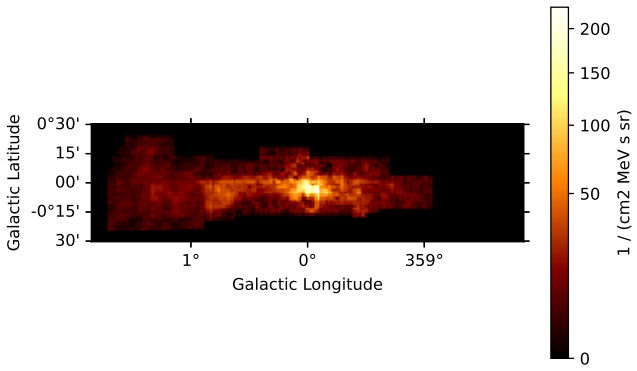

(a) Continuous injection

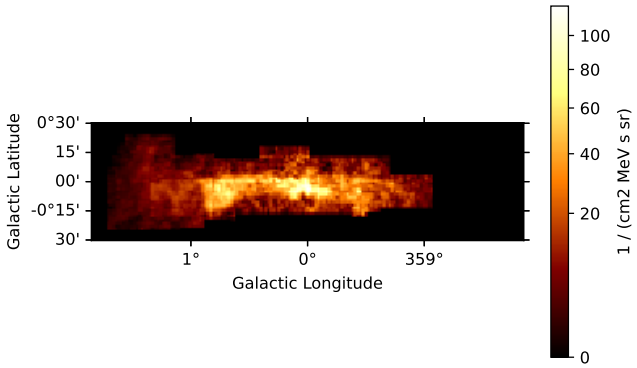

(b) Impulsive injection

Figure 6.2 Examples of γ-ray flux templates in the CMZ summed over the energy axis. The templates are built with the (a) continuous CR injection scenario and the (b) impulsive CR injection scenario. The colorbar indicates the γ-ray flux.

measurement of HESS J1745-290 [122]. PWN G359.95-0.04 can up-scatter large abundance of far infrared photons by the inverse Compton process and without suffering from the effect from strong synchrotron cooling. PWN G359.95-0.04 is also disfavoured due to the lack of consistency in the GeV regime of using the same emission mechanism [122]. The association of HESS J1745-290 with Sgr A*, on the other hand, is supported by a number of theories. For example, the accretion onto the SMBH causes protons to be injected into the ambient medium continuously or impulsively which could happen via the disruption of a nearby star by tidal forces [1, 122, 56]. This causes the γ-ray production through particle interaction, yet without much variability due to the diffusion timescale. These VHE γ-rays are visible in the vicinity of the black hole due to the lack of dense infrared radiation fields that would absorb

them by pair production processes. This results in VHE photons can escape from the region several Schwarzschild radii away from the black hole [122].

Apart from these sources, there are dense gas clumps or unknown components overlapping the region as indicated in Figure 6.1 (b). These include a diffuse emission component (or called the dense gas component) from the CMZ and a foreground emission component (or called the large-scale component) along the Galactic ridge. In addition, a previous study by H.E.S.S. (2018) revealed the possible existence of an additional Gaussian central component in the Galactic Centre [57]. Yet, it is interpreted as an ad-hoc component.

In the thesis, descriptions of the diffuse γ-ray emission in the CMZ through two CR injection scenarios are provided. These include the continuous and the impulsive injection of CRs from the source, presumably a single source located close to the Galactic Centre. In this case, it is assumed to be at the position of Sgr A*. The continuous injection scenario is a conventional scenario. The previous H.E.S.S. study [56] postulated the CR density exhibits a 1/r distribution in the inner 200 pc of the CMZ, where r is the projected longitudinal disance from Sgr A*. This is expected for a scenario in which CRs are injected and diffuse continuously in a steady state. On the other hand, the impulsive injection scenario can provide an alternative explanation by including the existence of an additional Gaussian central component in the Galactic Centre. Examples of these two different diffuse emission templates can be found in Figure 6.2. The construction method of these templates has been explained in Chapter 5. It can already be seen that the continuous template has more intense γ-ray flux in the Galactic Centre due to CRs being injected continuously from the source.

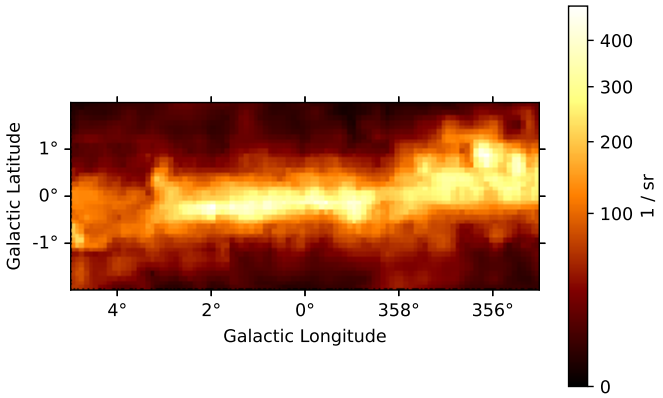

Figure 6.3 The spatial model template of the foreground component to account for the large-scaled γ-ray emission in the Galactic ridge. The γ-ray flux can be obtained by multiply the template with a spectral model. (Template from [34])

The foreground emission component consists of large-scale γ-ray emission component along the Galactic ridge, coming from the CR sea interaction with CO gases [44, 43, 2, 55]. It can be modelled using *HERMES*, a publicly available computational framework for creating sky maps of various galactic radiative processes [35]. This component is described using a spatial model template produced by Justine Devin (2022, priv. com. [34]) where the interaction in a $10^\circ \times 4^\circ$ region at the Galactic ridge is computed (excluding the CMZ region). An inhomogeneous CR density has been taken into account in the modelling [35]. This spatial template can be visualised in Figure 6.3. A power-law spectral model is assumed.

6.2 Dataset

The TeV γ-ray observations can constrain the CR injection scenario. Among the available instruments, H.E.S.S. provides a good view and high sensitivity across the energy range for this task. The location of the array in the southern hemisphere and the array configuration can provide the most sensitive view at TeV of the Galactic Centre due to the low energy threshold and high statistics at high energies [122]. In this section, both data and the selection criteria used in this analysis will be presented. The derivation of a run-wise background model will also be explained, followed by the estimation of the background uncertainty.

6.2.1 Data

The data used in this thesis are from the H.E.S.S. I and II eras, not including data taken from the H.E.S.S. IU era onwards. These data are extracted from the CT1-4 only, due to the stability of the CT1-4 data. Since this thesis focuses on the diffuse γ-ray emission at high energies, the inclusion of the CT5 data would only improve the sensitivity at a few tens of GeV, but not at high energies [75]. The runs from CT1-4 are selected and processed via the H.E.S.S. analysis pipeline, *HAP* (Heidelberg version). To ensure a high reconstruction accuracy, these runs are selected with pointing direction of a maximum angular offset of 2° from the Galactic Centre, a maximum zenith angle of 60° and a minimum run duration of 10 minutes. In addition, all CT1-4 telescopes are required to have been taking data during these runs in order to improve the accuracy in the event reconstruction [103].

The selected data set consist of 424 runs from the H.E.S.S. I era (taken between March 2004 to October 2012) and 215 runs from the H.E.S.S. II era (taken between June 2013 to June 2015). These comprise in total 639 runs with a livetime of ~ 293 hours and an average zenith angle of $\sim 20.9^\circ$. These runs have been processed using the configuration called *standard ImPACT full-enclosure*. This means the ImPACT reconstruction is used

for event reconstruction, the TMVA technique is used in the γ-hadron separation with standard analysis cuts, and no cut is applied on the PSF. Details have been discussed in Section 3.2.2 and 3.2.3. An energy reconstruction problem has been reported concerning the ImPACT reconstruction, where a clustering of reconstructed event energies occurs at energy edges of ImPACT templates. This issue arises from the discontinuing gradients in the likelihood landscape during the fitting process [103]. This is a typical problem for the 3D FoV background model construction, where the background is constructed from multiple observations and therefore the effect gets accumulated. A temporary fix to this issue has been introduced by Lars Mohrmann (2022, priv. com. [83]), where the defeated events are rejected in the FoV background construction based on defined cuts. These cuts reject the events with reconstructed energies $< 0.05\%$ to the ImPACT energy edges, also for those outside the condition of $0.1 \leq E_{\mathrm{Hillas}}/E_{\mathrm{ImPACT}} \leq 10$. The same cuts have applied to the events as well as the effective area in the reproduced IRFs.

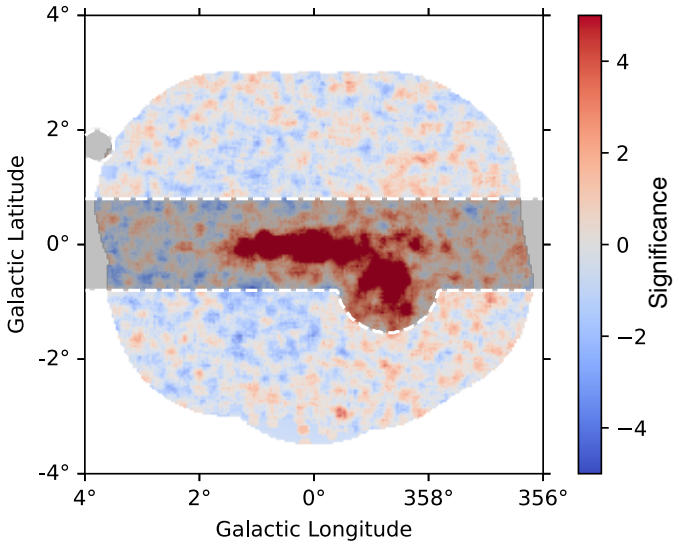

Figure 6.4 The Li & Ma significance map from the H.E.S.S. dataset at the Galactic Centre region, the map is smoothed with the H.E.S.S. PSF of 0.077°. This map has been stacked and summed over the energy axis. The colorbar indicates the significance. The dark grey area (including the small circle on the left) indicates the expected source region in the FoV.

For analysis, the data are adapted into *Gammapy* by mapping them with the pixel size of 0.02° and 8 energy bins per decade, ranging from $0.1 - 100$ TeV. Each of these data cubes contains the information of the γ-ray counts and the estimated hadronic background rate from the FoV background model. The Li & Ma significance map of the stacked data cube at this stage integrated along the energy axes can be visualised in Figure 6.4. A clear abundance of the γ-ray signals around the Galactic Centre is observed.

6.2.2 Run-Wise Fit

As discussed in Chapter 3, the energy threshold for the datasets need to be defined after the selection of the data. Afterwards a pre-fit process is required to adjust the FoV background model per run in order to correct different observational effects. Individual data cubes are stacked into a single data cube in the end, a spatial area of $4^\circ \times 4^\circ$ centered around the Galactic Centre is cropped out for further analysis. The procedure of the run-wise prefit process will be explained below, followed by the quantification of the background uncertainty.

Energy Threshold

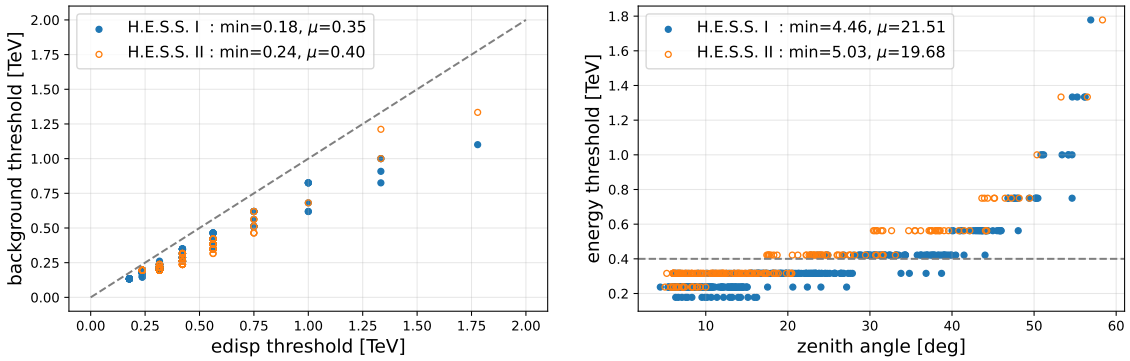

(a) (b)

Figure 6.5 The energy thresholds of each observations. (a) A comparison of the (< 10 %) energy dispersion thresholds and the background-model thresholds. (b) The energy dispersion thresholds as a function of the zenith angle. The minima and the means of the energy dispersion thresholds and the zenith angles are shown in each plot.

There are in general two kinds of energy threshold defined in this analysis. The first is the energy dispersion threshold derived from the IRFs, which is the energy at which reconstruction bias is within a 10% margin as introduced in Section 3.2.3. The second is the background threshold defined in the FoV background model. As mentioned in Section 3.2.4, the background energy threshold is needed to avoid large background fluctuation close to the instrument threshold. The background threshold of each observation is defined as the upper edge of the energy bin that contains the largest predicted background rate [84]. The corresponding background threshold and the energy dispersion threshold for runs from both the H.E.S.S. I and II observations can be found in Figure 6.5 (a). It is noticeable that the energy dispersion thresholds are always larger than the background thresholds in all runs. This is usually not the case, yet a decrease in optical efficiency of the telescopes can be the reason for the relatively higher energy dispersion threshold [84]. The energy threshold of

each run is defined as the maximum value among the energy dispersion and the background threshold. The energy thresholds range from 0.1 – 1.9 TeV. It can be seen in Figure 6.5 (b) that the energy dispersion thresholds increases with zenith angle. This is associated with a decrease in the shower image amplitude as discussed at the end of Section 3.2.1.

To avoid large systematic errors at low energies, as well as to compare the analysis results with publications, such as those by HGPS (2018), H.E.S.S. (2018), MAGIC (2020) and the preliminary results produced by Justine Devin (2022) [34] using the *HAP-Fr*[1] chain, an additional energy threshold is defined at 400 GeV. The energy thresholds for each observation are therefore defined as the maximum of the energy dispersion, the background or the additional threshold.

Runwise Background Fit

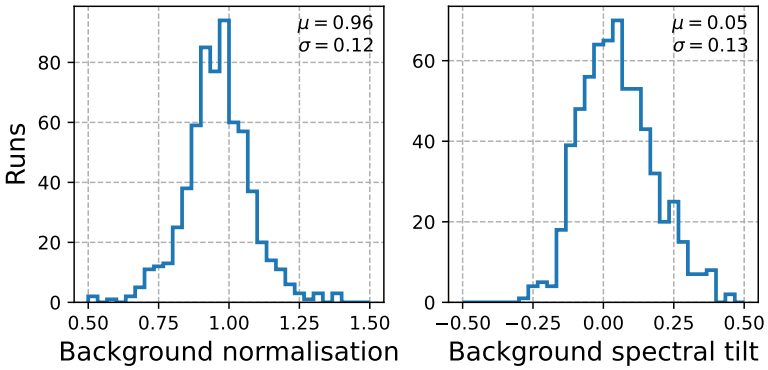

Figure 6.6 The distribution of the normalisation and tilting parameters of the FoV background model from all available runs. The corresponding mean and width of the distributions are stated in the plot.

Observational effects, such as the variation of NSB and the atmospheric transparency, can affect the background estimation in the individual runs. It is therefore necessary to prefit the FoV background model for all runs by adjusting the spectral model parameters as defined in Equation 4.20, before proceeding to further analysis. The prefit is performed with a masking of the source region to avoid contamination from the source. This exclusion mask follows the shape as indicated in the grey region of Figure 6.4, where most of the contribution from the observed sources are contained. The resulting distribution of the normalisation and tilting parameters from all runs can be found in Figure 6.6. The mean of the normalisation and tilting parameters are close to expected values, namely 1 and 0 respectively.

[1]The *HAP-Fr* (France version) analysis uses Hillas and/or Model 3D for the event reconstruction, and Paris-MVA for the γ-hadron separation [71, 9].

Stacked Dataset

After the background prefit, the individual data cubes are stacked. This means the counts, background and the reduced IRFs[2] are binned together in order to reduce the computational effort. To focus on the Galactic Centre region, a region of $4^\circ \times 4^\circ$ is cropped out for further analysis. The corresponding counts, background and the excess map of this stacked dataset can be found in Figure 6.7. A clear residual around the centre can be seen in the excess map and the Li & Ma significance map. To get rid of the excess γ-ray emission, a modelling of the sources and components is required. The FoV background model can again be adjusted by altering the spectral parameters in the fit.

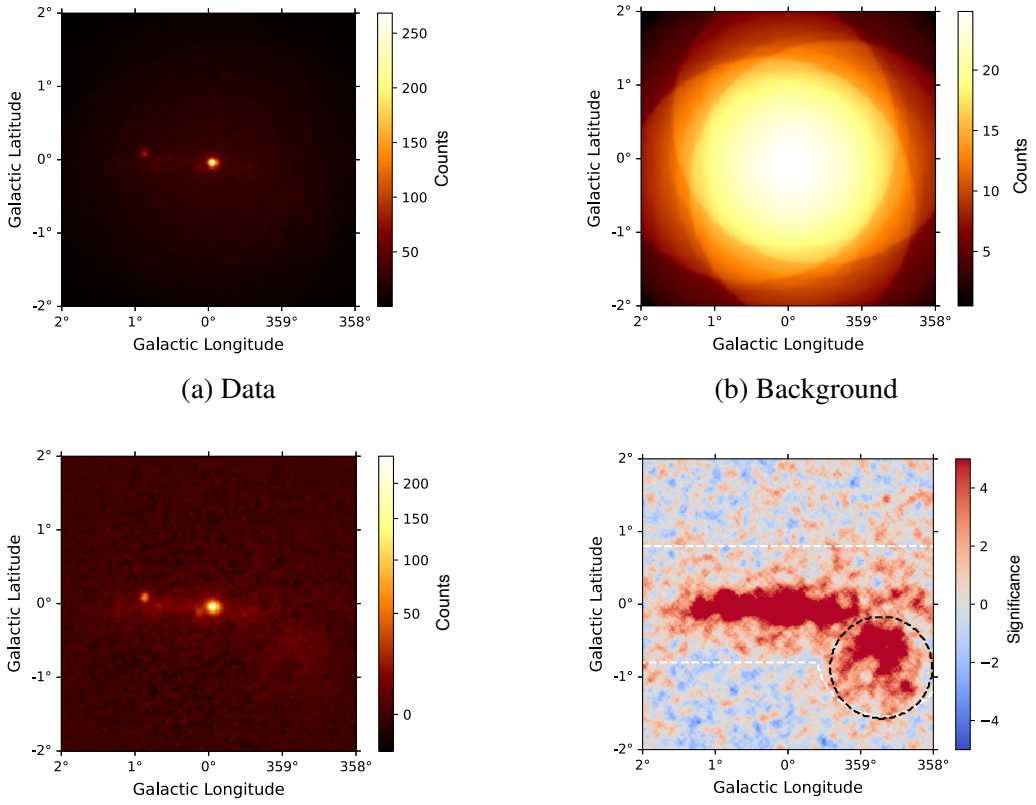

(a) Data

(b) Background

(c) Excess

(d) Significance

Figure 6.7 The stacked dataset used in this analysis. The data, background, excess and the Li & Ma significance map are presented in (a), (b), (c) and (d) respectively. The brightness of (a-c) indicates the counts and (d) indicates the significance. In the plot (d), the white contour indicates the area being excluded in the background prefit, whereas the black contour indicates the exclusion region in further analysis.

[2]Containing the exposure weighted average of PSF and energy dispersion

Note that HESS J1745-303 and HESS J1746-308 are not well defined and thus hard to model. Therefore an exclusion mask, as indicated in Figure 6.7 (d), is defined to avoid fitting these complicated regions.

Quantification of Background Uncertainties

The data and the background counts outside the exclusion region (defined in the background prefit) as a function of energy can be found in Figure 6.8 (a). By assuming no contribution from any γ-ray sources in the exclusion region, the discrepancies are connected to the statistical and systematic error. The quantification of the systematic uncertainty is, however, not straightforward and still a matter of investigation. The systematic uncertainty lookup table built from all runs, as mentioned in Section 4.2.4, is not available in the current ImPACT data. Thus the background uncertainty cannot be interpolated from the lookup table. The uncertainty is therefore estimated from the dataset itself, following the approach described in [103].

To begin with, the deviation D_i of the data N_i and the predicted counts M_i is computed per energy bin i using

$$D_i = \frac{N_i - M_i}{\sigma_{i,\mathrm{tot}}} = \frac{N_i - M_i}{\sqrt{\sigma_{i,\mathrm{stat}}^2 + \sigma_{i,\mathrm{sys}}^2}}, \tag{6.1}$$

where $\sigma_{i,\mathrm{tot}}$ is the total error that consists of the statistical error $\sigma_{i,\mathrm{stat}}$ and the systematic error $\sigma_{i,\mathrm{sys}}$. If the systematic error is purely from the background uncertainty $\delta_{i,\mathrm{bkg}}$, they can be related via

$$\sigma_{i,\mathrm{sys}} = \delta_{i,\mathrm{bkg}} M_i. \tag{6.2}$$

Assuming an intrinsic and energy-independent uncertainty, the RMS values of the distribution of the D_i before and after the inclusion of the background uncertainty can be derived. As shown in Figure 6.8 (b), the original RMS is 2.17, whereas a background uncertainty δ_{bkg} of 6.94% can reduce the RMS to 1. In practice, an energy-dependency of the background uncertainty is seen. Therefore the approach is modified in this thesis such that D_i is equal to 1 at each energy bin. The rough estimation of the energy-independent and energy-dependent background uncertainties are shown in Figure 6.9. In the case of energy-dependent background uncertainty, the uncertainties occasionally drop to 0% due to the discrepancy between the model and data being smaller than the statistical error. It is also noticeable that the uncertainties are high at high energies, which might be related to unconsidered sources of errors and the compatibility of the background model. These derived uncertainties will be

used at the end of this chapter in fitting nuisance parameters to account for the systematic effects.

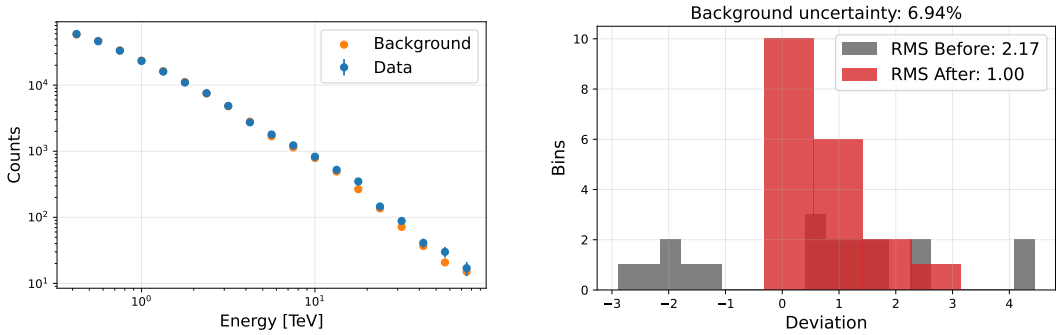

(a) (b)

Figure 6.8 The data and background discrepancy. (a) The data (blue) and background (orange) counts as a function of energy. (b) The RMS distribution of the data and background deviation. The gray and red color indicate the distribution before and after adding the background uncertainty respectively. A background uncertainty of 6.94% can reduce the RMS from 2.17 to 1.

In future, it is believed the systematic lookup table will provide a better and more accurate estimation of the background uncertainty for the ImPACT analysis. The rough estimation presented in this section can, nevertheless, be used to prove the applicability of the nuisance parameter fit in the complex Galactic region for the first time with H.E.S.S.

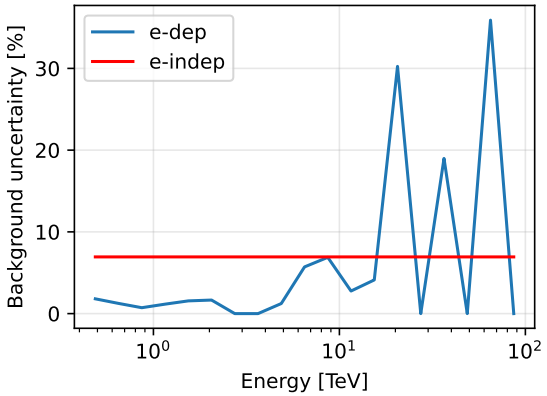

Figure 6.9 The background uncertainty as a function of energy. The red and blue lines indicate the derived energy-independent and energy-dependent uncertainty respectively.

6.3 Results with Continuous Cosmic-Ray Injection Template

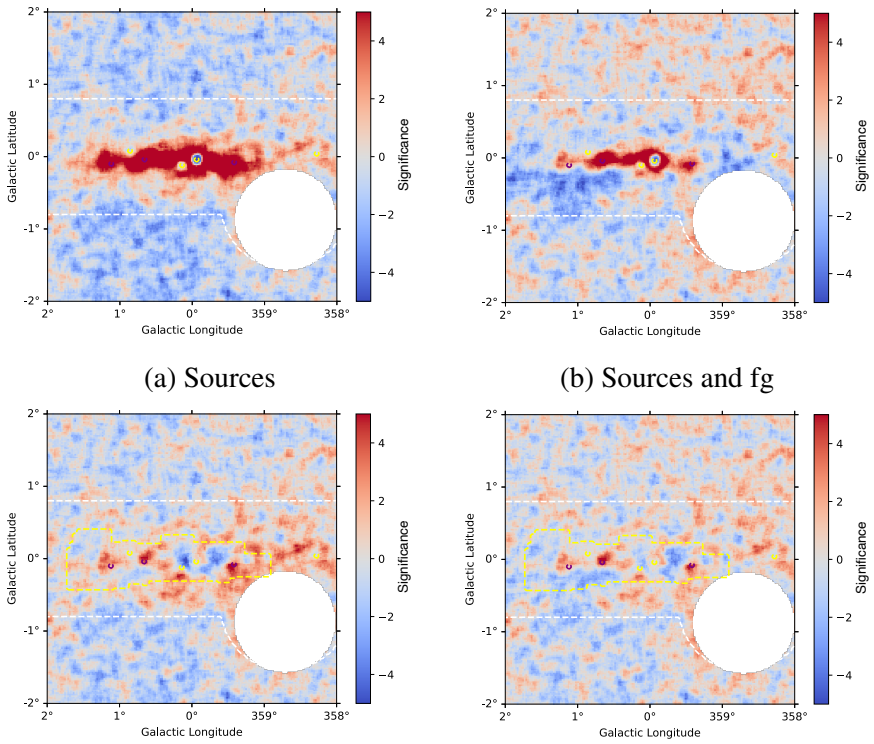

(a) Sources

(b) Sources and fg

(c) Sources and diffuse

(d) Sources, fg and diffuse

Figure 6.10 The Li & Ma significance map of the residual after the inclusion of different model components in the FoV, smoothed by the H.E.S.S. PSF. The term *fg* denotes the foreground component. The colorbar indicates the significance. The yellow contour indicates the fitted components, the purple contour indicates the molecular complexes (Sgr D, Sgr B and Sgr C from left to right), the white contour indicates the exclusion region in the run-wise background prefit and the void area indicates the exclusion region in the analysis. The diffuse emission template has been modelled with the continuous CR injection with an energy cutoff. The ΔTS of these plots relative to plot (d) are: (a) 3418; (b) 1198; (c) 294, (d) 0.

In this section, the results using the continuous CR injection model for the creation of the diffuse γ-ray emission template for the CMZ will be explained. This section starts with studies of the model properties of the FoV sources, foreground component and diffuse emission component. The derivation of the best-fit diffuse emission template parameters will be explained, followed by the detailed morphological and spectral results.

6.3.1 FoV Sources and Components

Several sources within the FoV described in Section 6.1 are modelled by spectro-morphological source models, namely HESS J1745-290, HESS J1747-281, HESS J1746-285 and HESS J1741-302. The extended sources HESS J1745-303 and HESS J1746-308 at around ($l = 358.716^\circ$, $b = -0.871^\circ$) are hard to model, thus being excluded by a mask with radius of 0.7°. In addition, the foreground emission (introduced in Section 6.1) and diffuse emission component are also modelled.

For an overview, it can be seen in Figure 6.10 (a) that non-negligible residuals are left in the Galactic Centre area if only the FoV sources are subtracted. The shape of these residuals follows the gas density distribution from the CS tracer (introduced in Chapter 5), which is believed coming from the diffuse γ-ray emission in the CMZ. The inclusion of the foreground component can significantly reduce the overall residual as indicated in Figure 6.10 (b), yet cannot fully explain the residuals in the CMZ. Alternatively, by replacing the foreground component with the diffuse emission component built from the continuous CR injection model (together with the CS tracer), most of the residuals in the CMZ are removed. By further including the contribution from the foreground component, the overall residual is also clearly reduced. The improvements in ΔTS are stated in Figure 6.10. Note that some molecular complexes are still left in the CMZ, these include Sgr D, Sgr B and Sgr C as shown in the purple contour from left to right of Figure 6.10 (d). This is associated with the gas tracers, including the CS tracer, suffer from self-absorption in extremely dense regions [57]. This is typically the case for Sgr B, where the residual is more significant.

The details of all model properties will be discussed in the following.

Model Properties of FoV Sources and the Foreground Component

Before proceeding, the source properties of HESS J1747-281 and the foreground component need to be discussed. HESS J1747-281, which is believed to be associated with the composite SNR G0.9+0.1, was described by a simple power-law spectral feature in the HGPS (2018) catalogue. Yet an improvement of $\Delta\text{TS} \approx 25$ is observed if an exponential energy cutoff is included in our expanded dataset. A comparison of the two energy spectra can be found in Figure 6.11, where the revised model gives a better match with the estimated fluxpoints in the third and fourth energy bins. Therefore the spectral model of HESS J1747-281 has been adopted as a power-law with an exponential cutoff in this analysis. The foreground component, on the other hand, is believed to follow a simple power-law spectrum as no energy cutoff is expected for Galactic CRs in the PeV energy regime (the comsic knee). Yet the lateral extension (10°) of this component is a factor of 2.5 larger than the size of the

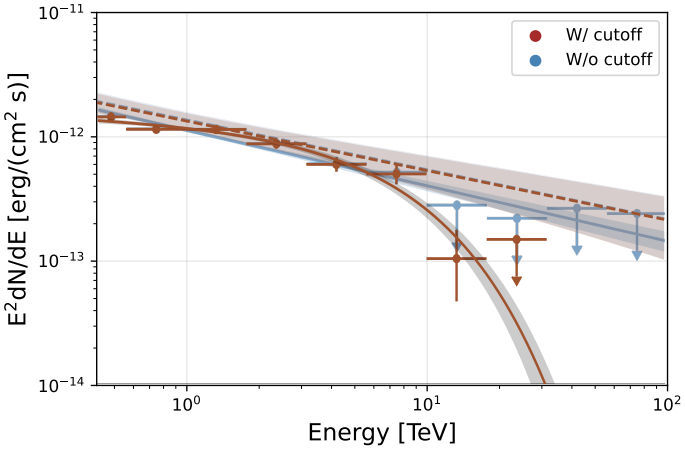

Figure 6.11 The energy spectra and the estimated fluxpoints of HESS J1747-281. The blue and brown solid lines represent the spectral model without and with the energy cutoff respectively. The dashed line represents the spectrum from the HGPS (2018). The presence of the energy cutoff gives an improvement of $\Delta TS \approx 25$.

analysis region (4°). It is therefore crucial to check whether the parameters of this component will change if a bigger map size is used. The significance map and the resulting foreground spectra can be found in Figure 6.12. The foreground component is equally well adapted in a larger map ($8° \times 8°$) as compared with that in a smaller map in Figure 6.10 (d). The spectrum gets slightly harder and reduced spectral amplitude when the larger map is used, however it is still in agreement with the $8° \times 8°$ map within the error band. The upper limit in the last energy bin deviates from the model, which might be related to the small statistics.

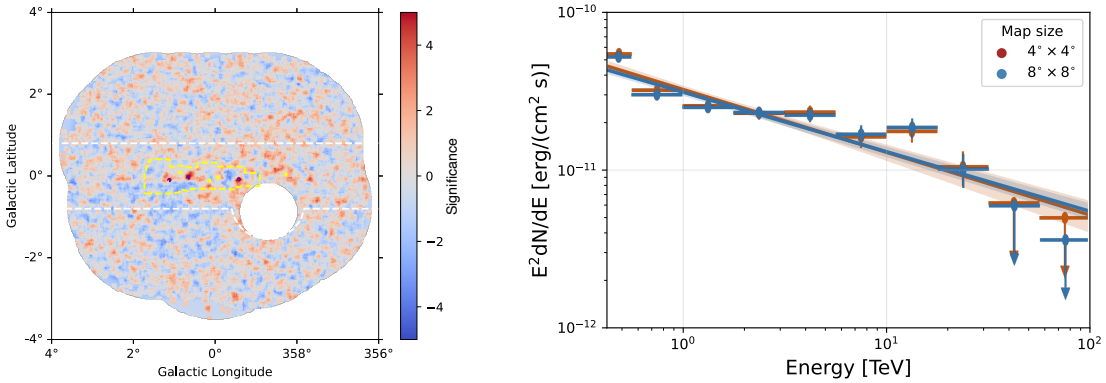

(a) (b)

Figure 6.12 Analysis results for larger map of $8° \times 8°$. (a) The Li & Ma residual significance map. (b) The fluxpoints of the foreground emission derived in the $4° \times 4°$ map (brown) and $8° \times 8°$ map (blue). The solid lines indicate the model.

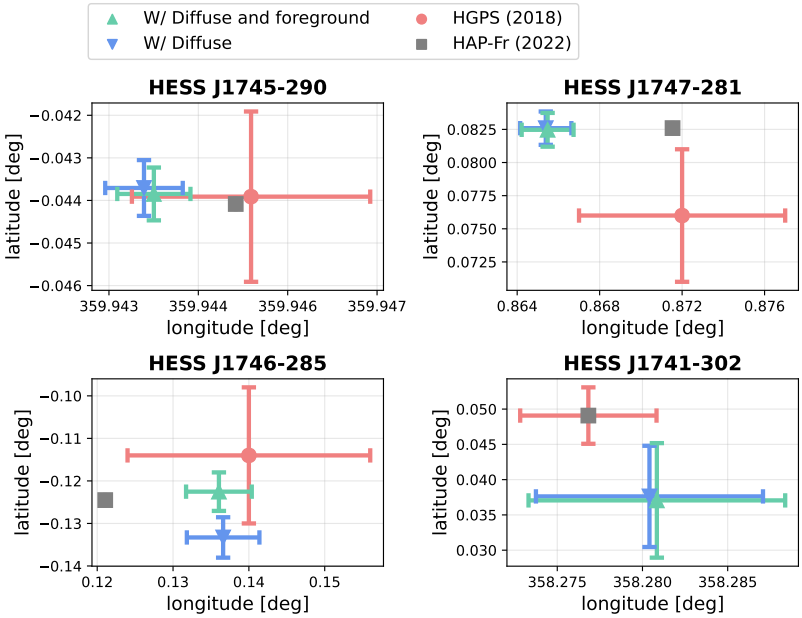

(a) Spatial parameters

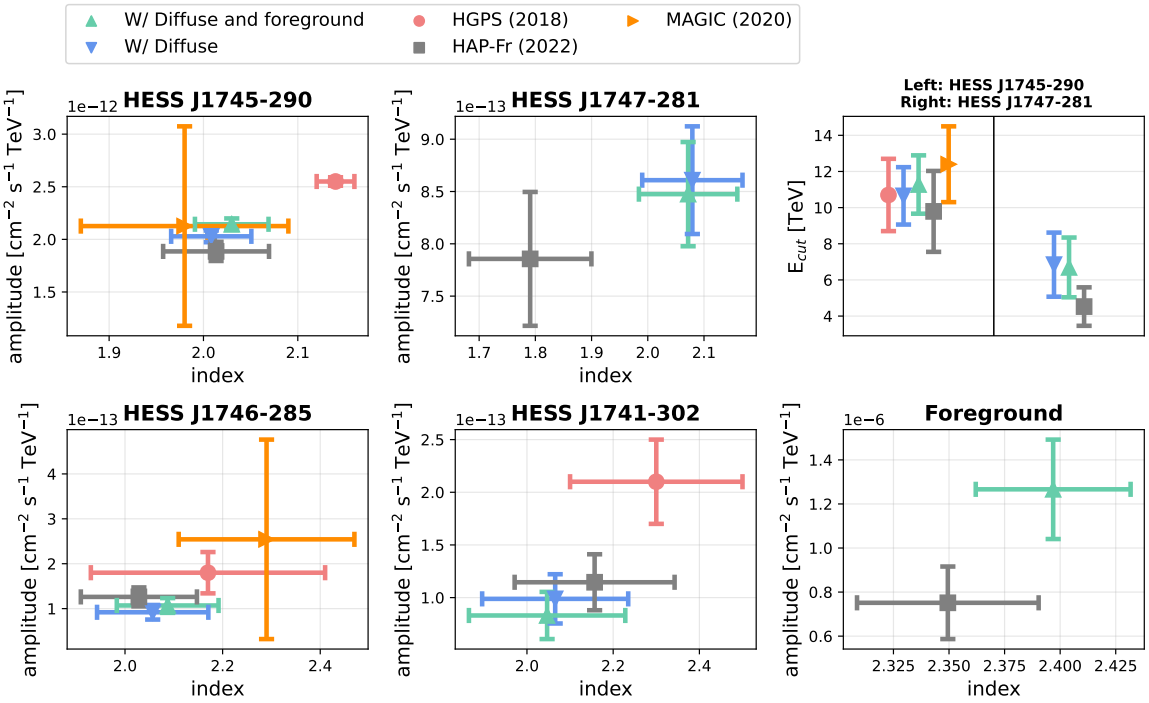

(b) Spectral parameters

Figure 6.13 Best-fit spatial (a) and spectral (b) model parameters for each FoV sources and components. The red and orange points are HGPS (2018) and MAGIC (2020) results. The grey points are the preliminary results from J. Devin [34] using the empirical diffusion model, where no errorbars are given for spatial parameters due to the positions are being frozen in the final fit. The blue and green points are the result of this work using the diffuse emission template of the continuous injection scenario, where the foreground component is excluded and included respectively. The reference energy in the amplitude is 1 TeV (except being 10 GeV for the foreground component).

Source or component	Spatial model	Spectral model
HESS J1745-290	Point	PLC
HESS J1747-281	Point	PLC
HESS J1746-285	Point	PL
HESS J1741-302	Point	PL
Foreground	Template	PL
Diffuse	Modified Template (Continuous injection with PLC)	

Table 6.1 Summary of model descriptions.

Details on the spatial and spectral models for all the FoV sources and components is given in Table 6.1. The corresponding best-fit parameters and their uncertainty can be found in Figure 6.13, for the case with and without the foreground component. The derived values are compared with previous measurements from HGPS (2018)[3] and MAGIC (2020). Note that both measurements did not model the diffuse emission and foreground emission component, thus only serve as rough references. The cross-check is also made with the preliminary study by Justin Devin [34] using the *HAP-Fr* (2022) chain (with an empirical diffuse emission model[4]). Yet slight discrepancies are expected due to the different analysis region size and modelling procedure.

In general, the best-fit positions of the FoV sources match with the previous measurements within the 1σ error boundaries. The spectral parameters show larger discrepancies. The spectral indices are mostly in agreement with the HGPS (2018), except for HESS J1745-290. This is mostly related to the inclusion of the diffuse emission and the foreground model, which can also explain the lower amplitudes in the FoV sources. Furthermore, HGPS (2018) used different event reconstruction technique and background estimation[5], which can cause some discrepancies with the result in this analysis.

The derived source amplitudes are, however, mostly in agreement with the preliminary result from *HAP-Fr* (2022) [34]. Yet a slight disagreement is found when comparing the spectral index of HESS J1747-281, where both studies have introduced an energy cutoff to this source. This can be due to the construction of the diffuse emission model, where *HAP-Fr* (2022) uses a 2D spatial model of the CMZ molecular clouds multiplied by a Gaussian of width 1.1°, together with a spectral model of power-law with an exponential cutoff. This

[3]These source parameters are taken from previous H.E.S.S. publications instead of being reanalysed in the HGPS (2018) program.

[4]The impulsive CR injection and an additional Gaussian central component are considered.

[5]Namely the standard Hillas reconstruction method and the adaptive ring model, where the inner and outer ring radii change adaptively to avoid the exclusion regions that cover a significant fraction of the FoV [59].

way of modelling can induce discrepancies in the source parameters. This might also be the reason for a slightly higher foreground amplitude in this analysis.

Note that the results are within uncertainties by including or excluding the foreground component. This ensures the inclusion of the newly foreground emission component is not affecting the main results of this thesis.

Model Properties of the Diffuse Emission Component

The above-mentioned results are derived using the continuous injection template with an exponential cutoff on the CR injection spectrum. As mentioned in Chapter 5, the projection of dense gas along the line-of-sight has considered in the template building procedure. It should already be pointed out that this projection method is promising. The morphology from both approaches, with and without the line-of-sight projection, can be seen in Figure 6.14. The ΔTS is improves by 134 when the projection is applied. The regions of the gas complexes are also better resolved.

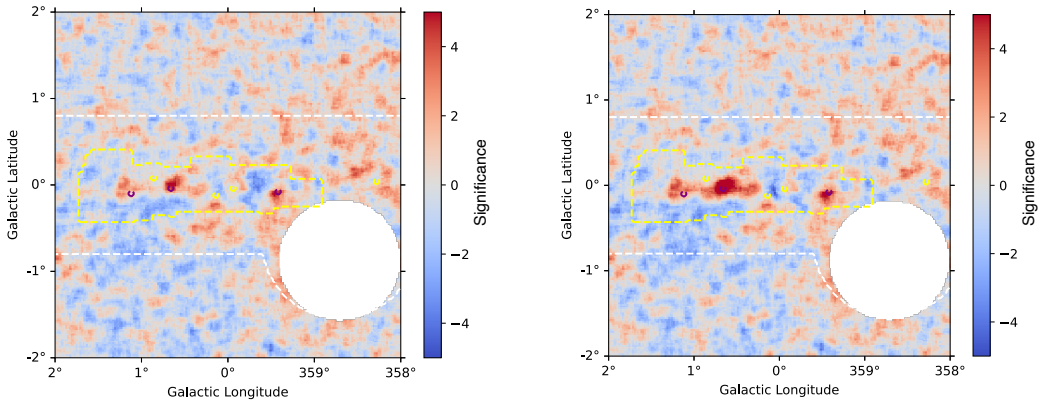

(a) (b)

Figure 6.14 The Li & Ma residual significance map with different treatment on the dense gas, namely with (a) or without (b) the line-of-sight projection described in Chapter 5. The projection method is better by $\Delta TS \approx 134$.

A comparison of γ-ray spectra for the diffuse emission component using different injection templates can be seen in Figure 6.15, both for cases excluding and including the foreground component. It is noted that the inclusion of the foreground component can improve the likelihood by $\Delta TS \approx 293$. Among the templates used in both cases, the scenario of continuous CR injection describe the region better than the impulsive CR injection by $\Delta TS \approx 80$. The inclusion of the proton energy cutoff in all cases can in general further improve the results by $\Delta TS \approx 30$. This essentially implies the best description is the continuous CR injection with an energy cutoff together with a foreground component.

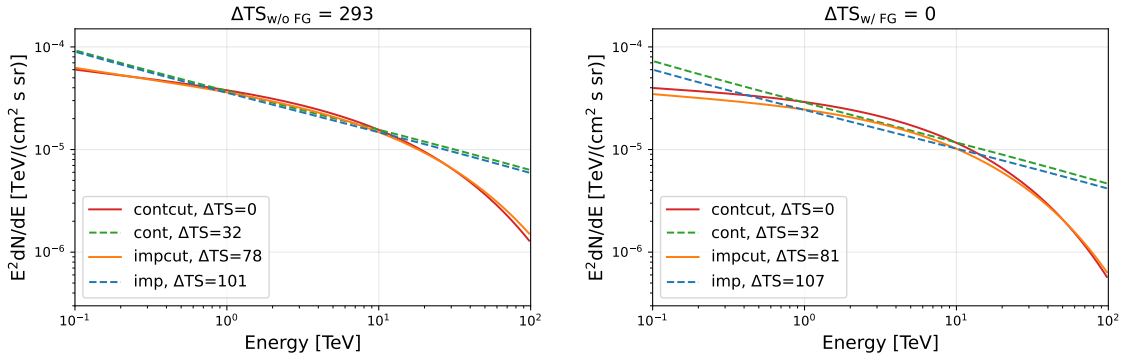

(a) Excluded the foreground emission (b) Included the foreground emission

Figure 6.15 The energy spectra of the diffuse emission component excluded and included the foreground component in the fitting. An extreme improvement of $\Delta TS \approx 293$ is shown by including the foreground component. Among the two cases, the diffuse emission spectra with the scenario of continuous injection (with and without the cutoff) and impulsive injection (with and without the cutoff) are also shown. The individual ΔTS values are shown in the legends.

The estimated fluxpoints derived from different diffusion models can be found in Figure 6.17. It is clearly shown that the inclusion of the foreground emission component will decrease the amplitude of the diffuse emission spectrum. For the case of continuous injection with a proton energy cutoff, the flux amplitude at 1 TeV is decreased by 20%. It is also shown that the inclusion of a proton energy cutoff can provide a better match with the estimated fluxpoints in any case, where the last three energy bins clearly indicate a dropping trend of the γ-ray flux.

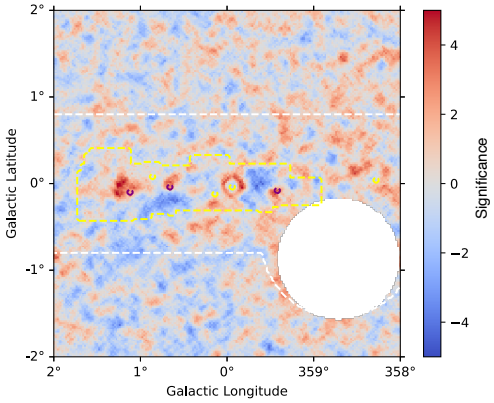

Figure 6.16 The Li & Ma residual significance map of using the impulsive injection template for modelling the diffuse emission in the CMZ. A ring-like feature appear around HESS J1745-290, which might hint at an unmodelled feature/component.

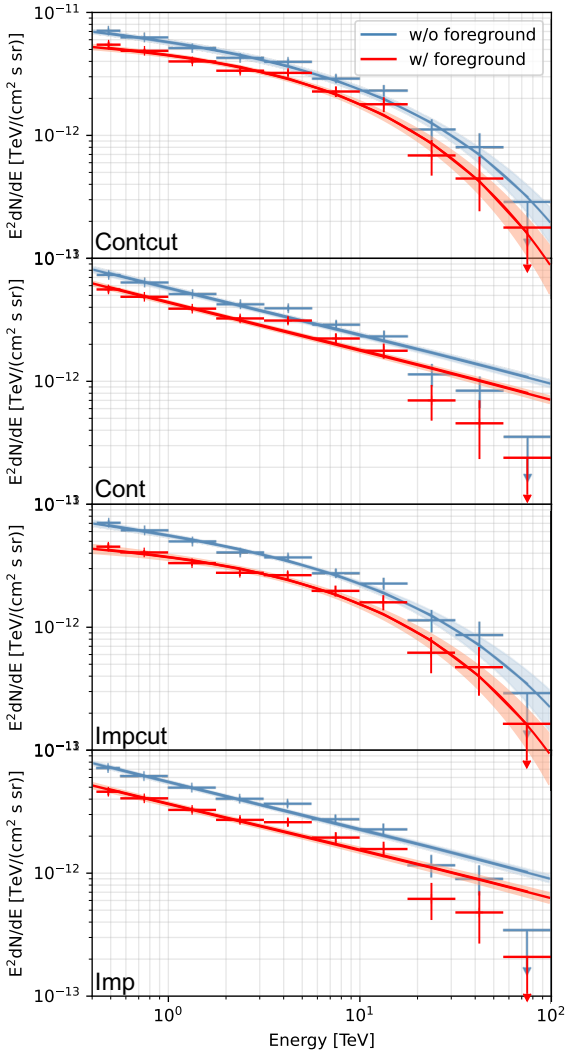

Figure 6.17 The diffuse emission spectra in different CR injection scenarios. The term *cont* and *imp* denote the continuous and impulsive injection scenario respectively. The term *cut* indicates the inclusion of a CR energy cutoff. The red and blue lines denote the fitting included or excluded the foreground component respectively. The errorbands indicate the statistical error at 1σ.

Although the spectrum seems to be also well described by the impulsive injection template with the proton energy cutoff, the effect of the increased ΔTS value can be visualised in Figure 6.16. A clear ring-like feature arises close to HESS J1745-290, which is believed to be associated with an additional central component and is possibly the same component used in H.E.S.S. (2018). Detailed results by using the impulsive injection template together with an additional central component will be discussed later in Section 6.4.

As a short summary, this section suggests that if only the above-mentioned FoV sources and components are considered, the scenario of continuous CR injection from a source close to Sgr A* is more likely. In addition, the γ-ray spectrum can be better described by including a proton energy cutoff in the proton injection spectrum. In the next section, the parameters of the diffuse emission template for arriving at such a description will be explored.

6.3.2 Diffuse Emission Template Parameters

As discussed in Section 5.3, the model parameters are degenerated when the continuous CR injection template is considered. This leads to a set of local minima in likelihood landscape, which are comprised of nearly the same γ-ray spectrum with $\Delta\text{TS} < 1$ (relative to the global minimum). The diffuse emission spectra of these local minima and the correlation of the five template parameters are shown in Figure 6.18 (a) and (c). Among these parameters, stronger correlations are found between the proton index α and the diffusion slope δ, and also between the proton number N_p and the diffusion coefficient D_0. As illustrated in Figure 6.18 (b), α and δ are degenerate in the range of $2.13 \leq \alpha + \delta \leq 2.15$. The parameter N_p and D_0 are degenerate in the range of of $-2 \leq \ln(N_p) - \ln(D_0) \leq 2.5$. The proton energy cutoff E_{cutoff} is however stably distributed at around 142 – 146 TeV. Examples of template parameters at these local minima is given in Table 6.2.

ΔTS	$N_p[\times 1.55\text{E+}52]$	α	D_0 [pc^2/yr]	δ	E_{cutoff} [TeV]
0	0.65±0.05	2.14±0.02	3.50±0.27	0.00±0.01	146.12±27.26
0.2	13.41±2.25	2.13±0.03	72.23±16.58	0.01±0.01	142.77±28.19
0.3	1617.41±240.00	2.06±0.05	6795.78±773.53	0.08±0.03	144.39±33.00
0.2	0.84±0.15	1.84±0.05	1.69±0.20	0.30±0.03	143.29±32.72
0.3	1681.01±463.62	1.80±0.05	2997.45±509.56	0.34±0.03	144.23±35.98
0.3	**0.40±0.09**	**1.77±0.04**	**0.64±0.09**	**0.37±0.02**	**142.82±31.09**
0.2	2.79±0.87	1.51±0.00	1.61±0.30	0.64±0.02	143.57±32.74
0.3	601.35±49.77	1.50±0.01	340.87±25.91	0.64±0.01	144.60±38.62
0.3	59.52±11.35	1.45±0.04	2738±6.02	0.70±0.02	143.86±29.23

Table 6.2 A table of continuous injection template parameters at different local minima in likelihood landscape. Three examples are chosen for $\delta \in (0, 0.3, 0.6)$. A diffusion time of 10^6 years is assumed. The bold parameters are chosen for the further analysis.

Before proceeding to the detailed analysis, the template parameters need to be decided. The diffuse emission is assumed to be connected to a source close to Sgr A*, the potential association of this source is HESS J1745-290. Though the spectral index of HESS J1745-290 has been derived in Section 6.3.1, the proton index of this source is not well determined. Alternatively, the proton injection spectrum can be constrained by the choice of δ. As

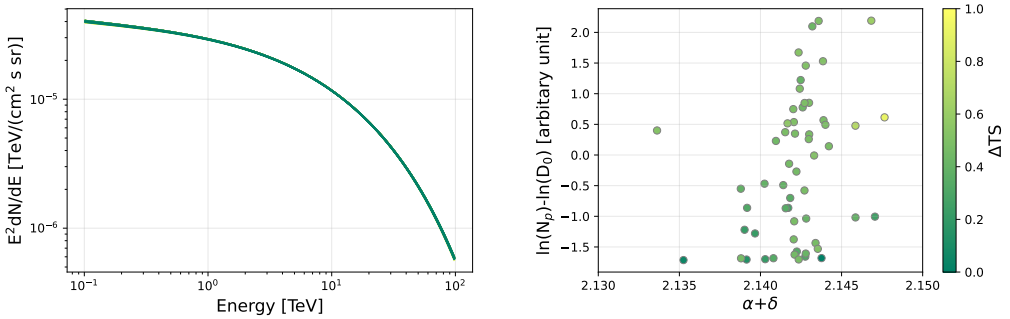

(a) (b)

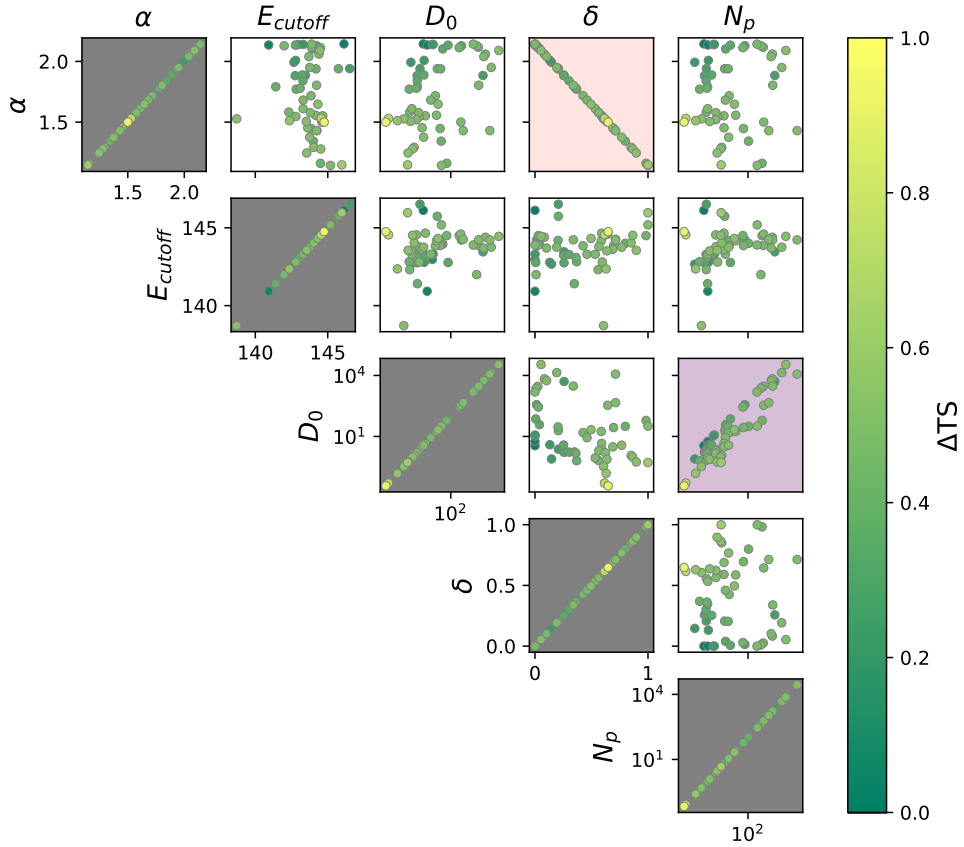

(c)

Figure 6.18 The correlation of the diffuse emission template parameters α, $E_{\rm cutoff}$ [TeV], D_0 [pc^2/yr], δ and N$_{\rm p}$[$\times$1.55E+52]. The diffusion time is assumed to be 10^6 years. (a) γ-ray spectra from all the best-fit template parameters. (b) The correlation between $\alpha+\delta$ and $\ln(N_p)-\ln(D_0)$. (c) The correlation between the individual parameters. The colorbar indicates ΔTS (relative to the global minimum).

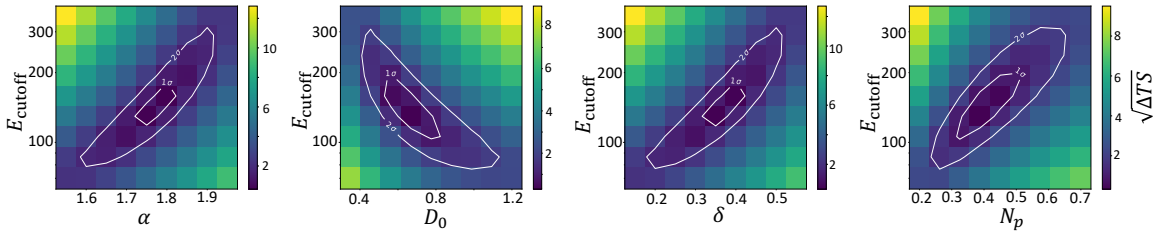

Figure 6.19 The 2D confidence contour map of the template parameters E_{cutoff} [TeV] with α, D_0 [pc^2/yr], δ and N$_\mathrm{p}$[$\times$1.55E+52]. The colorbar indicates the $\sqrt{\Delta\mathrm{TS}}$ (relative to the minima). The white contour denote the 1σ and 2σ confidence levels. Since (α, δ) and (D_0, N_p) degenerate, their opponents are fixed when deriving the contour map.

discussed in Section 2.3.1, $\delta \approx 0.3$ [23] is usually chosen to balance the CR isotropy, the ratio between the fluxes of cosmic boron and carbon from previous experiments, and the value constrained by current theories of turbulence. The D_0 can also be chosen to a value comparable to other CR propagation models, the typical value is $D_0 \approx 0.03$ pc^2/yr [41]. With these constraints, the parameters used for building the template in this analysis is highlighted in Table 6.2. With this choice of the D_0 and δ, the distance of any points in the CMZ with respect to the injection point is smaller than the diffusion radius r_{diff}, i.e. $r_{\mathrm{diff,min}} = 2.46$ kpc for $E_p \in (0.1...10^5)$ TeV. This means a steady-state is reached and a 1/r CR distribution is expected within the CMZ. Furthermore, the total number of injected CRs is $\sim 6.2 \times 10^{51}$. This corresponds to a total injection energy of $\sim 1.3 \times 10^{52}$ erg. The injection rate at $E_p \geq 10$ TeV is therefore calculated as 2.1×10^{38} erg/s. A comprehensive discussion of corresponding potential accelerators will be discussed at the end of this chapter in Section 6.7.

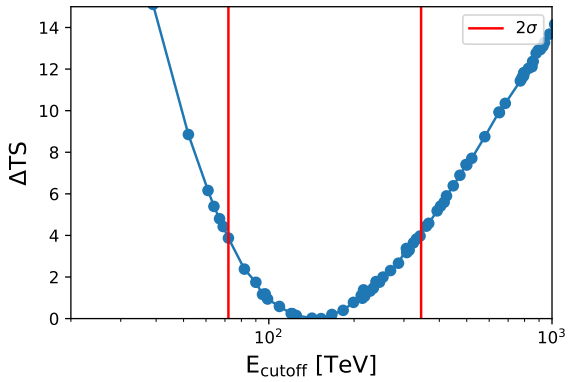

Figure 6.20 The likelihood scan of the proton cutoff energy. The red lines represent the 2σ confidence at $\approx 72 - 345$ TeV.

The resulting 2D confidence contour map of this choice of parameters can be found in Figure 6.19, where ellipsoidal shapes are shown. Since the 2D contour gives a smaller

coverage probability, i.e. 1σ is smaller than the confidence level of 68 %, the best way to study the lower limit of the E_{cutoff} is through the 1D likelihood scan. As can be seen in Figure 6.20, the lower limit and upper limit of the E_{cutoff} is $\approx$ 72 TeV and 345 TeV at the 95% confidence level respectively. A cutoff energy at 1 PeV is excluded at around 3.6σ.

6.3.3 Spatial and Spectral Results

After the determination of the template parameters as well as the inclusion of different FoV sources and component, the detailed spatial and spectral results will be shown in the following section. The summary of fitted parameters is listed in Appendix A.

Spatial Results: Li & Ma significance and spatial profiles

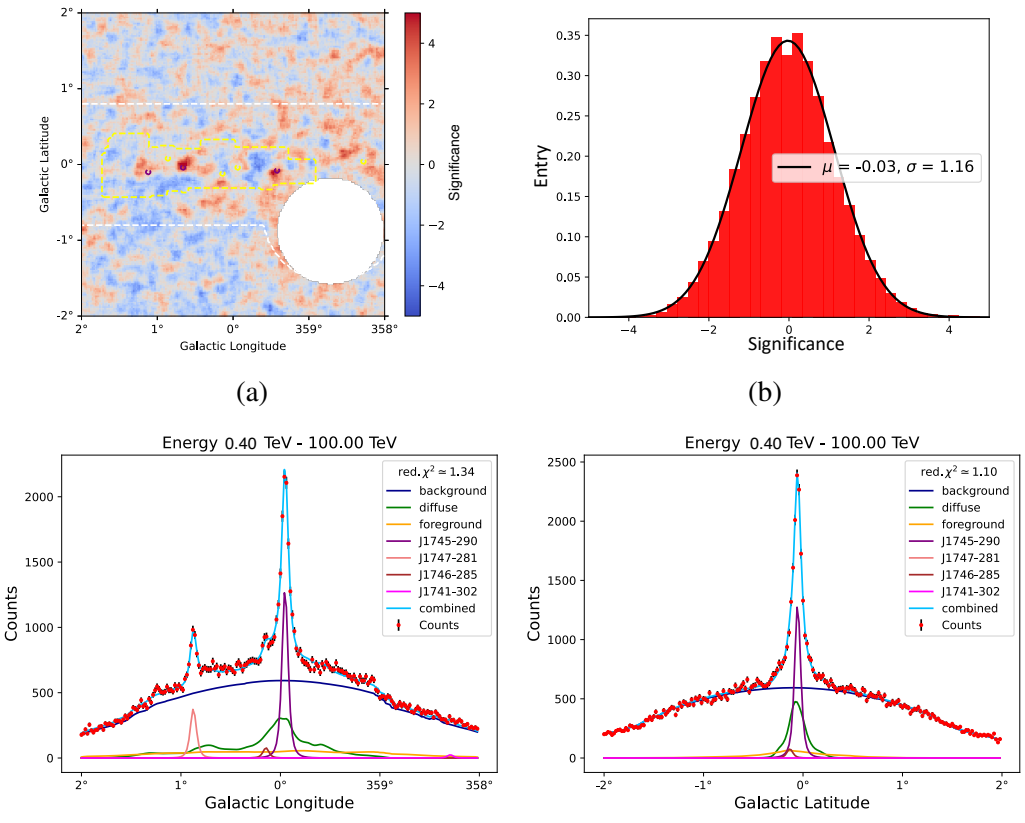

(a) (b)

(c)

Figure 6.21 The spatial result in the overall energy range from 0.4 – 100 TeV. (a) The Li & Ma residual significance map correlated with a top-hat kernel of size of H.E.S.S. PSF (0.077°). The colorbar indicates the Li & Ma significance. (b) Distribution of significances from (a). (c) The Galactic longitudinal and latitudinal counts profile.

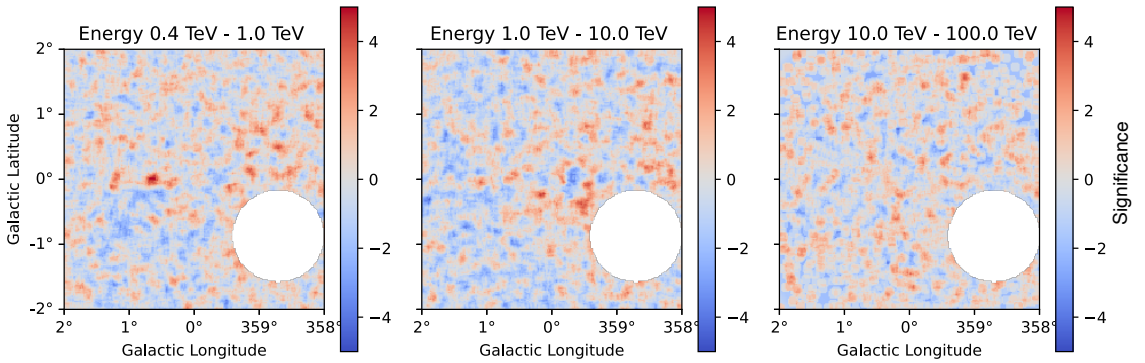

(a)

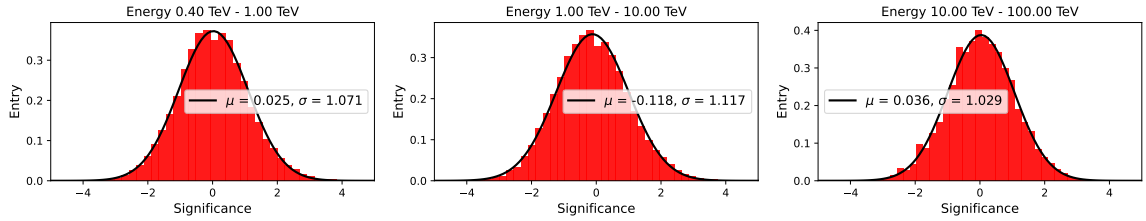

(b)

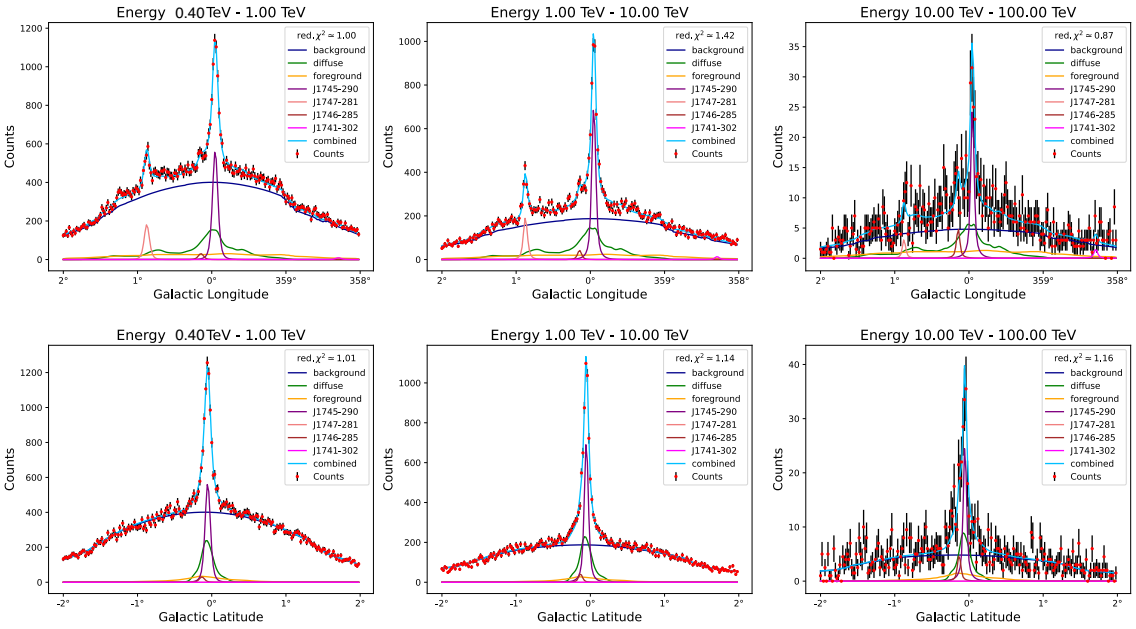

(c)

Figure 6.22 The spatial result in the sub-energy range from 0.4 – 1 TeV, 1 – 10 TeV and 10 – 100 TeV. (a) The Li & Ma residual significance map with correlation radius of 0.077°. The colorbar indicates the significance. (b) The Li & Ma significance distribution. (c) The Galactic longitudinal and latitudinal counts profile.

The spatial results can be analysed through the Li & Ma significance map and its entry distribution, together with the spatial counts profiles of the model in comparison with data. These results summed over the whole energy range can be found in Figure 6.21. The Li & Ma significance map is correlated with the H.E.S.S. PSF; the resulting significance distribution resembles a Gaussian distribution and has a mean of -0.03 and a standard deviation of 1.16. These values indicate a rather flat residual. Since the fitted sources and components are located close to the Galactic plane, one can look at the Galactic longitudinal counts profile specifically in that region. For this, a rectangular region of $4^\circ \times 0.5^\circ$ centered at the Galactic Centre is selected. The Galactic latitudinal counts profile is, on the other hand, defined at a rectangular region of $0.5^\circ \times 4^\circ$ centered at the Galactic Centre. The measured counts and the predicted counts are integrated in the defined regions and the profiles can be seen in Figure 6.21 (c). In general, the contribution from the background is clearly dominates over the sources in these regions. An exception is found for HESS J1745-290, where the signal is significantly stronger than the background. Nevertheless, the counts predicted by the full FoV models are mostly in agreement with the measured counts, with a χ^2_{red} of 1.34 and 1.10 in the longitudinal and latitudinal counts profiles respectively. The longitudinal counts profile has a higher reduced chi-square value mainly due to more source regions are covered than the latitudinal counts profile. Note that there is a drop of measured counts at the region around $l = 359^\circ$, which is mainly due to the region crosses the exclusion mask.

The same spatial results in the sub-energy ranges of 0.4 – 1 TeV, 1 – 10 TeV and 10 – 100 TeV can be found in Figure 6.22. It can be seen in the significance map that the emissions from the regions Sgr D and B are more noticeable in the energy range of 0.4 – 1 TeV. There are also unidentified residuals from 0.4 – 10 TeV, for instance on the right of Sgr B and below Sgr C. To ensure these are not the artefacts from the CS tracer, a comparison with the CO tracer will be made in Section 6.5. The residual on the top right quarter is also visible as compared to the emission on the bottom left quarter. This might be related to the Fermi bubble component or associated to background systematics. This will be studied again in more detail in Section 6.6. At the energy range of 10 – 100 TeV, the significance distribution is rather flat, whereas the standard deviation is about 1. For the longitudinal and latitudinal counts profiles in the sub-energy range, it can be seen that the predicted counts from each model component changes at different energy ranges due to the energy dependence of the spectrum. The corresponding χ^2_{red} are again within the reasonable range.

Spatial Results: γ-ray luminosity and CR energy density profiles

The γ-ray luminosity and CR energy profiles can also be investigated around the Galactic Centre. For that, a sequence of masked regions is defined following the approach from

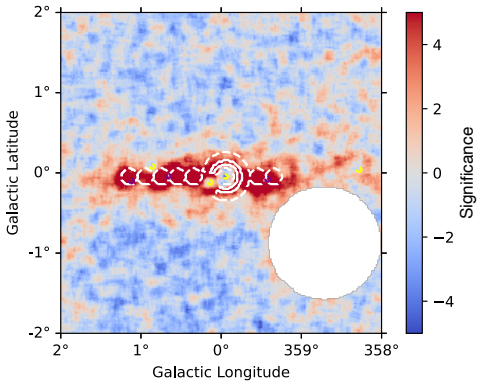

Figure 6.23 Visualisation of the regions (white lines) defined for extraction of the γ-ray luminosity and CR energy density profile in Figure 6.24.

H.E.S.S. (2016) [56]. These regions are visualised in Figure 6.23. An annulus centred at Sgr A* with an opening angle of 66°, such that HESS J1745-290 and HESS J1746-285 are adequately excluded from the analysis. Three ring regions of different sizes are defined within the annulus. Additionally, several circular regions are defined along the Galactic plane. In this way, the results extracted from these regions contributed solely by the diffuse emission. The resulting γ-ray luminosity and CR energy profiles in these regions can be found in Figure 6.24.

The γ-ray luminosities are calculated from the measured spectrum. The result from H.E.S.S. (2016) has considered the possible PSF leakage from HESS J1745-290. In the luminosity profile, a slight shift is observed when comparing the excess of this analysis with the result from H.E.S.S. (2016). This might be related to the different analysis chain, whereas the shifts also occur in the pacman region in their cross-check with the ImPACT data [61]. Moreover, H.E.S.S. (2016) estimated the background using the Ring Background method, while this analysis uses the 3D FoV Background method which is more suitable for an analysis of extended sources. Apart from that, the contributions from the diffuse emission template cannot fully cover the excess counts in the profile. This is related to the contamination from HESS J1745-290 and the foreground component.

The conversion of the γ-ray luminosity L_γ to the CR energy density w_{CR} can be done via the conversion stated in H.E.S.S. (2016) and MAGIC (2020) using

$$w_{CR}(\geq 10E_\gamma) \sim 1.8 \times 10^{-2} \left(\frac{\eta_N}{1.5}\right)^{-1} \left(\frac{L_\gamma(\geq E_\gamma)}{10^{34}\ \mathrm{erg/s}}\right) \left(\frac{M}{10^6 M_\odot}\right)^{-1} \mathrm{eV/cm^3}, \tag{6.3}$$

where $\eta_N \approx 1.5$ accounts for nuclei heavier than hydrogen and M is the mass of the gases in relevant regions. The result of this analysis can be found in Figure 6.24 (b). Again a

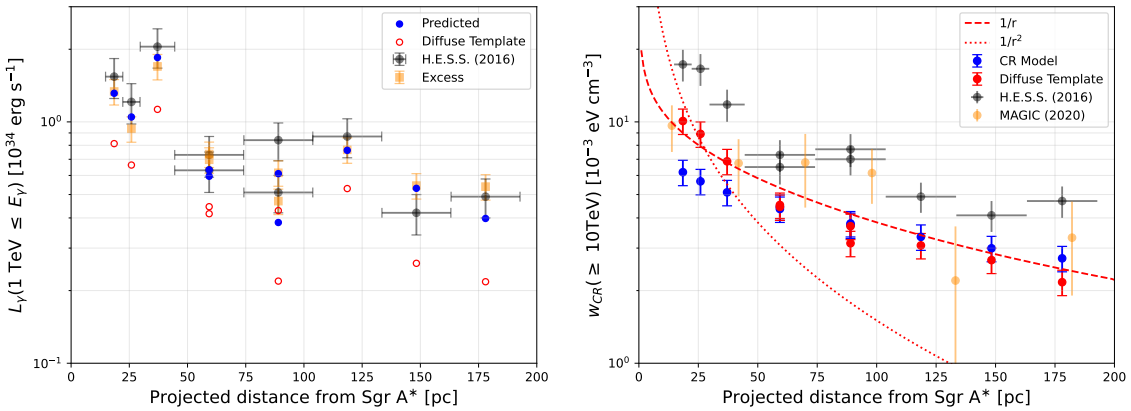

(a) (b)

Figure 6.24 (a) The γ-ray luminosity profile. The yellow and blue points denote the excess (data minus background) and predicted (from all FoV models) counts of this work. The red circles indicate the contribution from the diffuse emission template among the predicted counts. (b) The CR energy density profiles in the projected distance from Sgr A*. The red dashed lines in (b) indicate the 1/r and 1/r^2 fit performed to the calculated CR energy density from the diffuse emission template (red points, using Equation 6.3). The blue circles denote the CR distribution for building the template. The deviation of red and blue circles is related to the different γ-proton conversion approaches and the ambient gas distribution.

general shift is observed due to the reasons stated above. The calculated CR energy density nevertheless flavours the 1/r fit[6] rather than the 1/r^2 fit. This is mainly due to the CR diffusion is in a steady state, which will naturally give the 1/r distribution as discussed in Sections 5.1.1 and 5.3. The CR distribution can also be derived directly from the three-dimensional CR model in the diffuse emission template, which is also shown in the figure. Yet discrepancies are found, which is related to the energy-independent γ-proton conversion being considered in the calculation from H.E.S.S. (2016), whereas in the work the energy-dependent conversion was taken in to account for generation of the template. Moreover, the gas map is projected along the line-of-sight in this analysis. A similar discrepancy can also be seen in the result from MAGIC (2020, Figure 8) by using a similar projection method for the CMZ gas data.

Spectral Results

The energy spectra of all the fitted sources and components can be found in Figure 6.25. It can be seen that the spectral model of most sources are well suited for describing the energy spectra. The spectral models of HESS J1741-302 and the foreground component

[6]Note that this is a reduced chi-square fit. It is performed in the projected distance along the longitude from a 2D space.

show deviations in few energy bins, which might be related to background systematics. To check the necessity of the proton energy cutoff, the diffuse γ-ray spectra with and without the proton energy cutoff are shown in Figure 6.26. For the case where no cutoff has been considered, the model at above 20 TeV deviates from the fluxpoints and worsen the result by 5.7σ (whereas a cutoff at > 1 PeV is also disfavoured by 3.6σ). The lower limit for the proton energy cutoff is at 72 TeV at the 95% confidence level. The performance of the diffusion model can also be checked at different regions in the FoV. For that, a collection of 7 small boxes with total size of $\approx 4^\circ \times 0.5^\circ$ along the Galactic plane are defined as illustrated in Figure 6.27 (a). The scaled diffuse emission spectra derived from these regions can be seen in Figure 6.27 (b). In general, the model matches the estimated fluxpoints. The cutoff effect at high energies is still present in the different sub-regions. Note that some fluxpoints are missing at high energies in the outer regions. This might be related to the missing CMZ gas distribution at the edge of the template.

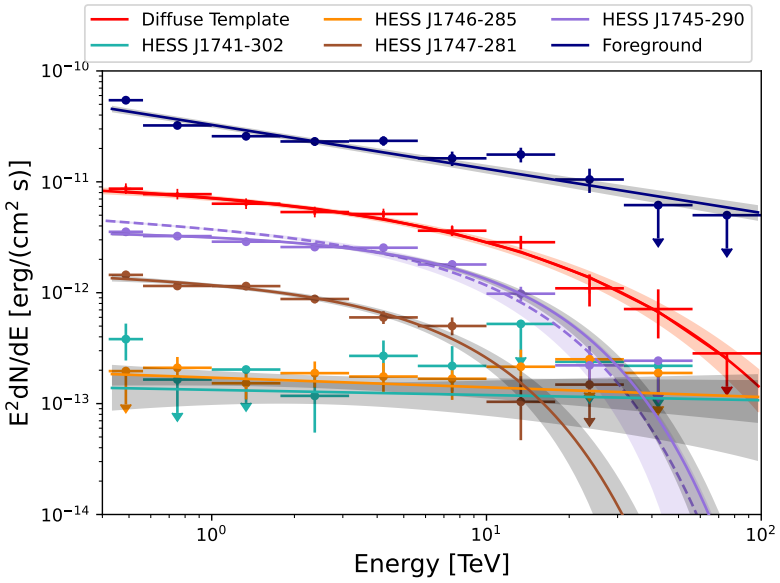

Figure 6.25 The overall energy spectra from all sources and components. The solid lines represent the results of this work, the dashed lines represent the result shown in HGPS (2018). The colorbands indicate the error of 1σ.

The performance of the diffuse emission template can also be investigated at smaller Galactic regions. For that a pacman and the Galactic ridge regions are chosen, the same as the region studied by previous measurements of H.E.S.S. (2016), H.E.S.S. (2018) and MAGIC (2020). The pacman region is defined as an annulus centred at Sgr A* with inner and outer radii of 0.15° and 0.45° and opening angles of $+10^\circ$ and -56° from the positive Galactic longitudinal axis [56]. The Galactic ridge region is defined as $|l| < 1^\circ$ and $|b| < 0.3^\circ$, and

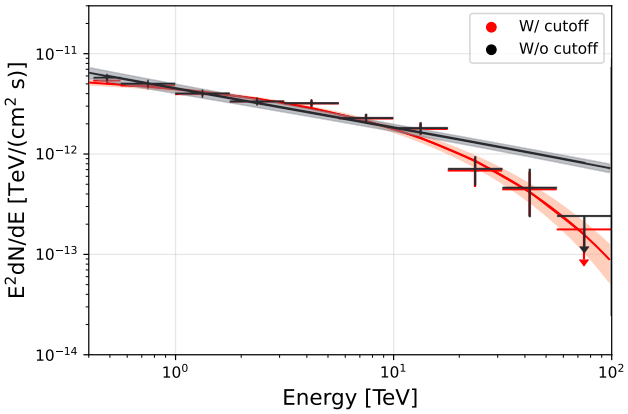

Figure 6.26 The diffuse emission spectra from the template with (red) and without (black) the proton energy cutoff. The colorbands indicate the error of 1σ.

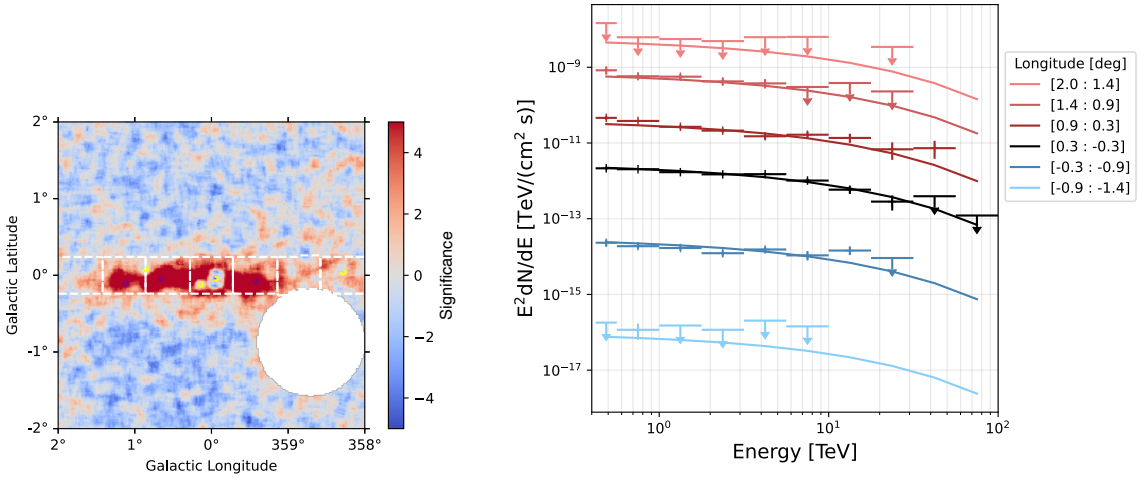

(a) (b)

Figure 6.27 (a) The boxes defined to derive the diffuse emission spectrum. The box size is $\approx 0.6^\circ \times 0.5^\circ$. (b) The energy spectra of the diffuse emission component in (a). The spectra are scaled relative to the spectrum at $l \in (-0.3^\circ : 0.3^\circ)$ for visualisation. The spectrum from the rightest box is not shown due to the no dense gas exists in that region.

two circular regions of 0.2° radius around G0.9+0.1 and Sgr A* and a circular region of 0.1° radius around HESS J1746-285 are excluded [57]. The illustrations of these regions are shown in Figure 6.28. The diffuse emission spectra can be found in Figure 6.29.

It can be seen that both diffuse emission spectra have a shift from previous measurements by a factor of 2. Apart from the fact that both results from H.E.S.S. (2016) and (2018) used the Ring background estimation method, there are also contaminations from HESS J1745-290 and the foreground. This is related to the same effect as discussed for Figure 6.24.

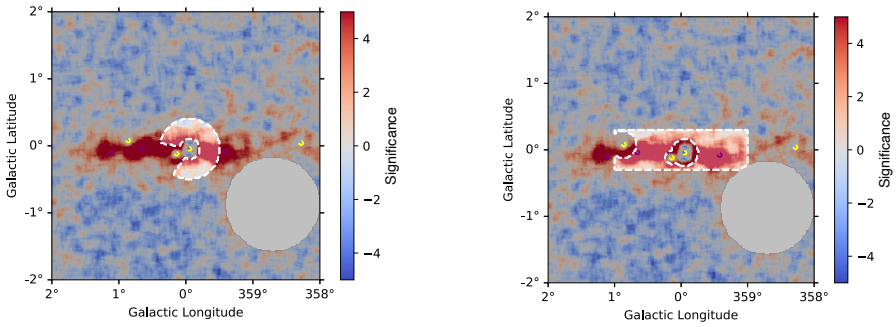

(a) (b)

Figure 6.28 The defined pacman region (a) and the Galactic ridge region (b) for Figure 6.29.

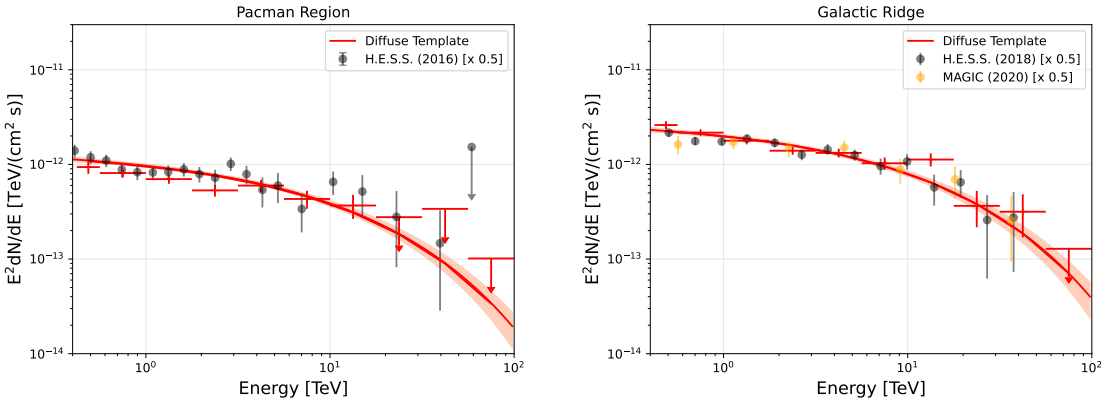

(a) (b)

Figure 6.29 The diffuse emission spectra derived from the pacman (a) and the Galactic ridge (b) region. The solid lines indicates the model, the points indicate the estimated fluxpoints. The reference data is also shown. A scaling by 0.5 has applied to the reference data to better compare the spectral shape.

The shift in the ridge region might be, in addition to the above-mentioned reasons, due to the methodology of the determination of the spectrum. The authors of H.E.S.S. (2018) divided the region into 11 rectangular boxes and performed the spectral analysis in each region. Those results are summed up to perform a global fit over all regions up to an energy of 45 TeV. This methodology is not used in the thesis. Aside from the shift, the diffuse emission template (in general) provides a good match with the estimated fluxpoints in the Galactic ridge region. A jump is observed at around 10 TeV, this might be related to the data/background construction since a similar jump is observed in Figure 6.8 (a). At the lowest energies, fluxes in the pacman region seems to deviations from the model, where the

model has a higher amplitude than the estimated fluxpoints. This might be a hint of a more complicated γ-ray emission scenario in the Galactic Centre.

Summary

This section has presented the result using a diffuse γ-ray emission template where the continuous injection of CRs from a source in the vicinity of Sgr A* is considered. HESS J1745-290, HESS J1746-285, HESS J1747-281, HESS J1741-302 and the foreground component have been taken into account. A summary of fitted parameter are listed in Appendix A. It has found that:

- A power-law spectrum of HESS J1747-281 is disfavoured at 5σ.
- The foreground component significantly improves the result by 17σ and has equal performance regardless of the map size.
- The gas projection method (for building the diffuse emission template) mentioned in Section 5.1.2 is 12σ better than without consider the line-of-sight projection.
- The proton energy cutoff for the diffuse emission template at 143 ± 31 TeV is preferred over a simple power-law by 5.7σ and preferred over a cutoff at > 1 PeV by 3.6σ. It has a lower limit at 72 TeV and upper limit at 345 TeV in the 95 % confidence level.
- CR energy density profile is well described by a 1/r fit in the inner 200 pc of the Galactic region.
- The diffuse emission spectrum in general agrees with the data in the CMZ. Yet deviation between the model and data in the pacman region around the Galactic Centre is seen at low energies.

Though the diffuse emission template with continuous CR injection and a proton energy cutoff can already give a good description for the diffuse emission from the Galactic Centre in the CMZ, the performance in the pacman region hints at a more complex scenario close to the Galactic Centre. For this, a study of the more complicated scenario has been carried out. The details will be discussed in the next Section 6.4.

6.4 Results with Impulsive Cosmic-Ray Injection Template

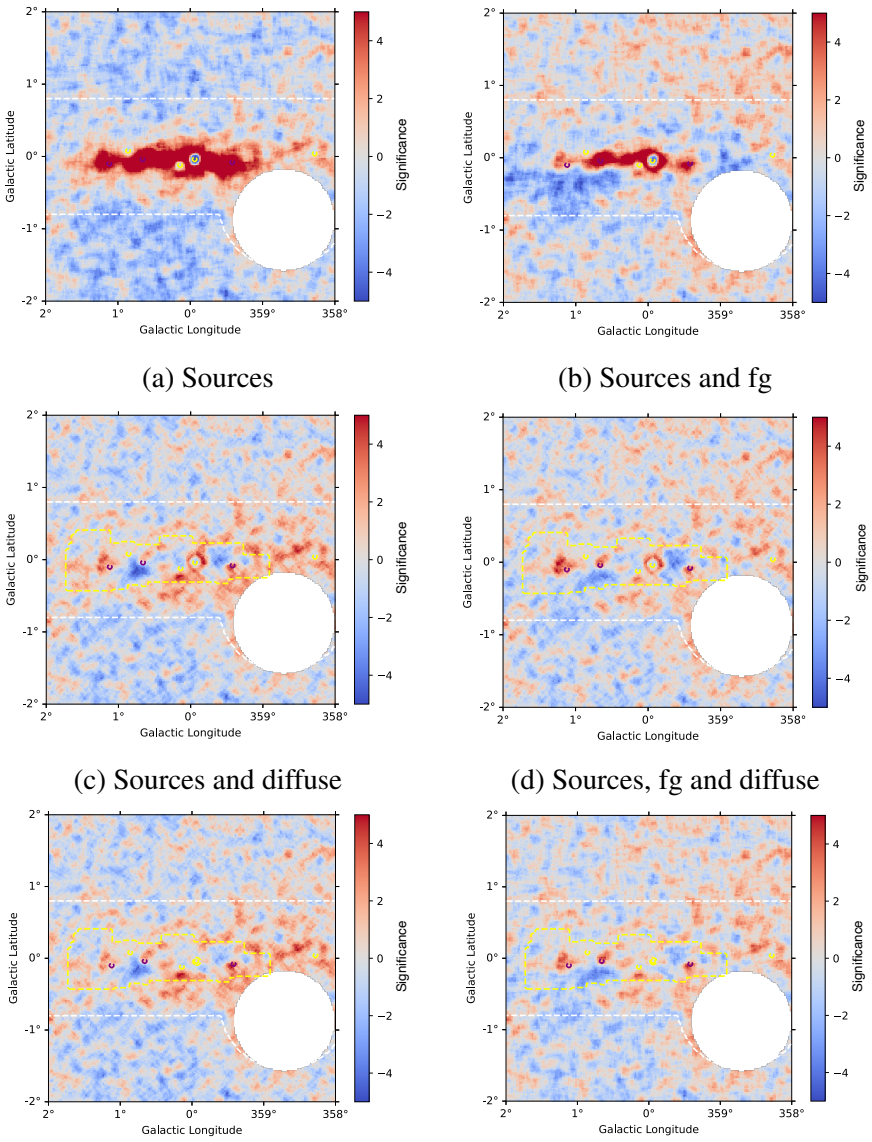

(a) Sources

(b) Sources and fg

(c) Sources and diffuse

(d) Sources, fg and diffuse

(e) Sources, cc and diffuse

(f) Sources, cc, fg and diffuse

Figure 6.30 The Li & Ma significance maps of the residual after the inclusion of different model components in the FoV, smoothed by the H.E.S.S. PSF. The term *fg* and *cc* denote the foreground and the additional central component. The colorbar indicates the significance. The yellow, purple and white contours indicate the fitted components, the molecular complexes and the exclusion region in the run-wise background prefit respectively. The void area indicates the exclusion region in the analysis. The diffuse emission template has been modelled with an impulsive CR injection with an energy cutoff. The abbreviation cc and fg denote the additional central component and the foreground component. The ΔTS of these plots relative to plot (f) are: (a) 3488, (b) 1267, (c) 441, (d) 151 ,(e) 268 and (f) 0.

In this section, the results using an impulsive CR injection model to account for the diffuse γ-ray emission in the CMZ will be presented. An additional Gaussian central component has been taken into account in this analysis. This section starts with the study of best-fit model properties of the FoV sources, foreground component, additional central component and diffuse emission component. The derivation of the best-fit diffuse template parameters will be explained, followed by detailed morphological and spectral results.

6.4.1 FoV Sources and Components

Same as the analysis presented in the previous section, several sources within the FoV mentioned in Section 6.1 have been included in this analysis. These include HESS J1745-290, HESS J1747-281, HESS J1746-285 and HESS J1741-302. An exclusion mask is applied to exclude the extended sources HESS J1745-303 and HESS J1746-308. Moreover, an additional Gaussian central component which was not presented in most of previous studies (e.g. HGPS (2018)) needs to be taken into account in order to explain the morphology.

For an overview, it can be seen in Figure 6.30 (a) that non-negligible residuals are left at the central Galactic plane area if only the FoV sources are subtracted. The shape of this residual follows that in the CS gas map, which related to the diffuse γ-ray emission in the CMZ. The inclusion of the foreground emission component can significantly improve the overall residual in Figure 6.30 (b), yet not covering the residual in the CMZ. Alternatively by adding the diffuse emission component built for an impulsive CR injection scenario, most of the residual in the CMZ can be covered, except the positions at around the dense gas region Sgr B, C and D due to the self-absorption [57]. A noteworthy ring-like residual is also present close to HESS J1745-290. By further including the contribution from the foreground component, the spatial residual clearly improves, though the ring-like residual remains. By introducing an additional Gaussian component close to HESS J1745-290, the ring-like residual is gone in both cases where the foreground component is or is not modelled.

The details of all FoV model properties will be discussed in the following.

Model Properties of FoV Sources and the Foreground Component

As mentioned in Section 6.3, a clear ring-like feature is found around HESS J1745-290 when an impulsive injection template is used. This ring-like feature, however, cannot be explained by a simple extension from HESS J1745-290. As can be seen in Figure 6.31, the inclusion of an additional central component is able to account for the ring-like feature, whereas a Gaussian extension of HESS J1754-290 cannot fully cover the ring-like residual around the source. The former can also improve the ΔTS by 61 in comparison with the latter. Therefore

an additional Gaussian central component is modelled in this analysis. The rest follows the finding from Section 6.3, where an energy cutoff in HESS J1747-281 and the inclusion of the foreground component are kept. Details of the spatial and spectral models for all FoV sources and components is given in Table 6.3. The corresponding best-fit parameters and their uncertainty can be found in Figure 6.32.

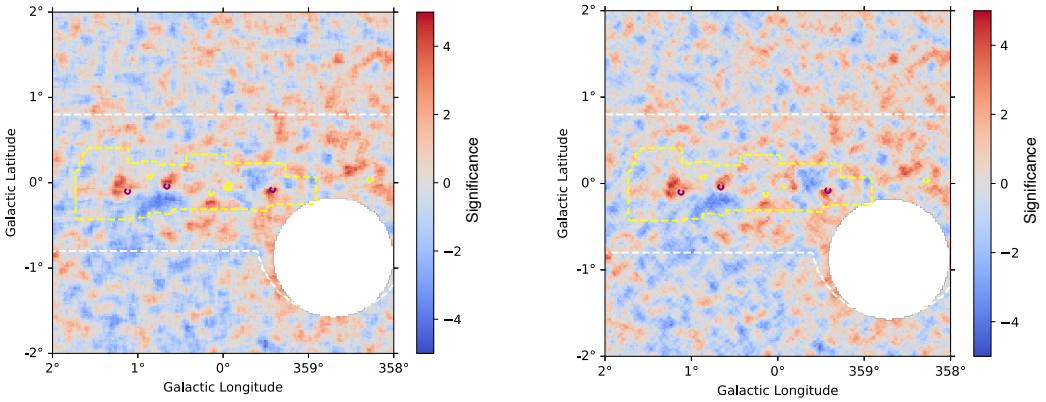

(a) (b)

Figure 6.31 The Li & Ma residual significance map of modelling an (a) additional central component or (b) extended HESS J1745-290. An improvement of $\Delta TS \approx 61$ is seen by comparing (a) to (b).

The derived values are again compared with previous measurements from HGPS (2018) and MAGIC (2020), and with the preliminary *HAP-Fr* (2022) result from Justine Devin [34]. In general, the best-fit positions and the spectral indices of the FoV sources match almostly with the reference values. The amplitudes are in general lower in this analysis, yet close to *HAP-Fr* (2022) result. This might again related to the different event reconstruction and background estimation methods, as well as the modelling of the diffuse emission and foreground components, where *HAP-Fr* (2022) uses a relatively similar configuration as this analysis. Yet deviations on the spectral indices of HESS J1745-290 and J1747-281 are observed. This might be due to the fact that the line-of-sight distribution of the CS gas is not being considered and a simple power-law with exponential cutoff spectrum is assumed for the diffuse component in the *HAP-Fr* analysis. The background systematics are also a possible source of these discrepancies.

A comparison of the central component parameters with *HAP-Fr* (2022) and H.E.S.S. (2018) can be found in Figure 6.33. H.E.S.S. (2018) has considered an empirical impulsive injection scenario as well as the inclusion of an ad-hoc central component. Deviations in the source positions and extension are observed. This might again have a linkage with the different modelling of the diffuse emission. Furthermore, both the CR injection position

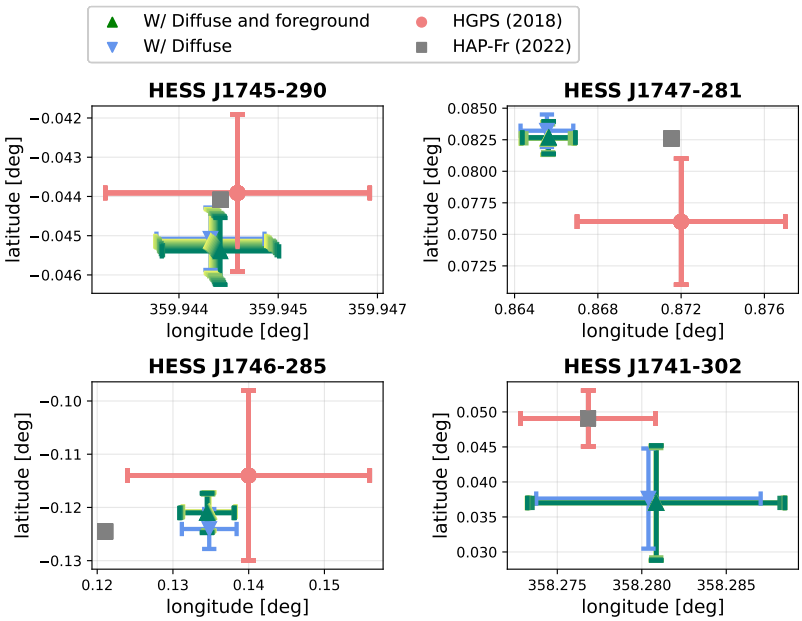

(a) Spatial parameters

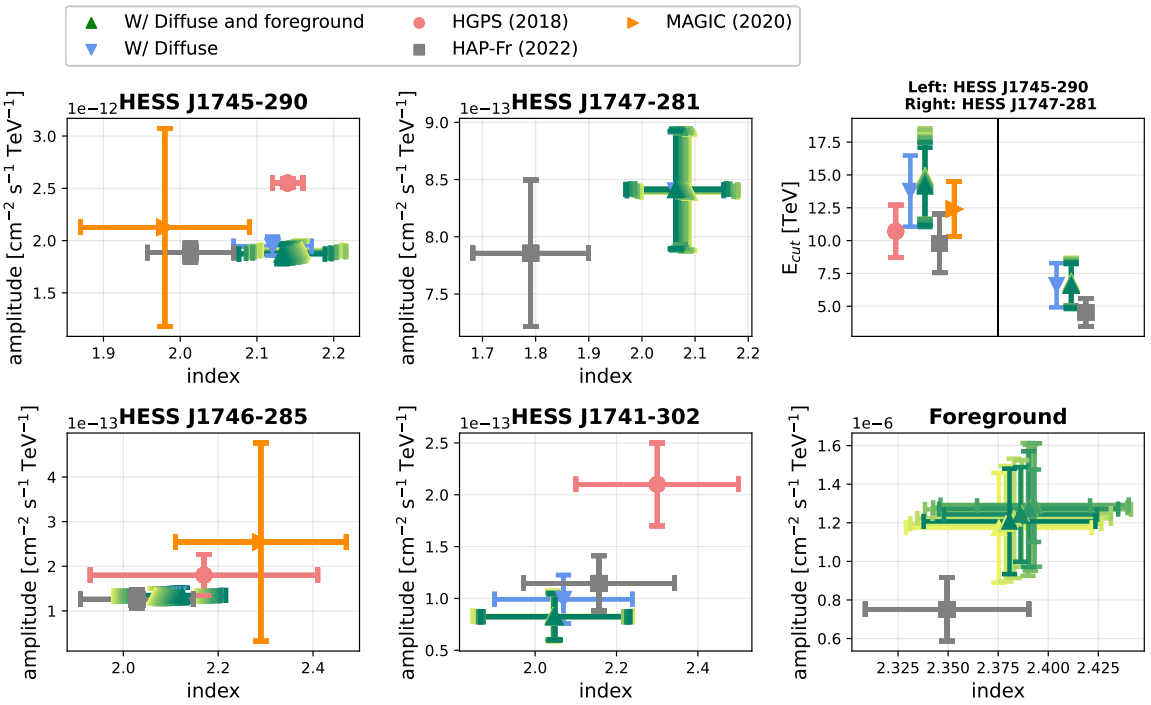

(b) Spectral parameters

Figure 6.32 Best-fit spatial (a) and spectral (b) parameters of the FoV sources and components. The red and orange points are the HGPS (2018) and MAGIC (2020) results. The grey points are the preliminary result from J. Devin [34] using the empirical diffusion model, where no errorbars are shown for the spatial parameters due to the final positions are being frozen in the fit. The blue and green are the result of this work using the impulsive injection template excluded and included the foreground component respectively. The points from green (best-fit) to yellow indicate the result of using the diffuse emission template with $\delta \in (0...1)$. The reference energy in the amplitude is 1 TeV (except being 10 GeV for the foreground component).

Source or component	Spatial model	Spectral model
HESS J1745-290	Point	PLC
HESS J1747-281	Point	PLC
HESS J1746-285	Point	PL
HESS J1741-302	Point	PL
Foreground	Template	PL
Central component	Gaussian	PLC
Diffuse	Modified Template (Impulsive injection with PLC)	

Table 6.3 Summary of full FoV model descriptions.

and the location of the additional central component are fixed to the Galactic Centre in H.E.S.S. (2018). This analysis, however, assumed the CR injection position at Sgr A* and the positions of the additional central component are free. These can essentially be the reasons for a larger extension found in H.E.S.S. (2018). If the exact location of this additional Gaussian component is further away from the Galactic Centre, the fitted extension will naturally be larger. Yet the discrepancy is smaller than the H.E.S.S. PSF of 0.077°. The spectral parameters of this source are, on the other hand, generally in agreement with the reference values.

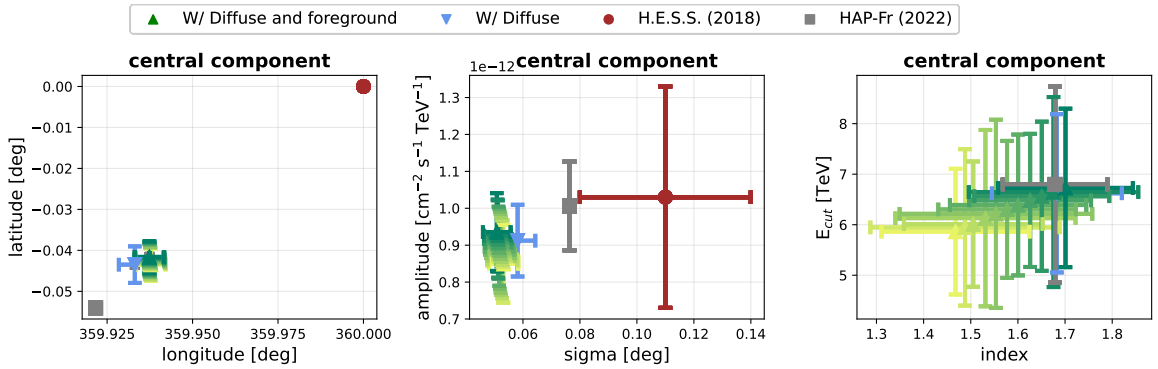

Figure 6.33 The best-fit parameters for the additional central component. The brown and grey points denote the result from H.E.S.S. (2018) and the preliminary results from J. Devin [34] using the empirical diffusion model on *HAP-Fr* data. The blue points denote the result of this work with the impulsive template but without the foreground component. The blue and green are the result of this work using the impulsive injection template excluded and included the foreground component respectively. The points from green (best-fit) to yellow indicate the result of using the diffuse emission template with $\delta \in (0...1)$.

The results using the impulsive injection templates with different values of δ are also shown in Figures 6.32 and 6.33. This indicates the influence of the diffuse emission template on the source parameters. Note again that the results of this work are.with uncertainties by

excluding or including the foreground component in the analysis. This ensures the inclusion of the newly foreground emission component is not vastly affecting the main results of this work.

Model Properties of the Diffuse Emission Component

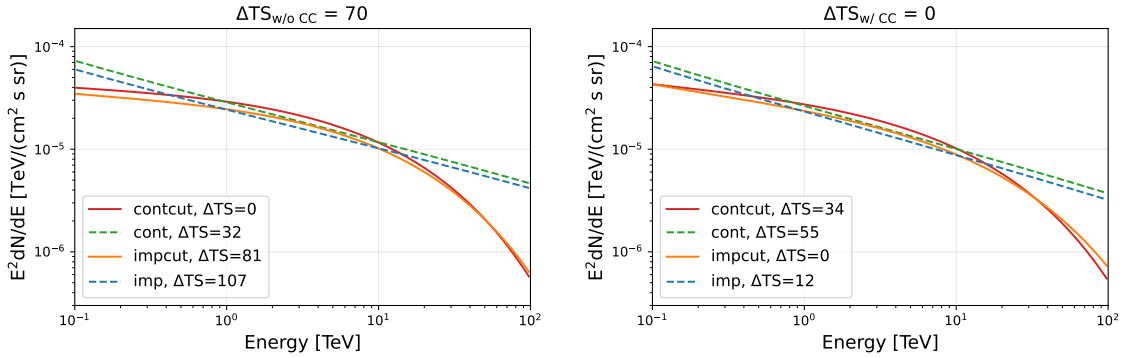

(a) (b)

Figure 6.34 The energy spectra of the diffuse emission component included the foreground component, without (a) and with (b) the inclusion of an additional central component. An extreme improvement of $\Delta TS \approx 70$ is shown in the latter case. Among the two cases, the templates with the scenario of continuous injection (with and without the cutoff) and impulsive injection (with and without the cutoff) are also shown. The individual ΔTS values (relative to the minima in each plot) are shown in the legend.

The diffuse emission template based on the impulsive CR injection with an proton energy cutoff is used in this section. The 3D dense gas map is still used in this section in order to derive more precise model parameters, as discussed in Section 6.3.1. A comparison of the diffuse emission spectrum of different CR injection scenarios with and without the additional central component can be found in Figure 6.34. An improvement of $\Delta TS \approx 70$ is observed in the best-fit scenario for the latter case. Among the diffuse emission spectra where the additional Gaussian central component is fitted, the impulsive diffusion with an energy cutoff gives the best result. Yet in comparison with the case excluded the additional central component, the inclusion of an energy cutoff gives relatively smaller improvement ($\Delta TS \approx 12$).

The estimated fluxpoints derived from different diffusion scenarios can be found in Figure 6.35, included or excluded the additional central component. In general, the inclusion of an proton energy cutoff provides a better match with the estimated fluxpoints in any cases. It can also be seen that spectral shapes are affected by the presence of the additional central component.

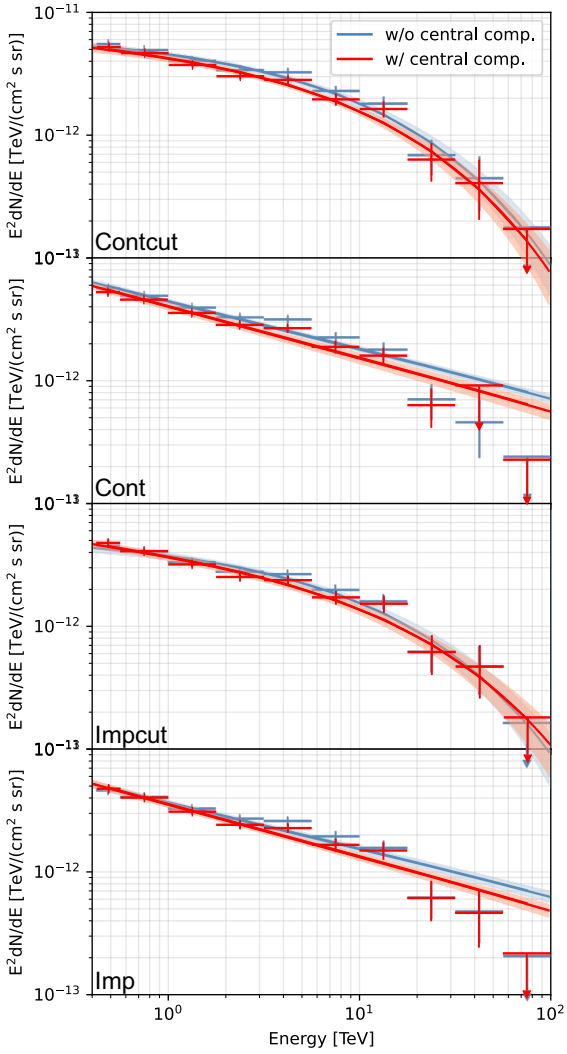

Figure 6.35 The diffuse emission spectra in different CR injection scenarios. The term *cont* and *imp* denote the continuous and impulsive injection scenario respectively. The term *cut* indicates the inclusion of a CR energy cutoff. The red and blue lines denote the fitting included and excluded the additional central component respectively. The errorbands indicate the statistical error at 1σ.

6.4.2 Diffuse Emission Template Parameters

In this section, the determination of the diffuse emission template parameters will be discussed. Unlike the case where a continuous CR injection is considered (Section 6.3.2), the parameters are not degenerate for the impulsive template. As can be seen in Figure 6.36 (a), a different choice of the diffusion slope $\delta \in (0...1)$ will result in a different spectral shape. This can be investigated by looking at the correlation of different template parameters in Fig-

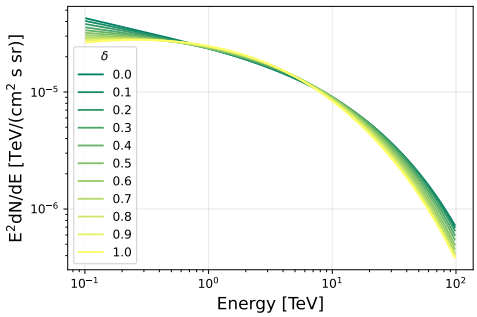

(a)

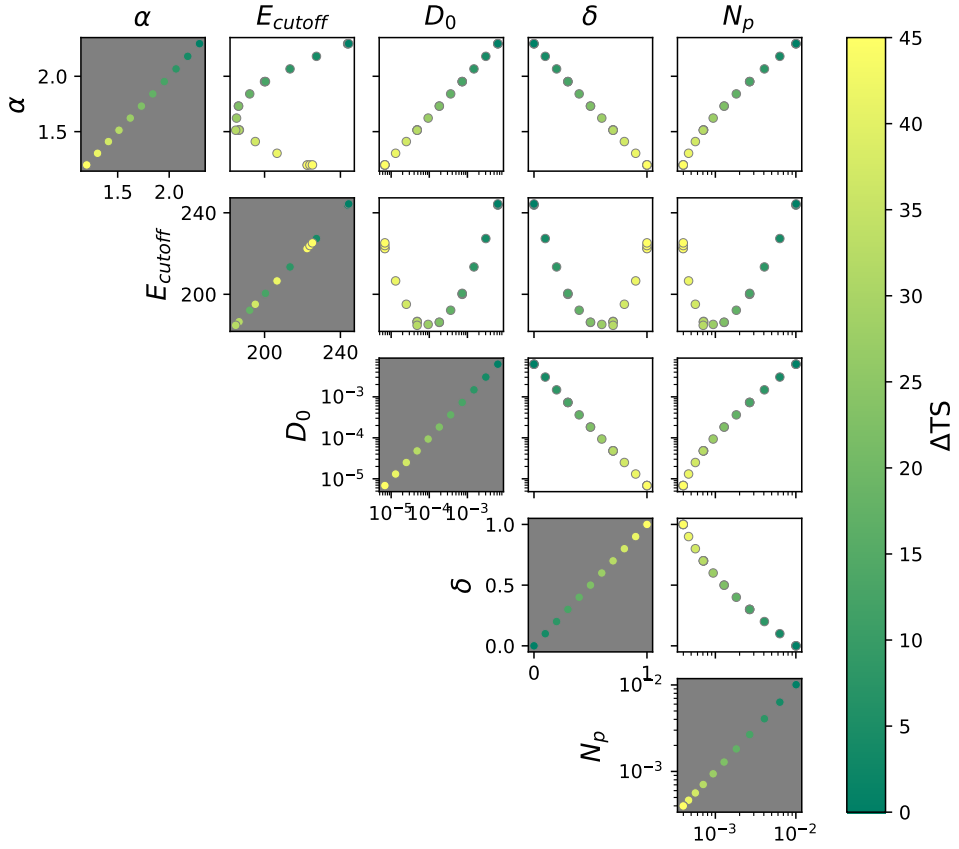

(b)

Figure 6.36 The correlation of template parameters α, E_{cutoff} [TeV], D_0 [pc^2/yr], δ and $\mathrm{N_p}[\times 1.55\mathrm{E}{+}52]$ in the impulsive injection. The diffusion time is assumed to be 10^6 years. (a) The γ-ray energy spectra with fixed δ. (b) The correlation between the different parameters. Note that δ is fixed at $\in (0...1)$ in the fitting, which results in the corresponding ΔTS values (relative to the global minimum) as shown in the colorbar.

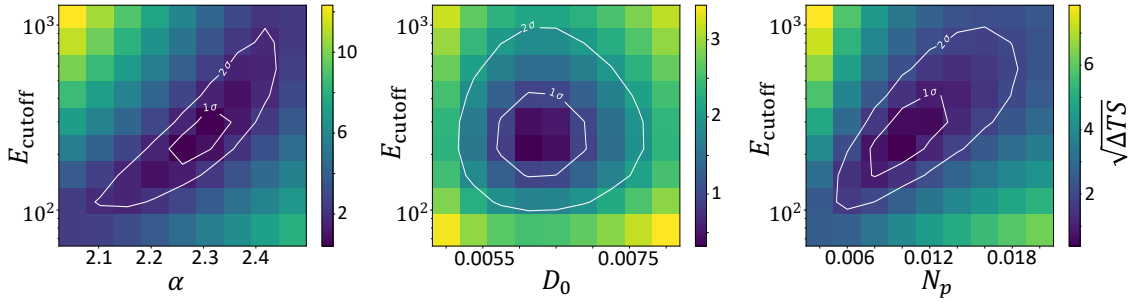

Figure 6.37 The 2D confidence contour map of the template parameters E_{cutoff} [TeV] with α, D_0 [pc^2/yr] and N$_{\mathrm{p}}$[$\times$1.55E+52]. The colorbar indicates the $\sqrt{\Delta \mathrm{TS}}$ (relative to the local minimum). The white contours denote the 1σ and 2σ confidence level. The map for δ is not shown due to it lies at the boundary set at 0.

ure 6.36 (b), where the diffusion slope δ is again fixed between $\in (0...1)$. The result clearly favours the energy-independent diffusion scenario where $\delta = 0$. By increasing the magnitude of δ, the ΔTS is increased up to 45. Yet it is still unclear whether the CR diffusion is truly energy-independent due to the ΔTS value being small when comparing it to for instance $\delta = 0.1$, which is $\Delta \mathrm{TS} < 4$. The analysis is therefore not sensitive to provide information on the energy-dependency of the diffusion. Yet a clear indication of the disfavour of the larger δ value is shown, for instance $\delta > 0.6$ will worsen the result by 5σ.

ΔTS	N$_{\mathrm{p}}$[$\times$1.55E+48]	α	D_0 [$\times$ 1E-4 pc^2/yr]	δ	E_{cutoff} [TeV]
0	**99.88±17.67**	**2.29±0.04**	**62.64±8.40**	**0±0.0001**	**242.60±85.15**
3.9	63.01±19.06	2.18±0.08	30.35±3.64	0.1	226.83±110.44
8.1	40.66±15.76	2.07±0.08	14.82±2.19	0.2	213.43±79.10
12.8	26.63±6.79	1.95±0.07	7.29±0.90	0.3	199.97±79.40
17.5	18.21±8.44	1.84±0.09	3.63±0.65	0.4	192.17±80.72
22.4	12.87±6.69	1.73±0.11	1.83±0.36	0.5	186.20±86.78
27.3	9.39±3.23	1.62±0.09	0.93±0.14	0.6	185.22±102.04
32.2	7.11±2.70	1.51±0.11	0.48±0.08	0.7	186.35±117.49
37.0	5.64±2.96	1.41±0.13	0.25±0.06	0.8	195.11±144.13
41.5	4.65±2.30	1.30±0.12	0.13±0.03	0.9	206.57±138.30
46.0	3.98±1.18	1.20±0.07	0.07±0.01	1.0	222.61±38.03

Table 6.4 The table of the best-fit parameters for building the impulsive injection template for fixed $\delta \in (0...1)$. A diffusion time of 10^6 years is assumed. The bold parameters are chosen for the further analysis.

The summary table of the best-fit parameters at $\delta \in (0...1)$ is presented in Table 6.4. It should also be noticed that D_0 is in general much smaller than the case for continuous injection when the same diffusion time of 10^6 years is considered. This essentially indicates

that the diffusion radius r_{diff} is smaller than the size of the CMZ region, i.e. $r_{\text{diff,min}} \approx 112$ pc and the size of the CMZ is ≈ 250 pc from the Galactic Centre. This means not all the CR particles are able to reach the edge of the CMZ yet. Therefore the distribution of the CR density is not expected to be a constant value, as discussed and indicated in Section 5.3. Furthermore, the total number of injected CRs is 1.6×10^{50}, which is corresponding to the total injected energy of 9.6×10^{49} erg. The injected energy in the impulsive scenario is smaller than the continuous scenario by two order of magnitude. The decrease in the injection energy is presumably related to the presence of the additional central component. The possible responsible accelerators will be discussed in Section 6.7.

Special attention should be given to the error estimation of the template parameters, in which the derived error for E_{cutoff} is relatively high. This can be related to the fact that CRs are accumulated at the inner part of the CMZ due to the small diffusion coefficient, which implies a change on this parameter will lead to a smaller change in the total likelihood as compared with the continuous injection scenario where most CRs pass the CMZ edge. In this case, the error estimation gives a higher value.

Since the energy-independent diffusion scenario gives the best-fit result, the highlighted parameters in Table 6.4 are used in the following detailed analysis. The corresponding 2D confidence contour map of the best-fit parameters can be found in Figure 6.37. Note that the contour map for δ is not given due to this value lies at the boundary, which is set as 0. The likelihood scan of the proton cutoff energy can be seen in Figure 6.38. The lower and upper limit of the E_{cutoff} is approximated to be 93 TeV and 1.05 PeV at the 95 % confidence level respectively.

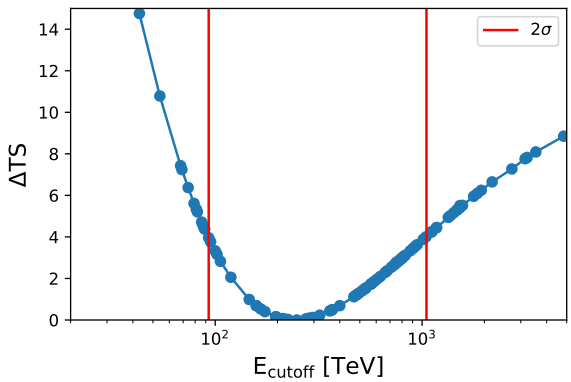

Figure 6.38 The likelihood scan of the proton cutoff energy. The red lines represent the 2σ confidence at $\approx 93 - 1050$ TeV.

6.4.3 Spatial and Spectral Results

After the determination of the best-fit template parameters, the detailed spatial and spectral results will be presented in the following. An additional Gaussian central component is included in this analysis. The summary of the fitted parameters is listed in Appendix A.

Spatial Results: Li & Ma significance and spatial profiles

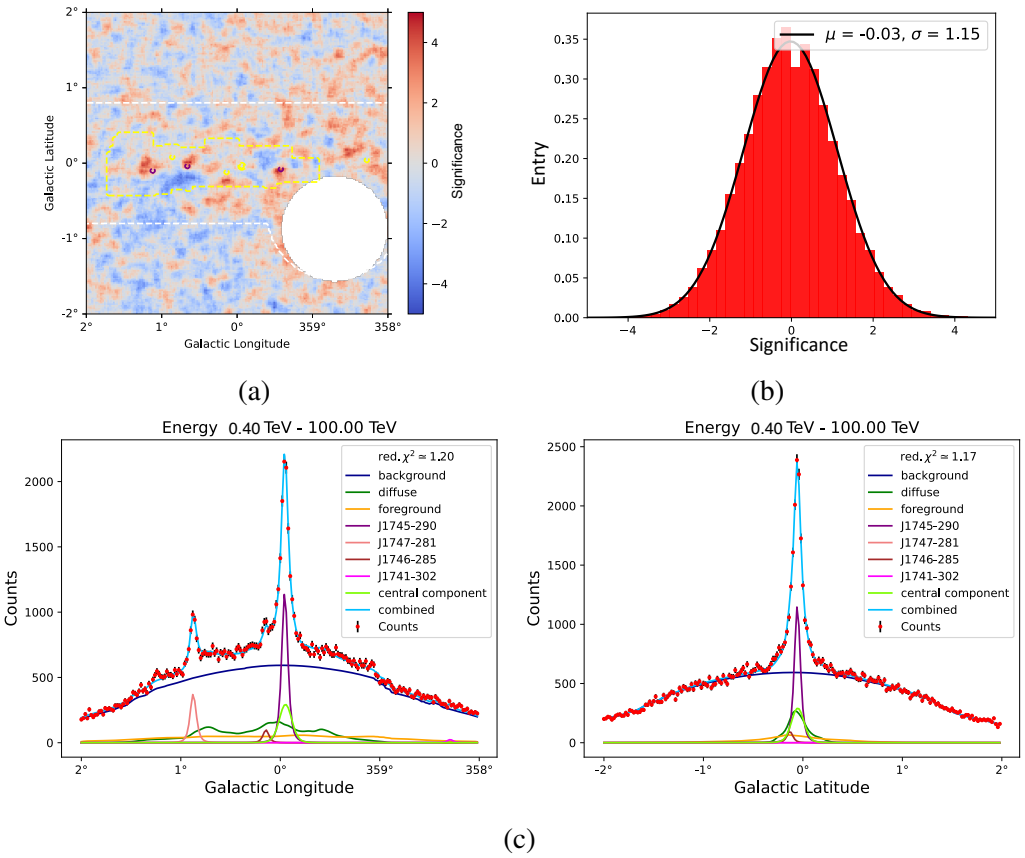

Figure 6.39 The spatial result in the overall energy range from 0.4 – 100 TeV. (a) The Li & Ma residual significance map correlated with a top-hat kernel of size of H.E.S.S. PSF (0.077°). The colorbar indicates the significance. (b) Distribution of significances from (a). (c) The Galactic longitudinal and latitudinal counts profile.

The spatial result from energies between 0.4 – 100 TeV can be seen in Figure 6.39. The Li & Ma significance map has a general improvement, compared to the result using simply a continuous injection template. The residual around HESS J1745-290 is typically gone when the additional central component is added to a similar position. A slight improvement on the standard deviation in the Li & Ma significance distribution by 0.01 is noticed. The Galactic longitudinal and latitudinal counts profiles derived using the method mentioned

in Section 6.3.3 are also shown. The reduced chi-squared value in the longitudinal counts profile shows an improvement where the value reduces from 1.34 to 1.2. The latitudinal counts profile is, however, slightly worsening from 1.1 to 1.17.

The results in the sub-energy range of 0.4 – 1 TeV, 1 – 10 TeV and 10 – 100 TeV can be found in Figure 6.41. The significance distribution at sub-energy ranges is also improved as compared with solely using a continuous injection template. Several residuals as found in the previous analysis can also be seen, for instance, the noticeable residual from Sgr D and B in the energy range of 0.4 – 1 TeV and the residual below Sgr C and on the right side of Sgr B, and the top right quarter of the map. Moreover, improvements are noticed in the longitudinal counts profile, yet the latitudinal counts profile is again slightly worsened.

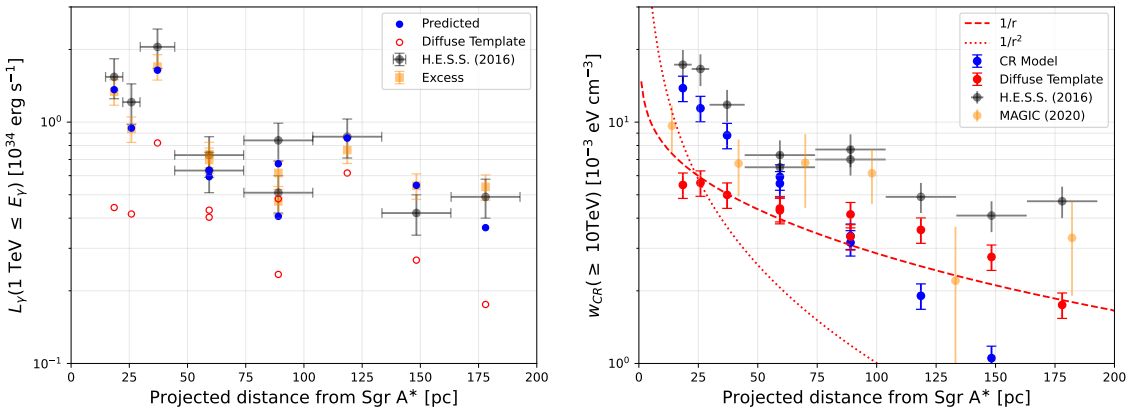

(a) (b)

Figure 6.40 (a) The γ-ray luminosity profile. The yellow and blue points denote the excess (data minus background) and predicted (from all FoV models) counts of this work. The red circles indicate the contribution from the diffuse emission template among the predicted counts. (b) The CR energy density profiles in the projected distance from Sgr A*. The red dashed lines in (b) indicate the 1/r and 1/r^2 fit performed to the calculated CR energy density from the diffuse emission template (red points, using Equation 6.3). The blue circles denote the CR distribution for building the template.

A comparison of the γ-ray luminosity and the CR energy density profiles can be found in Figure 6.40. In the γ-ray luminosity profile, the predicted counts match better with the excess inside the rings of the pacman region, compared to the case using the continuous injection template. Yet it can be seen that the contribution from the diffuse emission is much lower in the pacman region due to the contributions from HESS J1745-290, the foreground and the additional central component. The calculated CR energy density using the method mentioned in Section 6.3.3 is shown in Figure 6.40 (b). Since the diffused CRs follow a Gaussian distribution in the non-steady impulsive injection scenario, the emitted γ-rays,

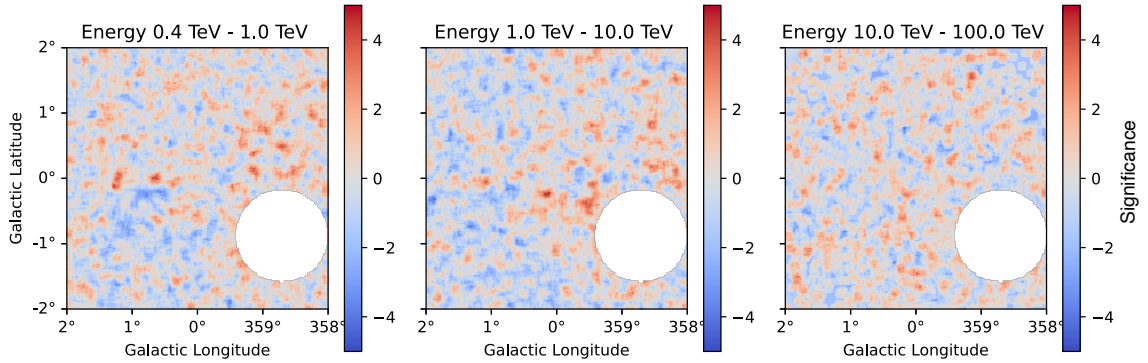

(a)

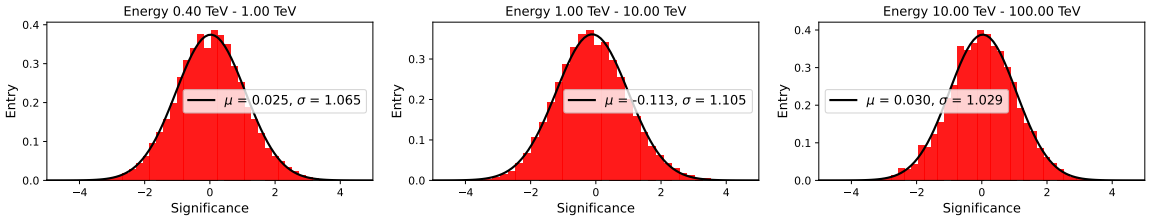

(b)

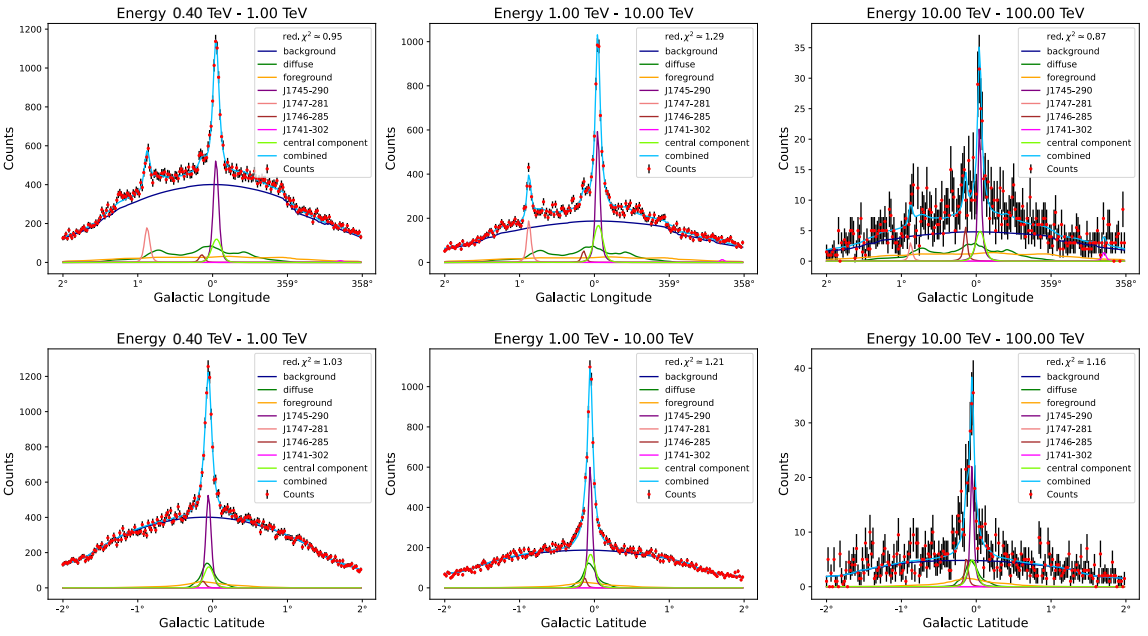

(c)

Figure 6.41 (a) The spatial result in the sub-energy range from 0.4 – 1 TeV, 1 – 10 TeV and 10 – 100 TeV. (a) The Li & Ma residual significance map correlated with a top-hat kernel of size of H.E.S.S. PSF (0.077°). The colorbar indicates the significance. (b) Distribution of significances from (a). (c) The Galactic longitudinal and latitudinal counts profile.

unlike the case where a continuous steady state can be reached, no longer follows the 1/r feature. The CR energy density from the template, which considered the energy-dependent proton-γ conversion and the gas distribution along the line-of-sight, shows a Gaussian feature. It is also clear that the CR energy density in the ring regions is higher than the calculation, which is opposite to the case of using the continuous diffusion model. This is mainly related to the accumulation of the CRs at the inner part of the CMZ, and the diffusion model has considered the line-of-sight distribution of the gas molecules. This might also related to no proton energy losses are being assumed in the CR propagation model.

Based on the result from Figure 6.40, it can be concluded that the γ-ray luminosity does show a decreasing feature when moving outward from the Galactic Centre. Yet CR particles are not following a 1/r distribution in this case. The deviation from the observed luminosity is compensated by contributions from the additional central component, HESS J1745-290, and the foreground component.

Spectral Results

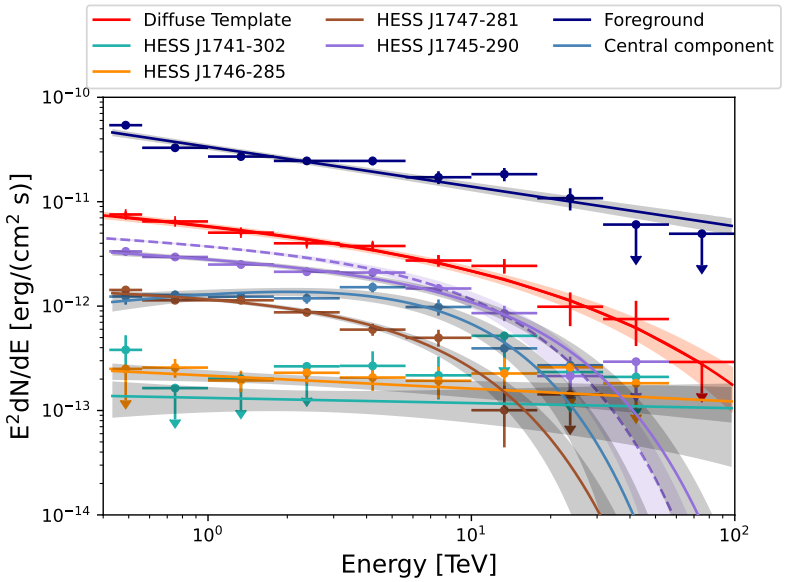

Figure 6.42 The energy spectra of all fitted sources and component when the impulsive CR injection is considered for the diffuse emission template. The solid lines represent the results of this work, the dashed lines represent the results shown in HGPS (2018). The colorbands indicate the 1σ statistical error.

The energy spectra of all fitted sources and components can be found in Figure 6.45. The models again match with the estimated fluxpoints, except for a few discrepancies found in the

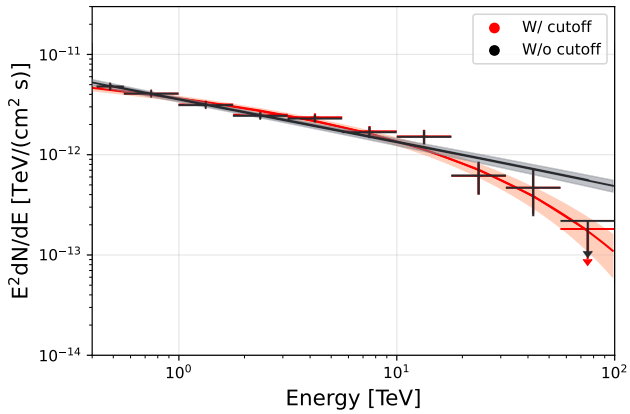

Figure 6.43 The diffuse emission spectrum with and without the proton energy cutoff. The data points indicate the estimated fluxpoints. The colorbands indicate the 1σ statistical error.

foreground model. This could be related to the background systematics. The performance of the diffusion model at the sub-region along the Galactic plane can be found in Figure 6.44. In general, the model matches with the data, though only the upper limit is able to be derived at regions with lower diffuse emission statistics, i.e. the regions away from the Galactic Centre. Yet a general energy cutoff feature can still be observed in these spectra.

The estimated fluxpoints for the impulsive diffusion spectrum, with and without the proton energy cutoff, can be found in Figure 6.43. Both spectra are well described at energy < 10 TeV, yet an energy cutoff fits better in the final three energy bins. The cutoff scenario is 3.5σ better than the no-cutoff scenario. It is also 2σ better than the scenario with an energy cutoff at > 1 PeV. Yet a small interference from the background systematics can change the conclusion of this work, which is whether a PeVatron exists in the Galactic Centre. The effect of the estimated background uncertainty will later be presented in Section 6.6.

The spectrum is also investigated in the pacman region and the Galactic ridge region. The derivation method has been introduced in Section 6.3.3. Again a general shift of about a factor of 2 is observed in both the spectra as compared to the publications. This shift is related to the contamination from HESS J1745-290, and the contributions from the foreground component and the additional Gaussian central component. In addition, a different modelling of the diffuse emission and the foreground emission is considered in this analysis. Yet unlike the result from the previous section, the diffusion model in general coincides with the data, even in the first four energy bins of the pacman region analysis. Again a jump is observed at around 10 TeV in the Galactic ridge, this might be related to the data/background construction since a similar spike is observed in Figure 6.8 (a).

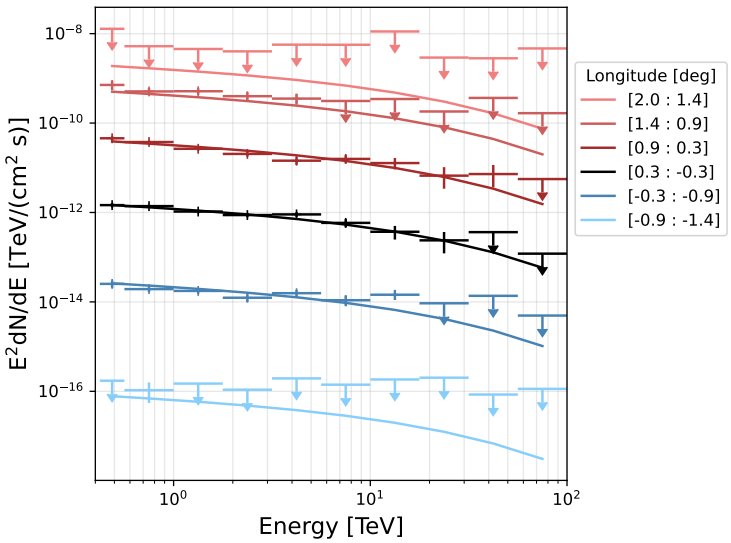

Figure 6.44 The energy spectra of the diffuse emission component in box regions along the Galactic longitude of $\pm 2^\circ$ and Galactic latitude at 0°. The spectra at $l \in (-0.3^\circ, 0.3^\circ)$ is not being scaled, while the rest are scaled for better visualisation.

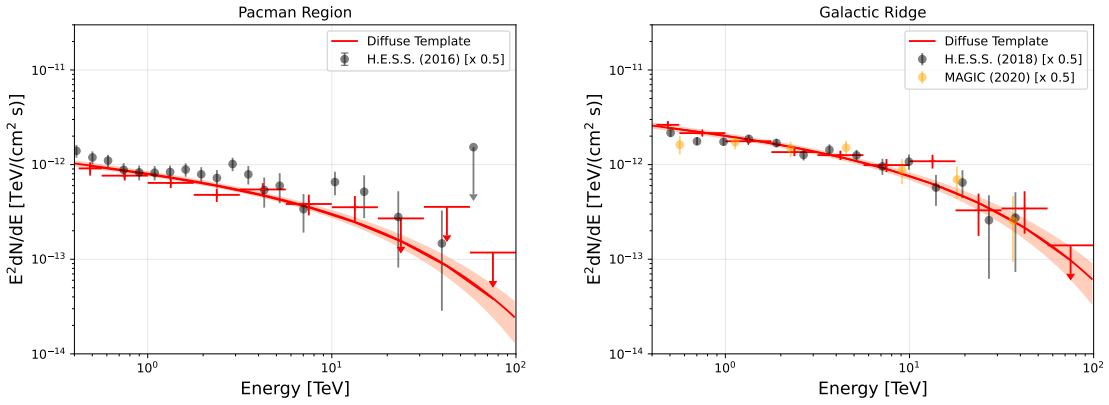

(a) (b)

Figure 6.45 The diffuse emission spectra derived from the pacman (a) and the Galactic ridge (b) region. The solid lines indicate the model, the points indicate the estimated fluxpoints. The color band indicates the error of 1σ. The reference data is also shown. A factor of 0.5 has multiplied by the reference data.

Summary

This section has presented the result using a diffuse emission template where the impulsive injection of CRs from a source in the vicinity of Sgr A*. HESS J1745-290, HESS J1746-285, HESS J1747-281, HESS J1741-302 and the foreground component have been taken into account. Furthermore, an additional Gaussian central component is modelled. A summary of fitted parameter are listed in Appendix A. It has found that:

- A clear central ring-like feature arouse when the impulsive CR injection scenario is considered.
- The ring-like feature can be eliminated by modelling an additional Gaussian central component, which is 8σ better than modelling an extended for HESS J1745-290.
- The impulsive CR injection scenario together with an additional Gaussian central component is 8σ better than the simple continuous CR injection scenario. This additional component can also explain the peaked γ-ray luminosity profile in the inner 200 pc of the Galactic region.
- The proton energy cutoff for the diffuse emission template at 243 ± 85 TeV is preferred over a simple power-law by 3.5σ and preferred over a cutoff at > 1 PeV by 2σ . It has a lower limit at 93 TeV and upper limit at 1.05 PeV in the 95% confidence level.
- The results favour the non-steady and energy-independent diffusion scenario.
- The diffuse emission spectrum in general agrees with the observed data in the CMZ, as well as the pacman region around the Galactic Centre.

Though the diffuse emission template with continuous CR injection and energy cutoff can already give a good description of the emission from the Galactic Centre, the performance of the impulsive template together with an additional Gaussian central component can further improve the result. This thesis, therefore, provides an new insight into the Galactic Centre study: the diffuse emission can be due to an impulsive injecting source rather than a continuously injecting source. The physical properties and the possible association of the additional Gaussian central component, however, needs to be determined. Before proceeding to the discussion, a list of cross-checks will be carried out using other gas tracers in the following Section 6.5 and the study of background uncertainties in Section 6.6.

6.5 Cross-Check with Alternative Gas Tracers

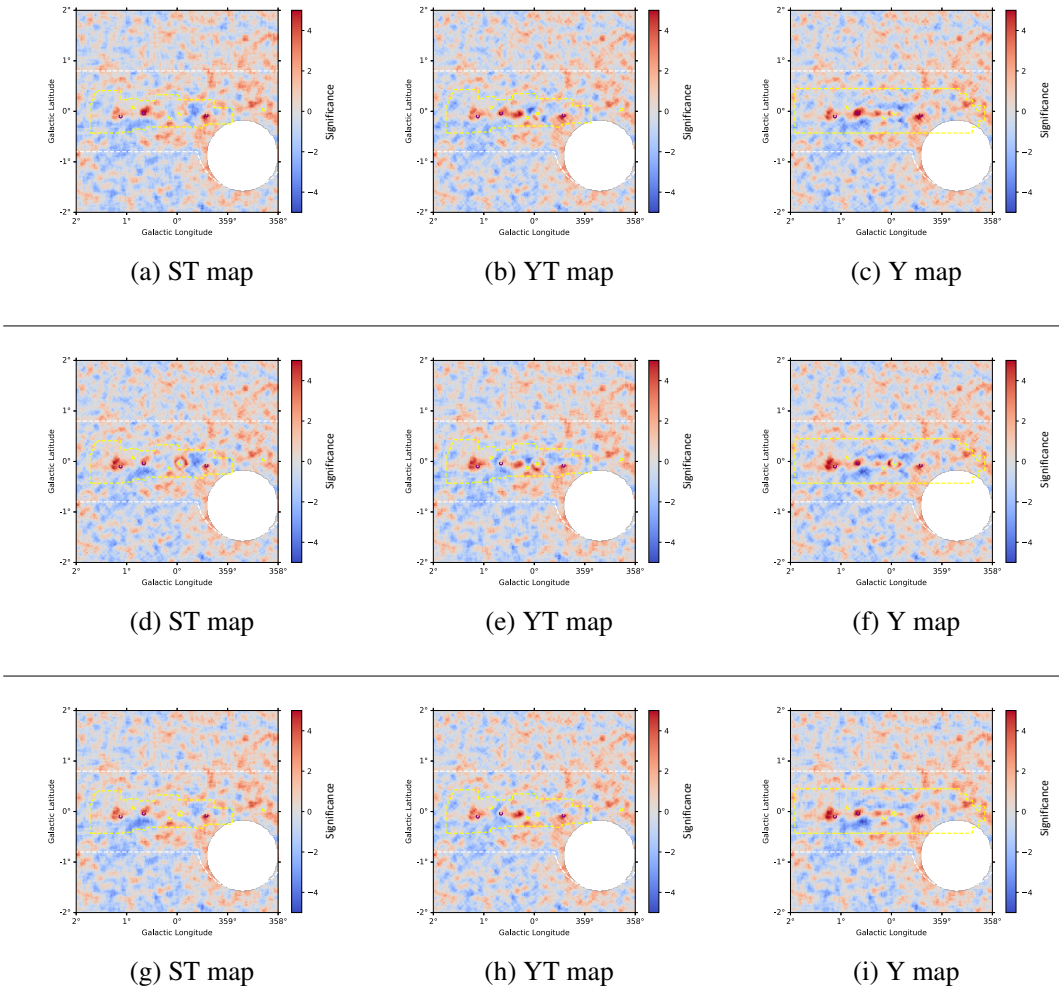

(a) ST map (b) YT map (c) Y map

(d) ST map (e) YT map (f) Y map

(g) ST map (h) YT map (i) Y map

Figure 6.46 The Li & Ma residual significance maps of the cross-checks. The ST denotes the projection of CS data from Tsuboi et. al. onto the CO/OH model from Sawada et. al. The YT denotes the projection of the CS data from Tsuboi et. al. onto the CO/OH model from Yan et. al. The Y denotes using the CO/OH data (binned in three-dimensions). Figures (a-c) are results from using the continuous injection template. Figures (d-f) are the results from using the impulsive injection template, whereas figures (g-i) further add the additional Gaussian central component.

To ensure the consistency of the results, a few findings need to be cross-checked with other gas tracer. The diffuse emission templates are compiled with the same method as the main analysis but with consideration of a different gas tracer. The gas tracer for the cross-check is the CO/OH observation from Yan et. al. (2017), which gives a three-dimensional

distribution of the gas molecules in the Galactic Centre with finer binning than Sawada et. al. (2004, used in the main analysis). Details about these two observations have been discussed in Section 5.1.2. Since the molecular distribution is available in three-dimensions, the cross-check can be done by solely using this data cube, as well as by also projecting the CS data from Tsuboi et. al. (1999, used in the main analysis) along the line-of-sight of this cube. The Li & Ma significance maps and the diffuse emission spectra by consideration of different tracers can be seen in Figures 6.46 and 6.47 respectively. The interpretations are as follow.

Ring-like Feature

As can be seen in Figure 6.46, the ring-like feature is not obvious when the continuous injection template is used. Yet, this feature with a similar extension appears in the results from all the gas tracers where the impulsive injection template is used (though some parts of the ring are missing when using the gas observation from Yan et. al.). The inclusion of the additional Gaussian central component together with the impulsive CR injection template can in any case remove the ring-like feature. This shows that the ring-like feature is likely caused by an unresolved component, rather than being an artefact of the gas tracers.

Remaining Residuals

A few residuals at a similar position are found in the significance map from all the tracers. For instance, the noticeable dense complexes at Sgr D, B and C, are believed to be due to the self-absorption effect when using the gas tracer. These residuals are especially clear when using the CO/OH data alone since the CO/OH tracer suffers from larger background contamination, and thus is less robust than the CS tracer. There are also clear residuals on the right side of Sgr B, the bottom of Sgr C and the arc source HESS J1746-285. These are commonly found in all the maps. This might essentially hint on the existence of unmodelled source(s). Besides, slightly enhanced residuals are spotted on the right corners in all the maps, which might be related to systematics connected to the background model used in the analysis.

Proton Energy Cutoff

The proton energy cutoffs are observed when using the continuous or the impulsive injection templates with the CS gas data. The same holds when using other gas tracers. The diffuse emission spectra can be seen in Figure 6.47, the proton energy cutoffs are preferred regardless of the template type. The cutoff energies are also similar among the use of different tracers.

For the case of continuous injection, the averaged proton energy cutoff is at around 129 TeV. The averaged proton energy cutoff in the case of the impulsive injection case rises to around 225 TeV. Among the three molecular maps, the ST map gives the best performance in terms of the likelihood, followed by the YT and Y map accordingly. This is essentially due to the CO/OH observation being less robust than the CS observation. Among the CO/OH models from Sawada et. al. and Yan et. al., the former is corporate better with the CS data in this analysis. Note also that the amplitude of these diffuse emission spectra are not coincide, which is related to the discrepancy in the gas distribution.

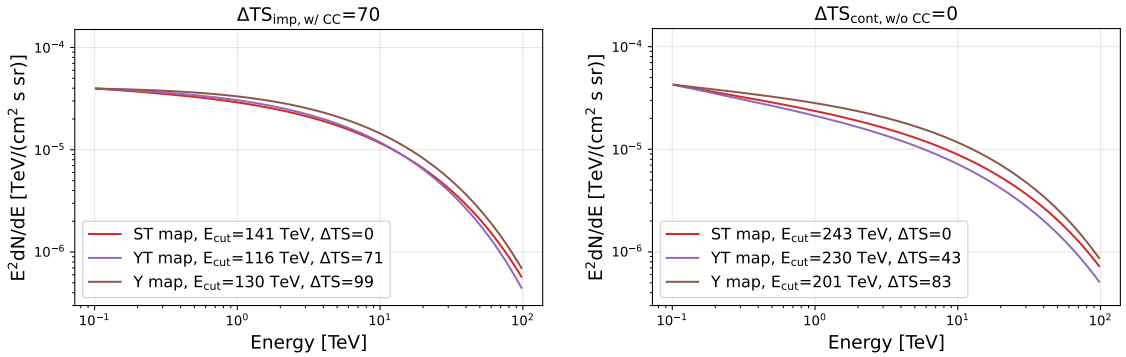

(a) (b)

Figure 6.47 The diffuse emission spectra derived by using different gas tracers and different CR injection scenarios. Scaled with respect to the spectrum from ST map. (a) The continuous injection scenario. (b) The impulsive injection scenario with an additional central component. The corresponding proton cutoff energy and the ΔTS value (relative to the result using ST map) of the individual cases are shown in the figures.

Comparison of Other Diffuse Template Parameters

The template parameters used for different tracers can be found in Table 6.5. A few constraints defined in the previous sections are still valid, for instance, $-2 \leq \ln(N_p) - \ln(D_0) \leq 2.5$ for the continuous injection and $\delta \approx 0$ for the impulsive injection. Yet for the continuous injection case, the lower limit of the constraint $\alpha + \delta$ extends from 2.13 to 2.06 when the gas tracer from Yan et. al. is considered. This is however within the error range.

There is also a noticeable increase of the D_0 in the case where the CS data is projected onto the CO/OH model from Yan et. al. This increase is presumably due to the different gas distribution along the line-of-sight (Section 5.1.2). The diffusion radius is nevertheless still smaller than the size of the CMZ, same as the result of using the projection model from Sawada et. al.

	Contcut					
Map	ΔTS	$N_p[\times 1.55E{+}52]$	α	D_0 [pc^2/yr]	δ	E_{cutoff} [TeV]
ST	0	0.40±0.09	1.77±0.04	0.64±0.09	0.37±0.02	142.82±31.09
YT	71	11303.81±1887.67	1.31±0.04	9079.83±2215.85	0.79±0.03	116.29±24.94
Y	99	3.36±0.78	1.42±0.04	20.00±2.98	0.64±0.02	130.45±26.54
	Impcut					
Map	ΔTS	$N_p[\times 1.55E{+}48]$	α	D_0 [$\times$1E-4 pc^2/yr]	δ	E_{cutoff} [TeV]
ST	0	99.88±17.67	2.29±0.04	62.64±8.40	0±0.0001	242.60±85.15
YT	43	126.07±48.41	2.34±0.08	118.83±26.23	0±0.0000	230.47±125.54
Y	83	8.22±3.04	2.21±0.07	56.28±7.72	0±0.0000	202.44±64.60

Table 6.5 The table of the best-fit parameters in building the continuous and impulsive injection template, using the ST, YT and Y map. The δ values in the impulsive injection scenarios lie at the boundary set as 0.

In conclusion, the main results of this thesis are consistent regardless of the type of the gas data and gas model. Similar residuals are found in any case. The ring-like feature remains when the impulsive diffusion is considered and is eliminated when an additional Gaussian central component is included. The magnitudes of the proton cutoff energy are within uncertainties, which are roughly 130 TeV and 225 TeV for the case involving continuous and impulsive CR injection respectively.

6.6 Background Systematics

In the last part of the analysis, the background systematics are included in the 3D likelihood fit, using the methodology mentioned in Section 4.2.4. The background uncertainties are quantified via a preliminary estimation method as mentioned in Section 6.2.2. The inclusion of the background systematics in the fitting is crucial for checking the necessity of the proton energy cutoff, given the statistics are low and the systematics are high at high energies. This is also the first time applying such a tool to the 3D analysis of a complicated region with H.E.S.S.

The results from the continuous and impulsive injection scenarios are shown in the following. The energy-dependent background uncertainties are used in this section. The results using the energy-independent background uncertainty can be found in Appendix A[7]. Note that due to a computational time limit, the nuisance matrix is down-sampled by 50 in this analysis. The nuisance cube has a spatial binning of $1^\circ \times 1^\circ$.

[7] An over-fitting issue is observed, which might be related to the background uncertainty being overestimated at the low energies and the spatial binning of the nuisance cube is too coarse.

Continuous Injection

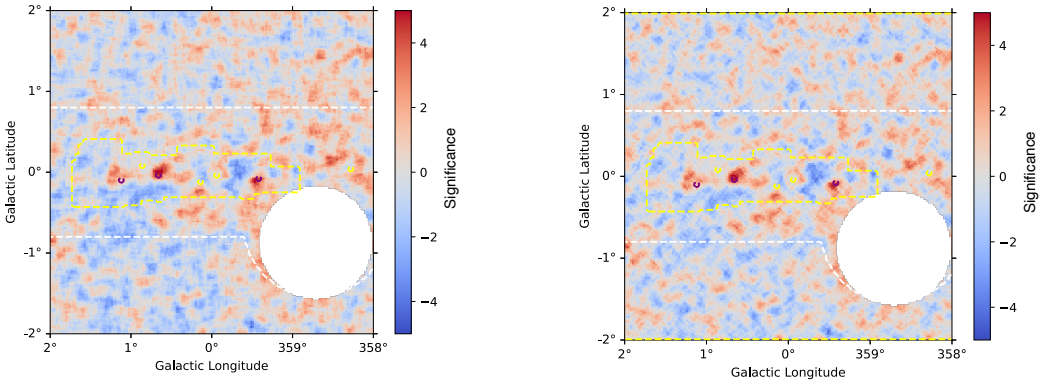

(a) Before (b) After

Figure 6.48 The Li & Ma residual significance maps before (a) and after (b) the inclusion of the background systematics, correlated with a top-hat kernel of size 0.077°. The colorbar indicates the significance. An improvement of $\Delta TS \approx 191$ is observed in (b).

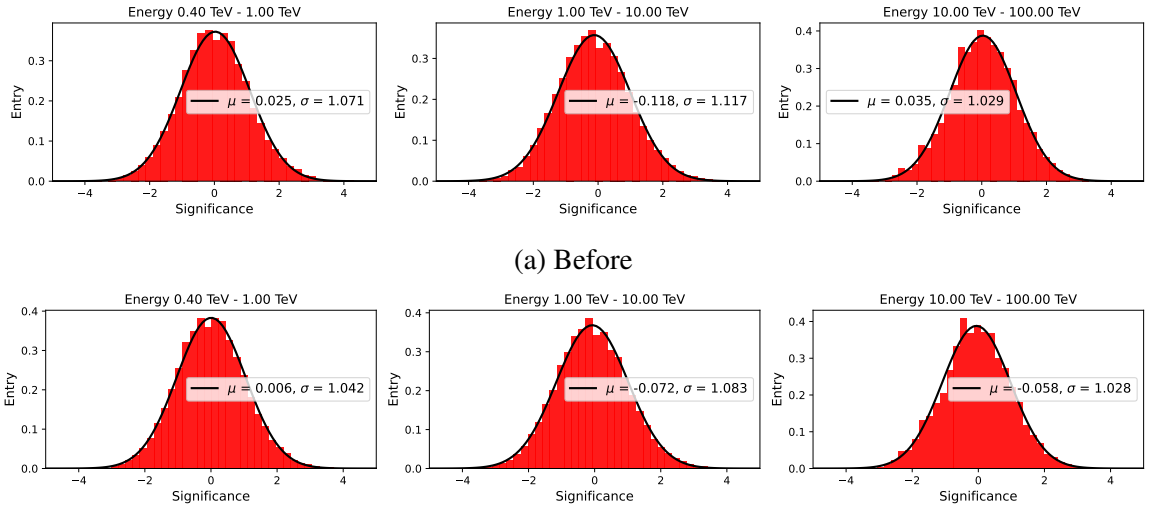

(a) Before

(b) After

Figure 6.49 The distributions of Figure 6.48, before (a) and after (b) the inclusion of the background systematics in the energy range of 0.4 – 1 TeV, 1 – 10 TeV and 10 – 100 TeV. The mean and the standard deviation of the distribution are shown in the figures.

The Li & Ma significance maps show a slight improvement after the inclusion of the background systematics, as indicated in Figure 6.48. The emissions at the top right area are especially improved. The ΔTS is improved by 191 when adopting energy-dependent background uncertainties. These improvements can also be seen in the significance distribution at

all sub-energy ranges, as indicated in Figure 6.49. A general improvement in the means and standard deviations is noticed, which are getting closer to 0 and 1 respectively. Yet this is not the case for the energy range of 10 – 100 TeV, where the means get slightly increased. This could be related to the low statistics at very high energies, where the nuisance fit reaches its performance limits. Yet improvements in standard deviations are still observed.

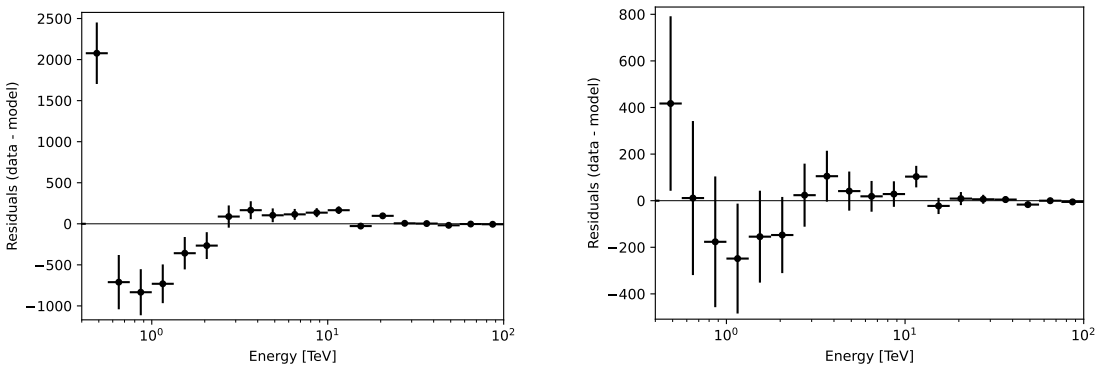

(a) Before (b) After

Figure 6.50 The model and data differences in terms of energy. (a) Before the nuisance fit. (b) After inclusion of the energy-dependent uncertainty. The 1σ statistical errors are shown.

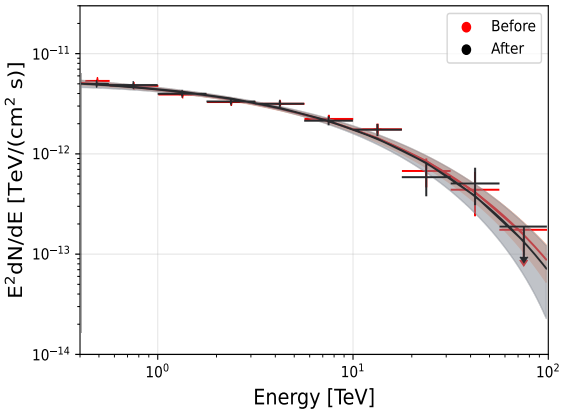

Figure 6.51 The diffuse emission spectra before (red line) and after (black line) applying the nuisance fit. The continuous injection scenario is considered. The 1σ statistical errors are shown.

The model and data differences in terms of energy can be seen in Figure 6.50, where the statistical errors are also shown. Large discrepancies are observed at low energies before the application of the nuisance fit, especially at the lowest energy of 0.4 TeV. This might be related to large statistical fluctuations in the construction of the FoV background model.

The discrepancies at the lowest energies are improved by an order of magnitude when the background uncertainties are taken into account. Improvements can also be seen in the rest of the energy range.

A comparison of the diffuse emission spectra can be found in Figure 6.51. A decreased scatter in fluxpoints is observed and a larger errorband is presented in the diffuse emission model. An obvious improvement in the first energy bin is seen, which is believed to be related to Figure 6.50 (a) where the largest deviation of model and data was spotted. The proton cutoff energy is decreased within its uncertainty from 143±31 TeV to 122±39 TeV.

Impulsive Injection (with an Additional Central Component)

The Li & Ma significance maps again show a slight improvement as indicated in Figure 6.52. The emissions at the top right area are also damped by the nuisance fit. With the inclusion of the energy-dependent background uncertainty, the ΔTS improves by 186. The magnitudes of the improvement is similar to the case where continuous injection is considered. The significance distribution in sub-energy ranges also shows an improvement as can be seen in Figure 6.49. General improvements in the means and standard deviations are observed, which are getting closer to 0 and 1 respectively. The means are, however, further away from 0 in the energy range of $10 - 100$ TeV. This is related to the same reasons as stated for the previous scenario, namely the low statistics at high energies.

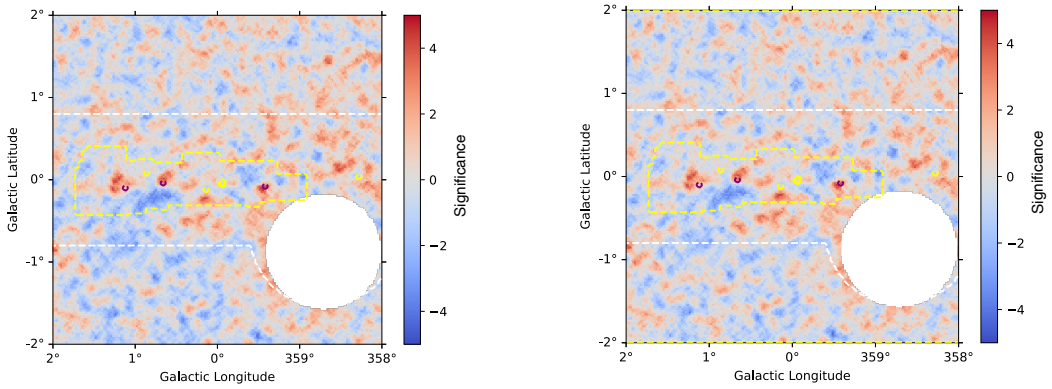

(a) Before (b) After

Figure 6.52 The Li & Ma significance maps before (a) and after (b) the inclusion of the energy- dependent background uncertainty, correlated with a top-hat kernel of size 0.077°. The colorbar indicates the significance. An improvement of $\Delta TS \approx 186$ is observed for (b).

The model and data differences in terms of energy can be seen in Figure 6.54, the statistical errors are also shown. As discussed, large discrepancies are observed at low

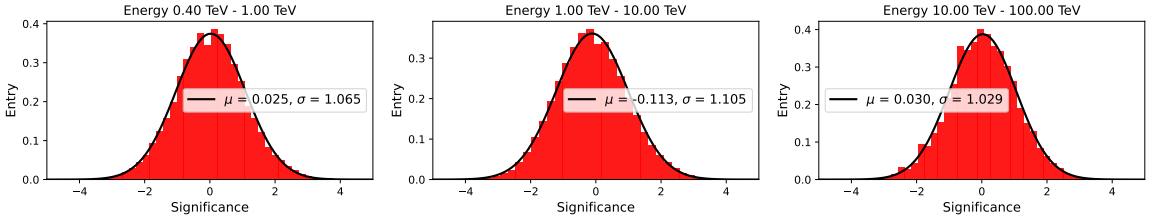

(a) Before

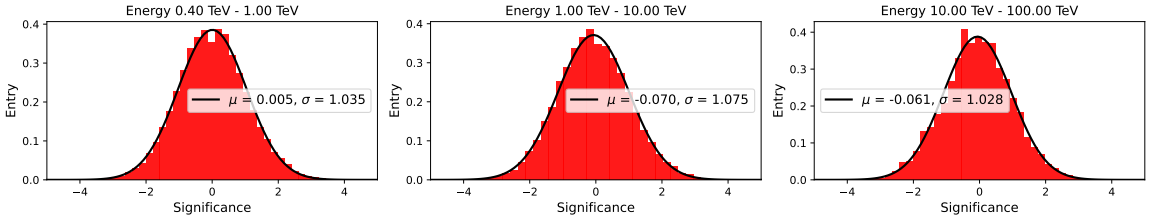

(b) After

Figure 6.53 The distribution of Figure 6.52, before (a) and after (b) the inclusion of the background systematics in the energy range of 0.4 – 1 TeV, 1 – 10 TeV and 10 – 100 TeV. The mean and the standard deviation of the distribution are shown in the figures.

energies before the nuisance fit. This is mainly due to the large background fluctuation. Improvements at low energies can be seen when the background uncertainties are taken into account. The same holds for high energies.

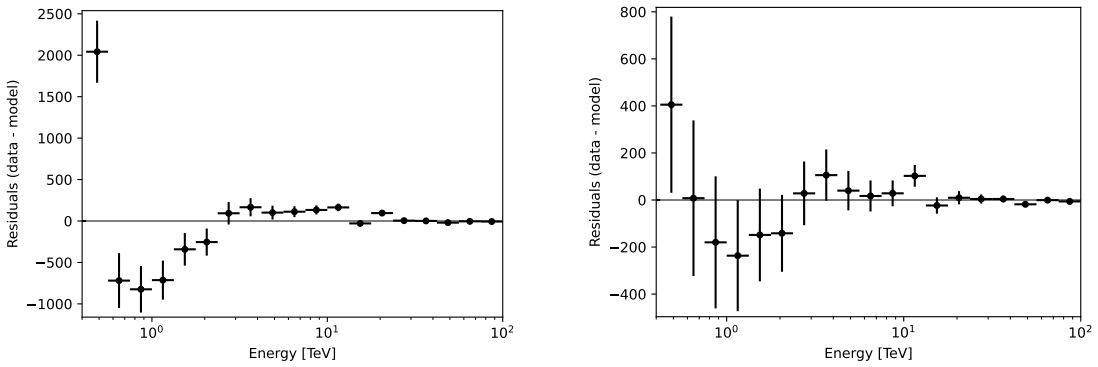

(a) Before (b) After

Figure 6.54 The model and data differences in terms of energy. (a) Before the nuisance fit. (b) After inclusion of the energy-dependent uncertainty. The 1σ statistical errors are shown.

A comparison of the diffuse emission spectra can be found in Figure 6.55. A decreased scatter in fluxpoints is again observed. The model now matches better with the data at low energies. The proton energy cutoff is decreased within its uncertainty from 243±85 TeV to

215±80 TeV. A slightly larger errorbar can be seen, especailly at low energies, due to the increased error magnitude from other template parameters.

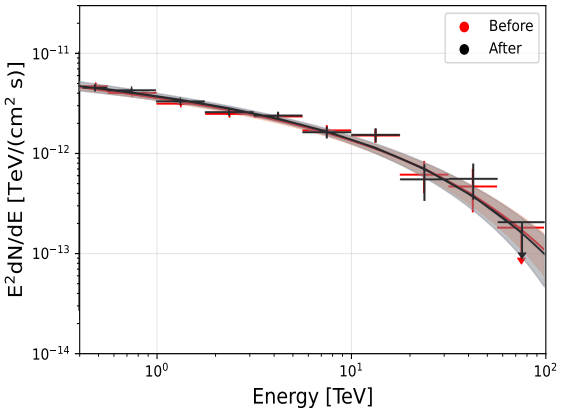

Figure 6.55 The diffuse emission spectra before (red line) and after (black line) the nuisance fit. The impulsive injection scenario is considered. The 1σ statistical errors are shown.

The summary of fitted FoV parameters is listed in Appendix A. In conclusion, both the morphological and spectral results are improved by the application of the nuisance parameter fit. From the morphological perspective, the improvement for the top right quarter of the map is noticeable. The reduced scatter of the fluxpoints are especially noticeable at low energies, where the background fluctuation is higher. The proton cutoff energies remain unchanged within uncertainties after the nuisance parameter fit. This indicates the necessity of the proton energy cutoff in the CR injection spectrum, thus the diffuse emission spectrum. Though background uncertainties cannot be precisely estimated, this section shows that the nuisance fit is an applicable and promising tool for taking background systematics into account for 3D likelihood fits. Despite the disadvantage of being sensitive to weak signals, yet this tool is still suitable in complex extended regions like the Galactic Centre.

6.7 Discussion

In this chapter, a comprehensive morphological and spectral studies of the diffuse γ-ray emission in the CMZ, by assuming a hadronic injecting source located close to Sgr A*, has been carried out. Both the continuous and impulsive injection scenarios have been studied.

Diffuse Emission Analysis	γ-ray index	γ-ray E_{cut} [TeV]	Proton index	Proton E_{cut} [TeV]
H.E.S.S. (2006)	2.29±0.27	None	–	–
H.E.S.S. (2016)	2.32±0.16	None	2.4	–
H.E.S.S. (2018)	2.28±0.23	None	–	–
VERITAS (2018)	2.19±0.2	None	–	–
MAGIC (2018)	$1.98^{+0.42}_{-0.36}$	$17.5^{+63.8}_{-11.45}$	–	–
This Work (Cont, δ=0.36)	($\approx$ 2.14)	($\approx$ 14.3)	1.77±0.04	143±31
This Work (Imp, δ=0)	($\approx$ 2.29)	($\approx$ 24.3)	2.29±0.04	243±85
This Work (Cont, δ=0.08)	($\approx$ 2.14)	($\approx$ 14.4)	2.06±0.05	144±33
This Work (Imp, δ=0.1)	($\approx$ 2.21)	($\approx$ 22.7)	2.18±0.08	227±110

Table 6.6 Summary of diffuse emission parameters from various studies and this study. The brackets indicate the estimated values. The last two rows indicate the results by consider other values for δ.

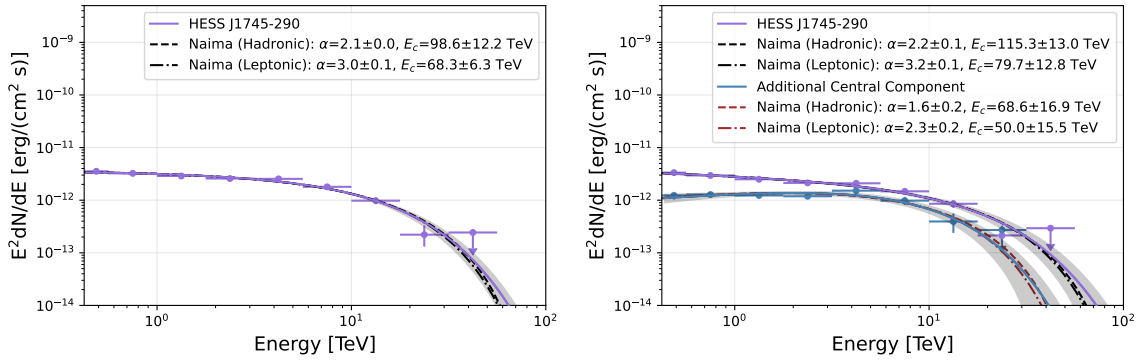

(a) Continuous injection

(b) Impulsive injection

Figure 6.56 The energy spectra of HESS J1745-290 (purple line) and the additional central component (blue line) derived from Naima [117], in the analysis of continuous (a) and impulsive (b) CR injection scenario. The Naima fitted parameters of the particle acceleration spectrum of HESS J1745-290 (black line) and the additional central component (red line) are shown in the figures. A simple pion decay (dashed line) and inverse Compton scattering (dashed dotted line) are modelled in this section, without consideration of photon absorption.

Proton Energy Cutoff

It is clear that the results of this thesis have some discrepancies as compared to previous publications. The γ-ray spectral index derived from this work (at ≈ 2.2) is within the range of $\approx 2-2.3$ defined by various experiments [54, 56, 57, 116, 24], as indicated in Table 6.6. The strongest disagreement, however, comes from the existence of the CR energy cutoff. The cutoff energy is found at 143±31 TeV and 243±85 TeV in the continuous and the impulsive injection scenarios respectively. Tthe difference in magnitude mainly comes from the existence of the additional central component. Each of these scenarios

imposes a lower limit on the cutoff at around 72 TeV and 93 TeV at the 95 % confidence level. Both the cross-check with the different gas tracer and the inclusion of the background systematics confirm the existence of the CR energy cutoff at the same order of magnitude. This result essentially opposes the existence of a PeVatron at the Galactic Centre, which was postulated by H.E.S.S. [56, 57] and the study using VERITAS data [24] due to the peaked CR profile along the Galactic ridge, and a simple power-law was well-fit to their diffuse emission spectrum. These studies propose a 95% lower limit on the cutoff energy at 400 TeV (H.E.S.S.) and 80 TeV (VERITAS) respectively. A recent study from MAGIC [116] proposed the existence of the proton energy cutoff at $\approx 0.1 - 1$ PeV at the 68 % confidence range, yet giving a marginal compatibility with the PeVatron hypothesis [116].

This study, on the other hand, proposes a significance of 5.7σ and 3.5σ for objecting the cases where no CR energy cutoff exists in the continuous and the impulsive injection scenarios respectively. The significance for cases where > 1 PeV cutoff exists is rejected at 3.6σ and 2σ respectively. However, the ultimate conclusion of the existence of a PeVatron in the Galactic Centre is vastly more sensitive at high energies ($E_\gamma \geq 10$ TeV), where the counts statistics are still limited and the background uncertainties are high. Moreover, the measurement is especially sensitive to the gas distribution, in particular regarding the line-of-sight distribution. Though cross-check with the CO/OH data and line-of-sight model have been made, both resolutions of the line-of-sight model from Sawada et. al. (2004) and Yan et. al. (2017) are still poor. It is therefore encouraged to update this study with higher statistics in the measurements at high energies (e.g. obtain more H.E.S.S. data and include data from future IACTs, such as CTA and SWGO) and with a improved radio survey of the Galactic Centre.

Continuous or Impulsive Injection?

Another disagreement points to the interpretation of the CR profile. Most of studies had assumed a 1/r CR profile, where r is the projected longitudinal distance from Sgr A*. This can provide a good match to the observation of the γ-ray luminosity around the Galactic Centre. Indeed this is well motivated in the scenario where particles undergo the steady-state diffusion from a continuously injecting source. Yet as inspired by the empirical model in H.E.S.S. (2018), the impulsively injecting source can also explain the γ-ray luminosity trend if an additional central component is included. An improvement of 8.4σ is observed in comparison with the simple continuous injection case. The additional component is, however, unlikely to be related to HESS J1745-290. This is not only due to the discrepancy in the spectral indices (≈ 1.7 for the additional component and ≈ 2.15 for HESS J1745-290), but also due to the fact that adding the additional component is preferred by 7.8σ over adding

an extension to HESS J1745-290. The question now goes to the identity of the additional Gaussian central component, as well as the source that is responsible for the CR injection.

CR Proton Injection Site

The proton indices after the diffusion are ≈ 2.14 and 2.29 (before the diffusion are ≈ 1.77 and 2.29) for the continuous and impulsive injection scenarios. Assuming a similar γ-ray spectral index based on the studies in Section 5.3, these numbers are close to the spectral index of HESS J1745-290, which is ranging from $\approx 2.03-2.13$ in this analysis. This hints at a possible linkage between HESS J1745-290 and the diffuse emission in the CMZ. A rough estimation of the proton index of this source is $\approx 2.1-2.2$ as shown in Figure 6.56 using Naima [117] (for modelling the non-thermal radiation), which further supports the statement. Though the identity of HESS J1745-290 is not confirmed, many associations are proposed as mentioned in Sections 2.3.1 and 6.1, including SMBH Sgr A*, SNR Sgr A East, PWN G359.95-0.04, a large population of millisecond pulsars, and even dark matter (with mass larger than 10 TeV) [122, 49]. In particular Sgr A* and Sgr A East are the popular choices in the assumption of a hadronic γ-ray emission origin. For instance, an average injection rate of 10^{39} erg/s for $E_p > 10$ TeV might able to supported by Sgr A* over the last 10^{6-7} years [56]. This is within the margin of the acceleration power of 10^{38} erg/s for 10^6 years that is necessary in the continuous injection case, as indicated in Section 6.3.2. Moreover, a total energy of 10^{51} erg is expected to be released by Sgr A East 5×10^4 years ago [48]. 10 % of this energy would be enough to cover the necessary energy for the impulsive injection scenario, which is $\approx 10^{50}$ erg as indicated in Section 6.4.2. At the same time, a small diffusion radius of ≈ 112 pc can still be sustained. Even Sgr A East is disfavoured to be the associate of HESS J1745-290, Sgr A* can also be the impulsively injecting source due to a sudden increase in injection from tidal disruptions of nearby stars [122].

Additional Central Component

In the impulsive injection scenario, the linkage of PWN G359.95-0.04 to the additional central component is plausible. PWN G359.95-0.04 was regarded as a highly disfavoured site to account for the enhanced CR profile close to the Galactic Centre in the studies from H.E.S.S. [57] (due to the non-existence of the energy cutoff in the central 0.45° region from the study in [56]). Yet for the PWN, the high infrared and optical photon field energy densities can produce the cutoff effect on its spectrum due to the Klein-Nishina suppression at the TeV regime [57]. The estimation of the large-scale magnetic field strength of $\leq 50\ \mu G$ also indicates the rapid cooling of the electrons via synchrotron radiation at TeV, resulting in compact γ-ray emission [122]. These can therefore explain the small extension of the

additional central component, as well as its energy cutoff at $\approx$ 6.7 TeV, apart from the absorption and attenuation of photons from the pair production in the ambient infrared radiation field (as also experienced by HESS J1745-290) [56]. Moreover, the γ-ray spectrum of this additional component is relatively hard ($\approx$ 1.7), which potentially hints to a leptonic origin due to PWN have a harder spectrum in general [59]. The rough estimation of the particle acceleration index indicated in Figure 6.56 is also more reasonable in the leptonic case ($\approx$ 2.3), as compared to the hadronic case ($\approx$ 1.6).

Diffusion Nature

Lastly, disagreements on the diffusion slope δ and the diffusion radius are found in the impulsive injection scenario. The energy-independent diffusion, i.e. $\delta = 0$ gives a better fit than the energy-dependent diffusion by about 2σ for δ = 0.1, and 3.6σ for δ = 0.3. Furthermore, though the diffusion emission template parameters in the continuous injection scenario suffer from parameter degeneracy as discussed in Section 5.3 and 6.3.2, the energy-independent diffusion might also be favoured. To match the proton injection index with the estimated proton index of HESS J1745-290 using Naima, δ will be at around 0.08. These results contradict the prediction by various turbulent magnetic theories and the boron/carbon ratio measurement, where $\delta \in (0.3...0.6)$. Apart from the (more than expected) complex magnetic field irregularities in the Galactic Centre region, this is also believed to be related to the poor angular resolution and low accuracy of the current gas data. Moreover, highly overlapping sources in the CMZ region might cause the confusion on the energy-dependency of the particle diffusion nature. Furthermore, this might also be related to a simple CR proton propagation is assumed in the analysis, where no proton and energy losses have been considered.

On the other hand, it was believed that CRs should have a diffusion radius that is able to cover the whole CMZ region, mainly due to the observed residual following the shape of the CMZ. This study, however, reveals a small diffusion radius of about 112 pc when considering the impulsive injection scenario. Yet the small diffusion radius can nevertheless cover the residual as indicated in Figure 6.30, even for the case when the foreground component is not considered. The non-steady diffusion scenario is therefore still valid.

Remarks

It should also be mentioned that the possible existence of Fermi bubbles at the top right quarter of the analysis region is noticeable. Fermi bubbles could have been produced by jet emission and hot plasma outflow driven by accretion onto the central supermassive black hole,

as well as the star formation activity [122]. Yet as can be seen in Section 6.6, this emission is relatively weak and can be partially covered by the background uncertainty, Fermi bubbles are therefore not modelled in this analysis. Furthermore, the existence of the energy cutoff in the diffuse emission spectrum might hint at the possibility of the leptonic γ-ray emission scenario [65, 78, 49], which can induce a cutoff in the spectrum above few TeV. For instance a previous study [66] was able to to re-generate the diffuse emission spectrum derived by H.E.S.S. (2016) with the TeV halos of a millisecond pulsar population. The scenario of numerous PWNe arranged coincidentally with the gas structure along the Galactic ridge also cannot be ruled out [82]. It is therefore worth to model the leptonic emission scenario as well. Moreover, though the simple CR propagation model can already provide a good description in this analysis, it is encourage to also consider the more complicated CR propagation model in the future.

"Opened the door a crack wide enough
for the entire world to pass through."

Gabriel García Márquez
Love in the Time of Cholera

Chapter 7

Summary

The detection of VHE diffuse γ-ray emission in the CMZ can provide an insight into the mechanism that produces the diffuse emission observed from the Galactic Centre. The goal of this thesis is to establish the best CR injection scenario to account for the diffuse γ-ray emission in the CMZ, under the assumption of a hadronic origin in the vicinity of the Galactic Centre. It also provides an opportunity to verify (or challenge) the existence of a local PeVatron in the Galactic Centre. This thesis included 11 years of data from H.E.S.S. analysed with improved IRFs, and applied advanced 3D analysis technique to the analysis. The diffuse γ-ray emission has been modelled with physically motivated templates. This makes this thesis be the first detailed 3D analysis study of the diffuse TeV γ-ray emission from the complex Galactic Centre region with H.E.S.S (phase I and II) and *Gammapy*.

Both continuous and impulsive CR proton injection scenarios have been analysed. If only the conventional FoV sources and components are included, a steady-state continuous CR injection scenario provides the best description regarding the diffuse γ-ray emission in the CMZ. By choosing the diffusion slope $\delta = 0.37 \pm 0.02$, a proton injection index of $\alpha = 1.77 \pm 0.04$ is found. The resulting diffuse γ-ray spectral index is around 2.14. This number is close to the spectral index of HESS J1745-290, which implies a possible linkage between HESS J1745-290 and this diffuse γ-ray emission. On the other hand, if a scenario of impulsive CR injection in the non-steady state is assumed, an additional Gaussian central component has to be introduced. The diffusion radius of ≈ 112 pc is smaller than the size of the CMZ. Moreover, an energy-independent diffusion scenario at $\delta \approx 0$ is favoured, which is not realistic in the physical case. This nevertheless yields an even better fitting result preferred by 8.4σ. A γ-ray spectral index is found at around 2.29, which is again close to the spectral index of HESS J1745-290. Both Sgr A* and Sgr A East are good candidates for the injection site, mainly due to the sufficient energy budget of these two sources to operate either the continuous or the impulsive injection. The non-steady nature of the impulsive injection

scenario might also be explained by the young lifetime of Sgr A East or sudden accretion onto Sgr A*. For the impulsive injection case, the existence of an additional Gaussian central component might not be surprising, given many overlapping sources in the Galactic Centre. This additional central component shows a rather low energy cutoff at ≈ 6.7 TeV and hard spectrum with index ≈ 1.7. One of the possible associates could be G359.95-0.04, where the cutoff can be due to the Klein-Nishina suppression, and the cooling of the electrons via synchrotron radiation [57, 122].

Apart from an improvement of $\approx 5\sigma$ by the inclusion of the exponential cutoff for spectrum of HESS J1747-281, and $\approx 16.7\sigma$ by the inclusion of the foreground component, another unexpected finding is the need for a CR energy cutoff. Previous studies had presented the diffuse emission spectrum with a simple power-law up to 100 TeV, implying the possible existence of a PeVatron in the Galactic Centre [56, 57]. Yet significant proton energy cutoffs at 143 ± 31 TeV and 243 ± 85 TeV are found in both the continuous and impulsive injection scenarios of this analysis respectively. These impose lower limits of the cutoff at 72 TeV and 93 TeV at the 95 % confidence level, and improvements of 5.7σ and 3.5σ individually as compared to the cases without the cutoff (and 3.6σ and 2σ respectively as compared to the case of > 1 PeV cutoff). The presence of the proton energy cutoff has also been tested in different situations, regardless of the inclusion of the foreground component, an extension of HESS J1745-290, the different line-of-sight model for the CMZ gas distribution and the inclusion of background uncertainties. Both CR injection scenarios favour an energy cutoff on the proton injection spectrum, which challenges the existence of a PeVatron in the Galactic Centre.

To further verify the best-fit result of this thesis, namely the description of an impulsive proton injection scenario (non-steady, energy-independent and presence of energy cutoff in the proton spectrum) together with the need of an additional Gaussian central component, several evaluations could be done in the future. For instance, a proper background uncertainty estimation and joint analysis are needed. Joint analysis has the advantage of not relying on intermediate IRFs from an exposure-weighted average, which can avoid the aroused systematics as compared to the stacked analysis. On the other hand, one can also combine the GeV data from Fermi LAT to check the consistency of the result via joint instrument analysis. It is also found that the result is sensitive to the gas distribution in the CMZ, in which both the current CO/OH line-of-sight distribution models presented in this thesis have poorer resolution as compared to H.E.S.S. A deeper radio survey is required to extract the precise diffuse emission template parameters in the future. In addition, a more complex CR propagation model could be considered in order to obtain an even better diffuse emission description. Moreover, a leptonic injection scenario cannot be ruled out. Given the non-steady

nature of the impulsive injection scenario, it is possible that a number of PWNe are arranged according to the molecular density along the Galactic ridge. This would result in a similar diffuse γ-ray emission but with leptonic origin. Last but not least, more statistics will also definitely be useful, especially at the high energy of above 10 TeV. This can be done by carrying out more observations with H.E.S.S., as well as combining data from the future IACTs.

As already previewed in Figure 3.1, future IACTs, like CTA, could provide a measurement of VHE γ-ray with better sensitivity and IRFs for the analysis up to 300 TeV. This can furnish a robust conclusion on the existence of an energy cutoff in the CR injection spectrum and thus the absence of a PeVatron in the Galactic Centre. To provide the data with the best accuracy, a high precision of the telescope pointing needs to be reached. In fact, a preliminary pointing model has been developed by the author for one of the medium-sized telescope (MST) prototypes of CTA. Details can be found in Appendix B.

Appendix A

Supplementary

Chapter 4

W Statistics

This approach is used when the expected number of background events $\mu_{\rm bkg}$ is unknown, in this case one needs to consider the ratio of acceptance α in order to estimate the background counts in the ON region based on the measurement in the OFF region. The likelihood is written as

$$\begin{aligned} L(N_{\rm ON}, N_{\rm OFF}, \alpha; \mu_{\rm sig}, \mu_{\rm bkg}) &= P(N_{\rm ON}; \mu_{\rm sig} + \mu_{\rm bkg}) + P(N_{\rm OFF}; \mu_{\rm bkg}/\alpha) \\ &= \frac{(\mu_{\rm sig} + \mu_{\rm bkg})^{N_{\rm ON}}}{N_{\rm ON}!} e^{-(\mu_{\rm sig}+\mu_{\rm bkg})} \times \frac{(\mu_{\rm bkg}/\alpha)^{N_{\rm OFF}}}{N_{\rm OFF}!} e^{-\mu_{\rm sig}/\alpha}. \end{aligned} \tag{A.1}$$

The W statistics is expressed as [114]

$$W = -2\ln L = 2(\mu_{\rm sig} + (1+1/\alpha)\mu_{\rm bkg} - N_{\rm ON}\log(\mu_{\rm sig} + \mu_{\rm bkg}) - N_{\rm OFF}\log(\mu_{\rm bkg}/\alpha)). \tag{A.2}$$

The significance is computed as $S = \sqrt{TS} = \sqrt{W_0 - W_1}$, where

$$W_0(\text{null hypothesis}) \rightarrow \mu_{\rm sig} = 0, \mu_{\rm bkg} = \frac{\alpha}{1+\alpha}(N_{\rm ON} + N_{\rm OFF}); \tag{A.3}$$

$$W_1(\text{alternative hypothesis}) \rightarrow \mu_{\rm sig} = N_{\rm ON} - \alpha N_{\rm OFF}, \mu_{\rm bkg} = \alpha N_{\rm OFF}. \tag{A.4}$$

Eventually this leads to the Li & Ma significance for the standard method [77] as

$$S = \sqrt{2}\Big\{N_{\rm ON}\ln\Big[\frac{1+\alpha}{\alpha}\Big(\frac{N_{\rm ON}}{N_{\rm ON}+N_{\rm OFF}}\Big)\Big] + N_{\rm OFF}\ln\Big[(1+\alpha)\Big(\frac{N_{\rm OFF}}{N_{\rm ON}+N_{\rm OFF}}\Big)\Big]\Big\}^{1/2}. \tag{A.5}$$

Chapter 5

Alternative Computational Diffusion Solution

An alternative way of solving the diffusion equation is by using the numerical finite difference method known as the Forward Time Centered Space (FTCS) method. One can, at first, write the Equation 5.2 in a discrete format

$$\frac{\partial n(x_i, y_j, z_k; E, t_m)}{\partial t} = D(E)\frac{\partial^2 n(x_i, y_j, z_k; E, t_m)}{\partial r^2}, \tag{A.6}$$

By letting $n(i\Delta x, j\Delta y, k\Delta z; E, m\Delta t) = n^m_{i,j,k}$, the discretised diffusion equation can be written as

$$\begin{aligned}\frac{n^{m+1}_{i,j,k} - n^m_{i,j,k}}{\Delta t} = D(E)\cdot\Bigg(&\frac{n^m_{i+1,j,k} - 2n^m_{i,j,k} + n^m_{i-1,j,k}}{(\Delta x)^2} + \frac{n^m_{i,j+1,k} - 2n^m_{i,j,k} + n^m_{i,j-1,k}}{(\Delta y)^2} \\ &+ \frac{n^m_{i,j,k+1} - 2n^m_{i,j,k} + n^m_{i,j,k-1}}{(\Delta z)^2}\Bigg),\end{aligned} \tag{A.7}$$

By letting $c = \frac{2D(E)\Delta t}{(\Delta x)^2}$, Equation A.7 can be simplified as

$$\begin{aligned}n^{m+1}_{i,j,k} = n^m_{i,j,k}(1-3c) + \frac{c}{2}\big(&n^m_{i+1,j,k} + n^m_{i-1,j,k} + n^m_{i,j+1,k} + n^m_{i,j-1,k} \\ &+ n^m_{i,j,k+1} + n^m_{i,j,k-1}\big),\end{aligned} \tag{A.8}$$

The proton density at any discrete grid point can be derived easily by setting up a $3\times3\times3$ convolutional kernel from *scipy.ndimage.convolve* such that at each timestamp, there is a factor of $3c$ protons diffusing out of the grid and a factor of $\frac{c}{2}$ neighbouring protons diffuse into the grid. Since the number of proton leaving the grid cannot be larger than its initial number, this puts a constraint onto the parameter c such that

$$3c = 3\frac{2D(E)\Delta t}{(\Delta x)^2} \leq 1. \tag{A.9}$$

Chapter 6

Summary of All FoV Parameters

Sources	Parameters	Cont(ST)	Imp(ST)	Cont(ST+Nui)	Imp(ST+Nui)	Cont(YT)	Imp(YT)	Cont(Y)	Imp(Y)
Diffuse	N_p [1.55E+52]	0.401±0.094	0.01±0.002	0.205±0.063	0.011±0.004	11303.809±1887.667	0.013±0.005	3.358±0.778	0.001±0.0
	α	1.771±0.038	2.293±0.04	2.071±0.081	2.277±0.066	1.306±0.043	2.341±0.083	1.421±0.044	2.205±0.07
	D_0 [pc^2/yr]	0.641±0.094	0.006±0.001	1.194±0.036	0.007±0.001	9079.831±2215.85	0.012±0.003	19.996±2.984	0.006±0.001
	δ	0.369±0.022	0.0±0.0	0.022±0.01	0.0±0.0	0.791±0.032	0.0±0.0	0.643±0.021	0.0±0.0
	E_{cut} [TeV]	142.819±31.094	242.598±85.147	121.801±38.999	214.955±80.457	116.29±24.936	230.471±125.544	130.452±26.537	202.442±64.6
Foreground	Γ	2.397±0.035	2.38±0.041	2.49±0.051	2.464±0.044	2.393±0.021	2.371±0.028	2.435±0.041	2.413±0.049
	Φ_{10GeV} [E-6 /(cm^2 s TeV)]	1.266±0.226	1.205±0.256	2.043±0.52	1.801±0.405	1.563±0.171	1.356±0.187	1.4±0.288	1.313±0.342
J1745-290	Γ	2.03±0.039	2.132±0.056	2.033±0.041	2.133±0.059	2.033±0.037	2.177±0.06	2.05±0.038	2.158±0.069
	Φ_{1TeV} [E-12 /(cm^2 s TeV)]	2.144±0.055	1.871±0.095	2.129±0.054	1.868±0.1	2.143±0.053	1.846±0.101	2.176±0.055	1.758±0.114
	λ [TeV^{-1}]	0.089±0.013	0.071±0.015	0.088±0.013	0.07±0.016	0.087±0.012	0.068±0.017	0.087±0.013	0.068±0.016
	lon [°]	359.943±0.001	359.945±0.001	359.943±0.001	359.945±0.001	359.943±0.001	359.945±0.001	359.944±0.001	359.944±0.001
	lat [°]	-0.044±0.001	-0.045±0.001	-0.044±0.001	-0.045±0.001	-0.046±0.001	-0.046±0.001	-0.045±0.001	-0.046±0.001
J1747-281	Γ	2.072±0.088	2.063±0.091	2.056±0.097	2.047±0.092	2.069±0.084	2.049±0.095	2.072±0.091	2.061±0.094
	Φ_{1TeV} [E-12 /(cm^2 s TeV)]	0.847±0.05	0.841±0.051	0.856±0.055	0.847±0.053	0.834±0.047	0.817±0.051	0.82±0.05	0.813±0.052
	λ [TeV^{-1}]	0.149±0.037	0.152±0.039	0.156±0.042	0.16±0.04	0.151±0.035	0.157±0.041	0.152±0.038	0.156±0.04
	lon [°]	0.865±0.001	0.866±0.001	0.865±0.001	0.866±0.001	0.866±0.001	0.866±0.001	0.866±0.001	0.866±0.001
	lat [°]	0.082±0.001	0.083±0.001	0.082±0.001	0.083±0.001	0.083±0.001	0.084±0.001	0.082±0.001	0.083±0.001
J1746-285	Γ	2.087±0.104	2.124±0.092	2.094±0.076	2.133±0.093	2.136±0.089	2.148±0.075	2.184±0.089	2.184±0.086
	Φ_{1TeV} [E-12 /(cm^2 s TeV)]	0.107±0.016	0.135±0.017	0.108±0.015	0.139±0.018	0.14±0.017	0.161±0.016	0.154±0.017	0.162±0.017
	lon [°]	0.136±0.004	0.134±0.004	0.136±0.004	0.135±0.004	0.137±0.004	0.137±0.003	0.136±0.003	0.135±0.003
	lat [°]	-0.123±0.005	-0.121±0.004	-0.123±0.004	-0.121±0.004	-0.12±0.004	-0.12±0.003	-0.116±0.003	-0.116±0.003
J1741-302	Γ	2.047±0.181	2.049±0.184	2.016±0.178	2.019±0.185	2.04±0.184	2.047±0.177	2.041±0.178	2.047±0.181
	Φ_{1TeV} [E-12 /(cm^2 s TeV)]	0.083±0.022	0.082±0.023	0.077±0.022	0.077±0.022	0.078±0.022	0.079±0.022	0.085±0.023	0.084±0.023
	lon [°]	358.281±0.008	358.281±0.008	358.281±0.008	358.281±0.008	358.281±0.008	358.281±0.007	358.281±0.007	358.281±0.007
	lat [°]	0.037±0.008	0.037±0.008	0.037±0.009	0.037±0.009	0.037±0.008	0.037±0.007	0.037±0.008	0.037±0.008
Additional	Γ		1.702±0.142		1.7±0.14		1.51±0.178		1.746±0.151
	Φ_{1TeV} [E-12 /(cm^2 s TeV)]		0.936±0.106		0.945±0.107		0.827±0.114		0.999±0.122
	λ [TeV^{-1}]		0.149±0.035		0.15±0.035		0.168±0.042		0.138±0.032
	lon [°]		359.937±0.004		359.938±0.004		359.94±0.004		359.945±0.004
	lat [°]		-0.042±0.004		-0.042±0.004		-0.054±0.004		-0.046±0.003
	σ [°]		0.051±0.005		0.051±0.005		0.045±0.004		0.042±0.004

Table A.1 Summary of parameters from all FoV sources and components, fitted in continuous and impulsive CR injection scenarios. *ST*, *YT* and *Y* denote the different gas data, *Nui* denotes the inclusion of the nuisance parameter fit.

Energy-Independent Background Systematics

As derived in Section 6.2.2, the energy-independent background uncertainty is 6.94%. The corresponding nuisance fit results are presented in the following. For the continuous CR injection scenario, the residual in terms of energy and diffuse emission spectrum are shown in Figure A.1. An over-fitting is observed in the residual, which might be related to the background uncertainty being overestimated at the low energies and the spatial binning of the nuisance cube is too coarse. Similar effect can be observed for the impulsive CR injection scenario.

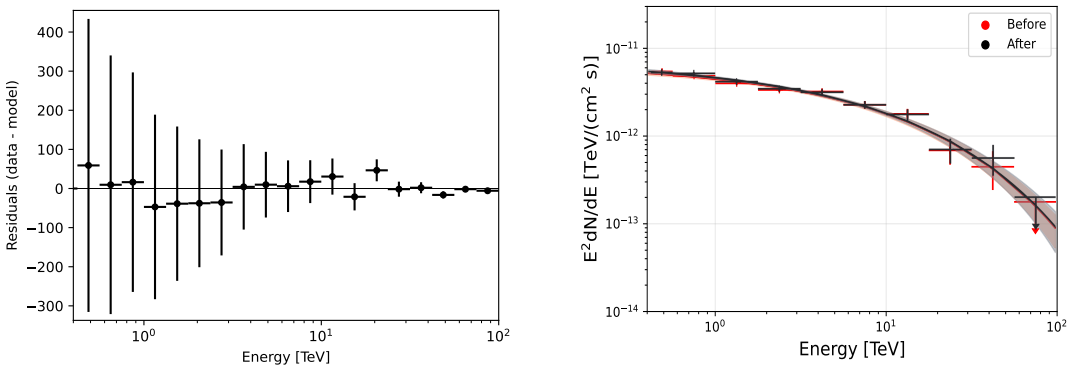

(a) (b)

Figure A.1 The nuisance fitting result for the continuous CR injection scenario. (a) The model and data differences in terms of energy. (b) Diffuse emission spectrum before and after the nuisance fit. The 1σ statistical errors are shown.

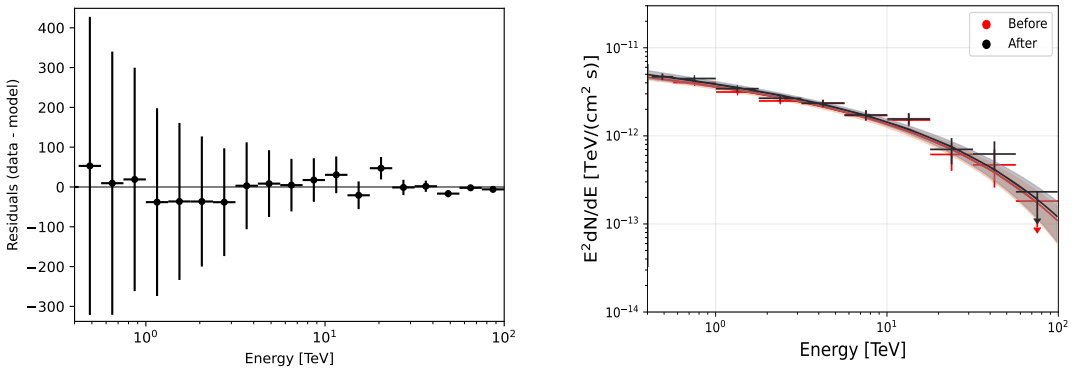

(a) (b)

Figure A.2 The nuisance fitting result for the impulsive CR injection scenario. (a) The model and data differences in terms of energy. (b) Diffuse emission spectrum before and after the nuisance fit. The 1σ statistical errors are shown.

Appendix B

CTA MST Pointing Model

B.1 Motivation and Summary

Figure B.1 The single-CCD camera prototype in the 2018 MAGIC campaign. (Photo credit: Markus Garczarczyk)

The main goal of the Cherenkov Telescope Array is to capture Cherenkov light, which enables the reconstruction of the incoming γ-ray position. It is thus crucial to determine the telescope orientation precisely. Yet it is deviated from the nominal alignment due to different errors. A pointing model is used for the correction. The overall goal for the future CTA medium-sized telescope (MST) is to reach an accuracy of 7" [109]. This will be done with the help of a single-CCD camera.

The CCD camera prototype was tested on the MAGIC telescope in the mid-2018 in La Palma, the same location as the future CTA. In this work, a detailed description of the offline pointing model for the MAGIC campaign is presented. A pointing accuracy of < 10" is reached. This preliminary result is promising given the MAGIC telescope is lighter than the MST telescope. In future, a test of this pointing model and the single-CCD concept on observation-runs data of the MST can be performed.

B.2 Principle of Pointing

Two error categories are affecting the precision of the telescope orientation. One is the mechanical errors (reproducible errors), including the offset of the drive system, the tilting of the telescope, the bending of the telescope masts and the non-perpendicularity of the azimuth and altitude axis. The other is the non-reproducible errors, including the wind dragging, contamination from the tracking rail and more. The correction of both errors can be done in the offline pointing control using a defined mechanical structure. The construction method of the pointing model has took reference from previous publications [20, 46].

B.2.1 Offline Pointing Control

The offline pointing control takes place during the pointing-runs, where the telescope points directly to a collection of known stars at different telescope orientations. A single CCD-camera is attached to the centre of the telescope mirror dish. It provides enough field-of-view and resolution to capture the Cherenkov camera lid and the surrounding night sky. A offline pointing model consists of two sub-models, which are the LID model (for reproducible errors) and the SKY model (for non-reproducible errors).

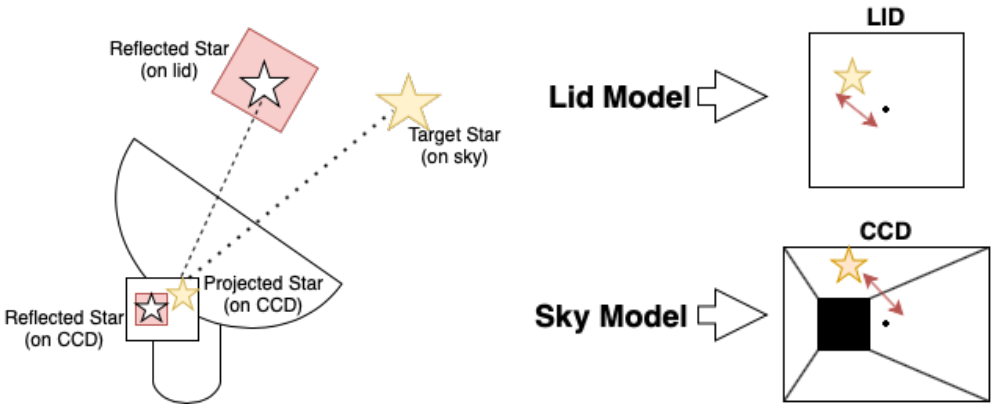

(a) (b)

Figure B.2 The schematic of a pointing-runs. (a) The telescope points to a target star. The light from the target star is reflected to the lid. The CCD camera is able to capture the reflected star on the lid and the night sky. (b) The illustration of the LID and SKY model.

The LID model describes the deviation of the Cherenkov camera centre and the reflected position of a target star on the lid as shown in Figure B.2. In other words, it transforms the nominal telescope orientation(in Alt/Az coordinate) to the reflected star position on the lid (in CCD pixel coordinate). The SKY model, on the other hand, describes the deviation of the CCD camera centre and the nominal telescope orientation. This nominal telescope

orientation is being projected onto the CCD chip coordinate in pixel. In other words, it transforms the CCD orientation (in Alt/Az coordinate) to the projected nominal telescope orientation (in CCD pixel coordinate). During the pointing-runs, the nominal telescope orientation is equivalent to the target position of a star.

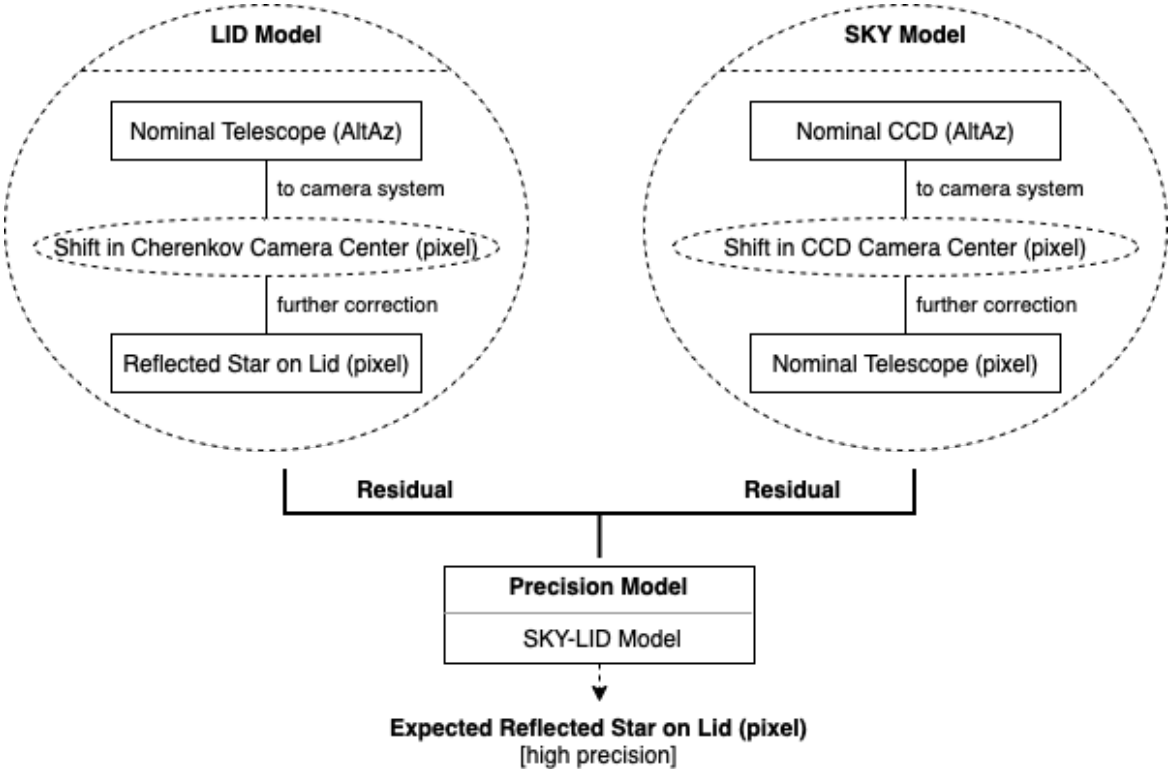

Figure B.3 The components of a pointing model in the offline pointing control.

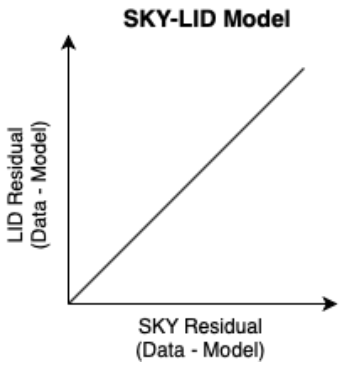

Figure B.4 The SKY-LID model.

In an ideal case, a linear relation between the residuals of these two sub-models is expected. This is due to the same mechanical effects acting on the CCD camera and the

telescope. A SKY-LID model (or the precision model) can therefore be built. This model predicts the reflected star position on the Cherenkov camera lid with a finer precision. The visualisations of the offline pointing control and the SKY-LID model can be found in Figure B.3 and B.4.

B.2.2 Mechanical Structure

Both LID and SKY models are built with the same mechanical structure. This structure includes the drive system offset, tilting, global camera offset, bending, non-perpendicularity and the atmospheric refraction as shown in Table B.1. The implementation procedure, as adapted from the H.E.S.S. pointing model [20, 62], will be shown below.

Nominal Telescope Orientation (Alt/Az)
$\rightarrow$ Drive System Correction$[\lambda_{\Delta,a,\Omega}, \beta_{\Delta,a,\Omega}]$
$\rightarrow$ Tilting Correction$[\lambda_{\phi,\theta}]$
Transform Shift to Camera System
$\rightarrow$ Camera Offset Correction$[\mathrm{x}_{\Delta}, y_{\Delta}]$
$\rightarrow$ Bending Correction$[\mathrm{x}_{b_1,b_2}, y_{b_1,b_2,b_3}]$
$\rightarrow$ Non-Perpendicularity Correction$[\mathrm{x}_{\delta}]$
$\rightarrow$ Refraction Correction$[\mathrm{y}_{r}]$
Add Total Shift to Cherenkov Camera Centre
Predict Reflected Star Position on Lid (pixel)

Table B.1 The overall procedure for building the mechanical structure.

The nominal telescope orientation is defined as

$$\vec{c_0} = \begin{pmatrix} \lambda_0 \\ \beta_0 \end{pmatrix}, \tag{B.1}$$

where λ_0 is the azimuth angle originates from the North in the clockwise direction, and β_0 is the altitude angle with 90° at the zenith. The first correction is the drive system correction due to the mis-calibration of the alt-azimuth-mount. It consists the drive system offset Δ, and the amplitude a and phase Ω for different sinusoidal signals relative to analogue verniers. The corrected tracking orientation is

$$\vec{c_c} = \begin{pmatrix} \lambda_c \\ \beta_c \end{pmatrix} = \begin{pmatrix} \lambda_0 \\ \beta_0 \end{pmatrix} + \begin{pmatrix} \lambda_\Delta \\ \beta_\Delta \end{pmatrix} + \begin{pmatrix} \lambda_a \cdot \sin(\lambda_0 + \lambda_\Omega) \\ \beta_a \cdot \sin(\beta_0 + \beta_\Omega) \end{pmatrix}. \tag{B.2}$$

Next, a tilting correction is needed due to the misalignment of the azimuth axis of the telescope in the vertical direction. It tilts towards the azimuth direction λ_ϕ by an angle λ_θ. To reduce the complexity, this effect is studied in the 3D Cartesian coordinate($\vec{c_c} \rightleftharpoons \hat{t}$). This gives

$$\vec{c_c} \rightleftharpoons \hat{t} = x\hat{e}_x + y\hat{e}_y + z\hat{e}_z = \begin{pmatrix} \sin(90^\circ - \beta_c) \cdot \cos\lambda_c \\ \sin(90^\circ - \beta_c) \cdot \sin\lambda_c \\ \cos(90^\circ - \beta_c) \end{pmatrix} = \begin{pmatrix} \cos\beta_c \cdot \cos\lambda_c \\ \cos\beta_c \cdot \sin\lambda_c \\ \sin\beta_c \end{pmatrix}, \tag{B.3}$$

with $\hat{e}_x$ points to the North and $\hat{e}_y$ points to West. The tilting correction is then done via a double rotation matrix. First is to rotate the system around $\hat{e}_z$ by λ_ϕ. This gives an new $\hat{e}_x$ axis

$$\hat{e}'_x = \begin{pmatrix} \cos\lambda_\phi \\ \sin\lambda_\phi \\ 0 \end{pmatrix}. \tag{B.4}$$

Then rotate the new axis $\hat{e}'_x$ by λ_θ. This can be done using the Rodrigues' rotation formula

$$R = (\cos\lambda_\theta)I + (\sin\lambda_\theta)[\hat{e}'_x]_\times + (1 - \cos\lambda_\theta)(\hat{e}'_x \otimes \hat{e}'_x), \tag{B.5}$$

where $\hat{e}'_x \otimes \hat{e}'_x$ is the outer product that is equivalent to $\hat{e}'_x \hat{e}'^{\mathsf{T}}_x$ and $[\hat{e}'_x]_\times$ is the cross product matrix, which can be represented by the skew-symmetric matrix as matrix multiplication. The rotation matrix can therefore be written as

$$R = \begin{pmatrix} \cos\lambda_\theta + \cos^2\lambda_\phi(1 - \cos\lambda_\theta) & \sin\lambda_\phi\cos\lambda_\phi(1 - \cos\lambda_\theta) & \sin\lambda_\phi\sin\lambda_\theta \\ \sin\lambda_\phi\cos\lambda_\phi(1 - \cos\lambda_\theta) & \cos\lambda_\theta + \sin^2\lambda_\phi(1 - \cos\lambda_\theta) & -\cos\lambda_\phi\sin\lambda_\theta \\ -\sin\lambda_\phi\sin\lambda_\theta & \cos\lambda_\phi\sin\lambda_\theta & \cos\lambda_\theta \end{pmatrix}. \tag{B.6}$$

Since this rotation direction is anticlockwise (from North to West), it has to reverse such that it rotates in the clockwise direction. At the end the corrected tracking direction $\hat{t}'$ is given by

$$\hat{t}' = \begin{pmatrix} x_c \\ y_c \\ z_c \end{pmatrix} = R^{\mathsf{T}}\hat{t}. \tag{B.7}$$

The Cartesian tracking orientation can then transform back to the horizontal coordinate

$$\vec{c_v} = \begin{pmatrix} \lambda_v \\ \beta_v \end{pmatrix}, \tag{B.8}$$

with

$$\beta_v = \sin^{-1} z_c, \quad \lambda_v = \begin{cases} \cos^{-1} \frac{x_c}{\cos\beta_v} \ , \ y_c \geq 0 \\ 360^\circ - \cos^{-1} \frac{x_c}{\cos\beta_v} \ , \ y_c < 0 \end{cases} \tag{B.9}$$

The angular shift can be transformed to a shift in the camera system $\Delta\vec{s}_s$ relative to the Cherenkov camera centre. Together with the global camera offset correction $\Delta\vec{s}_\Delta$, bending correction $\Delta\vec{s}_B$, non-perpendicularity correction of the altitude axis with respect to the azimuth axis $\Delta\vec{s}_{NPE}$ and refraction correction for the apparent height of a star $\Delta\vec{s}_r$, the total correction can be written as

$$\Delta\vec{s} = \Delta\vec{s}_s + \Delta\vec{s}_\Delta + \Delta\vec{s}_B + \Delta\vec{s}_{NPE} + \Delta\vec{s}_r = \begin{pmatrix} \Delta x \\ \Delta y \end{pmatrix}, \tag{B.10}$$

with

$$\Delta\vec{s}_s = (\vec{c}_v - \vec{c}_0) \begin{pmatrix} \cos\beta_v \\ 1 \end{pmatrix}, \tag{B.11}$$

$$\Delta\vec{s}_\Delta = \begin{pmatrix} x_\Delta \\ y_\Delta \end{pmatrix}, \quad \Delta\vec{s}_r = \begin{pmatrix} 0 \\ y_r \tan(90^\circ - \beta_v) \end{pmatrix}, \tag{B.12}$$

$$\Delta\vec{s}_B = \begin{pmatrix} x_{b_1} \sin\beta_v + x_{b_2}\beta_v \\ y_{b_1} \cos(\beta_v + y_{b_3}) + y_{b_2}\beta_v \end{pmatrix}, \quad \Delta\vec{s}_{NPE} = \begin{pmatrix} \sin^{-1}(\sin x_\delta \sin\beta_v) \\ \sin^{-1}(\cos x_\delta \sin\beta_v) \approx 0 \end{pmatrix}. \tag{B.13}$$

The angular shift can then convert to the pixel coordinate. The expected reflected star position on the lid is therefore equivalent to

$$\Delta\vec{s} \cdot \frac{3600}{\text{arcs/pixel}} + \text{Cherekov camera centre position.} \tag{B.14}$$

B.3 CCD Image Analysis

Unlike the double-CCD camera system adopted by H.E.S.S. [46], the single-CCD camera aims at capture the image of the Cherenkov Camera Lid and the night sky simultaneously. This can reduce the complexity and the cost. The image of the Cherenkov camera lid is used to determine the Cherenkov camera centre by reference LEDs and record the reflected star position on the lid during pointing-runs. These are essential for building the LID model. The night sky image is used to reconstruct the pointing direction of the CCD camera by reference background stars, which is essential for building the SKY model. To capture these details, a focal length of 50 mm and a exposure time of 10s are set for the CCD camera. The image consists of 3246×2472 pixels, which gives 22.6 "/pixel. To avoid the image distortion

from the chip expansion within the MST working temperature as shown in the previous study [128], the chip temperature is set to -22 °C. This number has been tested specifically for this prototype.

B.3.1 LEDs

Determination of LED Positions

There are 12 LEDs distributed around the Cherenkov camera lid of the MAGIC telescope. They are mounted behind the 15 mm diameter holes on the lid and distributed evenly in a circle with a diameter of 1260 mm across the Cherenkov camera centre. In practice, only a maximum of 8 LEDs are operating. An example of a lid image can be seen in Figure B.5

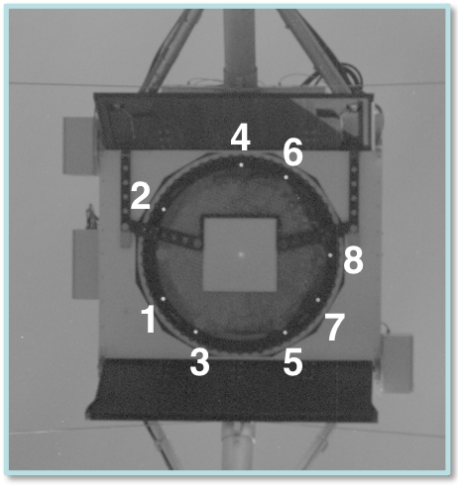

Figure B.5 A zoom-in image of the Cherenkov camera lid. Eight LEDs are distributed in a circular shape around the Cherenkov camera centre. A star is reflected onto the lid.

The intensities of LEDs follow the volcano distribution due to the reflection in the hole. The typical shape has a diameter of about 15 pixels as shown in Figure B.8. The position is determined using the centre of gravity method. These LED positions and corresponding errors are derived using the functions:

$$(< x >, < y >) = \left\{ \frac{\sum_{x=0}^{N-1}\sum_{y=0}^{M-1} x \cdot I(x,y)}{\sum_{x=0}^{N-1}\sum_{y=0}^{M-1} I(x,y)}, \frac{\sum_{x=0}^{N-1}\sum_{y=0}^{M-1} y \cdot I(x,y)}{\sum_{x=0}^{N-1}\sum_{y=0}^{M-1} I(x,y)} \right\} \tag{B.15}$$

$$(\sigma^2_{<x>}, \sigma^2_{<y>}) = \left\{ \frac{\sum_{x=0}^{N-1}\sum_{y=0}^{M-1} I(x,y)(x- < x >)^2}{\sum_{x=0}^{N-1}\sum_{y=0}^{M-1} (I(x,y))^2}, \frac{\sum_{x=0}^{N-1}\sum_{y=0}^{M-1} I(x,y)(y- < y >)^2}{\sum_{x=0}^{N-1}\sum_{y=0}^{M-1} (I(x,y))^2} \right\} \tag{B.16}$$

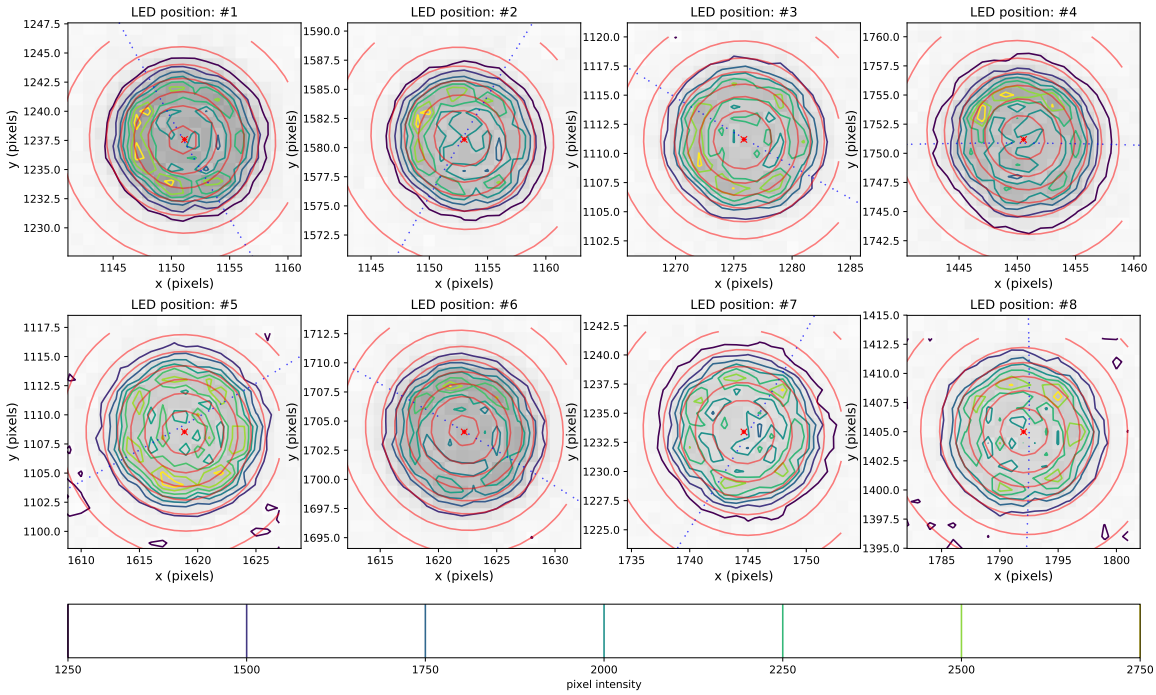

Figure B.6 The pixel intensity contours and the positions (red cross) of each LED. The colorbar indicates the intensity. The red lines indicate the Gaussian fit to the intensity. The blue dashed line is the circle fit for locating the Cherenkov camera centre.

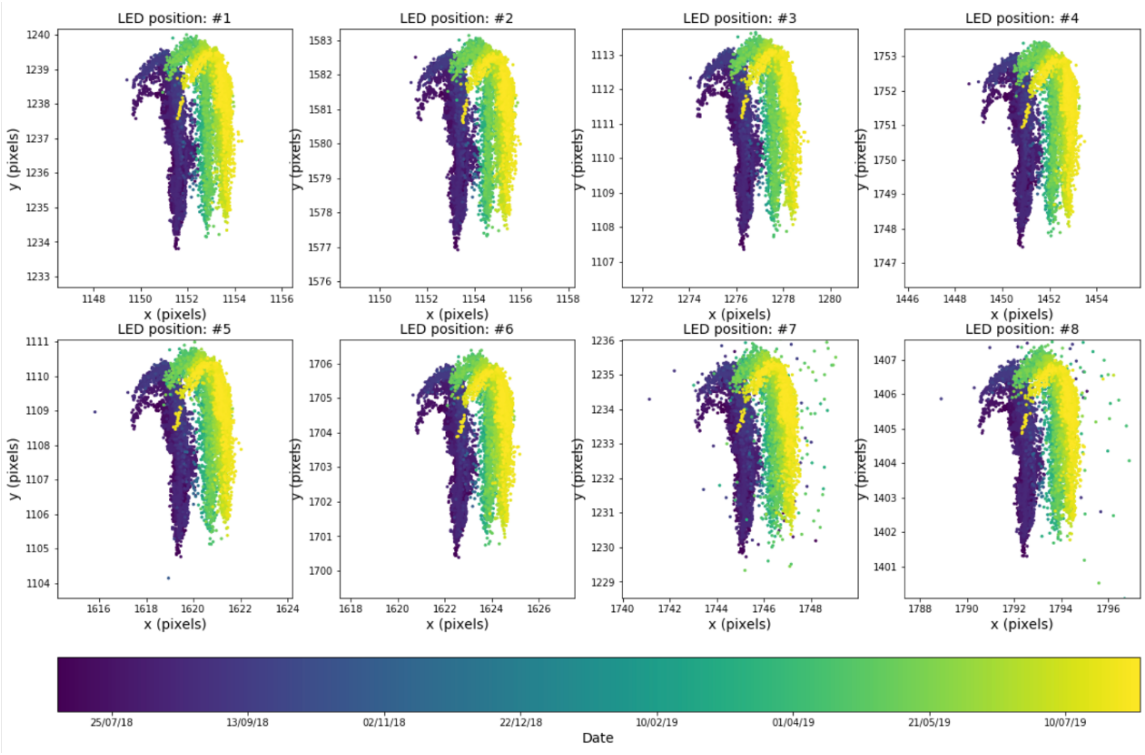

Figure B.7 The time evolution of the LED positions.

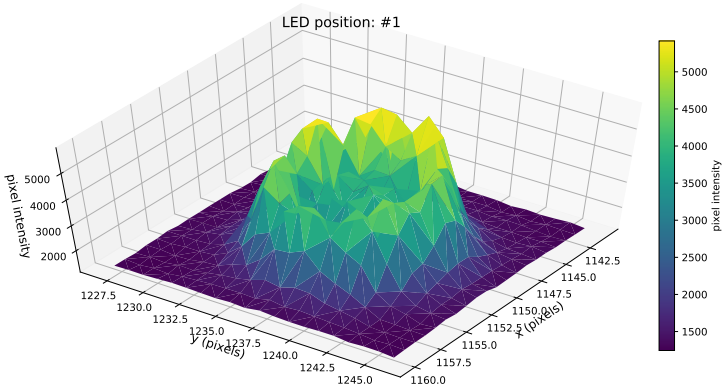

Figure B.8 The intensity distribution of a LED.

The intensity contours and the locations of all LEDs can be seen in Figure B.6. The time evolution of LED positions over 2018-2019 is shown in Figure B.7. All LEDs experience the same bending effect from the mast. Large time-dependent shifts are observed due to the CCD camera was being re-positioned due to operation reasons.

Determination of the Cherenkov Camera Centre

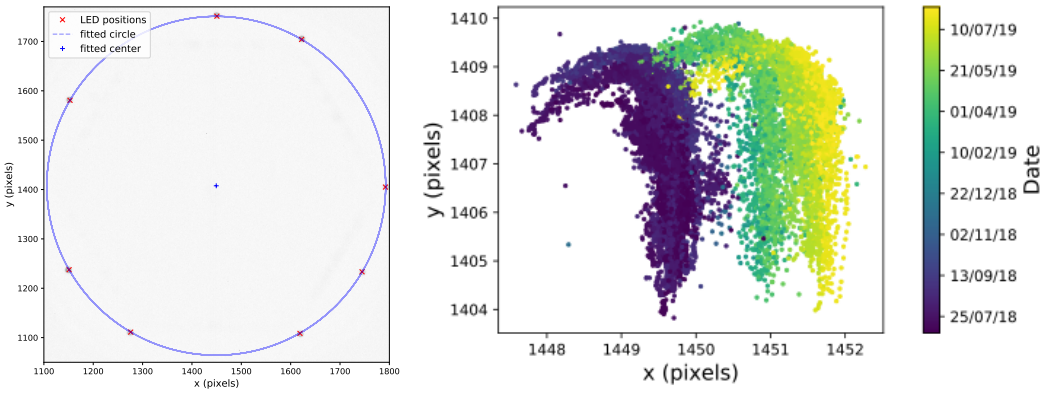

(a) (b)

Figure B.9 The determination of the Cherenkov camera centre. (a) The centre is located by a circle fit on the 8 LEDs. (b) The time evolution of the Cherenkov camera centre positions.

Due to LEDs are arranged in a circular shape, a simple circle fit can be used to determine the Cherenkov camera centre. The fit algorithm is built based on the orthogonal distance regression. The fitting is performed when 8 LEDs are ON as illustrated in Figure B.9 (a). The resulting Cherenkov camera centre positions in 2018-2019 can be seen in Figure B.9 (b). These positions show the same time evolution feature as for LEDs. A night-to-night change

is expected. The mean error of extracting the Cherenkov camera centre position for a random night is about 0.005 pixels, which corresponds to 0.1".

The Effect of Missing LEDs

The derivation of the Cherenkov camera centre is affected by LED positions. The missing of some LEDs can result in a different degree of impacts as indicated in Figure B.10. The deviation can reach up to 7.5" when 2 LEDs are missing. Since these deviations follow certain patterns, one can in future model them. This is however not built for the MAGIC telescope since this study focuses on the case where 8 LEDs are operating.

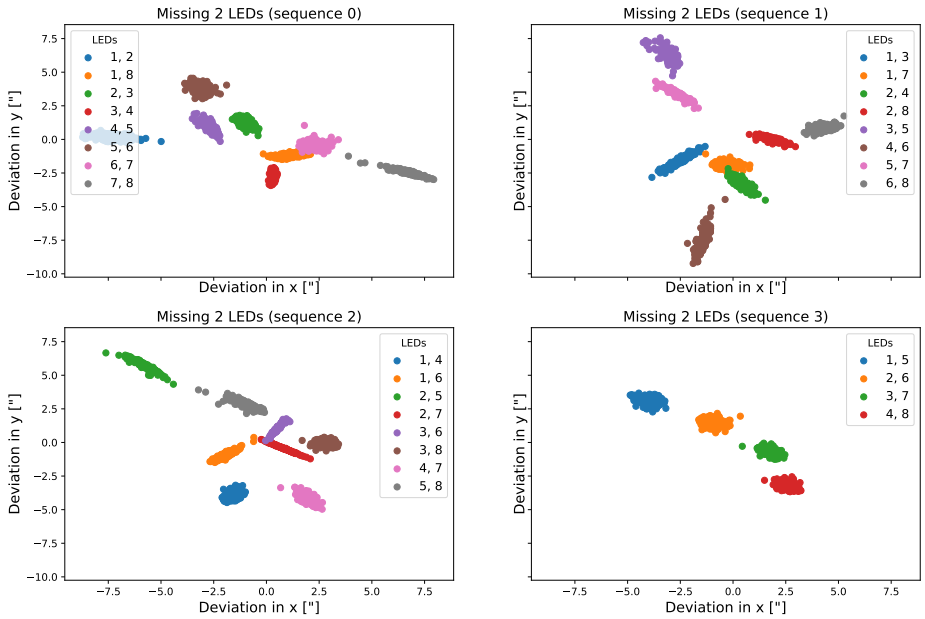

Figure B.10 The shift of the Cherenkov camera centre when any two LEDs are missing. The order of the LEDs are denoted in Figure B.5.

Rotation Model

A certain rotation of the Cherenkov camera is expected due to the structure might not tightly screwed. To determine the degree of rotation, the polar coordinate of LEDs can be compared with their reference positions in the technical design. Note that a rotation to the left on the image represents a rotation to the right in reality as indicated in Figure B.11 due to the image is inverted. A cosine function

$$a + b \cdot \cos(el) \tag{B.17}$$

is fitted to the data as shown in Figure B.13. As illustrated by a dataset in 2019, a rotation of 0.03° is observed at altitude from 0° to 90°.

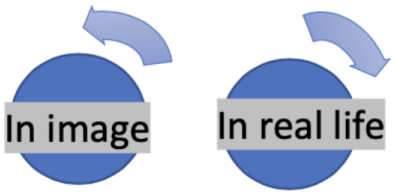

Figure B.11 The rotation direction of the Cherenkov camera (blue circle) in the image and real life.

Bending Model

The mast bending effect is expected due to the gravitational pull of the telescope structure. When the telescope is pointing to a higher altitude, the Cherenkov camera will shift upwards relative to the CCD camera in the reality as illustrated in Figure B.12. Since the CCD image is being inverted, this means a shift to the downwards direction is expected in the image.

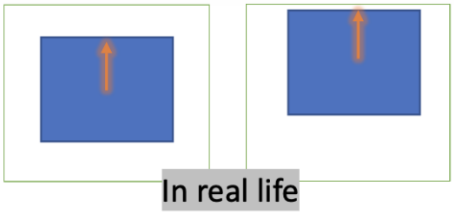

Figure B.12 The movement of the Cherenkov camera (blue square) relative to the CCD camera (green square) in the real life. The orange arrow indicates the relative shift of the Cherenkov camera when the telescope is pointing to higher altitude.

To describe the bending in the vertical direction, a cosine function (with a phase term) and an addition linear function can be used, where

$$a_y + b_y \cdot \cos(el + c_y) + d_y \cdot el. \tag{B.18}$$

The phase term is needed due to the rotation effect, the additional linear term is an ad-hoc that is necessary for the fitting. In the normal case, no bending in the horizontal direction is expected. However this is not the case for the MAGIC telescope. A sinusoidal function and again an addition linear term are needed. This function can be expressed as

$$a_x + b_x \cdot \sin(el) + d_x \cdot el. \tag{B.19}$$

Both bending effects and the models can be seen in Figure B.13. Clear night-to-night changes can be observed. The overall bending effect in the vertical direction is smaller than

6 pixels and 3 pixels from 0° to 90° in altitude, which corresponds to 10.8mm and 5.4 mm on the plane.

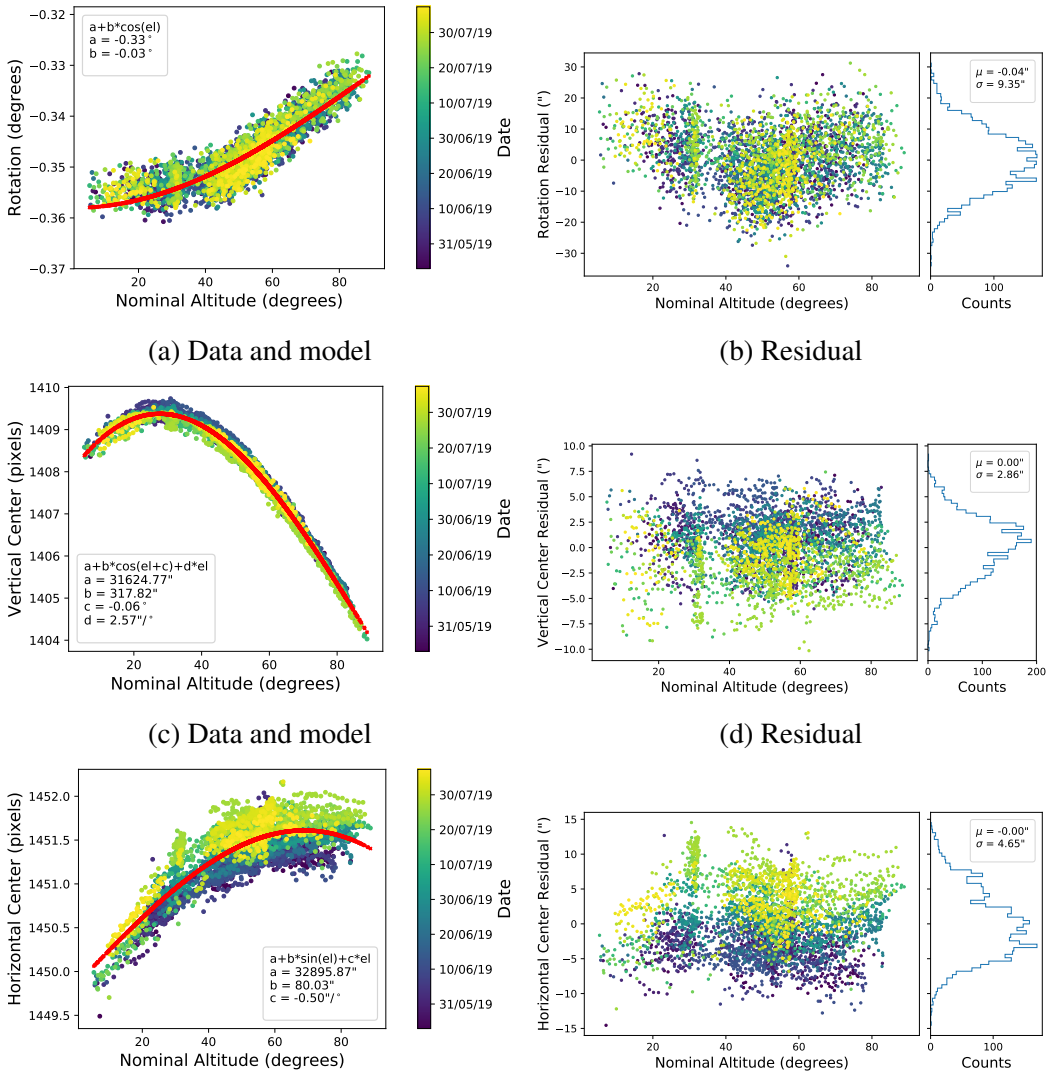

(a) Data and model (b) Residual

(c) Data and model (d) Residual

(e) Data and model (f) Residual

Figure B.13 The rotation (a and b), vertical bending (c and d) and horizontal bending (e and f) models and the corresponding residuals. The red lines indicate the models. The data are taken from a pointing-runs period in 2019.

B.3.2 Reflected Star on the Lid

During a pointing-runs, a target star is being reflected onto the Cherenkov camera lid as shown in Figure B.5. The centre of gravity method is used to locate its position. This position is essential for building the LID model. The intensity distribution of a reflected star is shown

in Figure B.14, which is not following a perfect Gaussian shape. A typical width is about 20 pixels. The distribution of the reflected positions in CCD images from 2018-2019 is shown in Figure B.15. The corresponding 2D RMS is 40.15".

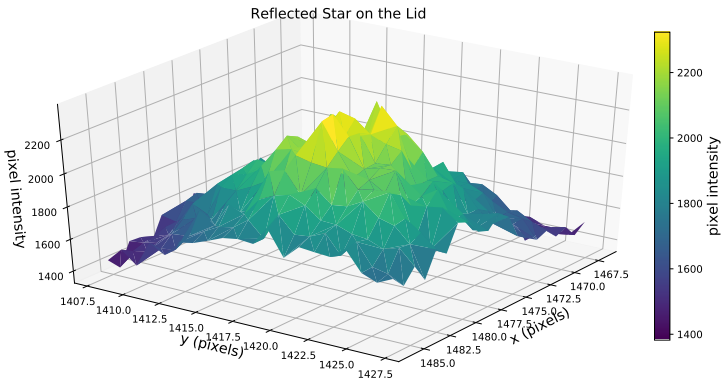

Figure B.14 The pixel intensity distribution of a reflected star. The colorbar indicates the intensity.

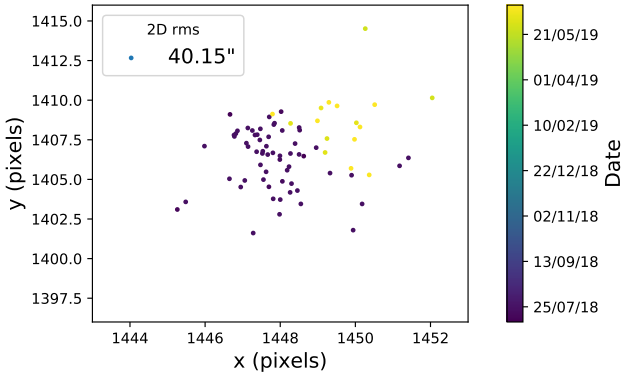

Figure B.15 The distribution of the reflected star position from 2018-2019. The 2D RMS is 40.15".

B.3.3 CCD Pointing Reconstruction

The CCD pointing reconstruction is essential for building the SKY model. This reconstruction is done using the software *libPointingMST* (2020) developed by Domenico Tiziani [118]. According to [118], one has to first extract positions of background star-like spots in the image using the centre of gravity method. These positions, originally in the pixel coordinate, are being transformed to the equatorial coordinate. The algorithm then take a 4-star constellation in the image and attempt to match a geometric hash-codes inside a pre-compiled index file

based on the Tycho-2 catalog. The geometric hash-code describes the relative positions of all stars in a quad, which is invariant under translation, scaling and rotation. Once a match is found, the remaining spots in the image will be compared to hypothetical catalog star positions. If they match again, all spots will then fit to the World Coordinate System (WCS) through twisting, scaling, rotation and translation until they match with catalog stars positions. The algorithm of the WCS fitting consists of a loop of different nonlinear derivative-free optimizations, aiming to search for a minimum within a reasonable time range. Example of spots and stars identification can be found in Figure B.16.

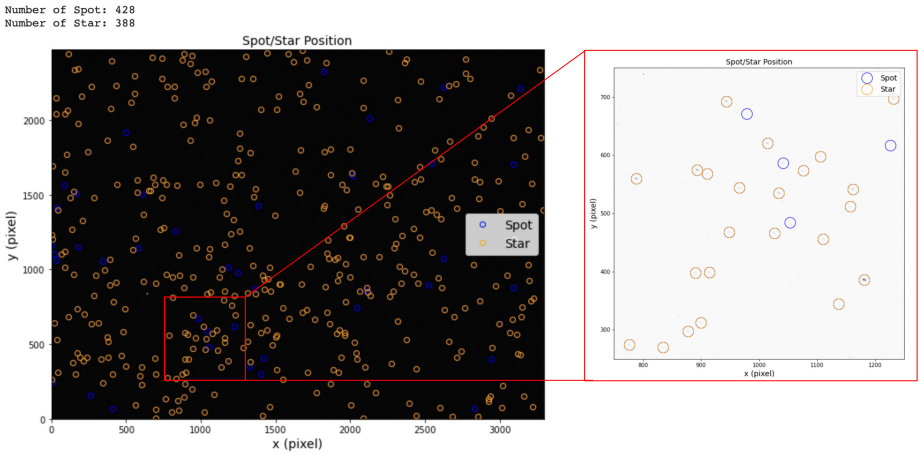

Figure B.16 The spot extraction and WCS fitting result. The blue circles indicate star-like spot positions, the orange circles indicate star positions from the Tycho-2 catalog. Some spots are not covered by stars due to the magnitude limit in the catalog or mis-extraction.

Note that the Cherenkov camera and part of the telescope structure are within the field-of-view of the CCD camera. Therefore a mask is required to exclude unnecessary regions as indicated in Figure B.17 (a). The overall telescope and CCD orientations recorded from 2018-2020 are presented in Figure B.17 (b). A comprehensive sky coverage is shown.

B.4 Offline Pointing Model

The offline pointing model consists of both LID and SKY models as discussed in Section B.2.1. These two models are built based on the same mechanical structure from Section B.2.2. At the end, a precision model can be built based on the residual from these two sub-models. The 2D RMS of the reflected star positions in the focal plane indicates the pointing accuracy of the telescope.

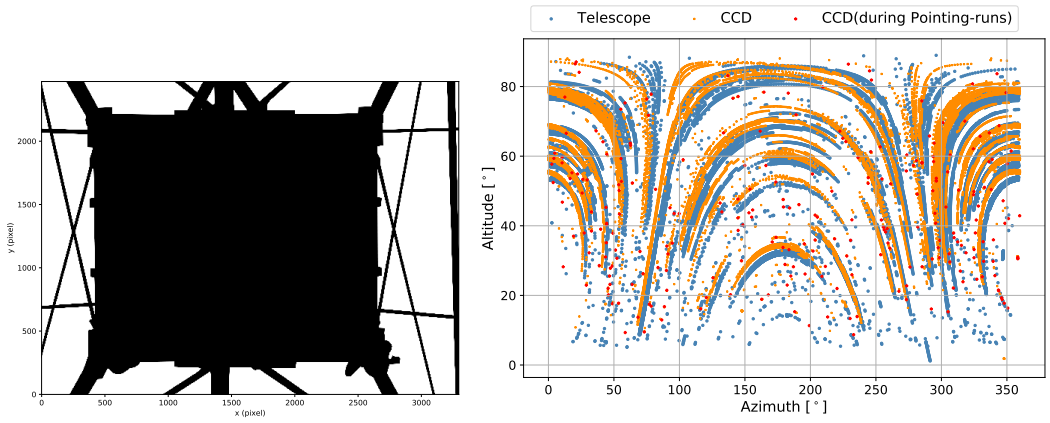

(a) (b)

Figure B.17 (a) The mask for covering the MAGIC and MST telescope structure frame. (b) The sky coverage of the telescope and CCD orientation. The CCD camera is following the tracking of MAGIC. The red dots indicate the pointing-runs period.

B.4.1 Pointing Data

There are several properties exist in the data. For instance the time offset between the MAGIC and CCD camera system. The MAGIC pointing data are also modified with the atmospheric refraction, which should be taken into account by the pointing model instead. This correction has removed using *Astropy* with a set of tested atmospheric parameters. In addition, the pointing-runs statistics is very low as can be seen in Figure B.17 (b). In the following, the building process of the pointing model focuses only on one of the pointing-runs period where the statistics is sufficient in the time duration of < 3 days. The purpose is to eliminate the large night-to-night deviation. The sky coverage of this dataset can be found in Figure B.18. To build the necessary sub-models, a 2.5 RMS cut and 6 fitting iterations are performed to get rid of impacts from out-liners.

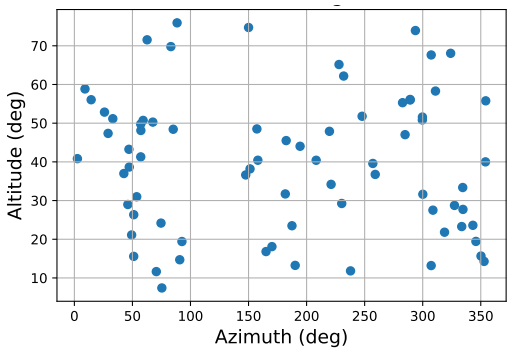

Figure B.18 The sky coverage of the dataset for building the pointing model.

B.4.2 LID Model

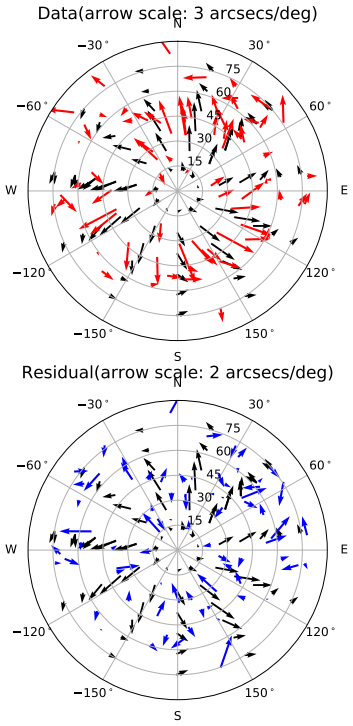

(a)

Parameters	Value
$\lambda_\Delta[^\circ]$	0.0038
$\lambda_a[^\circ]$	-0.0004
$\lambda_\Omega[^\circ]$	-0.0211
$\beta_\Delta[^\circ]$	0.0494
$\beta_a[^\circ]$	-0.1589
$\beta_\Omega[^\circ]$	0.0570
$\lambda_\phi[^\circ]$	0.3502
$\lambda_\theta[^\circ]$	-0.0028
$x_\Delta[^\circ]$	-0.0068
$y_\Delta[^\circ]$	0.0496
$x_{b_1}[^\circ]$	-0.0002
$x_{b_2}[^\circ]$	-0.0000
$y_{b_1}[^\circ]$	-0.0304
$y_{b_2}[^\circ]$	0.0008
$y_{b_3}[^\circ]$	0.0878
$x_\delta[^\circ]$	-0.0002
$y_r[^\circ]$	-0.0110

(b)

Figure B.19 (a) The LID model and the residual. The black, red and blue arrows indicate the model, data and residual respectively. (b) The parameters of the LID model.

The LID Model is built based on the mechanical structure presented in Section B.2.2, aiming to correct reproducible errors. The nominal telescope orientation is the input parameter. The shift of the reflected star relative to the Cherenkov camera centre is being modelled. The derivation of the Cherenkov camera centre has discussed in Section 3.2.1.

The LID model, residuals and parameters can be found in Figure B.19. The vertical and horizontal residuals of the data in terms of altitude and azimuth are shown in Figure B.20 respectively. The residuals are mostly flat. This gives an error of 15.31" and 10.39" in vertical and horizontal direction respectively as indicated in Figure B.21. The 2D RMS of the reflected star positions is able to reduce from 21.52" to 11.25" after the the application of the LID Model as shown in Figure B.22.

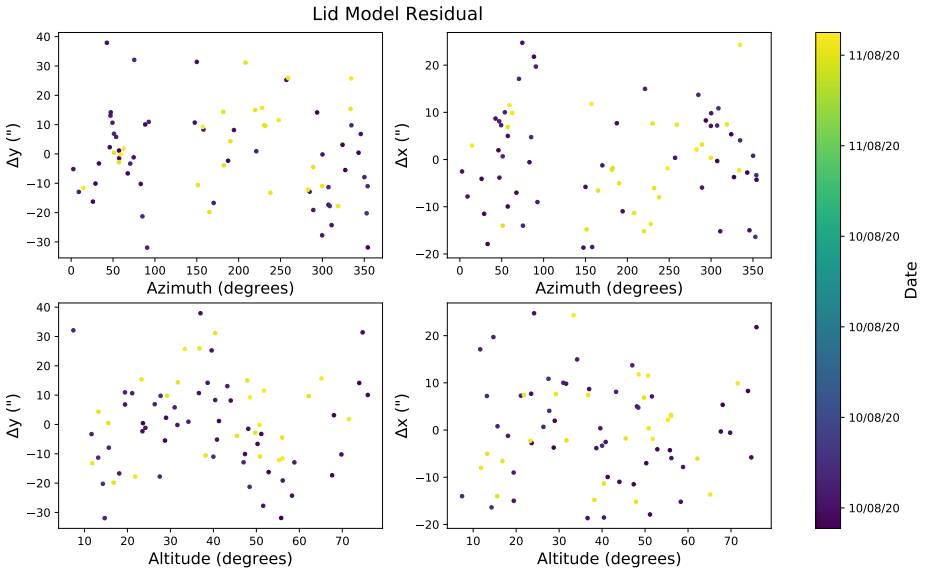

Figure B.20 The vertical and horizontal residuals in terms of altitude and azimuth after the application of the LID model.

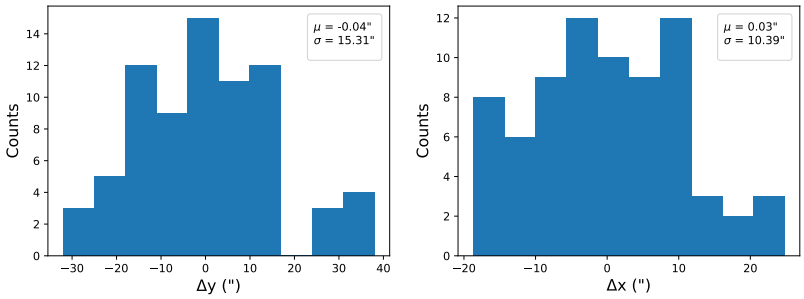

Figure B.21 The residual distribution in the vertical (left) and horizontal (right) directions respectively. The means and standard deviations are shown.

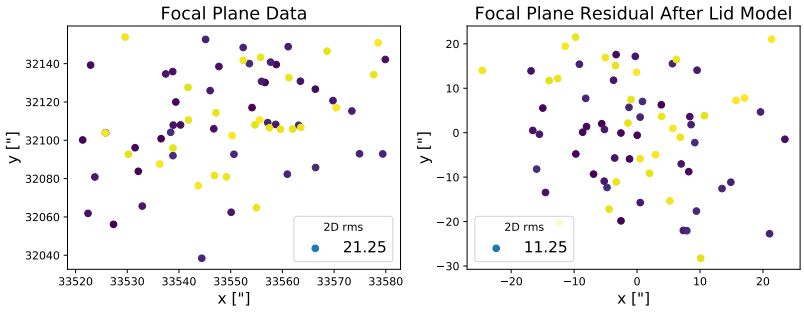

Figure B.22 (Left) The original reflected star position on the lid. (Right) The corrected reflected star position on the lid. The 2D RMS is 11.25".

B.4.3 SKY Model

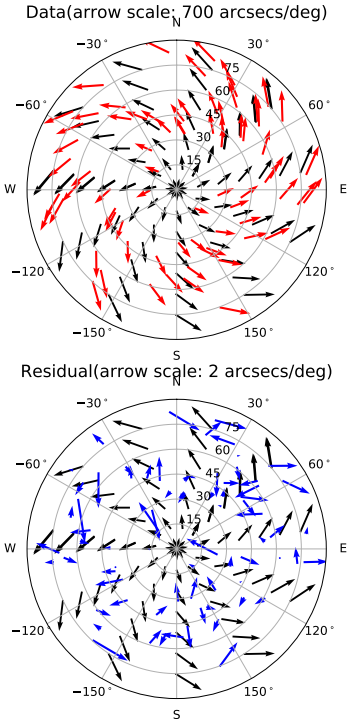

(a)

Parameters	Value
$\lambda_\Delta[^\circ]$	-1.1896
$\lambda_a[^\circ]$	-0.0060
$\lambda_\Omega[^\circ]$	-104.6007
$\beta_\Delta[^\circ]$	-2.0924
$\beta_a[^\circ]$	-3.3123
$\beta_\Omega[^\circ]$	-2.2873
$\lambda_\phi[^\circ]$	39.0733
$\lambda_\theta[^\circ]$	-0.0060
$x_\Delta[^\circ]$	-1.0583
$y_\Delta[^\circ]$	-2.5210
$x_{b_1}[^\circ]$	0.9943
$x_{b_2}[^\circ]$	-0.0421
$y_{b_1}[^\circ]$	2.4234
$y_{b_2}[^\circ]$	0.0747
$y_{b_3}[^\circ]$	-0.8416
$x_\delta[^\circ]$	0.9923
$y_r[^\circ]$	0.0210

(b)

Figure B.23 (a) The SKY model and the residual. The black, red and blue arrows indicate the model, data and residual respectively. (b) The parameters of the SKY model.

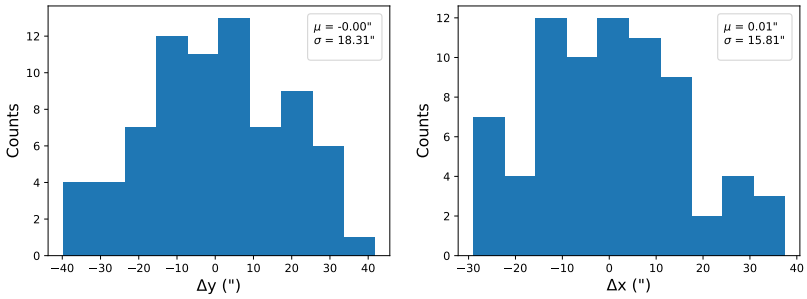

Figure B.24 The residual distribution in the vertical (left) and horizontal (right) directions respectively. The means and standard deviations are shown.

The SKY Model is again built based on the mechanical structure presented in Section B.2.2 and it is responsible for non-reproducible errors. The nominal CCD orientation derived from the *libPointingMST* is the input parameter. In order to use the mechanical structure with the same coordinate system, the nominal telescope orientation (in equatorial

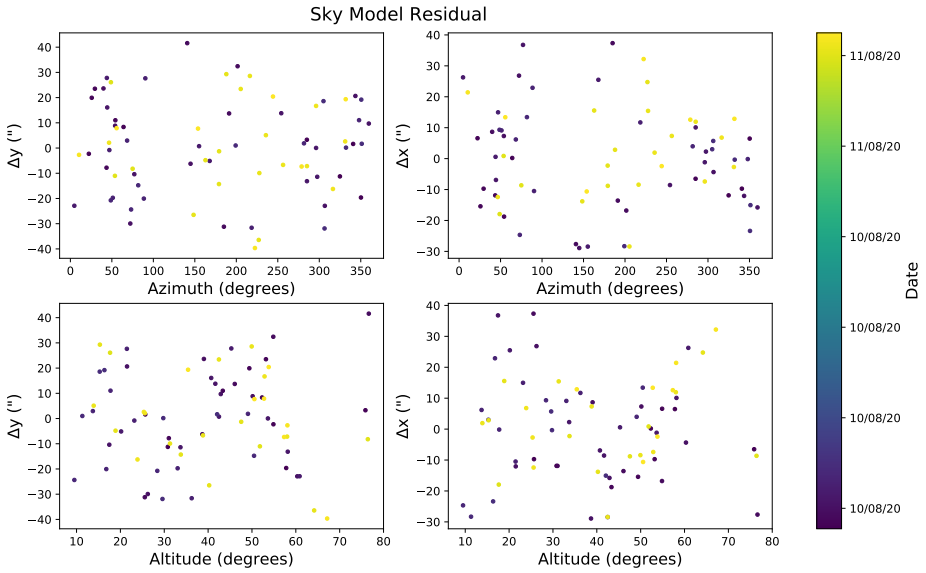

Figure B.25 The vertical and horizontal residuals in terms of altitude and azimuth after the application of the SKY model.

coordinate) has been projected onto the CCD chip (in CCD pixel coordinate). This is done through the proper transformation using the H.E.S.S. pipeline, *HAP*. Note that the nominal telescope orientation is essentially the target star position during the pointing runs. The SKY model therefore describes the shift of the projected star relative to the CCD camera centre.

The SKY model, residuals and parameters can be found in Figure B.23. It gives an error of 18.31" and 15.81" in vertical and horizontal direction respectively as stated in Figure B.24, which is in general larger than the result from the LID model. This might due to the CCD camera is not tightly screwed or the distortion of spots in the night sky background, which then affect the derivation of the CCD orientation.

B.4.4 Precision Model/SKY-LID Model

As discussed in Section B.2.1, the mispointing of the LID model should essentially be the same as the SKY model. Therefore one can fit a linear function to the residual from both models using

$$p_1 + p_2 \Delta_{\text{sky}}, \tag{B.20}$$

where Δ_{sky} is the vertical/horizontal SKY residual. The resulting fine correction is illustrated in Figure B.26 and B.27. The precision model gives an error of 10.95" and 8.45" in the vertical and horizontal directions of the reflected star position respectively. The residual

is still large in the vertical direction. This might come from the wobbling effect due to the lightweight carbon fibre-epoxy composite tubes of the MAGIC telescope.

Nevertheless, the pointing model of this work allows the MAGIC telescope to attain an accuracy of 9.78". This shows the feasibility of the single-CCD concept onto the future CTA MST.

Parameters	Altitude	Azimuth
p_1	0.0038	-4.0074
p_2	0.2943	0.3871

Table B.2 The parameters of the precision model.

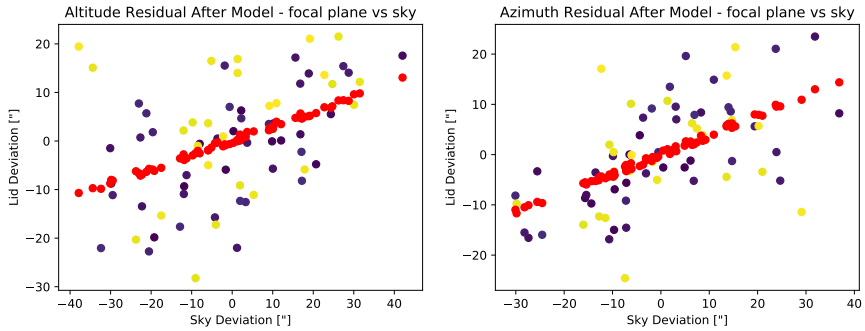

Figure B.26 The altitude (left) and azimuth (right) residuals of the LID and SKY model. The red points denote the precision model.

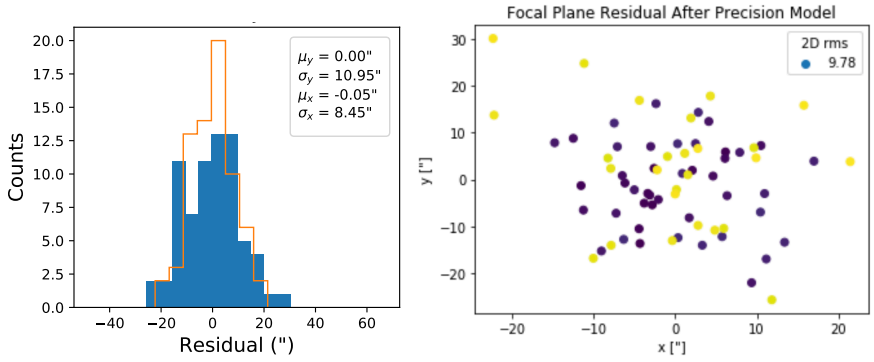

(a) (b)

Figure B.27 (a) The altitude and azimuth residual from the precision model. The means and standard deviations are shown. (b) The corrected reflected star position on the lid. The 2D RMS is 9.78".

References

[1] Aharonian, F. et al. (2008). High energy astrophysics with ground-based gamma ray detectors. *Reports on Progress in Physics*, 71:096901. [link].

[2] Aharonian, F. et al. (2020). Probing the sea of galactic cosmic rays with Fermi-LAT. *Physical Review D*, 101:083018. [link].

[3] Aharonian, F. and H.E.S.S. Collaboration (2006). Observations of the Crab nebula with H.E.S.S. *Astronomy and Astrophysics*, 457:899–915. [link].

[4] Aharonian, F. A. and Atoyan, A. M. (1996). On the emissivity of π^0-decay gamma radiation in the vicinity of accelerators of galactic cosmic rays. *Astronomy and Astrophysics*, 309:917–928. [link].

[5] Aharonian, F. A. and Bogovalov, S. V. (2003). Exploring physics of rotation powered pulsars with sub-10 GeV imaging atmospheric Cherenkov telescopes. *New Astronomy*, 8:85–103. [link].

[6] Apel, W. et al. (2013). KASCADE-Grande measurements of energy spectra for elemental groups of cosmic rays. *Astroparticle Physics*, 47:54–66. [link].

[7] Arnaud, K. A. (2022). *Parameter estimation in X-ray astronomy in the Chandra and XMM-Newton era*. PhD thesis, NASA/Xanadu/Xspec. [link].

[8] Bakunin, O. G. (2008). *Turbulence and Diffusion: Scaling Versus Equations*. Springer, Moskva, first edition.

[9] Becherini, Y. (2011). A new analysis strategy for detection of faint gamma-ray sources with Imaging Atmospheric Cherenkov Telescopes. *Astroparticle Physics*, 34:858–870. [link].

[10] Bednarek, W. and Sobczak, T. (2013). Gamma-rays from millisecond pulsar population within the central stellar cluster in the Galactic Center. *Monthly Notices of the Royal Astronomical Society*, 435:14–18. [link].

[11] Bell, A. R. (2013). Cosmic ray acceleration. *Astroparticle Physics*, 43:56–70. [link].

[12] Bell, A. R. et al. (2013). Cosmic-ray acceleration and escape from supernova remnants. *Monthly Notices of the Royal Astronomical Society*, 431:415–429. [link].

[13] Berezhko, E. G. and Völk, H. J. (2008). Hadronic versus leptonic origin of the gamma-ray emission from supernova remnant RX J1713.7-3946. *Astronomy and Astrophysics*, 492:695–701. [link].

[14] Berezinsky, V. et al. (2006). On astrophysical solution to ultrahigh energy cosmic rays. *Physical Review D*, 74:4. [link].

[15] Berge, D. et al. (2007). Background Modelling in Very-High-Energy γ-ray Astronomy. *Astronomy and Astrophysics*, 466:1219–1229. [link].

[16] Biskamp, D. (1986). Magnetic reconnection via current sheets. *The Physics of Fluids*, 29:1520. [link].

[17] Blasi, P. et al. (2007). Gamma rays from clusters of galaxies. *International Journal of Modern Physics A*, 22:681–706. [link].

[18] Blumenthal, G. R. and Gould, R. J. (1970). Bremsstrahlung, Synchrotron Radiation, and Compton Scattering of High-Energy Electrons Traversing Dilute Gases. *Reviews of Modern Physics*, 42:237–270. [link].

[19] Bose, D. et al. (2022). Galactic and Extragalactic Sources of Very High Energy Gamma-rays. *The European Physical Journal Special Topics*, 231:27–66. [link].

[20] Braun, I. (2007). *Improving the Pointing Precision of the H.E.S.S. Experiment*. PhD thesis, Universität Heidelberg. [link].

[21] Caprioli, D. (2012). Cosmic-ray acceleration in supernova remnants: non-linear theory revised. *Journal of Cosmology and Astroparticle Physics*, 2012:038. [link].

[22] Cash, W. (1979). Parameter estimation in astronomy through application of the likelihood ratio. *Astrophysical Journal*, 228:939–947. [link].

[23] Castellina, A. and Donato, F. (2012). *Planets, Stars and Stellar Systems: Astrophysics of Galactic charged cosmic rays*. Springer, first edition. [link].

[24] Colin, A. (2021). VERITAS Observations of the Galactic Center Region at Multi-TeV Gamma-Ray Energies. *The Astrophysical Journal*, 913:115. [link].

[25] Commichau, S. C. (2008). Monte Carlo Studies of Geomagnetic Field Effects on the Imaging Air Cherenkov Technique for the MAGIC Telescope Site. *Nuclear Instruments and Methods in Physics Research Section A*, 595:3. [link].

[26] Coroniti, F. V. (1990). Magnetically Striped Relativistic Magnetohydrodynamic Winds: The Crab Nebula Revisited. *Astrophysical Journal*, 349:538. [link].

[27] Crank, J. (1956). *The Mathematics of Diffusion*. Clarendon Press, Oxford, second edition.

[28] Cristofari, P. (2021). The Hunt for Pevatrons: The Case of Supernova Remnants. *Universe*, 7:324. [link].

[29] CTA Consortium (2021). Sensitivity of the Cherenkov Telescope Array to a dark matter signal from the Galactic centre. *Journal of Cosmology and Astroparticle Physics*, 2021:057. [link].

[30] CTAO (2021). CTAO Instrument Response Functions - prod5 version v0.1. [link].

[31] de Naurois, M. (2012). *L'astronomie γ de très haute énergie. Ouverture d'une nouvelle fenêtre astronomique sur l'Univers non thermique*. PhD thesis, Ecole polytechnique. [link].

[32] de Naurois, M. (2021). The Making of Catalogues of Very-High-Energy γ-ray Sources. *Universe*, 7:421. [link].

[33] Deil, C. et al. (2017). Open high-level data formats and software for gamma-ray astronomy. *AIP Conference Proceedings*, 1792:070006. [link].

[34] Devin, J. (2022). private communication: devin@lupm.in2p3.fr. CNRS-LUPM (France).

[35] Dundovic, A. et al. (2021). Simulating the Galactic Multi-messenger Emissions with HERMES. *Astronomy and Astrophysics*, 653:A18. [link].

[36] Dungey, J. W. (1961). Interplanetary Magnetic Field and the Auroral Zones. *Physical Review Letters*, 6:47. [link].

[37] Engel, R. et al. (2011). Extensive Air Showers and Hadronic Interactions at High Energy. *Annual Review of Nuclear and Particle Science*, 61:467–489. [link].

[38] Erlykin, A. D. and Wolfendale, A. (2015). Vela as a source of cosmic rays responsible for the formation of the knee in the energy spectrum. *Bulletin of the Russian Academy of Sciences: Physics*, 79:308–310. [link].

[39] Funk, S. (2015). Ground- and Space-Based Gamma-Ray Astronomy. *Annual Review of Nuclear and Particle Science*, 65:245–277. [link].

[40] Gabici, S. (2013). Cosmic Rays and Molecular Clouds. *Astrophysics and Space Science Proceedings*, 34:221–247. [link].

[41] Gabici, S. et al. (2009). Broad-band non-thermal emission from molecular clouds illuminated by cosmic rays from nearby supernova remnants. *Monthly Notices of the Royal Astronomical Society*, 396:1629–1639. [link].

[42] Gaensler, B. M. et al. (2006). The Evolution and Structure of Pulsar Wind Nebulae. *Annual Review of Astronomy and Astrophysics*, 44:17–47. [link].

[43] Gaggero, D. et al. (2017a). Diffuse cosmic rays shining in the Galactic center: A novel interpretation of H.E.S.S. and Fermi-LAT gamma-ray data. *Physical Review Letters*, 119:031101. [link].

[44] Gaggero, D. et al. (2017b). Hard Cosmic Ray Sea in the Galactic Center: a consistent interpretation of H.E.S.S. and Fermi-LAT γ-ray data. *ICRC*, 0:0. [link].

[45] Gaug, M. et al. (2019). Using Muon Rings for the Calibration of the Cherenkov Telescope Array: A Systematic Review of the Method and Its Potential Accuracy. *The Astrophysical Journal Supplement Series*, 243:1. [link].

[46] Gillessen, S. (2003). Arcsecond Level Pointing Of The H.E.S.S. Telescopes. *The 28th International Cosmic Ray Conference*, 5:2899. [link].

[47] Globus, N. et al. (2008). Propagation of high-energy cosmic rays in extragalactic turbulent magnetic fields: resulting energy spectrum and composition. *Astronomy & Astrophysics*, 479:97–110. [link].

[48] Grasso, D. and Maccione, L. (2006). Sgr A East as a high energy neutron and neutrino factory in the galactic centre. *Journal of Physics: Conference Series*, 39:429. [link].

[49] Guépin, C. et al. (2018). Pevatron at the Galactic Center: multi-wavelength signatures from millisecond pulsars. *Journal of Cosmology and Astroparticle Physics*, 07:042. [link].

[50] Guépin, C. et al. (2020). Proton acceleration in pulsar magnetospheres. *Astronomy and Astrophysics*, 635:A138. [link].

[51] Hanlon, W. F. (2008). The energy spectrum of ultra high energy cosmic rays measured by the High Resolution Fly's Eye observatory in stereoscopic mode. *The University of Utah*, AAT 3325870. [link].

[52] Haungs, A. (2015). Cosmic Rays from the Knee to the Ankle. *Physics Procedia*, 61:425–434. [link].

[53] Hermann, G. (1997). The HESS array: a new system of 100 GeV IACTs for stereoscopic observations. [link].

[54] H.E.S.S. Collaboration (2006). Discovery of Very-High-Energy Gamma-Rays from the Galactic Centre Ridge. *Nature*, 439:695–698. [link].

[55] H.E.S.S. Collaboration (2014). Diffuse Galactic gamma-ray emission with H.E.S.S. *Physical Review D*, 90:122007. [link].

[56] H.E.S.S. Collaboration (2016). Acceleration of petaelectronvolt protons in the Galactic Centre. *Nature*, 531:476–479. [link].

[57] H.E.S.S. Collaboration (2018a). Characterising the VHE diffuse emission in the central 200 parsecs of our Galaxy with H.E.S.S. *Astronomy and Astrophysics*, 612:A9. [link].

[58] H.E.S.S. Collaboration (2018b). H.E.S.S. first public test data release. *H.E.S.S. Webpage*. [link].

[59] H.E.S.S. Collaboration (2018c). The H.E.S.S. Galactic plane survey. *Astronomy and Astrophysics*, 612:A1. [link].

[60] H.E.S.S. Collaboration (2020). Detection of very-high-energy γ-ray emission from the colliding wind binary η Car with H.E.S.S. *Astronomy and Astrophysics*, 635:A167. [link].

[61] H.E.S.S. Confluence (2016). Calculation Note. [link].

[62] H.E.S.S. Confluence (2019). H.E.S.S. Pointing Mechanical Model. [link].

[63] H.E.S.S. Website (2022). The H.E.S.S. Telescopes. [link].

[64] Hillas, A. M. (1985). Cherenkov Light Images of EAS Produced by Primary Gamma Rays and by Nuclei. *Proceedings from the 19th International Cosmic Ray Conference*, 3:445. [link].

[65] Hooper, D. (2018). TeV gamma rays from Galactic Center pulsars. *Physics of the Dark Universe*, 21:40–46. [link].

[66] Hooper, D. and Linden, T. (2018). Millisecond pulsars, TeV halos, and implications for the Galactic Center gamma-ray excess. *Physical Review D*, 98:043005. [link].

[67] James, F. and Roos, M. (1975). Minuit - a system for function minimization and analysis of the parameter errors and correlations. *Computer Physics Communications*, 10:343–367. [link].

[68] Joshi, V. (2019). *Reconstruction and Analysis of Highest Energy γ-Rays and its Application to Pulsar Wind Nebulae*. PhD thesis, University of Heidelberg. [link].

[69] Jörg, R. H. (2010). Cosmic rays at the highest energies. *Progress in Particle and Nuclear Physics*, 64:351–359. [link].

[70] Kelner, S. R. et al. (2006). Energy spectra of gamma-rays, electrons and neutrinos produced at proton-proton interactions in the very high energy regime. *Physical Review D*, 74:034018. [link].

[71] Khelifi, B. (2015). HAP-Fr, a pipeline of data analysis for the H.E.S.S. II experiment. *ICRC*, 837:8. [link].

[72] Kino, M. et al. (2002). Energetics of TeV Blazars and Physical Constraints on Their Emission Regions. *The Astrophysical Journal*, 564:97. [link].

[73] Knödlseder, J. et al. (2016). GammaLib and ctools: A software framework for the analysis of astronomical gamma-ray data. *Astronomy and Astrophysics*, 593:A1. [link].

[74] Kosack, K. and Badran, H. M. (2004). TeV Gamma-Ray Observations of the Galactic Center. *The Astrophysical Journal*, 608:L97. [link].

[75] Krayzel, F. et al. (2013). *Improved sensitivity of H.E.S.S.-II through the fifth telescope focus system*. PhD thesis, ICRC. [link].

[76] Lagage, P. O. and Cesarsky, C. J. (1983). The maximum energy of cosmic rays accelerated by supernova shocks. *Astronomy and Astrophysics*, 125:249–257. [link].

[77] Li, T.-P. and Ma, Y.-Q. (1983). Analysis methods for results in gamma-ray astronomy. *Astrophysical Journal*, 272:317–324. [link].

[78] Linden, T. and Buckman, B. J. (2018). Pulsar TeV Halos Explain the Diffuse TeV Excess Observed by Milagro. *Physical Review Letters*, 120:121101. [link].

[79] Lloyd, N. M. and Petrosian, V. (2000). Synchrotron Radiation as the Source of Gamma-Ray Burst Spectra. *The Astrophysical Journal*, 543:722. [link].

[80] Longair, M. S. (2011). *High Energy Astrophysics*. Cambridge University Press, Cambridge, third edition. [link].

[81] Mattox, J. R. et al. (1996). The Likelihood Analysis of EGRET Data. *Astrophysical Journal*, 461:396. [link].

[82] Melia, F. and Fatuzzo, M. (2011). Diffusive cosmic-ray acceleration at the Galactic Centre. *Monthly Notices of the Royal Astronomical Society: Letters*, 410:23–27. [link].

[83] Mohrmann, L. (2022). private communication: lars.mohrmann@mpi-hd.mpg.de. MPIK (Germany).

[84] Mohrmann, L. et al. (2019). Validation of open-source science tools and background model construction in γ-ray astronomy. *Astronomy and Astrophysics*, 632:A72. [link].

[85] Mészáros, P. (2006). Gamma-ray bursts. *Reports on Progress in Physics*, 69:2259. [link].

[86] Nakashima, K. (2022). https://github.com/kaoriinakashima/HESS_3Dbkg_syserror. ECAP (Germany).

[87] NASA (2017a). Cassiopeia A Supernova Remnant. [link].

[88] NASA (2017b). Messier 1 (The Crab Nebula). [link].

[89] Nazar, R. I. (1991). Particle acceleration and main parameters of ultra-high energy gamma-ray binaries. *Astrophysics and Space Science*, 184:297–311. [link].

[90] Nekrassov, D. (2010). A detailed study of the H.E.S.S. data from the Galactic Center region. [link].

[91] Nieppola, E. et al. (2008). Blazar sequence – an artefact of Doppler boosting. *Astronomy and Astrophysics*, 488:867–872. [link].

[92] Nigro, C. et al. (2021). Evolution of Data Formats in Very-High-Energy Gamma-Ray Astronomy. *Universe*, 7:374. [link].

[93] Norbury, J. W. (2010). Pion Production Data Needed for Space Radiation. *40th International Conference on Environmental Systems*. [link].

[94] Ohm, S. et al. (2009). Gamma-Hadron Separation in Very-High-Energy gamma-ray astronomy using a multivariate analysis method. *Astroparticle Physics*, 31:383–391. [link].

[95] Parker, E. N. (1958). Cosmic-Ray Modulation by Solar Wind. *Physical Review*, 110:1445. [link].

[96] Parsons, R. D. et al. (2015). HESS II Data Analysis with ImPACT. *ICRC*, 06:322. [link].

[97] Parsons, R. D. and Hinton, J. A. (2014). A Monte Carlo Template based analysis for Air-Cherenkov Arrays. *Astroparticle Physics*, 56:26–34. [link].

[98] Pascal, V. (2005). H.E.S.S. Phase II. *29th ICRC*, 5:163–166. [link].

[99] Peratt, A. L. (1996). Electric space: Evolution of the plasma universe. *Astrophysics and Space Science*, 244:89–103. [link].

[100] Ptuskin, V. S. et al. (1993). Diffusion and drift of very high energy cosmic rays in galactic magnetic fields. *Astronomy and Astrophysics*, 268:726–735. [link].

[101] Sano, H. and Fukui, Y. (2021). The interstellar medium in young supernova remnants: key to the production of cosmic X-rays and γ-rays. *Astronomy and Astrophysics*, 612:A1. [link].

[102] Sawada, T. et al. (2004). A Molecular Face-on View of the Galactic Centre Region. *Monthly Notices of the Royal Astronomical Society*, 349:1167–1178. [link].

[103] Specovius, A. C. (2021). *A new analysis of the PeVatron candidate HESS J1646–458 using a novel analysis technique*. PhD thesis, Friedrich-Alexander-Universität Erlangen-Nürnberg. [link].

[104] Spengler, G. (2020). Search for Galactic Pevatron candidates in a population of unidentified γ-ray sources. *Astronomy and Astrophysics*, 633:A138. [link].

[105] Stecker, F. W. (1971). *Cosmic gamma rays*. NASA Special Publication. [link].

[106] Storm, E. et al. (2017). SkyFACT: High-dimensional modeling of gamma-ray emission with adaptive templates and penalized likelihoods. *Journal of Cosmology and Astroparticle Physics*, 2017:022. [link].

[107] Streil, K. (2022). private communication: katrin.streil@fau.de. ECAP (Germany).

[108] Strong, A. W. et al. (2007). Cosmic-ray propagation and interactions in the Galaxy. *Annual Review of Nuclear and Particle Science*, 57:285–327. [link].

[109] CTA Website (2022). CTA MST requirements. [link].

[110] Data formats for gamma-ray astronomy (2022). Observation index table. [link].

[111] Fermi LAT Collaboration (2011). Observations of the young supernova remnant RX J1713.7-3946 with the Fermi Large Area Telescope. *The Astrophysical Journal*, 734:28. [link].

[112] Fermi-LAT Collaboration (2015). Fermi-LAT Observations of High-Energy Gamma-Ray Emission Toward the Galactic Center. *The Astrophysical Journal*, 819:44. [link].

[113] Gamma-ray astronomy community (2022). Data formats for gamma-ray astronomy. v0.2. [link].

[114] Gammapy Website (2022). Gammapy documentation v0.19. [link].

[115] HEGRA Collaboration (2000). On the optimum spacing of stereoscopic imaging atmospheric Cherenkov telescopes. *Astroparticle Physics*, 13:253–258. [link].

[116] MAGIC Collaboration (2020). MAGIC observations of the diffuse *gamma*-ray emission in the vicinity of the Galactic center. *Astronomy and Astrophysics*, 642:A190. [link].

[117] Naima Website (2022). Naima documentation. [link].

[118] Tiziani, D. (2020). *The first analysis of very-high-energy gamma rays from the Large Magellanic Cloud with a novel analysis technique*. PhD thesis, Friedrich-Alexander-Universität Erlangen-Nürnberg. [link].

[119] Tjus, J. B. and Merten, L. (2020). Closing in on the origin of Galactic cosmic rays using multimessenger information. *Physics Reports*, 872:1–98. [link].

[120] Tsuboi, M. et al. (1999). Dense Molecular Clouds in the Galactic Center Region. I. Observations and Data. *The Astrophysical Journal Supplement Series*, 120:1. [link].

[121] Uchiyama, Y. et al. (2007). Extremely fast acceleration of cosmic rays in a supernova remnant. *Nature*, 449:576–578. [link].

[122] van Eldik, C. (2015). Gamma rays from the Galactic Centre region: a review. *Astroparticle Physics*, 71:45–70. [link].

[123] Vernetto, S. and Lipari, P. (2016). Absorption of very high energy gamma rays in the Milky Way. *Physical Review D*, 94:3009. [link].

[124] Vieu, T. et al. (2022). Cosmic ray production in superbubbles. *Monthly Notices of the Royal Astronomical Society*, 512:1275–1293. [link].

[125] Völk, H. J. and Bernlöhr, K. (2009). Imaging very high energy gamma-ray telescopes. *Experimental Astronomy*, 25:173–191. [link].

[126] Wagner, R. M. (2006). *Measurement of very high energy gamma-ray emission from four blazars using the MAGIC telescope and a comparative blazar study*. PhD thesis, Technische Universität München. [link].

[127] Wilks, S. S. (1938). The Large-Sample Distribution of the Likelihood Ratio for Testing Composite Hypotheses. *Annals of Mathematical Statistics*, 9:60–62. [link].

[128] Wong, Y. W. (2018). Characterization and Optimization of a Single-CCD Concept for the Pointing of Medium-Sized Telescopes (MSTs) for the Cherenkov Telescope Array (CTA). [link].

[129] Yan, Q. Z. et al. (2017). Towards a three-dimensional distribution of the molecular clouds in the Galactic Centre. *Monthly Notices of the Royal Astronomical Society*, 471:2523–2536. [link].

[130] Yang, R.-Z. et al. (2018). Exploring the shape of the γ-ray spectrum around the "π^0-bump". *Astronomy and Astrophysics*, 615:11. [link].

Acknowledgements

Time flies unbelievably fast, yet leaves me with precious knowledge, experience, and memories. Hereby, I would like to express my gratitude to many people.

First of all, many thanks to Prof. Dr. Christopher van Eldik for providing me with a chance to pursue my PhD in ECAP. Also, for his thorough guidance and insight towards this work. Thanks to Prof. Dr. Stefan Funk for being the reviewer of my thesis and providing fruitful discussion in our analysis meeting. Thanks to Dr. Justine Devin, Dr. Lars Mohrmann, and Katrin Streil for allowing me to include their preliminary yet remarkable work in this thesis. Thanks to Dr. Anne Lemiere and Dr. Régis Terrier for their helpful discussions and collaboration with our group. The H.E.S.S. collaboration for the use of their data and constructive discussions. Thanks to Dr. Johannes Veh and Dr. Domenico Tiziani for offering a lot of help in the MST telescope pointing project and computing issues. Thanks to Dr. Markus Garczarczyk and the MAGIC collaboration for the MAGIC campaign and taking care of the CCD-prototype of CTA MST in La Palma.

Thanks a lot to people who were involved in reading the manuscript or giving valuable advice for this thesis, including Katrin, Andi S., Sam, Vikas, Johannes V., Alison, Dima and Tim. Thanks also to Kaori for the discussion towards the Galactic Centre topic. Thanks to Franzi for the joy and comfort she brought to the office 312. Thanks to all my current and former colleagues and workers in ECAP for their infectious laughter, the friendly and cheerful atmosphere, and lending a hand whenever I need help. It was such a long journey, and I am pleased and lucky to have all of you by my side.

Thank you to my friends from CUHK physics. The weekly colloquium is always full of interesting debates. Your accompaniment during the lockdown was unforgettable. Though we are all in different parts of the world, I cherish our connection a lot. Thanks also to my friends for caring and listening to me and providing me with mental health support. Thanks to the existence of a lot of good books, which have accompanied me during all these foreign adventure years and as always.

Lastly, I would like to thank my mum, dad and brother who have given me lots of love, support, and happiness. I always regain my strength when I see their warm smiles and funny pictures. Thanks for rising and growing up with me.

感謝媽媽、爸爸和哥哥，你們的愛成就了今天的我。